



UNIVERSITÄT
BAYREUTH

Fluorescent Sensor Materials based on 3d Transition Metal Complexes

DISSERTATION

zur Erlangung des akademischen Grades einer
Doktorin der Naturwissenschaften (Dr. rer. nat.)
in der Bayreuther Graduiertenschule für Mathematik und Naturwissenschaften
(BayNAT)
der Universität Bayreuth

vorgelegt von

Hannah Kurz

geboren in Aalen

Bayreuth, 2021

Die vorliegende Arbeit wurde in der Zeit von 11.2017 bis 10.2021 an der Universität Bayreuth an der Professur Anorganische Chemie IV unter Betreuung von Frau Prof. Dr. Birgit Weber angefertigt.

Vollständiger Abdruck der von der Bayreuther Graduiertenschule für Mathematik und Naturwissenschaften (BayNAT) der Universität Bayreuth genehmigten Dissertation zur Erlangung des akademischen Grades einer Doktorin der Naturwissenschaften (Dr. rer. nat.).

Dissertation eingereicht am: 01.10.2021

Zulassung durch das Leitungsgremium: 05.11.2021

Wissenschaftliches Kolloquium: 08.04.2022

Amtierender Direktor: Prof. Dr. Hans Keppler

Prüfungsausschuss:

Prof. Dr. Birgit Weber (Gutachterin)

Prof. Dr. Roland Marschall (Gutachter)

Prof. Dr. Rainer Schobert (Vorsitz)

Prof. Dr. Hans-Werner Schmidt

Meiner Mama gewidmet

„I'm so excited, and I just can't hide it!“

My complexes/The Pointer Sisters

Table of Contents

Abbreviations.....	III
1 Summary / Zusammenfassung	1
1.1 Summary	1
1.2 Zusammenfassung.....	3
2 Introduction	7
2.1 Sensitivity of 3 <i>d</i> Schiff Base-like Complexes.....	7
2.2 Photophysical Processes in Metal Complexes	11
2.3 3 <i>d</i> Metal-based Photoluminescent Sensor Materials	15
2.4 Photoluminescent Sensors Based on Micelles	17
2.5 Jäger-type Schiff Base-like Ligand System	20
3 Synopsis.....	29
4 Individual Contributions to Joint Publications	41
5 A Fluorescence-Detected Coordination-Induced Spin State Switch.....	43
4.1 Introduction	44
4.2 Results and Discussion.....	46
4.3 Conclusion.....	66
4.4 Notes and References	67
4.6 Supporting Information	73
6 Quenched Lewis Acidity: Studies on the Medium Dependent Fluorescence of Zinc(II) Complexes.....	107
5.1 Introduction	108
5.2 Results and Discussion.....	109
5.3 Conclusions	126
5.4 Experimental Section	127
5.5 Notes and References	130
5.6. Supporting Information	134
7 Self-Assembled Fluorescent Block Copolymer Micelles with Responsive Emission..	153
6.1 Introduction	154
6.2 Results and Discussion.....	155
6.3 Conclusion.....	165
6.4 Notes and References	165
6.5 Supporting Information	169
8 List of Publications.....	193

9	Acknowledgement.....	197
10	(Eidesstattliche) Versicherungen und Erklärungen.....	199

Abbreviations

A	absorbance
Ac	acetyl
ACQ	aggregation-caused quenching
AD-CISSS	absorbance-detected CISSS
AIE(E)	aggregation-induced emission (enhancement)
<i>b</i>	block
BCP	block copolymer
bISC	back intersystem crossing
CASSCF	complete active space self-consistent field
CHN	elemental analysis
CISSS	coordination-induced spin state switch(ing)
cmc	critical micelle concentration
CN	coordination number
CT	charge-transfer
D	donor
DCM	dichloromethane
D_{core}	core diameter
DET	Dexter electron transfer
DFT	density-functional theory
$D_{\text{h}}/D_{\text{hydro}}$	hydrodynamic diameter
DLS	dynamic light scattering
DMAP	4-dimethylaminopyridine
DMF	<i>N,N</i> -dimethylformamide
DMSO	dimethylsulfoxide
DN	donor number
<i>E</i>	energy
Et	ethyl
eq/equiv	equivalent(s)
FD-CISSS	Fluorescence-detected coordination-induced spin state switch(ing)
FRET	Förster resonance energy transfer
FSR	fluorophore-spacer-receptor
<i>g</i>	gerade
<i>G</i>	Gibbs energy

h	hour(s)
<i>H</i>	enthalpy
HOMO	highest occupied molecular orbital
HS	high spin
IC	internal conversion
I_F	Fluorescence Intensity
ILCT	intraligand charge-transfer
IR	infrared
ISC	intersystem crossing
<i>K</i>	equilibrium constant
KS	Kohn-Sham
LC	ligand-centered
LD-CISSS	light-driven coordination-induced spin state switch
LMCT	ligand-to-metal charge-transfer
LS	low spin
LUMO	lowest unoccupied molecular orbital
M	metal
MC	metal-centered
MC-PDFT	multi-configurational pair-density functional theory
Me	methyl
min	minute(s)
MLCT	metal-to-ligand charge-transfer
MO	molecular orbital
MS	mass spectrometry
NIR	near-infrared
NMR	nuclear magnetic resonance
OAc	acetate
<i>p</i>	pressure
<i>P</i>	spin pairing energy
PL	photoluminescence
ppm	parts per million
PS	polystyrene
<i>p</i> -TSA	<i>p</i> -toluenesulfonic acid
PXRD	powder X-ray diffraction
py	pyridine
P4VP	poly(4-vinylpyridine)

QY	quantum yield
S	entropy
S	total spin
S	singlet state
salen	N,N' -bis(salicylidene)ethylenediamine
salophen	N,N' -bis(salicylidene)phenylenediamine
SCO	spin crossover
SQUID	superconducting quantum interference device
SqPy	square-pyramidal
T	temperature
T	triplet state
TADF	thermally activated delayed fluorescence
TCSPC	time-correlated single photon counting
TD-DFT	time-dependent density-functional theory
TEM	transmission electron microscopy
T_g	glass transition temperature
THF	tetrahydrofuran
Tol	toluene
TTF	tetrathiafulvalene
u	ungerade
UV	ultraviolet
vis	visible
vs	versus
XRD	X-ray diffraction
δ	chemical shift
Δ_o	ligand field splitting in an octahedral coordination sphere
ε	molar extinction coefficient
τ	excited state lifetime
ϕ	quantum yield
4-CN-Py	4-cyanopyridine

1 Summary / Zusammenfassung

1.1 Summary

The aim of this work was the design of photoluminescent sensor materials based on 3d transition metal complexes composed of Schiff base-like ligands. In this work, the focus was on the influence of axial coordination on the emission properties.

In the first project the effect of coordination-induced spin state switching (CISSS) on the optical properties of a series of nickel(II) complexes, bearing a fluorescent phenazine backbone was investigated. UV-vis measurements of titration series of the non-coordinating solvent chloroform and the strong Lewis base pyridine showed continuous and drastic changes of the absorption properties with growing pyridine amount. Thereby, the pyridine equivalents required to induce a CISSS strongly depend on the Lewis acidity of the nickel(II) metal center. While the complexes **[Ni(1–3)]** all require similar amounts of pyridine, the introduction of electron withdrawing CF₃ substituents in **[Ni(4)]** and through this, the strongly enhanced Lewis acidity of the Ni(II) metal center, result in a drastically increased sensitivity towards pyridine. Due to the acid-base character of the coordination process, the sensitivity of the nickel(II) complexes towards axial donors correlates as well with the basicity of the donor. Remarkably, **[Ni(1–3)]** feature fluorescence in the non-coordinating solvent chloroform with quantum yields of $5 \pm 1\%$ and excited state lifetimes in the order of 1 ns at room temperature. In contrast, **[Ni(4)]** is non-emissive in all solvents. DFT calculations point to a substitution-dependent nature of the lowest excited states. Even though, the HOMOs and LUMOs of all complexes are predominantly phenazine centered, the transition dipoles of the leading optical transitions of **[Ni(1–3)]** and **[Ni(4)]** point in opposite directions. While for **[Ni(1–3)]** a charge shift from the [NiN₂O₂] chelate to the phenazine was observed, the opposite is the case for **[Ni(4)]**. This leads to a MLCT-like transition for **[Ni(1–3)]** and a LMCT-like transition for **[Ni(4)]**, causing non-radiative deactivation. The emission spectra of chloroform/pyridine series of **[Ni(1–3)]** showed successive fluorescence quenching upon pyridine addition. Contrary to the implication of solely static quenching upon coordination in the ground state, the upward-curved Stern-Volmer plot hints towards additional dynamic quenching in the excited state. In agreement, comparing the pyridine concentration dependency of the absorbance and the emission reveals a higher sensitivity of the fluorescence-detected CISSS (FD-CISSS). This is also reflected in a solvent series of **[Ni(1)]**, where most solutions are CISSS-silent in the absorbance spectra, but CISSS-

active in the emission spectra. The degree of quenching can be clearly correlated to the basicity of the solvent. The enhanced sensitivity of the FD-CISSS can be attributed to a drastically increased Lewis acidity of the formally nickel(III) metal center of **[Ni(1–3)]** in the excited state due to the MLCT-like character of the lowest excited state.

Coordination-induced emission changes are not limited to nickel(II) complexes. As zinc(II) complexes tend to overcome the unfavored square-planar coordination sphere through stacking into dimers/oligomers, coordination-induced destacking can affect the emission properties as well. The effect of targeted destacking on the emission was studied for a series of zinc(II) complexes bearing nitrile substituents in the ligand backbone. While the absorbance behavior of **[Zn(5–7)]** only slightly depends on the Lewis basicity of the solvent, drastic changes were observed in the emission behavior. Thereby, a strong emission was observed in coordinating solvents, whereas a close-to-zero emission was observed in non/weakly-coordinating solvents. As a result, chloroform/pyridine series of **[Zn(5–7)]** showed a remarkable turn-on emission behavior based on coordination-induced destacking. Even though the optical behavior is qualitatively similar to that of the closely related **[Zn(sal)]**, an enormous sensitivity reduction was observed for **[Zn(5–7)]**. As DFT calculations revealed an even higher Lewis acidity for **[Zn(5–7)]** relative to **[Zn(sal)]**, the sensitivity decrease must be based on strongly stabilized stacked dimers/oligomers. Indeed, DFT calculations revealed the formation of a completely new stacking motif based on (ZnO)₂ macrocycles.

In the next step, the complex **[Zn(5)]** was encapsulated into polystyrene-*block*-poly(4-vinylpyridine) (PS-*b*-P4VP) block copolymer micelles (BCP), that form through self-assembly in toluene. The micelles are composed of a PS shell and a P4VP core providing pyridine coordination sites. The **[Zn(5)]@BCP** hybrids show a strong green emission due to coordination of pyridine moieties to the zinc(II) complexes within the micelle core. All **[Zn(5)]@BCP** hybrids exhibit higher quantum yields and longer lifetimes than pure **[Zn(5)]** in pyridine, suggesting the prevention of dynamic quenching processes upon embedment in the P4VP core. Chloroform/toluene series were studied to investigate the effects of micelle formation on the emission properties. DLS measurements confirmed the absence of micelles in chloroform-rich solutions, whereas micelles were observed above a toluene content of 20 vol%. Since no turn-on behavior could be obtained due to a non-negligible amount of coordinated **[Zn(5)]** in chloroform, the chloroform was acidified to receive the nearly non-emissive ligand. This acidification indeed leads to a remarkable turn-on emission sensor behavior that correlates with the micelle formation.

1.2 Zusammenfassung

Das Ziel dieser Arbeit war die Entwicklung photolumineszenter Sensormaterialien basierend auf *3d* Übergangsmetallkomplexen, die aus Schiffsbasis-ähnlichen Liganden aufgebaut sind. In dieser Arbeit lag der Schwerpunkt auf dem Einfluss der axialen Koordination auf die Emissionseigenschaften.

Im ersten Projekt wurde die Auswirkung des *coordination-induced spin state switching* (CISSS) auf die optischen Eigenschaften einer Reihe von Nickel(II)-Komplexen untersucht, die ein fluoreszentes Phenazin-Grundgerüst besitzen. UV-Vis Messungen von Titrationsreihen des nicht koordinierenden Lösungsmittels Chloroform und der starken Lewis Base Pyridin zeigten kontinuierliche und drastische Veränderungen der Absorptionseigenschaften mit zunehmender Pyridinmenge. Dabei hängen die zur Induktion eines CISSS erforderlichen Pyridin-Äquivalente stark von der Lewis-Azidität des Nickel(II)-Metallzentrums ab. Während die Komplexe **[Ni(1–3)]** alle ähnliche Mengen an Pyridin benötigen, bewirkt die Einbringung von elektronenziehenden CF₃-Substituenten in **[Ni(4)]** und die dadurch stark erhöhte Lewis-Azidität des Ni(II)-Metallzentrums eine drastisch gesteigerte Empfindlichkeit gegenüber Pyridin. Aufgrund des Säure-Base-Charakters des Koordinationsprozesses korreliert die Empfindlichkeit der Nickel(II)-Komplexe gegenüber axialen Donoren auch mit der Basizität des Donors. Bemerkenswert ist, dass **[Ni(1–3)]** im nicht koordinierenden Lösungsmittel Chloroform Fluoreszenz mit Quantenausbeuten von $5 \pm 1\%$ und Lebensdauern des angeregten Zustandes in der Größenordnung von 1 ns bei Raumtemperatur aufweisen. Im Gegensatz dazu ist **[Ni(4)]** in allen Lösungsmitteln nicht emittierend. DFT-Berechnungen deuten auf eine substitutionsabhängige Natur der niedrigsten angeregten Zustände hin. Obwohl die HOMOs und LUMOs aller Komplexe überwiegend phenazin-zentriert sind, zeigen die Übergangsdipole der entscheidenden optischen Übergänge von **[Ni(1–3)]** und **[Ni(4)]** in entgegengesetzte Richtungen. Während für **[Ni(1–3)]** eine Ladungsverschiebung vom [NiN₂O₂]-Chelat zum Phenazin beobachtet wurde, ist bei **[Ni(4)]** das Gegenteil der Fall. Daraus ergibt sich ein MLCT-ähnlicher Übergang für **[Ni(1–3)]** und ein LMCT-ähnlicher Übergang für **[Ni(4)]**, was zu einer strahlungslosen Deaktivierung führt. Die Emissionsspektren der Chloroform/Pyridin-Reihen von **[Ni(1–3)]** zeigten eine sukzessive Fluoreszenzlöschung bei Zugabe von Pyridin. Im Gegensatz zu der Annahme, dass es sich bei der Koordination im Grundzustand um eine rein statische Löschung handelt, deutet der nach oben gekrümmte Stern-Volmer-Plot auf eine zusätzliche dynamische Löschung im angeregten Zustand hin. Im Einklang dazu offenbart der Vergleich der Pyridin-Konzentrationsabhängigkeit der Absorption und Emission eine höhere Empfindlichkeit des Fluoreszenz-detektierten CISSS (FD-CISSS). Dies spiegelt sich auch in

einer Lösungsmittelsreihe von **[Ni(1)]** wider, bei der die meisten Lösungen in den Absorptionsspektren CISSS-inaktiv, in den Emissionsspektren jedoch CISSS-aktiv sind. Das Ausmaß der Löschung kann eindeutig mit der Basizität des Lösungsmittels korreliert werden. Die erhöhte Empfindlichkeit des FD-CISSS kann auf eine drastisch erhöhte Lewis-Azidität des formalen Nickel(III)-Metallzentrums von **[Ni(1-3)]** im angeregten Zustand aufgrund des MLCT-artigen Charakters des niedrigsten angeregten Zustands zurückgeführt werden.

Koordinationsbedingte Emissionsänderungen sind nicht auf Nickel(II)-Komplexe beschränkt. Da Zink(II)-Komplexe dazu neigen, die ungünstige quadratisch-planare Koordinationssphäre durch *stacking* zu Dimeren/Oligomeren zu überwinden, kann das koordinationsinduzierte *destacking* auch die Emissionseigenschaften beeinflussen. Die Auswirkung des gezielten *destacking* auf die Emission wurde für eine Reihe von Zink(II)-Komplexen untersucht, die Nitrilsubstituenten im Ligandengerüst enthalten. Während das Absorptionsverhalten von **[Zn(5-7)]** nur geringfügig von der Lewis-Basizität des Lösungsmittels abhängt, wurden drastische Änderungen im Emissionsverhalten beobachtet. Dabei wurde in koordinierenden Lösungsmitteln eine starke Emission beobachtet, während in nicht/schwach koordinierenden Lösungsmitteln eine Emission nahe Null zu beobachten war. Infolgedessen zeigte die Chloroform/Pyridin-Reihe von **[Zn(5-7)]** ein bemerkenswertes Einschalt-Emissionsverhalten, das auf koordinationsinduziertem *destacking* beruht. Obwohl das optische Verhalten dem des eng verwandten **[Zn(sal)]** qualitativ ähnlich ist, wurde für **[Zn(5-7)]** eine enorme Verringerung der Empfindlichkeit beobachtet. Da DFT-Berechnungen eine noch höhere Lewis-Azidität für **[Zn(5-7)]** im Vergleich zu **[Zn(sal)]** ergaben, muss die Empfindlichkeitsabnahme auf stark stabilisierten gestapelten Dimeren/Oligomeren beruhen. Tatsächlich offenbarten DFT-Berechnungen die Bildung eines völlig neuen Stacking-Motivs basierend auf (ZnO)₂-Makrozyklen.

Im nächsten Schritt wurde der Komplex **[Zn(5)]** in Polystyrol-*block*-poly(4-vinylpyridin) (PS-*b*-P4VP) Blockcopolymermizellen (BCP) eingekapselt, die sich durch *self-assembly* in Toluol bilden. Diese bestehen aus einer PS-Schale und einem P4VP-Kern, der Pyridin-Koordinationsstellen enthält. Die **[Zn(5)]@BCP**-Hybride zeigen eine starke grüne Emission, die auf die Koordination der Pyridineinheiten an die Zink(II)-Komplexe innerhalb des Mizellenkerns zurückzuführen ist. Alle **[Zn(5)]@BCP**-Hybride weisen höhere Quantenausbeuten und längere Lebensdauern auf als reines **[Zn(5)]** in Pyridin, was auf die Verhinderung dynamischer Lösprozesse bei der Einbettung in den P4VP Kern hindeutet. Um die Auswirkungen der Mizellbildung auf die Emissionseigenschaften zu untersuchen, wurden Chloroform/Toluol-Reihen untersucht. DLS-Messungen bestätigten das Fehlen von Mizellen

in chloroformreichen Lösungen, während Mizellen oberhalb eines Toluolgehaltes von 20 Vol% beobachtet wurden. Da aufgrund einer nicht zu vernachlässigenden Menge an koordiniertem **[Zn(5)]** in Chloroform kein Einschaltverhalten erzielt werden konnte, wurde das Chloroform angesäuert, um den nahezu nicht emittierenden Liganden zu erhalten. Diese Ansäuerung führt tatsächlich zu einem bemerkenswerten Emissions-Einschaltverhalten des Sensors, das mit der Mizellbildung korreliert.

2 Introduction

Switchable transition metal complexes have attracted great interest as molecular sensor materials in the last decade. These materials need to combine a sensitive behavior towards external physical or chemical stimuli with a read-out. Optical read-out possibilities such as photoluminescence are interesting in this approach as they are readily detectable. However, photoluminescent complexes are so far mostly based on precious as well as rare-earth metals due to their manifold photophysical properties. Their replacement with abundant and low cost metals is not only of economic but also of ecological interest.¹ In this context, 3*d* transition metal complexes are particularly interesting candidates as some of them show highly sensitive behavior. The sensitivity of these 3*d* metals is often based on an externally induced spin state change as observed in phenomena such as spin crossover or coordination-induced spin state switching. Alternatively, sensitive behavior can be based on metal-mediated structural reorganisation as observed in stacking/destacking processes. However, coupling of a photoluminescent unit with earth-abundant 3*d* transition metals is not trivial. Main challenges are the need of a successful (electronic) coupling of the sensitive with the photoluminescent behavior and the suppression of emission quenching due to low lying metal-centered states. In general, the understanding of the underlying photoluminescent processes is extremely important as this might open the way to a conscious ligand design of highly sensitive photoluminescent sensor materials.

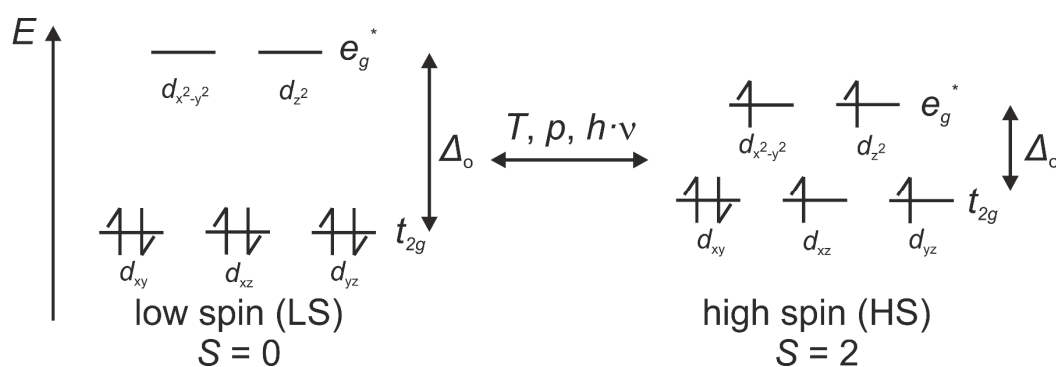
2.1 Sensitivity of 3*d* Schiff Base-like Complexes

Introducing a metal ion into a non-spherical ligand field results in a ligand field splitting of the *d* orbitals. The nature of the orbital splitting depends on the symmetry of the coordination sphere. The tetradentate Schiff base-like ligands used herein typically dictate a square-planar coordination sphere, that can be extended by axial ligands resulting in a square-pyramidal or octahedral coordination sphere. As the five *d* orbitals are no longer degenerated, neither in square-planar, square-pyramidal, nor octahedral coordination spheres, chemical or physical stimuli can impact the occupation of the *d* orbitals. This change in the electronic structure has a strong influence on the structural, magnetic, and optical properties. Even though the spin state

is not changed, metal-dictated stacking among coordination units can alter the properties as well.

Spin crossover

The spin crossover (SCO) phenomenon is mostly observed in $3d^4$ - $3d^7$ metal complexes in an octahedral coordination sphere. Depending on the strength of the ligand field splitting (Δ_o) relative to the size of the spin pairing energy (P) two different border cases can be observed. In case of $\Delta_o \gg P$ the low spin (LS) state with the maximum number of paired electrons and a minimum spin multiplicity is realized. In contrast, for $\Delta_o \ll P$, the high spin (HS) state with a maximum number of unpaired electrons and a maximum spin multiplicity is observed. SCO from HS to LS or *vice versa* can be observed, when none of these extreme cases are realized and the energies are in the same order of magnitude due to an intermediate ligand field strength.²⁻⁴ SCO can then be triggered by an external physical stimulus such as a variation of temperature,^{5,6} pressure,^{7,8} or by light irradiation.^{7,9} The change in the electronic occupation of the d orbitals strongly alters the structural, magnetic, and optical properties of the complexes. For this reason, SCO can be followed by a wide range of methods such as temperature-dependent X-ray diffraction, SQUID magnetometry, or UV-vis spectroscopy. In the past three decades, much focus was given to octahedral iron(II) complexes with a $3d^6$ electronic configuration as a complete SCO results in a drastic magnetic change between the diamagnetic LS ($S = 0$) and the paramagnetic HS ($S = 2$) state (see Scheme 1).



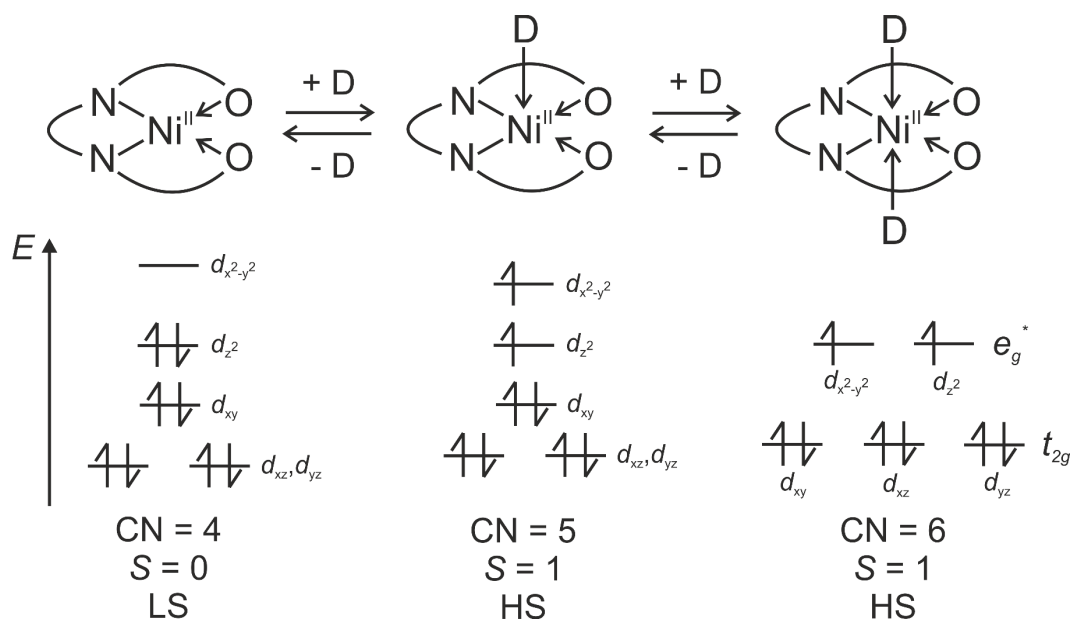
Scheme 1: Schematic representation of the spin crossover (SCO) behavior of a metal center with a $3d^6$ electronic configuration (for example iron(II)).

Spin crossover complexes are promising candidates for various applications in the field of molecular switches including sensor materials, molecular memory units, smart contrast agents, and molecular units for spintronics.¹⁰⁻¹³ A complete and abrupt SCO with a wide thermal hysteresis around room temperature is desired due to bistability at easily accessible temperatures and the memory effect. To obtain this kind of SCO, a high degree of cooperativity

between the metal centers is compulsory. For this reason, SCO is mostly studied in the solid crystalline state, where a high degree of (intermolecular) interactions is present. In contrast, in solution only gradual SCO can be observed that follows the Boltzmann distribution due to a lack of cooperativity. Cooperativity can be based on long range interactions given in coordination polymers,¹⁴ or on short range interactions such as a hydrogen bond network, van der Waals interactions, and/or π - π stacking.¹⁵⁻¹⁷

Coordination-induced spin state switching (CISSS)

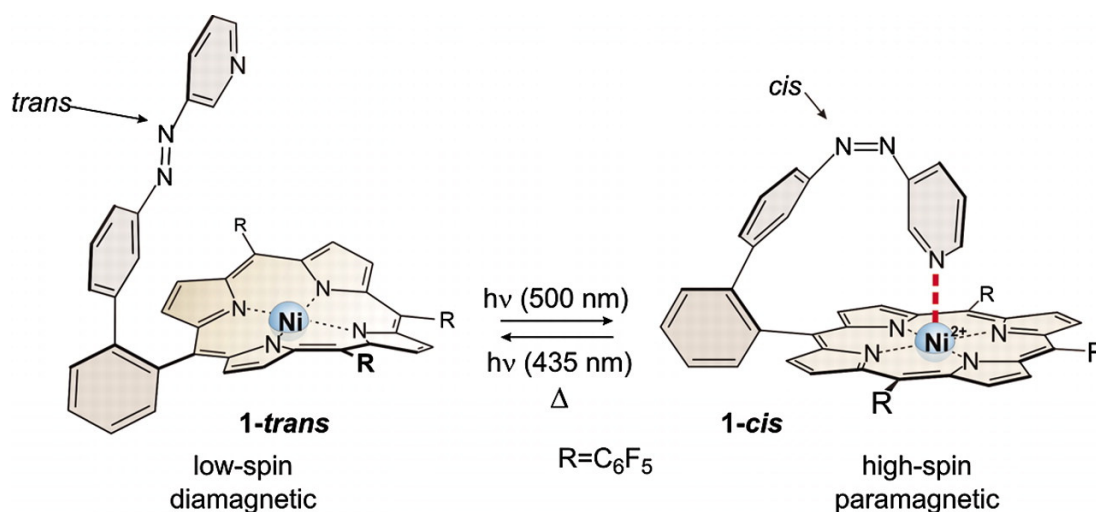
In contrast to SCO, a spin state change of a $3d$ metal complex can be observed as well through alteration of the coordination number. This phenomenon is called coordination-induced spin state switching (CISSS) and is typically studied in solution, as a high flexibility and mobility is required upon the coordination process. Nickel(II) complexes ($3d^8$) in a square-planar coordination sphere (e.g. porphyrin) are typical examples for CISSS-active complexes. Thereby, the nickel(II) metal center can be switched from the square-planar coordination sphere ($S=0$) to the square-pyramidal or octahedral coordination sphere ($S=1$) upon axial coordination as shown in Scheme 2.^{18,19}



Scheme 2: Schematic representation of the coordination-induced spin state switching (CISSS) behavior of a metal center with a $3d^8$ electronic configuration such as nickel(II).

The ligation process is temperature-dependent, which allows to observe CISSS not only in concentration-dependent titration series, but also upon a temperature change.^{20,21} The overall endothermic triplet (HS) to singlet (LS) transition is strongly dominated by the entropy. Thereby, the entropy loss due to a multiplicity decrease is overcompensated by the high entropy

gain upon ligand dissociation. As a result, CN 5/6 is favored at low temperatures, whereas CN 4 is favored at high temperatures and temperature increase results in ligand dissociation.²¹ This results in an inverse temperature-dependency compared to SCO complexes, where the LS is obtained at low temperatures. The structural changes upon CISSS leading to an electronic change strongly affect magnetic and optical properties. For this reason, CISSS can be followed by SQUID magnetometry in solution, NMR spectroscopy (Evans method), and UV-vis spectroscopy. CISSS was mostly studied donor concentration-dependently in titration series. However, Herges *et al.* reported on a completely different approach that utilized light irradiation as the external physical stimulus. Hereby, the axial proto-ligand is covalently linked to the tetradentate square-planar porphyrin to give an azopyridine functionalized Ni-porphyrin. Upon light irradiation, the *trans-cis* change in the azo-group results in a light-driven coordination-induced spin state switching (LD-CISSS) of the nickel complex, that can be reversibly driven back upon irradiation with another wavelength (Scheme 3).^{18,22} Further ligand design makes these complexes promising candidates for water soluble contrast agents for magnetic resonance imaging applications.^{23–25}

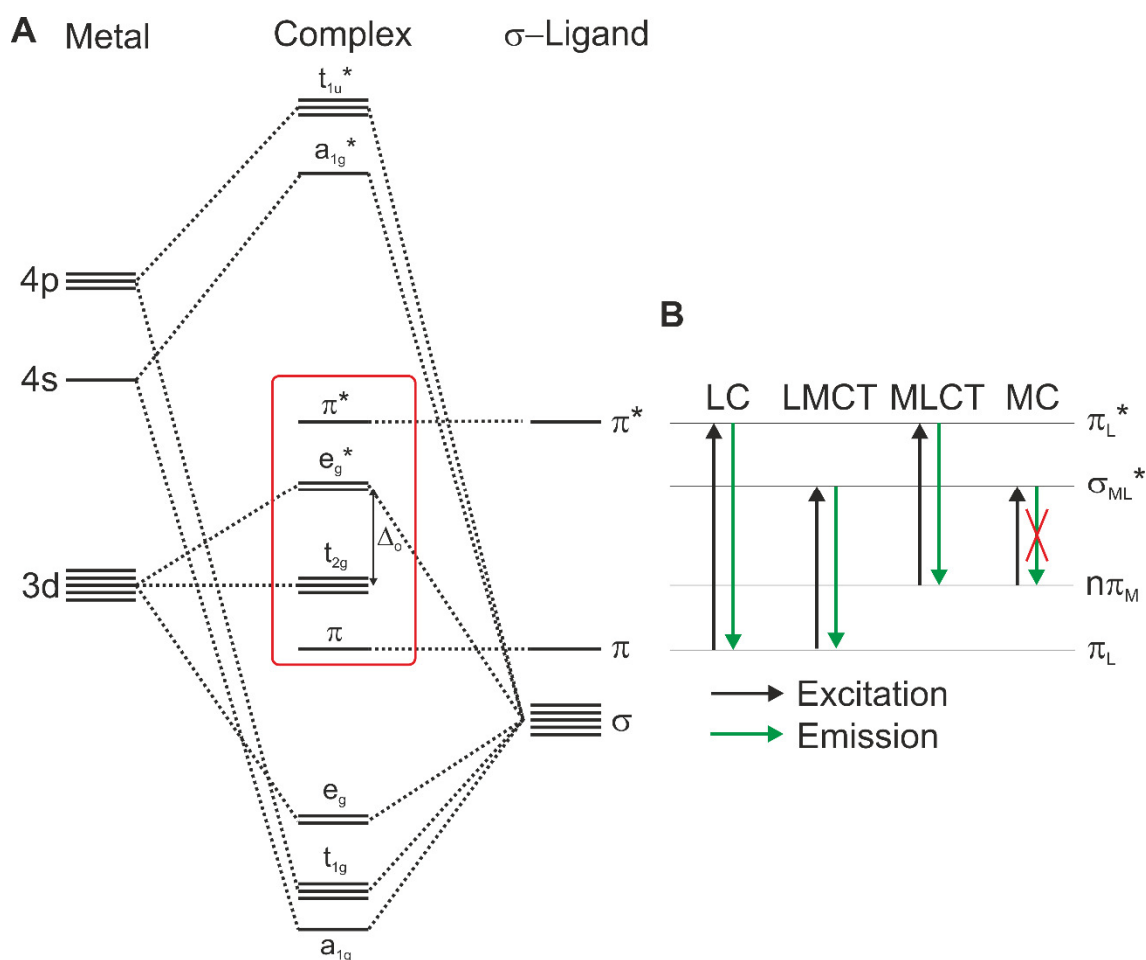


Scheme 3: Schematic representation of the light-driven coordination-induced spin state switch (LD-CISSS) behavior of an azopyridine-functionalised nickel(II) porphyrin complex as reported by Herges *et al.*¹⁸ Reprinted with permission from AAAS.

Metal-dictated stacking

Zinc(II) complexes of tetradentate ligands that dictate a square-planar coordination sphere possess a remarkably high Lewis acidity. This property can be related to the internal strain that is induced by the ligand structure, which hinders the formation of the tetrahedral coordination sphere, where the coordination sites feature the greatest possible distance. In presence of Lewis bases, the coordinatively unsaturated zinc(II) metal center is stabilized by axial coordination of

ground state often decay in a non-radiative way due to the large vibrational overlap of the states (energy gap law).¹ In addition, charge-transfer states can be observed that involve both, metal and ligand orbitals. The classification into metal- or ligand-based orbitals does not indicate a sole contribution of either the ligand or the metal but gives the predominant contribution. Metal-to-ligand charge-transfer (MLCT) is based on a charge shift from a metal center in a low oxidation state to a ligand that can be easily reduced.³⁹ A typical example is $[\text{Ru}(\text{bipy})_3]^{2+}$, that is a well-known candidate for photoredox catalysis due to its highly reactive excited state.⁴⁰ In contrast, strongly electron donating ligands in combination with metal centers in high oxidation states result in ligand-to-metal charge-transfer (LMCT). These conditions are fulfilled for example in $\text{Zr}(\text{IV})$ complexes.^{1,41}



Scheme 5: Simplified molecular orbital diagram for an octahedral (O_h) ML_6 complex with σ -donor ligands showing no π -bonding (A). Assignment of the four characteristic electronic transitions in complexes: ligand-centered (LC), ligand-to-metal charge-transfer (LMCT), metal-to-ligand charge-transfer (MLCT), and metal-centered (MC) (B). Representation based on Heinze *et al.*¹

In general, electronic transitions must follow the selection rules. On the one hand, spin reversal with a change of the multiplicity is formally forbidden. This spin selection rule can be overcome

by a strong spin-orbit coupling as given in heavy atoms.⁴² On the other hand, the transitions have to follow the Laporte rule, which states that transitions that conserve the parity are Laporte-forbidden in centrosymmetric chromophores.³⁹ Therefore, transitions between g orbitals (g: “gerade”; such as $s \rightarrow s$, $s \rightarrow d$, $d \rightarrow s$, and $d \rightarrow d$) and transitions between u orbitals (u: “ungerade”; such as $p \rightarrow p$, $p \rightarrow f$, $f \rightarrow p$, and $f \rightarrow f$) are Laporte-forbidden. For this reason, the characteristic MC $d-d$ states are Laporte-forbidden, whereas CT states that involve a change of the parity are generally allowed. However, these transitions without a change of the parity are weakly allowed in non-centrosymmetric complexes for example in tetrahedral symmetry (T_d). In centrosymmetric complexes (e.g., with octahedral (O_h) symmetry), weak transitions are only allowed by dynamic symmetry lowering/breaking, as provided by Jahn-Teller distortions. Moreover, small deviations from the centrosymmetric O_h symmetry are often dictated by chelate and polydentate ligands resulting in a slightly distorted coordination sphere with reduced symmetry. The degree of deviation from the selection rules strongly impacts the intensity of transitions. A measure for the intensity of transitions in absorption processes is the extinction coefficient ε . The extinction coefficients differ strongly between the very weak Laporte-forbidden $d-d$ states ($\varepsilon = 1-10 \text{ l}\cdot\text{mol}^{-1}\cdot\text{cm}^{-1}$) and the intense fully-allowed CT states ($\varepsilon = 10^3-10^6 \text{ l}\cdot\text{mol}^{-1}\cdot\text{cm}^{-1}$).^{39,43}

Photoluminescence

Photoluminescence is defined as spontaneous light emission from an electronically excited state after photoexcitation. The processes involved in photoluminescence are shown in the Perrin-Jablonski diagram in Figure 1. The absorption of a photon can lead to the excitation of an electron from the ground state S_0 into a vibrational state of the excited electronic state S_1 . This process is followed by vibrational relaxation into the vibrational ground state of S_1 . Thereupon, various radiative or non-radiative processes can occur. Isoenergetic internal conversion (IC) into an excited vibrational state of S_0 results in a non-radiative decay. However, the excitation energy can also result in a radiative decay called photoluminescence. The direct $S_1 \rightarrow S_0$ relaxation upon emission of photons is called fluorescence. Especially, systems with a high spin-orbit coupling can undergo intersystem crossing (ISC) to the excited triplet state T_1 . This is typically the case for second and third row transition metals including the precious metals Ru(II), Ir(II), Pt(II), and Pd(II), as the spin orbit coupling is proportional to the fourth power of the atomic number.^{40,42} The isoenergetic $S_1 \rightarrow T_1$ transition is spin-forbidden due to the change in multiplicity. After vibrational relaxation either a non-radiative deactivation, or a radiative deactivation can occur (again including a spin-forbidden transition), which is called phosphorescence. Based on the vibrational relaxation and the energy loss, the emission is red-

shifted compared to the absorption wavelength. This wavelength shift is named Stokes shift. The emission properties are typically independent of the excitation energy due to the fast disposal of the excess energy upon vibrational relaxation into the vibrational ground state (Kasha's rule).^{44,45}

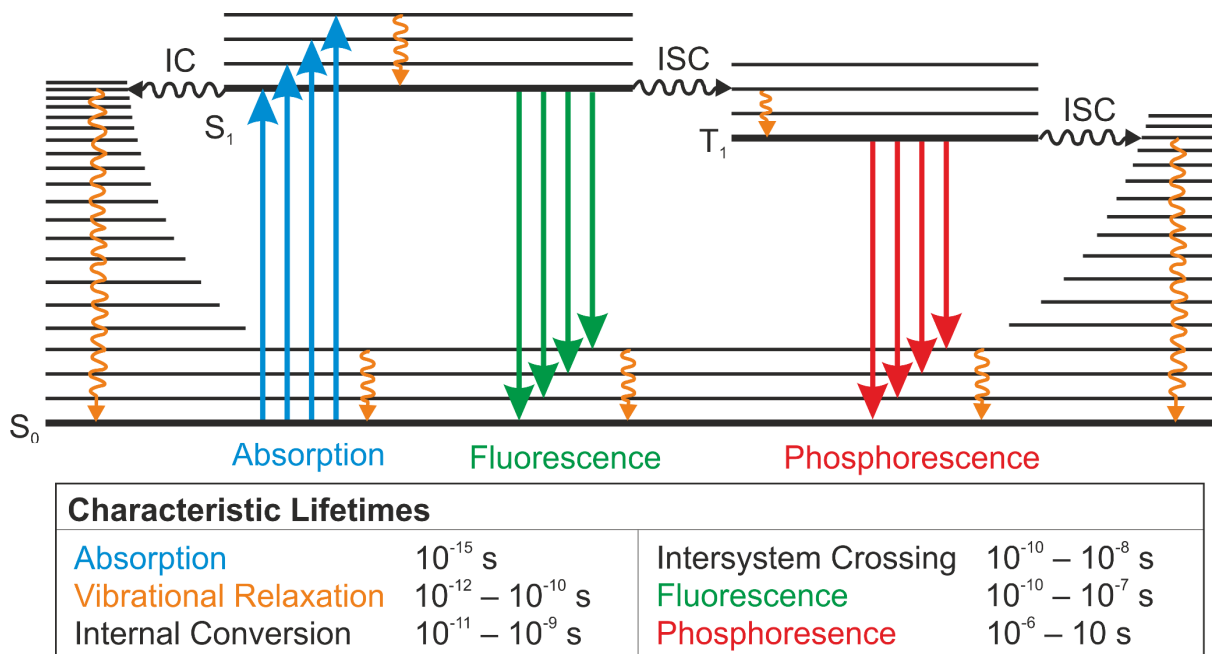


Figure 1: Perrin-Jablonski diagram showing all relevant phenomena involved in photoluminescence. Characteristic lifetimes are taken from Valeur *et al.*⁴⁵

The two photoluminescent processes fluorescence and phosphorescence can be distinguished by their characteristic excited state lifetimes τ . The excited state lifetime is defined as the time it takes the fluorescence intensity (I_F) to reach $1/e$ of the original value after excitation. It is thereby a measure for the time that an average molecule stays in the excited state before it relaxes back to the ground state in a radiative way.⁴⁶ Fluorescence exhibits lifetimes of $\tau = 10^{-10} - 10^{-7}$ s, whereas drastically longer lifetimes of $\tau = 10^{-6} - 10$ s are observed for phosphorescence, due to the involved spin-forbidden multiplicity changes.⁴⁵ One intriguing exception is given in molecules that show thermally activated delayed fluorescence (TADF) due to a thermal back intersystem crossing (bISC). TADF is possible when the triplet state is long-lived, the singlet-triplet gap is rather small, and the temperature is high enough to overcome the singlet-triplet gap.⁴⁷ Photoluminescent processes are also characterised by their quantum yield ϕ . The quantum yield is defined as the number ratio of emitted photons to absorbed photons. It strongly depends on the rate of non-radiative decay that summarizes the rate of IC, ISC, and quenching processes. Quenching processes can be based on a large variety of molecular interactions between the fluorophore and a quencher molecule. Static quenching

describes the formation of non-fluorescent complexes composed of the quencher and the fluorophore in the ground state, as it is often observed in dye aggregates. In contrast, dynamic quenching describes interactions between a quencher and the fluorophore in the excited state. Dynamic quenching can be based on a large variety of processes including excited-state reactions, energy transfer reactions such as Förster resonance energy transfer (FRET) or Dexter electron transfer (DET), or exciplex formation.⁴⁰ In general, the emission behavior is strongly sensitive to the surrounding medium. Physical parameters such as temperature or pressure, as well as chemical parameters such as polarity, viscosity, pH, or the concentration of quencher molecules play a crucial role.⁴⁵ This high sensitivity towards physical and chemical stimuli and the easy read-out through fluorescence spectroscopy or even with the naked eye makes photoluminescence an attractive read-out option for the design of molecular sensor materials.

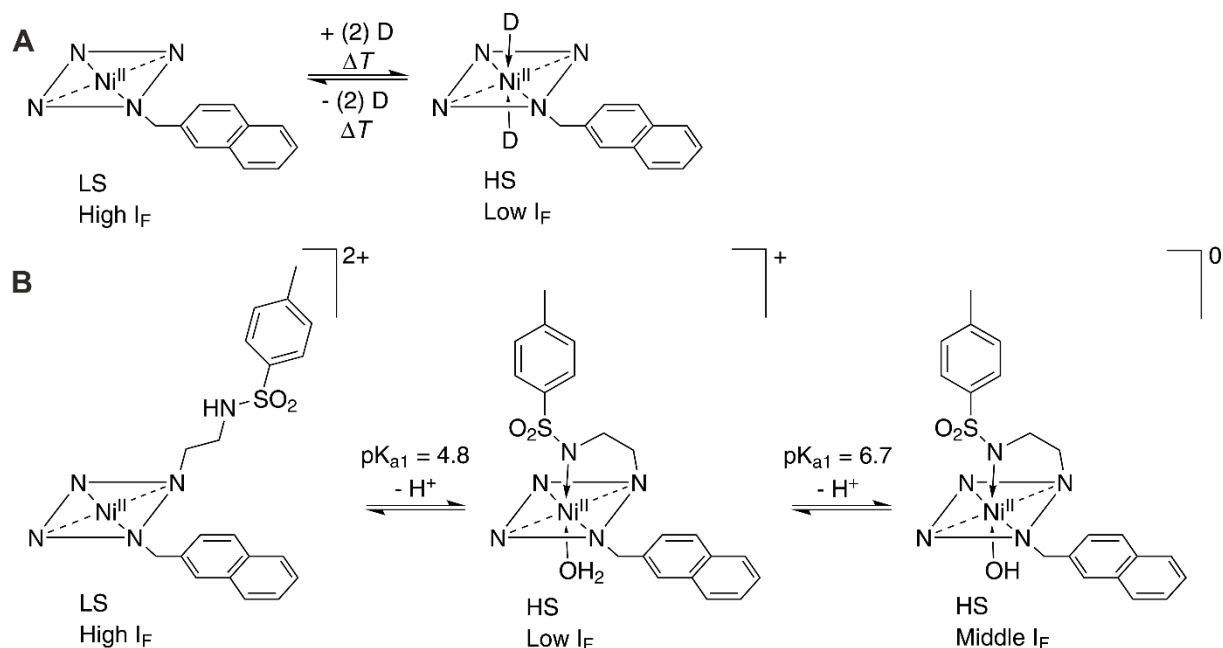
2.3 3d Metal-based Photoluminescent Sensor Materials

The design of photoluminescent 3d transition metal complexes is rather challenging, as especially complexes composed of open shell metal centers are mostly non-emissive. However, several attempts were already reported to couple sensitivity provided by SCO, CISSS, or stacking with photoluminescence to obtain molecular sensors based on 3d metal complexes. In recent years, many photoluminescent sensors based on iron(II) SCO complexes were investigated. To this end, two main strategies have been used: Firstly, the doping of SCO complexes with a fluorophore to obtain composite materials. Secondly, the combination in one photoluminescent SCO compound by complexation of a SCO-active metal ion with a photoluminescent ligand or the usage of photoluminescent counterions.⁴⁸ The composite approach allows a relatively simple synthetic strategy. However, successful coupling between SCO and photoluminescence remains challenging due to the rather close spatial proximity and the often-observed lack of interactions between the two compounds. Since the two compounds are not electronically coupled, the correlation of an emission change with the SCO is mostly based on the structural changes upon SCO, which cause a mechanical strain on the fluorophore. Successful coupling was realized through grafting fluorophores onto SCO nanoparticles,^{49,50} incorporating of fluorophores in Hofmann-type metal organic frameworks,⁵¹ bilayer thin films of a SCO compound and a fluorophore,^{52,53} and through cocrystallization.⁵⁴

Molecular photoluminescent SCO materials are mostly based on intrinsically luminescent ligands or counteranions. The proximity enables strong interactions between the two units. However, introduction of metal centers with an open *d* shell character such as the typical SCO

metal ions iron(II/III), often results in a complete quenching of the photoluminescence independent of the spin state. Nevertheless, successful coupling has been reported in some mononuclear iron(II) complexes,^{55–57} 1D/2D coordination polymers,^{58–61} or heterometallic compounds.⁶² As iron(II) complexes are notorious for their fast non-radiative deactivation due to low lying MC states,^{63,64} it seems reasonable that in most reported SCO-luminescence compounds the photoluminescent unit is not electronically coupled to the metal center. Instead, the change in emission behavior is due to SCO-induced changes of the absorption, reflection, or structure.⁶⁵

To obtain a photoluminescent switch with a sharp on-off/off-on character in solution, the usage of iron(II) SCO complexes is not a reasonable choice. The lack of cooperativity in solution typically results in gradual SCO.⁶⁶ Moreover, limitations of the stability and solubility and especially the small operative temperature range impede the usage of SCO complexes as sensor materials in solution.⁶⁷ Due to the environmental flexibility in solution, sensor materials in solution are easily addressable with chemical stimuli. One approach including a chemically driven spin change of the metal center is the coupling of CISSS behavior with photoluminescence. However, similar to iron(II)/(III), nickel(II) also exhibits an open *d* shell, which in most cases leads to an emission quenching independent of the spin state. It is exactly this open-shell character that renders porphyrins, which are the typical CISSS ligand class, notorious for being non-emissive with excited state lifetimes in the ps regime.^{68,69}



Scheme 6: Schematic representation of the basic principles of a temperature-dependent (A) and pH-dependent (B) photoluminescent CISSS sensor reported by Fabbrizzi *et al.*^{20,70}

Only very few examples of photoluminescent sensor materials based on CISSS have been reported so far. Fabbri *et al.* reported on a fluorescent thermometer, consisting of a Ni(II) cyclam to which a naphthalene unit is covalently linked (see Scheme 6A). The temperature-dependent emission change was attributed to the association/deassociation process of solvent molecules on the nickel(II) metal center.²⁰ A pH-dependent emission tuning was observed by grafting a potentially coordinative unit on the cyclam as shown in Scheme 6B.⁷⁰ Weber *et al.* reported in 2015 on a nickel(II) complex composed of a Schiff base-like ligand system with a fluorescent phenazine backbone. The nickel(II) complex exhibited an emission quenching in the presence of pyridine, which was discussed in terms of axial coordination. These changes in the emission intensity and lifetime were attributed to a favored non-radiative energy transfer.¹⁷

Emission quenching, that is often observed with 3d transition metal complexes, can be avoided by using metal centers with a closed *d* shell such as Zr(IV), Zn(II), or Cu(I).^{1,41,71} Particularly, zinc(II) complexes were studied as molecular sensor materials due to their interesting supramolecular (de)stacking behavior, which indirectly alters the emission as a response to environmental changes. Wang *et al.* reported on luminescent mechanochromic and vapochromic properties of a zinc(II) complex based on a Schiff base ligand equipped with dinitrile substituents.⁷² In a similar study from Di Bella *et al.* (in which the photoluminescent behavior was not studied) this reversible grinding-vaporing behavior was attributed to phase transitions between the J-stacked aggregate and the adduct bearing an axial ligand.³³ In recent years, many derivatives of these Schiff base zinc(II) complexes were studied in solution for their medium-dependent photoluminescent properties. In none of these studies, emission was observed in the absence of potential Lewis bases, whereas a strong emission was observed upon addition of Lewis bases. Di Bella *et al.* studied this effect in detail, both experimentally and computationally, and attributed the lack of emission in absence of donors to a stacking of the complexes into dimers or oligomers.^{27,29,37,73,74} Upon addition of axial donors, destacking and axial ligation results in a strong emission of the resulting mononuclear zinc(II) complexes (CN 5/6). Zhang *et al.* addressed the disassembly of zinc(II) aggregates on purpose. They observed a strong emission increase upon addition of Hg²⁺ ions that induce metal-aromatic interactions.⁷⁵

2.4 Photoluminescent Sensors Based on Micelles

The drastic sensitivity of fluorophores towards the physical and chemical properties of the surrounding medium is often studied directly in titration series by a change of the medium or concentration of quencher molecules. However, the strong medium-dependency can be

investigated as well by an indirect medium change through encapsulation of the fluorophore into nanocontainers. Nanocontainers are 3D structures such as coordination cages, zeolites, or micelles, that offer a nanoscale confinement. Hereby, medium properties such as polarity and viscosity can differ strongly inside the nanoconfinement and outside in the surrounding medium. Furthermore, the low degree of solvation/hydration and the increased guest concentration can result into guest-host and guest-guest interactions including aggregation, that might alter the optical properties as well.^{76,77}

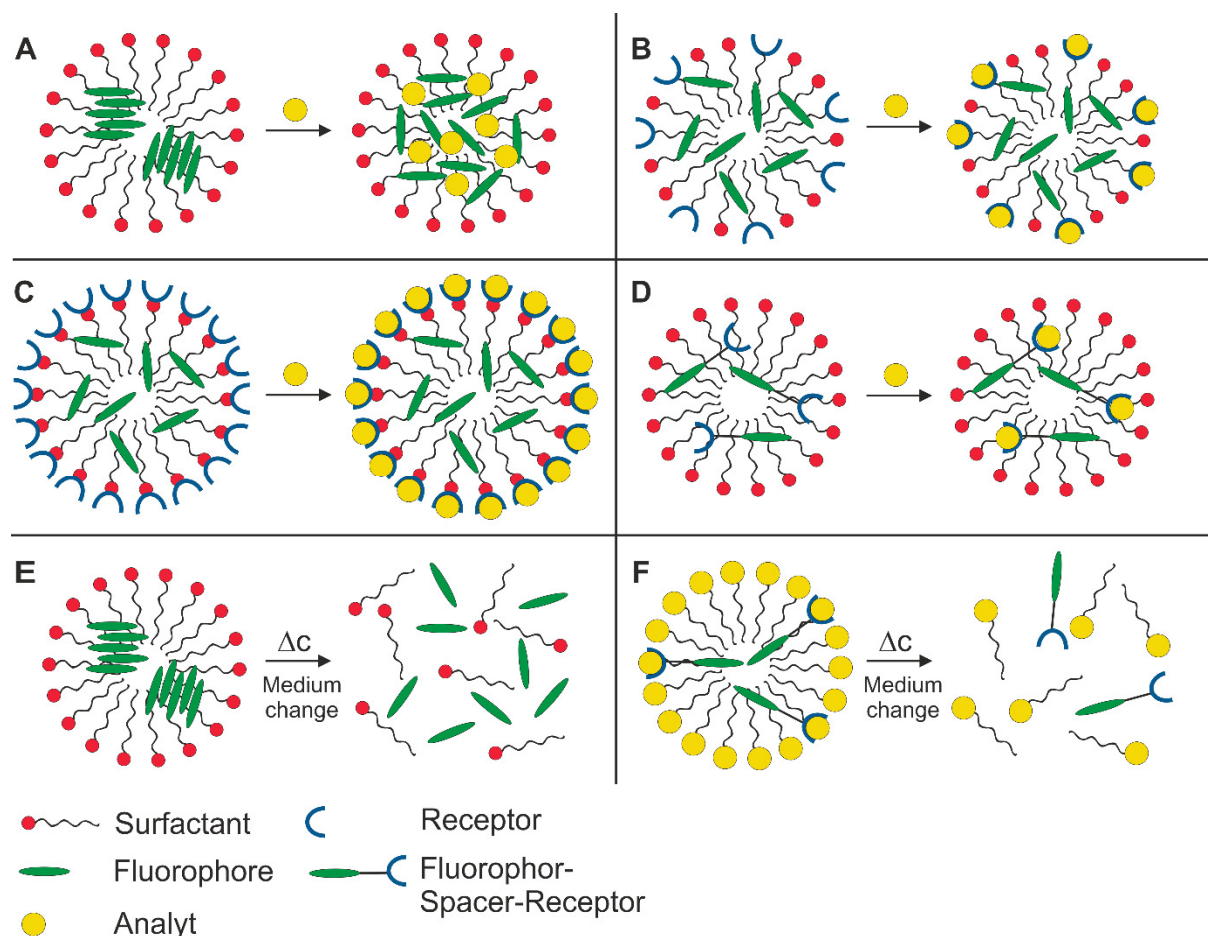


Figure 2: Simplified representations of the different strategies to obtain a photoluminescent self-assembled sensor material based on micelles. Dependent on the system photoluminescent on-off/off-on or ratiometric sensors can be designed.

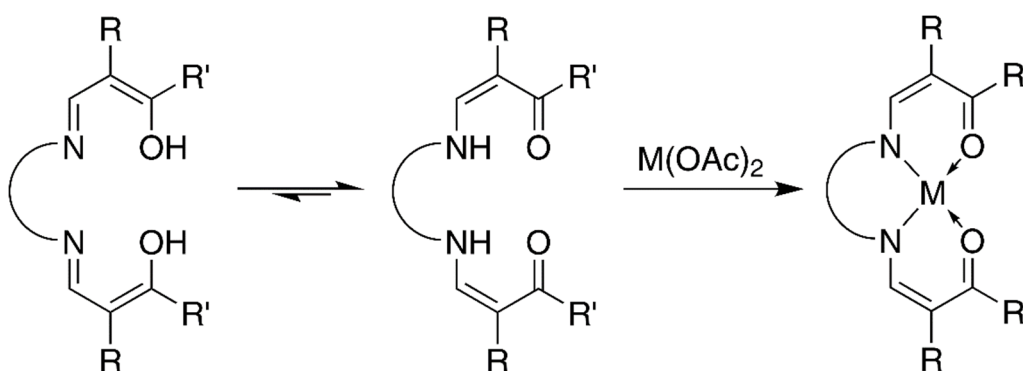
In recent years, much focus was given to the usage of micelles, composed of surfactants or block copolymers, as nanocontainers for self-assembled photoluminescent sensors. So far, these systems have been studied with respect to the recognition and sensing of ions, metal ions, explosives, bioanalytes/proteins, and pH changes.^{76,78-82} Different strategies were reported to obtain an indirect photoluminescent on-off/off-on or ratiometric sensor material based on micelles (see Figure 2A-F). One strategy is the usage of the surfactants/block copolymers to

define the nanoconfinement, while the micelle is not directly involved in the sensing and recognition process. The altered polarity inside the micelles can result in the formation of fluorophore aggregates, that can be disassembled upon addition of an analyt resulting into an emission change (see Figure 2A). This effect was utilized by Ghosh *et al.* to create a fluorescent micelle sensor, in which aggregated pyrene molecules respond to the pH-dependent encapsulation of copper(II) ions.⁸³ A second approach without direct interactions between the surfactant and the fluorophore is the coencapsulation of lipophilic receptors into the micelle, which are not covalently linked to the fluorophore (see Figure 2B). Intramolecular electron or energy transfer mechanisms can thereby result in an emission quenching upon binding of the analyt to the receptor.^{76,84} The surfactant can be equipped with a recognition unit as well and thereby act as a receptor. In this context, interactions between the surfactant and an analyt can alter the microenvironment of the encapsulated fluorophores, which can result in an emission change (see Figure 2C).^{85,86} Another well-investigated approach is based on encapsulation of fluorophore-spacer-receptor systems (FSR) into micelles as shown in Figure 2D. In presence of the analyt, direct interactions between the receptor and the analyt can alter the emission. Again, the surfactant/blockcopolymer micelle is not directly involved in the sensing process. Nevertheless, the micelle enables the stabilization of the mostly organic FSR systems in aqueous medium, which is especially important for biological applications. Moreover, encapsulation can strongly enhance the quantum yield as the rate of non-radiative pathways is often reduced in micelles due to a decreased mobility and flexibility.^{79,87}

As the micelle formation process strongly depends on the concentration of the surfactant and the properties of the medium such as pH or polarity, sensor materials based on micelle (de)formation can be designed (see Figure 2E/F).⁸⁸ The altered polarity and concentration inside the micelles compared to the surrounding medium can result in aggregation leading to aggregation-induced emission (AIE), emission shifts, or aggregation-caused quenching (ACQ). As a result, micelle (de)formation can result in a drastic emission change.⁸⁹ Several workgroups utilized this effect to determine the critical micelle concentration (cmc) by measuring the emission changes of the fluorophore pyrene.^{90,91} Furthermore, a direct sensor material can be designed, where interactions between the surfactant/block copolymer and the fluorophore result into altered optical properties (see Figure 2F). These interactions can be based, for example, on the coordination of potential coordination sites of the surfactant/copolymer micelle on the metal center of a complex, resulting in coordination-induced emission changes.

2.5 Jäger-type Schiff Base-like Ligand System

Jäger-type Schiff base-like ligands were originally established by Jäger *et al.* in 1966⁹² and investigated as bioinorganic model systems featuring interesting redox activities.^{93,94} Weber *et al.* further investigated the SCO behavior of a large number of complexes based on these Jäger-type ligand systems. The tetradentate ligands provide a [N₂O₂] chelate that usually dictates a square-planar coordination sphere. They are close congeners to the well-established Schiff base systems such as *salen* (*N,N'*-bis(salicylidene)ethylenediamine) or *salophen* (*N,N'*-bis(salicylidene)phenylenediamine). In contrast to the latter systems, the keto-enamine/enol-imine equilibrium is strongly shifted to the keto-enamine side in Jäger-type ligands as shown in Scheme 7.⁹⁵ In the deprotonated form, the ligand forms neutral complexes with various divalent metal ions such as iron(II),^{6,17} zinc(II),⁹⁶ copper(II),^{96,97} nickel(II),^{96,97} and cobalt(II).⁹⁸ In addition, neutral complexes with one additional anionic ligand can be obtained upon coordination of trivalent metal ions such as iron(III).⁹⁵ The properties of the Schiff base-like complexes can be easily varied through changing the substituents R/R', altering the equatorial backbone, or the usage of different kinds of axial ligands. Especially, the variation of the ligand backbone allows the integration of additional properties resulting in multifunctional materials.



Scheme 7: Equilibrium of the enol-imine (left) and keto-enamine (middle) tautomers of the Jäger-type Schiff base-like ligands. Conversion of the ligand with a metal acetate to obtain the respective neutral complex (right).

Weber *et al.* reported on a wide variety of iron(II) mononuclear complexes and 1D coordination polymers that showed various kinds of SCO behavior.^{6,15,99} For instance, introduction of the tetrathiafulvalene (TTF) unit in the axial ligand or the backbone of the equatorial ligand results in multifunctional redox-active SCO complexes.^{100,101} Amphiphilic SCO complexes were obtained by equipping the equatorial ligand with long alkyl chains of variable length. These complexes were studied in detail to gain insight into the influence of the phase transition on the magnetic properties.^{102–104} The concatenation of photoluminescence and CISSS/SCO behavior

was investigated in Ni(II) and Fe(II) complexes that are based on a phenazine backbone. Remarkably, these complexes exhibit fluorescent sensor behavior towards external stimuli and a successful coupling of the switching process with the photoluminescence behavior was obtained.^{61,96} A phosphorescent CISSS sensor could be designed upon covalently linking a phosphorescent Ru(II) unit to the equatorial ligand backbone leading to a dinuclear Ni(II)-Ru(II) complex.⁵⁷ Weber *et al.* previously showed that iron(II) Schiff base-like complexes can be nanostructured by encapsulation into polystyrene-*block*-poly(4-vinyl)pyridine (PS-*b*-P4VP) block copolymer micelles, while conserving their interesting SCO behavior.¹⁰⁵⁻¹⁰⁷

References

- (1) Förster, C.; Heinze, K. Photophysics and photochemistry with Earth-abundant metals - fundamentals and concepts. *Chem. Soc. Rev.* **2020**, *49* (4), 1057–1070. DOI: 10.1039/C9CS00573K.
- (2) Sieklucka, B.; Pinkowicz, D., Eds. *Molecular magnetic materials: Concepts and applications*; Wiley-VCH, 2017.
- (3) Gütllich, P.; Goodwin, H. A. *Spin Crossover in Transition Metal Compounds I*; Topics in Current Chemistry, Vol. 233; Springer, 2004. DOI: 10.1007/b40394-9.
- (4) Halcrow, M. A., Ed. *Spin-crossover materials: Properties and applications*; Wiley, 2013.
- (5) Šalitroš, I.; Madhu, N. T.; Boča, R.; Pavlik, J.; Ruben, M. Room-temperature spin-transition iron compounds. *Monatsh. Chem.* **2009**, *140* (7), 695–733. DOI: 10.1007/s00706-009-0128-4.
- (6) Weber, B. Spin crossover complexes with N₄O₂ coordination sphere – The influence of covalent linkers on cooperative interactions. *Coord. Chem. Rev.* **2009**, *253* (19-20), 2432–2449. DOI: 10.1016/j.ccr.2008.10.002.
- (7) Khusniyarov, M. M. How to Switch Spin-Crossover Metal Complexes at Constant Room Temperature. *Chem. Eur. J.* **2016**, *22* (43), 15178–15191. DOI: 10.1002/chem.201601140.
- (8) Gütllich, P.; Ksenofontov, V.; Gaspar, A. Pressure effect studies on spin crossover systems. *Coord. Chem. Rev.* **2005**, *249* (17-18), 1811–1829. DOI: 10.1016/j.ccr.2005.01.022.
- (9) Gütllich, P.; Hauser, A.; Spiering, H. Thermal and Optical Switching of Iron(II) Complexes. *Angew. Chem. Int. Ed.* **1994**, *33* (20), 2024–2054. DOI: 10.1002/anie.199420241.
- (10) Kumar, K. S.; Ruben, M. Sublimable Spin-Crossover Complexes: From Spin-State Switching to Molecular Devices. *Angew. Chem. Int. Ed.* **2021**, *60* (14), 7502–7521. DOI: 10.1002/anie.201911256.
- (11) Kumar, K. S.; Šalitroš, I.; Moreno-Pineda, E.; Ruben, M. Spacer type mediated tunable spin crossover (SCO) characteristics of pyrene decorated 2,6-bis(pyrazol-1-yl)pyridine (bpp) based Fe(II) molecular spintronic modules. *Dalton Trans.* **2017**, *46* (30), 9765–9768. DOI: 10.1039/c7dt02219k.
- (12) Tsukiashi, A.; Min, K. S.; Kitayama, H.; Terasawa, H.; Yoshinaga, S.; Takeda, M.; Lindoy, L. F.; Hayami, S. Application of spin-crossover water soluble nanoparticles for use as MRI contrast agents. *Sci. Rep.* **2018**, *8* (1), 14911. DOI: 10.1038/s41598-018-33362-6.
- (13) Boukheddaden, K.; Ritti, M. H.; Bouchez, G.; Sy, M.; Dîrtu, M. M.; Parlier, M.; Linares, J.; Garcia, Y. Quantitative Contact Pressure Sensor Based on Spin Crossover Mechanism for Civil Security Applications. *J. Phys. Chem. C* **2018**, *122* (14), 7597–7604. DOI: 10.1021/acs.jpcc.8b00778.
- (14) Kurz, H.; Sander, J.; Weber, B. Influence of CF₃ Substituents on the Spin Crossover Behavior of Iron(II) Coordination Polymers with Schiff Base-like Ligands. *Z. Anorg. Allg. Chem.* **2020**, *646* (13), 800–807. DOI: 10.1002/zaac.201900354.
- (15) Kurz, H.; Hörner, G.; Weber, B. An Iron(II) Spin Crossover Complex with a Maleonitrile Schiff base-like Ligand and Scan Rate-dependent Hysteresis above Room Temperature. *Z. Anorg. Allg. Chem.* **2021**, *647* (8), 896–904. DOI: 10.1002/zaac.202000407.
- (16) Weber, B.; Bauer, W.; Pfaffeneder, T.; Dîrtu, M. M.; Naik, A. D.; Rotaru, A.; Garcia, Y. Influence of Hydrogen Bonding on the Hysteresis Width in Iron(II) Spin-Crossover Complexes. *Eur. J. Inorg. Chem.* **2011**, *2011* (21), 3193–3206. DOI: 10.1002/ejic.201100394.
- (17) Lochenie, C.; Heinz, J.; Milius, W.; Weber, B. Iron(II) spin crossover complexes with diamionaphthalene-based Schiff base-like ligands: mononuclear complexes. *Dalton Trans.* **2015**, *44* (41), 18065–18077. DOI: 10.1039/C5DT03048J.

- (18) Venkataramani, S.; Jana, U.; Dommaschk, M.; Sönnichsen, F. D.; Tucek, F.; Herges, R. Magnetic bistability of molecules in homogeneous solution at room temperature. *Science* **2011**, *331* (6016), 445–448. DOI: 10.1126/science.1201180.
- (19) Thies, S.; Bornholdt, C.; Köhler, F.; Sönnichsen, F. D.; Näther, C.; Tucek, F.; Herges, R. Coordination-induced spin crossover (CISCO) through axial bonding of substituted pyridines to nickel-porphyrins: sigma-donor versus pi-acceptor effects. *Chem. Eur. J.* **2010**, *16* (33), 10074–10083. DOI: 10.1002/chem.201000603.
- (20) Engeser, M.; Fabbrizzi, L.; Licchelli, M.; Sacchi, D. A fluorescent molecular thermometer based on the nickel(II) high-spin/low-spin interconversion. *Chem. Commun.* **1999** (13), 1191–1192. DOI: 10.1039/A901931F.
- (21) Boiocchi, M.; Fabbrizzi, L.; Foti, F.; Vazquez, M. Further insights on the high-low spin interconversion in nickel(II) tetramine complexes. Solvent and temperature effects. *Dalton Trans.* **2004** (17), 2616–2620. DOI: 10.1039/B408085H.
- (22) Dommaschk, M.; Schütt, C.; Venkataramani, S.; Jana, U.; Näther, C.; Sönnichsen, F. D.; Herges, R. Rational design of a room temperature molecular spin switch. The light-driven coordination induced spin state switch (LD-CISSS) approach. *Dalton Trans.* **2014**, *43* (46), 17395–17405. DOI: 10.1039/c4dt03048f.
- (23) Dommaschk, M.; Gutzeit, F.; Boretius, S.; Haag, R.; Herges, R. Coordination-induced spin-state-switch (CISSS) in water. *Chem. Commun.* **2014**, *50* (83), 12476–12478. DOI: 10.1039/c4cc05525j.
- (24) Dommaschk, M.; Peters, M.; Gutzeit, F.; Schütt, C.; Näther, C.; Sönnichsen, F. D.; Tiwari, S.; Riedel, C.; Boretius, S.; Herges, R. Photoswitchable Magnetic Resonance Imaging Contrast by Improved Light-Driven Coordination-Induced Spin State Switch. *J. Am. Chem. Soc.* **2015**, *137* (24), 7552–7555. DOI: 10.1021/jacs.5b00929.
- (25) Heitmann, G.; Schütt, C.; Gröbner, J.; Huber, L.; Herges, R. Azoimidazole functionalized Ni-porphyrins for molecular spin switching and light responsive MRI contrast agents. *Dalton Trans.* **2016**, *45* (28), 11407–11412. DOI: 10.1039/c6dt01727d.
- (26) Oliveri, I. P.; Maccarrone, G.; Di Bella, S. A Lewis basicity scale in dichloromethane for amines and common nonprotogenic solvents using a zinc(II) Schiff-base complex as reference Lewis acid. *J. Org. Chem.* **2011**, *76* (21), 8879–8884. DOI: 10.1021/jo2016218.
- (27) Consiglio, G.; Oliveri, I. P.; Failla, S.; Di Bella, S. On the Aggregation and Sensing Properties of Zinc(II) Schiff-Base Complexes of Salen-Type Ligands. *Molecules* **2019**, *24* (13). DOI: 10.3390/molecules24132514.
- (28) Kleij, A. W. Zinc-centered salen complexes: versatile and accessible supramolecular building motifs. *Dalton Trans.* **2009** (24), 4635–4639. DOI: 10.1039/B902866H.
- (29) Di Bella, S. Lewis acidic zinc(II) salen-type Schiff-base complexes: sensing properties and responsive nanostructures. *Dalton Trans.* **2021**, *50* (18), 6050–6063. DOI: 10.1039/D1DT00949D.
- (30) Forte, G.; Oliveri, I. P.; Consiglio, G.; Failla, S.; Di Bella, S. On the Lewis acidic character of bis(salicylaldiminato) zinc(II) Schiff-base complexes: a computational and experimental investigation on a series of compounds varying the bridging diimine. *Dalton Trans.* **2017**, *46* (14), 4571–4581. DOI: 10.1039/c7dt00574a.
- (31) Chakraborty, S.; Bhattacharjee, C. R.; Mondal, P.; Prasad, S. K.; Rao, D. S. S. Synthesis and aggregation behavior of luminescent mesomorphic zinc(II) complexes with 'salen' type asymmetric Schiff base ligands. *Dalton Trans.* **2015**, *44* (16), 7477–7488. DOI: 10.1039/c4dt03989k.
- (32) Giannicchi, I.; Portalone, G.; Dalla Cort, A. Molecular aggregation of novel Zn(II)-salophenpyridyl derivatives. *Supramol. Chem.* **2013**, *25* (9-11), 709–717. DOI: 10.1080/10610278.2013.819976.

- (33) Oliveri, I. P.; Malandrino, G.; Di Bella, S. Phase transition and vapochromism in molecular assemblies of a polymorphic zinc(II) Schiff-base complex. *Inorg. Chem.* **2014**, *53* (18), 9771–9777. DOI: 10.1021/ic5013632.
- (34) Consiglio, G.; Oliveri, I. P.; Punzo, F.; Thompson, A. L.; Di Bella, S.; Failla, S. Structure and aggregation properties of a Schiff-base zinc(II) complex derived from cis-1,2-diaminocyclohexane. *Dalton Trans.* **2015**, *44* (29), 13040–13048. DOI: 10.1039/c5dt01148e.
- (35) Consiglio, G.; Oliveri, I. P.; Failla, S.; Di Bella, S. Supramolecular Aggregates of Defined Stereochemical Scaffolds: Aggregation/Deaggregation in Schiff-Base Zinc(II) Complexes Derived from Enantiopure trans-1,2-Diaminocyclohexane. *Inorg. Chem.* **2016**, *55* (20), 10320–10328. DOI: 10.1021/acs.inorgchem.6b01580.
- (36) Consiglio, G.; Oliveri, I.; Failla, S. Supramolecular Aggregation of a New Substituted Bis(salicylaldiminato)zinc(II) Schiff-Base Complex Derived from trans-1,2-Diaminocyclohexane. *Inorganics* **2018**, *6* (1), 8. DOI: 10.3390/inorganics6010008.
- (37) Salassa, G.; Coenen, M. J. J.; Wezenberg, S. J.; Hendriksen, B. L. M.; Speller, S.; Elemans, J. A. A. W.; Kleij, A. W. Extremely strong self-assembly of a bimetallic salen complex visualized at the single-molecule level. *J. Am. Chem. Soc.* **2012**, *134* (16), 7186–7192. DOI: 10.1021/ja3030802.
- (38) Oliveri, I. P.; Failla, S.; Malandrino, G.; Di Bella, S. Controlling the Molecular Self-Assembly into Nanofibers of Amphiphilic Zinc(II) Salophen Complexes. *J. Phys. Chem. C* **2013**, *117* (29), 15335–15341. DOI: 10.1021/jp4038182.
- (39) Weber, B. *Koordinationschemie*; Springer Berlin Heidelberg, 2014. DOI: 10.1007/978-3-642-41685-9.
- (40) Arias-Rotondo, D. M.; McCusker, J. K. The photophysics of photoredox catalysis: a roadmap for catalyst design. *Chem. Soc. Rev.* **2016**, *45* (21), 5803–5820. DOI: 10.1039/c6cs00526h.
- (41) Zhang, Y.; Lee, T. S.; Favale, J. M.; Leary, D. C.; Petersen, J. L.; Scholes, G. D.; Castellano, F. N.; Milsmann, C. Delayed fluorescence from a zirconium(IV) photosensitizer with ligand-to-metal charge-transfer excited states. *Nat. Chem.* **2020**, *12* (4), 345–352. DOI: 10.1038/s41557-020-0430-7.
- (42) Ravotto, L.; Ceroni, P. Aggregation induced phosphorescence of metal complexes: From principles to applications. *Coord. Chem. Rev.* **2017**, *346*, 62–76. DOI: 10.1016/j.ccr.2017.01.006.
- (43) Ford, P. C. From curiosity to applications. A personal perspective on inorganic photochemistry. *Chem. Sci.* **2016**, *7* (5), 2964–2986. DOI: 10.1039/c6sc00188b.
- (44) Lakowicz, J. R. *Principles of fluorescence spectroscopy*, 3. edition, corrected at 4. printing; Springer, 2010.
- (45) Valeur, B.; Berberan-Santos, M. N. *Molecular fluorescence: Principles and applications*, 2. edition.; Wiley-VCH, 2012. DOI: 10.1002/9783527650002.
- (46) Sauer, M.; Hofkens, J.; Enderlein, J. *Handbook of fluorescence spectroscopy and imaging: From single molecules to ensembles*; Wiley-VCH, 2011. DOI: 10.1002/9783527633500.
- (47) Förster, C.; Heinze, K. Preparation and Thermochromic Switching between Phosphorescence and Thermally Activated Delayed Fluorescence of Mononuclear Copper(I) Complexes. *J. Chem. Educ.* **2020**, *97* (6), 1644–1649. DOI: 10.1021/acs.jchemed.0c00171.
- (48) Senthil Kumar, K.; Ruben, M. Emerging trends in spin crossover (SCO) based functional materials and devices. *Coord. Chem. Rev.* **2017**, *346*, 176–205. DOI: 10.1016/j.ccr.2017.03.024.
- (49) Suleimanov, I.; Kraieva, O.; Sánchez Costa, J.; Fritsky, I. O.; Molnár, G.; Salmon, L.; Bousseksou, A. Electronic communication between fluorescent pyrene excimers and spin

- crossover complexes in nanocomposite particles. *J. Mater. Chem. C* **2015**, *3* (19), 5026–5032. DOI: 10.1039/c5tc00667h.
- (50) Titos-Padilla, S.; Herrera, J. M.; Chen, X.-W.; Delgado, J. J.; Colacio, E. Bifunctional Hybrid SiO₂ Nanoparticles Showing Synergy between Core Spin Crossover and Shell Luminescence Properties. *Angew. Chem. Int. Ed.* **2011**, *50*, 3290–3293. DOI: 10.1002/anie.201007847.
- (51) Delgado, T.; Meneses-Sánchez, M.; Piñeiro-López, L.; Bartual-Murgui, C.; Muñoz, M. C.; Real, J. A. Thermo- and photo-modulation of exciplex fluorescence in a 3D spin crossover Hofmann-type coordination polymer. *Chem. Sci.* **2018**, *9* (44), 8446–8452. DOI: 10.1039/c8sc02677g.
- (52) Bas, A.-C.; Thompson, X.; Salmon, L.; Thibault, C.; Molnár, G.; Palamarciuc, O.; Routaboul, L.; Bousseksou, A. Bilayer Thin Films That Combine Luminescent and Spin Crossover Properties for an Efficient and Reversible Fluorescence Switching. *Magnetochemistry* **2019**, *5* (2), 28. DOI: 10.3390/magnetochemistry5020028.
- (53) Matsuda, M.; Kiyoshima, K.; Uchida, R.; Kinoshita, N.; Tajima, H. Characteristics of organic light-emitting devices consisting of dye-doped spin crossover complex films. *Thin Solid Films* **2013**, *531*, 451–453. DOI: 10.1016/j.tsf.2013.01.094.
- (54) Kershaw Cook, L. J.; Halcrow, M. A. Doping ruthenium complexes into a molecular spin-crossover material. *Polyhedron* **2015**, *87*, 91–97. DOI: 10.1016/j.poly.2014.10.021.
- (55) Benaicha, B.; van Do, K.; Yangui, A.; Pittala, N.; Lusson, A.; Sy, M.; Bouchez, G.; Fourati, H.; Gómez-García, C. J.; Triki, S.; Boukheddaden, K. Interplay between spin-crossover and luminescence in a multifunctional single crystal iron(II) complex: towards a new generation of molecular sensors. *Chem. Sci.* **2019**, *10* (28), 6791–6798. DOI: 10.1039/c9sc02331c.
- (56) Yuan, J.; Wu, S.-Q.; Liu, M.-J.; Sato, O.; Kou, H.-Z. Rhodamine 6G-Labeled Pyridyl Aroylhydrazone Fe(II) Complex Exhibiting Synergetic Spin Crossover and Fluorescence. *J. Am. Chem. Soc.* **2018**, *140* (30), 9426–9433. DOI: 10.1021/jacs.8b00103.
- (57) Kurz, H.; Lochenie, C.; Wagner, K. G.; Schneider, S.; Karg, M.; Weber, B. Synthesis and Optical Properties of Phenanthroline-Derived Schiff Base-Like Dinuclear Ru^{II}-Ni^{II} Complexes. *Chem. Eur. J.* **2018**, *24* (20), 5100–5111. DOI: 10.1002/chem.201704632.
- (58) Ghosh, S.; Kamilya, S.; Pramanik, T.; Rouzières, M.; Herchel, R.; Mehta, S.; Mondal, A. ON/OFF Photoswitching and Thermoinduced Spin Crossover with Cooperative Luminescence in a 2D Iron(II) Coordination Polymer. *Inorg. Chem.* **2020**, *59* (18), 13009–13013. DOI: 10.1021/acs.inorgchem.0c02136.
- (59) Ge, J.-Y.; Chen, Z.; Zhang, L.; Liang, X.; Su, J.; Kurmoo, M.; Zuo, J.-L. A Two-Dimensional Iron(II) Coordination Polymer with Synergetic Spin-Crossover and Luminescent Properties. *Angew. Chem. Int. Ed.* **2019**, *58* (26), 8789–8793. DOI: 10.1002/anie.201903281.
- (60) Wang, C.-F.; Yang, G.-Y.; Yao, Z.-S.; Tao, J. Monitoring the Spin States of Ferrous Ions by Fluorescence Spectroscopy in Spin-Crossover-Fluorescent Hybrid Materials. *Chem. Eur. J.* **2018**, *24* (13), 3218–3224. DOI: 10.1002/chem.201704901.
- (61) Lochenie, C.; Schötz, K.; Panzer, F.; Kurz, H.; Maier, B.; Puchtler, F.; Agarwal, S.; Köhler, A.; Weber, B. Spin-Crossover Iron(II) Coordination Polymer with Fluorescent Properties: Correlation between Emission Properties and Spin State. *J. Am. Chem. Soc.* **2018**, *140* (2), 700–709. DOI: 10.1021/jacs.7b10571.
- (62) Schäfer, B.; Bauer, T.; Faus, I.; Wolny, J. A.; Dahms, F.; Fuhr, O.; Lebedkin, S.; Wille, H.-C.; Schlage, K.; Chevalier, K.; Rupp, F.; Diller, R.; Schünemann, V.; Kappes, M. M.; Ruben, M. A luminescent Pt₂Fe spin crossover complex. *Dalton Trans.* **2017**, *46* (7), 2289–2302. DOI: 10.1039/c6dt04360g.

- (63) Wagenknecht, P. S.; Ford, P. C. Metal centered ligand field excited states: Their roles in the design and performance of transition metal based photochemical molecular devices. *Coord. Chem. Rev.* **2011**, *255* (5-6), 591–616. DOI: 10.1016/j.ccr.2010.11.016.
- (64) Wenger, O. S. Is Iron the New Ruthenium? *Chem. Eur. J.* **2019**, *25* (24), 6043–6052. DOI: 10.1002/chem.201806148.
- (65) Chábera, P.; Liu, Y.; Prakash, O.; Thyraug, E.; Nahhas, A. E.; Honarfar, A.; Essén, S.; Fredin, L. A.; Harlang, T. C. B.; Kjær, K. S.; Handrup, K.; Ericson, F.; Tatsuno, H.; Morgan, K.; Schnadt, J.; Häggström, L.; Ericsson, T.; Sobkowiak, A.; Lidin, S.; Huang, P.; Styring, S.; Uhlig, J.; Bendix, J.; Lomoth, R.; Sundström, V.; Persson, P.; Wärnmark, K. A low-spin Fe(III) complex with 100-ps ligand-to-metal charge-transfer photoluminescence. *Nature* **2017**, *543* (7647), 695–699. DOI: 10.1038/nature21430.
- (66) Weber, B.; Walker, F. A. Solution NMR studies of iron(II) spin-crossover complexes. *Inorg. Chem.* **2007**, *46* (16), 6794–6803. DOI: 10.1021/ic062349e.
- (67) Halcrow, M. A. *Spin-Crossover Materials*; John Wiley & Sons Ltd, 2013. DOI: 10.1002/9781118519301.
- (68) Harriman, A. Luminescence of porphyrins and metalloporphyrins. Part 1. – Zinc(II), nickel(II) and manganese(II) porphyrins. *J. Chem. Soc., Faraday Trans. 1* **1980**, *76* (0), 1978. DOI: 10.1039/F19807601978.
- (69) Kim, D.; Holten, D. Picosecond measurements on the binding and release of basic ligands by excited states of Ni(II) porphyrins. *Chem. Phys. Lett.* **1983**, *98* (6), 584–589. DOI: 10.1016/0009-2614(83)80247-4.
- (70) Fabbrizzi, L.; Foti, F.; Licchelli, M.; Poggi, A. pH-controlled fluorescent emission in the nickel(II) complex of a bifunctional tetramine macrocycle. *Inorg. Chem.* **2002**, *41* (18), 4612–4614. DOI: 10.1021/ic025620a.
- (71) Wenger, O. S. Photoactive Complexes with Earth-Abundant Metals. *J. Am. Chem. Soc.* **2018**, *140* (42), 13522–13533. DOI: 10.1021/jacs.8b08822.
- (72) Yan, X.; Song, X.; Mu, X.; Wang, Y. Mechanochromic luminescence based on a phthalonitrile-bridging salophen zinc(II) complex. *New J. Chem.* **2019**, *43* (40), 15886–15891. DOI: 10.1039/c9nj03704g.
- (73) Consiglio, G.; Failla, S.; Oliveri, I. P.; Purrello, R.; Di Bella, S. Controlling the molecular aggregation. An amphiphilic Schiff-base zinc(II) complex as supramolecular fluorescent probe. *Dalton Trans.* **2009** (47), 10426–10428. DOI: 10.1039/b914930a.
- (74) Consiglio, G.; Oliveri, I. P.; Cacciola, S.; Maccarrone, G.; Failla, S.; Di Bella, S. Dinuclear zinc(II) salen-type Schiff-base complexes as molecular tweezers. *Dalton Trans.* **2020**, *49* (16), 5121–5133. DOI: 10.1039/d0dt00494d.
- (75) Cai, Y.-B.; Zhan, J.; Hai, Y.; Zhang, J.-L. Molecular assembly directed by metal-aromatic interactions: control of the aggregation and photophysical properties of Zn-salen complexes by aromatic mercuration. *Chem. Eur. J.* **2012**, *18* (14), 4242–4249. DOI: 10.1002/chem.201103332.
- (76) Pallavicini, P.; Diaz-Fernandez, Y. A.; Pasotti, L. Micelles as nanosized containers for the self-assembly of multicomponent fluorescent sensors. *Coord. Chem. Rev.* **2009**, *253* (17-18), 2226–2240. DOI: 10.1016/j.ccr.2008.11.010.
- (77) Burkhardt, M.; Martinez-Castro, N.; Tea, S.; Drechsler, M.; Babin, I.; Grishagin, I.; Schweins, R.; Pergushov, D. V.; Gradzielski, M.; Zezin, A. B.; Müller, A. H. E. Polyisobutylene-*block*-poly(methacrylic acid) diblock copolymers: self-assembly in aqueous media. *Langmuir* **2007**, *23* (26), 12864–12874. DOI: 10.1021/la701807b.
- (78) Fan, J.; Ding, L.; Bo, Y.; Fang, Y. Fluorescent Ensemble Based on Bispyrene Fluorophore and Surfactant Assemblies: Sensing and Discriminating Proteins in Aqueous Solution. *ACS Appl. Mater. Interfaces* **2015**, *7* (40), 22487–22496. DOI: 10.1021/acsami.5b06604.

- (79) Qiao, M.; Ding, L.; Lv, F. Surfactant assemblies encapsulating fluorescent probes as selective and discriminative sensors for metal ions. *Coord. Chem. Rev.* **2021**, *432*, 213696. DOI: 10.1016/j.ccr.2020.213696.
- (80) Fan, J.; Ding, L.; Fang, Y. Surfactant Aggregates Encapsulating and Modulating: An Effective Way to Generate Selective and Discriminative Fluorescent Sensors. *Langmuir* **2019**, *35* (2), 326–341. DOI: 10.1021/acs.langmuir.8b02111.
- (81) Dey, N.; Bhattacharya, S. A Glimpse of Our Journey into the Design of Optical Probes in Self-assembled Surfactant Aggregates. *Chem. Rec.* **2016**, *16* (4), 1934–1949. DOI: 10.1002/tcr.201600012.
- (82) Ding, L.; Bai, Y.; Cao, Y.; Ren, G.; Blanchard, G. J.; Fang, Y. Micelle-induced versatile sensing behavior of bispyrene-based fluorescent molecular sensor for picric acid and PYX explosives. *Langmuir* **2014**, *30* (26), 7645–7653. DOI: 10.1021/la5011264.
- (83) Bandyopadhyay, P.; Ghosh, A. K. pH-Controlled "off-on-off" switch based on Cu(2+)-mediated pyrene fluorescence in a PAA-SDS micelle aggregated supramolecular system. *J. Phys. Chem. B* **2009**, *113* (41), 13462–13464. DOI: 10.1021/jp907337r.
- (84) Fernandez, Y. D.; Gramatges, A. P.; Amendola, V.; Foti, F.; Mangano, C.; Pallavicini, P.; Patroni, S. Using micelles for a new approach to fluorescent sensors for metal cations. *Chem. Commun.* **2004** (14), 1650–1651. DOI: 10.1039/B404543B.
- (85) Zhang, Y.; Cao, J.; Ding, L. Fluorescent ensemble based on dansyl derivative/SDS assemblies as selective sensor for Asp and Glu in aqueous solution. *J. Photochem. Photobiol.* **2017**, *333*, 56–62. DOI: 10.1016/j.jphotochem.2016.10.018.
- (86) Hu, W.; Ding, L.; Cao, J.; Liu, L.; Wei, Y.; Fang, Y. Protein binding-induced surfactant aggregation variation: a new strategy of developing fluorescent aqueous sensor for proteins. *ACS Appl. Mater. Interfaces* **2015**, *7* (8), 4728–4736. DOI: 10.1021/am508421n.
- (87) Kumari, N.; Jha, S.; Misra, S. K.; Bhattacharya, S. A Probe for the Selective and Parts-per-Billion-Level Detection of Copper(II) and Mercury(II) using a Micellar Medium and Its Utility in Cell Imaging. *ChemPlusChem* **2014**, *79* (7), 1059–1064. DOI: 10.1002/cplu.201402016.
- (88) Grisci, G.; Kozma, E.; Mróz, W.; Pagano, K.; Ragona, L.; Galeotti, F. Self-assembly of a water soluble perylene and surfactant into fluorescent supramolecular ensembles sensitive to acetylcholinesterase activity. *RSC Adv.* **2016**, *6* (69), 64374–64382. DOI: 10.1039/c6ra08869d.
- (89) Lera-Garrido, F. de; Sánchez-Ruiz, A.; Rodríguez-López, J.; Tolosa, J.; García-Martínez, J. C. Enhancement of emission by surfactant-induced aggregation in poly(phenylenevinylene)-based lipochromophores. *Dyes Pigm.* **2020**, *179*, 108410. DOI: 10.1016/j.dyepig.2020.108410.
- (90) Pergushov, D. V.; Remizova, E. V.; Feldthusen, J.; Zezin, A. B.; Müller, A. H. E.; Kabanov, V. A. Novel Water-Soluble Micellar Interpolyelectrolyte Complexes. *J. Phys. Chem. B* **2003**, *107* (32), 8093–8096. DOI: 10.1021/jp027526l.
- (91) Yan, S.; Wan, L.-Y.; Ju, X.-J.; Wu, J.-F.; Zhang, L.; Li, M.; Liu, Z.; Wang, W.; Xie, R.; Chu, L.-Y. K⁺-Responsive Block Copolymer Micelles for Targeted Intracellular Drug Delivery. *Macromol. Biosci.* **2017**, *17* (9). DOI: 10.1002/mabi.201700143.
- (92) Wolf, L.; Jäger, E.-G. α -(Aminomethylen)- β -dicarbonylverbindungen als Komplexliganden. I. Kupfer- und Nickelchelate von Diaminderivaten. *Z. Anorg. Allg. Chem.* **1966**, *346* (1-2), 76–91. DOI: 10.1002/zaac.19663460109.
- (93) Jäger, E.-G.; Hussler, E.; Rudolph, M.; Schneider, A. Struktur-Reaktivitäts-Beziehungen bei koordinativ-ungesättigten Chelatkomplexen. VI. Synthese, Adduktbildung, Redoxpotentiale und photochrome Iodderivate von Eisen(II)-Komplexen Schiffischer Basen mit elektronenziehenden Substituenten. *Z. Anorg. Allg. Chem.* **1985**, *525* (6), 67–85. DOI: 10.1002/zaac.19855250609.

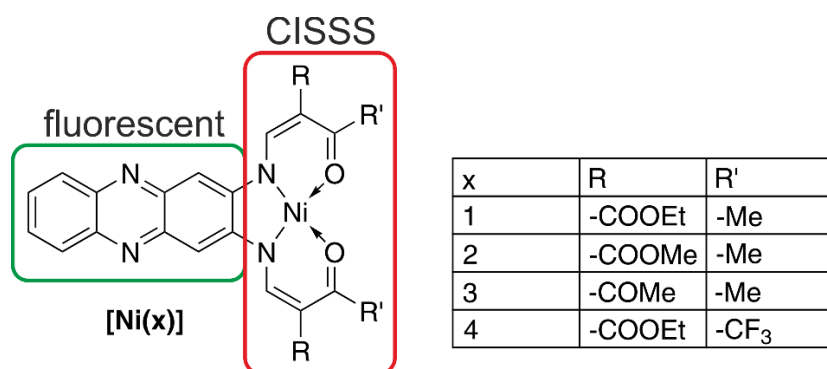
- (94) Jäger, E.-G. “Bioinspired” Metal Complexes of Macrocyclic $[N_4^{2-}]$ and Open Chain $[N_2O_2^{2-}]$ Schiff Base Ligands – a Link between Porphyrins and Salicylaldimines. In *Chemistry at the Beginning of the Third Millennium*; Fabbrizzi, L., Poggi, A., Eds.; Springer Berlin Heidelberg, 2000; pp 103–138. DOI: 10.1007/978-3-662-04154-3_6.
- (95) Weber, B.; Jäger, E.-G. Structure and Magnetic Properties of Iron(II/III) Complexes with $N_2O_2^{2-}$ Coordinating Schiff Base Like Ligands. *Eur. J. Inorg. Chem.* **2009**, 2009 (4), 465–477. DOI: 10.1002/ejic.200800891.
- (96) Lochenie, C.; Wagner, K. G.; Karg, M.; Weber, B. Modulation of the ligand-based fluorescence of 3d metal complexes upon spin state change. *J. Mater. Chem. C* **2015**, 3 (30), 7925–7935. DOI: 10.1039/c5tc00837a.
- (97) Lochenie, C.; Schlamp, S.; Railliet, A. P.; Robeyns, K.; Weber, B.; Garcia, Y. Water channels and zipper structures in Schiff base-like Cu(II) and Ni(II) mononuclear complexes. *CrystEngComm* **2014**, 16 (27), 6213–6218. DOI: 10.1039/C4CE00710G.
- (98) Jäger, E.-G.; Knaudt, J.; Rudolph, M.; Rost, M. Activation of Molecular Oxygen by Biomimetic Schiff Base Complexes of Manganese, Iron, and Cobalt. *Eur. J. Inorg. Chem.* **1996**, 129 (9), 1041–1047. DOI: 10.1002/cber.19961290911.
- (99) Lochenie, C.; Bauer, W.; Railliet, A. P.; Schlamp, S.; Garcia, Y.; Weber, B. Large Thermal Hysteresis for Iron(II) Spin Crossover Complexes with *N*-(Pyrid-4-yl)isonicotinamide. *Inorg. Chem.* **2014**, 53 (21), 11563–11572. DOI: 10.1021/ic501624b.
- (100) Schönfeld, S.; Hörner, G.; Heinemann, F. W.; Hofmann, A.; Marschall, R.; Weber, B. Spin States of 1D Iron(II) Coordination Polymers with Redox Active TTF(py)₂ as Bridging Ligand. *Z. Anorg. Allg. Chem.* **2021**, 647 (4), 295–305. DOI: 10.1002/zaac.202000286.
- (101) Schönfeld, S.; Dankhoff, K.; Baabe, D.; Zaretzke, M.-K.; Bröring, M.; Schötz, K.; Köhler, A.; Hörner, G.; Weber, B. Iron(II) Spin Crossover Complexes Based on a Redox Active Equatorial Schiff-Base-Like Ligand. *Inorg. Chem.* **2020**, 59 (12), 8320–8333. DOI: 10.1021/acs.inorgchem.0c00725.
- (102) Schlamp, S.; Thoma, P.; Weber, B. Influence of the alkyl chain length on the self-assembly of amphiphilic iron complexes: an analysis of X-ray structures. *Chem. Eur. J.* **2014**, 20 (21), 6462–6473. DOI: 10.1002/chem.201304653.
- (103) Weihermüller, J.; Schlamp, S.; Dittrich, B.; Weber, B. Kinetic Trapping Effects in Amphiphilic Iron(II) Spin Crossover Compounds. *Inorg. Chem.* **2019**, 58 (2), 1278–1289. DOI: 10.1021/acs.inorgchem.8b02763.
- (104) Weihermüller, J.; Schlamp, S.; Milius, W.; Puchtler, F.; Breu, J.; Ramming, P.; Hüttner, S.; Agarwal, S.; Göbel, C.; Hund, M.; Papastavrou, G.; Weber, B. Amphiphilic iron(II) spin crossover coordination polymers: crystal structures and phase transition properties. *J. Mater. Chem. C* **2019**, 7 (5), 1151–1163. DOI: 10.1039/C8TC05580G.
- (105) Klimm, O.; Göbel, C.; Rosenfeldt, S.; Puchtler, F.; Miyajima, N.; Marquardt, K.; Drechsler, M.; Breu, J.; Förster, S.; Weber, B. Synthesis of Fe(L)(bipy)_n spin crossover nanoparticles using blockcopolymer micelles. *Nanoscale* **2016**, 8 (45), 19058–19065. DOI: 10.1039/C6NR06330F.
- (106) Göbel, C.; Klimm, O.; Puchtler, F.; Rosenfeldt, S.; Förster, S.; Weber, B. Synthesis of Fe(L_{eq})(L_{ax})_n coordination polymer nanoparticles using blockcopolymer micelles. *Beilstein J. Nanotechnol.* **2017**, 8, 1318–1327. DOI: 10.3762/bjnano.8.133.
- (107) Göbel, C.; Hils, C.; Drechsler, M.; Baabe, D.; Greiner, A.; Schmalz, H.; Weber, B. Confined Crystallization of Spin-Crossover Nanoparticles in Block-Copolymer Micelles. *Angew. Chem. Int. Ed.* **2020**, 59 (14), 5765–5770. DOI: 10.1002/anie.201914343.

3 Synopsis

This thesis comprises three publications, which are all accepted articles in peer-reviewed journals (Chapter 5, 6, and 7). The individual contributions to joint publications are pointed out in Chapter 4.

The overall aim described in this work is the design of photoluminescent sensor materials, that are based on 3d transition metal complexes composed of Schiff base-like ligands. Thereby, the tetradentate ligand acts as the photoluminescent unit, whereas the metal center provides the sensitive behavior towards external stimuli. In this work the focus is set on coordination-induced changes of the optical properties studied in solution. The sensitivity towards potent donors is due to vacant axial coordination sites of the square-planar coordination sphere, which is dictated by the Schiff base-like ligand. In nickel(II) complexes with an electron configuration of d^8 , this coordination can induce a coordination-induced spin state switching (CISSS) from $S = 0$ to $S = 1$ that can affect the emission properties. Even though, a spin change is not possible for zinc(II) complexes with a closed d shell, coordination-induced (de)stacking processes can alter the emission properties as well.

The work in chapter 5 follows up previous results from Dr. Charles Lochenie, who investigated the CISSS behavior of a phenazine-based nickel(II) complex.¹ This work extends the principle to a whole series of nickel(II) complexes and aims at a broader investigation and deeper understanding of the underlying processes.



Scheme 1: Structure of the presented nickel(II) complexes based on a Schiff base-like CISSS unit with a fluorescent phenazine backbone.

In this study, four derivatives of a nickel(II) complex have been investigated for their optical sensor behavior. The complexes derive from Schiff base-like ligands with a phenazine backbone, which acts as the fluorescent unit. The CISSS unit has been equipped with different substituents as shown in Scheme 1. **[Ni(1–3)]** differ only slightly in the nature of “R” (ester, ketone). In contrast, **[Ni(4)]** features electron-withdrawing CF_3 substituents to increase the Lewis acidity of the nickel(II) metal center. Crystal structures of **[Ni(1)]** and **[Ni(4)(H₂O)₂·H₂O·DMF]** could be obtained from a pyridine/water or DMF/water vapor-vapor slow diffusion setup, respectively. Even though both complexes crystallized in the presence of strong Lewis bases, only **[Ni(4)]** features an octahedral coordination sphere (CN 6), whereas **[Ni(1)]** exhibits a square-planar coordination sphere (CN 4). This finding already hints at a drastically increased Lewis acidity of the nickel(II) metal center in the CF_3 decorated **[Ni(4)]**.

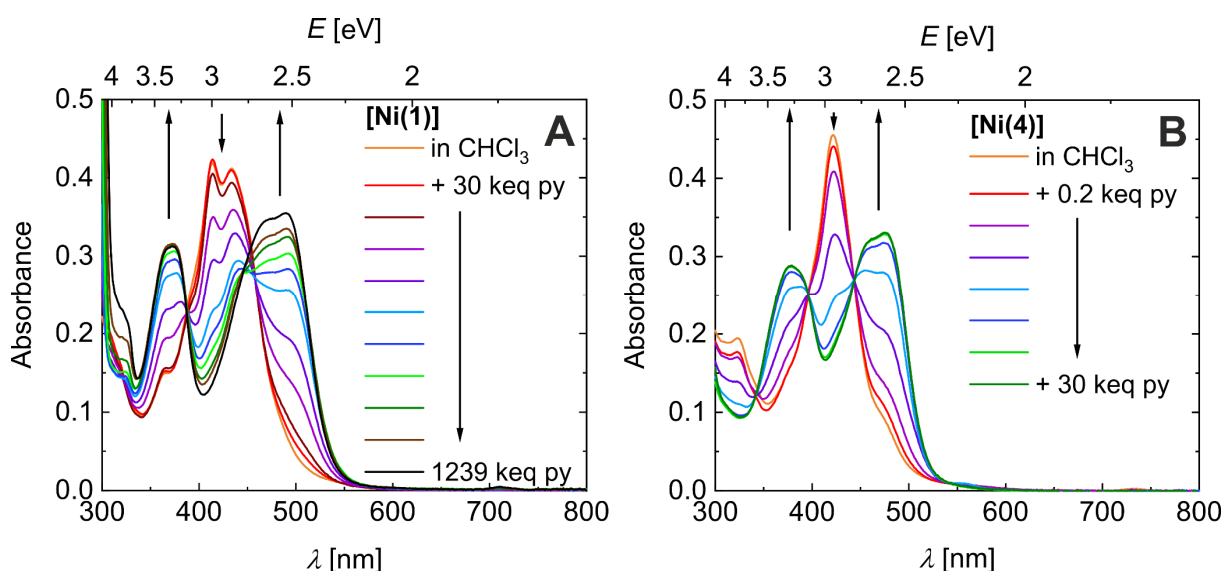


Figure 1: (Absorbance-detected) CISSS. Absorbance spectra of **[Ni(1)]** (A) and **[Ni(4)]** (B) in a chloroform/pyridine series at room temperature.

The sensitivity towards external chemical stimuli of **[Ni(1–4)]** was investigated by UV-vis measurements of chloroform/pyridine titration series. These series revealed a drastic change of the absorption behavior upon addition of the strong Lewis base pyridine to the non-coordinating solvent chloroform (see Figure 1). The intense changes can be attributed to CISSS from a square-planar (CN 4) to a square-pyramidal/octahedral (CN 5/6) coordination sphere. Interestingly, the amount of pyridine (given by the molar excess of pyridine relative to the nickel(II) complex) to induce a CISSS, is very similar for **[Ni(1–3)]**, but strongly differs for **[Ni(4)]**. While for **[Ni(1–3)]** over 100 keq pyridine are needed to significantly bleach the characteristic band of the CN 4 species, the CISSS is already completed at 30 keq pyridine for **[Ni(4)]**. These differences in the Lewis acidity of the metal center are also reflected in a

remarkable difference in the calculated Gibbs energies of $\Delta\Delta_{\text{CISSS}}G(\text{DFT}) = 37 \text{ kJ}\cdot\text{mol}^{-1}$ (experimental: $\Delta\Delta_{\text{CISSS}}G(\text{experimental}) = 30 \text{ kJ}\cdot\text{mol}^{-1}$).

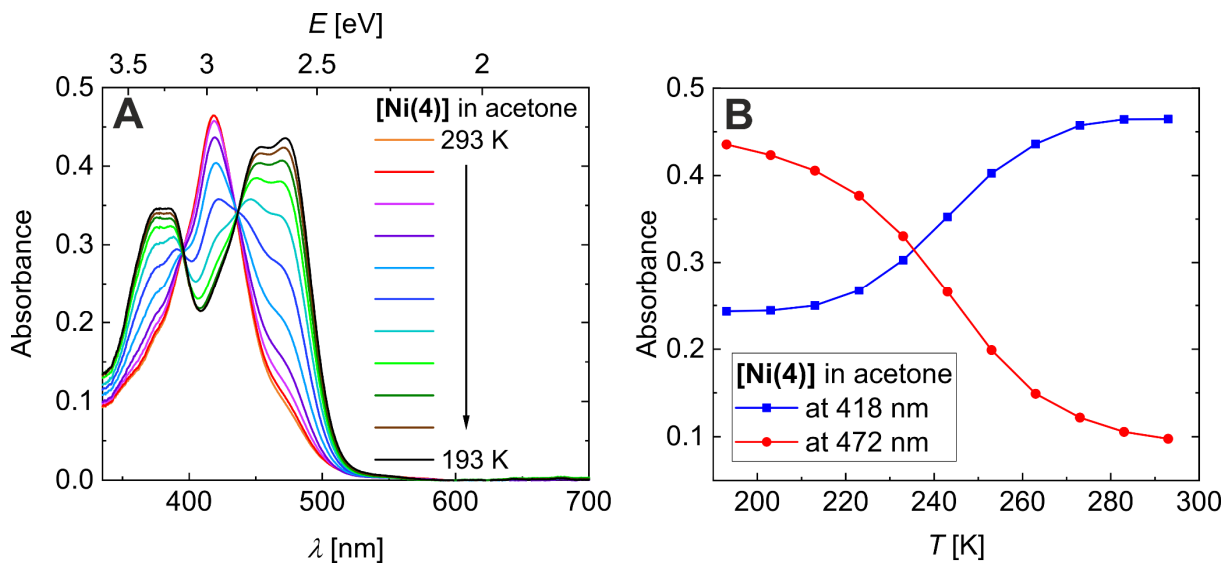


Figure 2: (Absorbance-detected) temperature-dependent CISSS. Absorbance spectra of [Ni(4)] in acetone at different temperatures (A). Plot of the absorbance intensity vs T at the characteristic absorbance maxima of the CN 4 ($\lambda = 418 \text{ nm}$) and the CN 5/6 species ($\lambda = 472 \text{ nm}$) (B).

The Lewis acid-base character of the CISSS does not only allow to alter the sensitivity range by tuning the acidity of the metal center, but also by varying the basicity of the potential donor. A donor concentration-dependent series with three different pyridine derivatives confirms this effect as increasing the basicity of the axial donor results in a reduction of the required equivalents to induce CISSS ($[\text{DMAP}] \ll [\text{Py}] \ll [4\text{-CN-Py}]$ with DMAP: 4-(dimethylamino)pyridine; Py: pyridine; 4-CN-Py: 4-cyanopyridine). Solvent series of [Ni(1)] and [Ni(4)] reveal a clear “black-or-white” behavior, as either the characteristic absorption spectra of the CN 4 or the CN 5/6 species is observed. The CISSS state nicely follows the Gutmann’s donor number (DN) of the solvents, which is a measure for the basicity. While for [Ni(1)] only the pyridine solution is CISSS-active, in [Ni(4)] more solutions show the characteristic spectrum of the CN 5/6 species. The two borderline cases are acetone in CN 4 and MeOH, where the absorption spectrum of CN 5/6 was obtained. As the coordination/decoordination is an entropically driven process, it is possible to design a temperature-dependent CISSS sensor. In variable temperature UV-vis measurements of [Ni(1)] and [Ni(4)] in DCM/pyridine solution mixtures, heating results in dissociation of the axial ligand leading to a higher ratio of the CN 4 species in the spectra. Remarkably, cooling an acetone solution of [Ni(4)] from 293 K to 193 K yields a temperature-sensor that covers the whole CISSS process in this narrow temperature range as shown in Figure 2. The temperature-

dependent CISSS behavior was studied as well by ^1H and ^{19}F NMR measurements of **[Ni(1)]** in (D_5)pyridine and **[Ni(4)]** in (D_6)acetone. Heating of the solutions results in both cases in a sharpening of the signals accompanied by a high-field shift of some signals due to a decreased amount of paramagnetic CN 5/6 species.

Remarkably, the three complexes **[Ni(1–3)]** are fluorescent in the non-coordinating solvent chloroform, showing quantum yields ϕ of $5 \pm 1\%$ and excited state lifetimes τ in the order of 1 ns. This finding is striking, as inclusion of an open shell $3d$ metal center typically results in emission quenching due to low lying MC states. In this case, the emission is only slightly reduced compared to the ligands **H₂(1–3)**, which feature quantum yields ϕ of $6 \pm 1\%$. In contrast, the CF_3 decorated **[Ni(4)]** is non-emissive in all investigated solvents, even though emission was observed for the ligand **H₂(4)**. According to DFT calculations, the HOMOs and LUMOs of all complexes are predominantly phenazine centered with small contribution from the $[\text{NiN}_2\text{O}_2]$ core. The introduction of CF_3 substituents results in stabilization of both donor and acceptor MOs. DFT calculations show that the leading transitions of all complexes are based on a charge shift between the chelate and the phenazine unit. However, a comparison of the transition dipoles of **[Ni(1–3)]** and **[Ni(4)]** reveals that they point into opposite direction: while for **[Ni(1–3)]** the charge is shifted from the $[\text{NiN}_2\text{O}_2]$ core to the phenazine backbone, the phenazine unit in **[Ni(4)]** acts as electron donor and the $[\text{NiN}_2\text{O}_2]$ core as the acceptor. This renders the transition MLCT-like for **[Ni(1–3)]** leading to a formal excited state of $[\text{Ni}^{\text{III}}(1-3)^{\bullet-}]$. The transition, in contrast, is LMCT-like for **[Ni(4)]** with a formal excited state of $[\text{Ni}^{\text{I}}(4)^{*\text{+}}]$. We associate the lack of emission of **[Ni(4)]** to the LMCT character that might result in secondary MC states that decay in a non-radiative way.

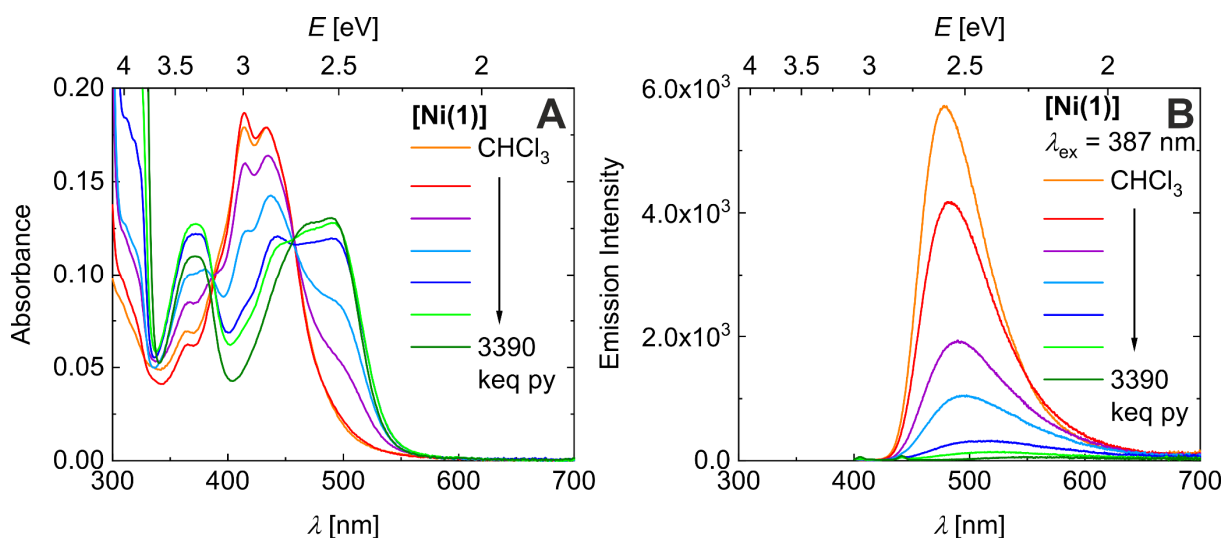


Figure 3: Fluorescence-detected CISSS (FD-CISSS). Absorbance (A) and steady-state emission spectra (B) of a chloroform/pyridine series of **[Ni(1)]** at room temperature.

In contrast to chloroform solutions, pyridine solutions of **[Ni(1–3)]** are non-emissive. The effects of CISSS on the emission properties were studied in detail by steady-state emission measurements of chloroform/pyridine titration series. A drastic emission quenching upon increasing the pyridine content was observed for all three complexes **[Ni(1–3)]** (see Figure 3B exemplary for **[Ni(1)]**). These three complexes are the first examples of fluorescent sensors based on fluorescence-detected CISSS (FD-CISSS). Comparison of the fluorescence excitation spectra of the CHCl_3 /pyridine mixtures confirms that the emission in all mixtures is based on the native CN 4 species, which decreases upon addition of pyridine. This finding and the successive changes of both the absorbance and emission spectra suggest that the (AD-)CISSS and the FD-CISSS are based on the same origin, namely CISSS in the ground state that results in static emission quenching.

However, the Stern-Volmer plot of **[Ni(1)]** is strongly bent upward, which indicates additional dynamic quenching. This unexpected finding is further strengthened by comparing the pyridine-dependent absorbance and emission dynamics. Hereby, a higher sensitivity of the FD-CISSS in comparison to the (AD-)CISSS was revealed. This increased sensitivity can be nicely seen in the optical spectra of **[Ni(1)]** in various 1/1 chloroform/solvent mixtures (mixtures were used due to solubility issues). Although all solutions except the pyridine-containing mixture are CISSS-silent in the absorption spectra, emission quenching occurs in most mixtures (see Figure 4).

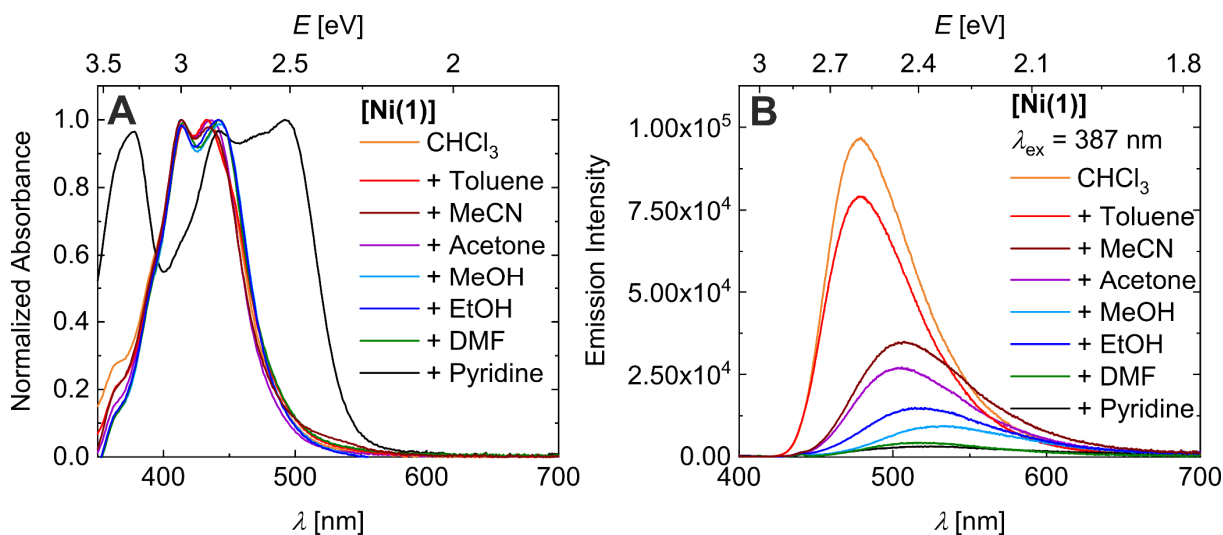
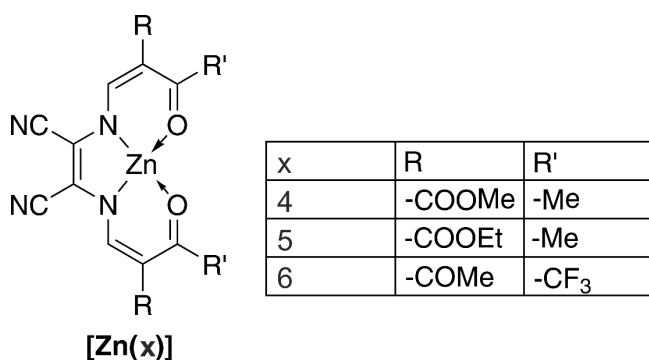


Figure 4: Normalized absorbance spectra (A) and emission spectra (B) of **[Ni(1)]** in different 1/1 solvent mixtures with CHCl_3 .

Remarkably, both the emission intensity and the Stokes shift clearly correlate with the donor number of the solvent. We attribute this effect to dynamic emission quenching via axial

coordination in the singlet-excited state. The higher sensitivity towards coordination in the excited state compared to the ground state originates from the higher acidity of the metal center in the excited state. As discussed before, the leading optical transitions of **[Ni(1–3)]** are MLCT-like with a charge shift from the $[\text{NiN}_2\text{O}_2]$ core to the phenazine backbone. The thereby increased Lewis acidity of the nickel(II) metal center in the excited state results in a favored coordination and a strongly increased sensitivity of the FD-CISSS compared to the AD-CISSS. To the best of our knowledge, **[Ni(1–3)]** are so far the only reported examples of emissive nickel(II) complexes based on Schiff base-like ligand systems. A wide range of nickel(II) complexes synthesized during my PhD projects were non-emissive, independently of the spin state. In most cases, both the ligands and the zinc(II) complexes are emissive, which hints towards emission quenching based on the open shell character of the nickel(II) metal center. To overcome this metal-based quenching, zinc(II) complexes are promising candidates as their closed shell character prevents quenching through low lying MC states. Chapter 6 deals with such photoluminescent zinc(II) complexes, where coordination-induced destacking results in a drastic emission enhancement.

Three new zinc(II) complexes **[Zn(5–7)]** having Schiff base-like ligands equipped with nitrile substituents were investigated (Scheme 2). Five different crystal structures could be obtained from various media. These crystal structures already indicate the tendency of **[Zn(5–7)]** to overcome the coordinatively unsaturated square-planar coordination sphere by ligation of one/two axial ligand(s) in the presence of potent donors. In the crystal structures of **[Zn(5,6)]**, the zinc(II) metal center is enclosed in a N_2O_3 or N_3O_2 square-pyramidal coordination sphere. In contrast, increasing the Lewis acidity by inclusion of electron withdrawing CF_3 substituents in **[Zn(7)]** results into the coordination of two axial ligands leading to an octahedral coordination sphere.



Scheme 2: Structure of the presented zinc(II) complexes **[Zn(5–7)]** based on a Schiff base-like ligand equipped with dinitrile substituents.

A solvent series of **[Zn(5)]** showed that the solvent only has a minor impact on the absorption behavior. On the other hand, the emission properties drastically depend on the choice of the solvent: that is, in non/weakly-coordinating media such as CHCl_3 and MeCN a close-to-zero emission was observed, whereas in coordinating solvents such as EtOH, THF, or pyridine a strong green emission was observed. Interestingly, the emission intensity scales with the basicity/DN of the solvent, indicating that the emission is based on the coordinated species. DFT and wave-function methods were applied to determine the underlying photophysical processes. Both methods reveal that the HOMO as well as the LUMO are predominantly located at the chelate ligand. The optical leading transitions are characterised as intraligand CT (ILCT) transition from the chelate to the dinitrile backbone. In theory, the axial ligand X is not involved in these transitions and the nature of X should therefore not significantly alter the optical properties, which contradicts the experimental findings at least in the emission behavior.

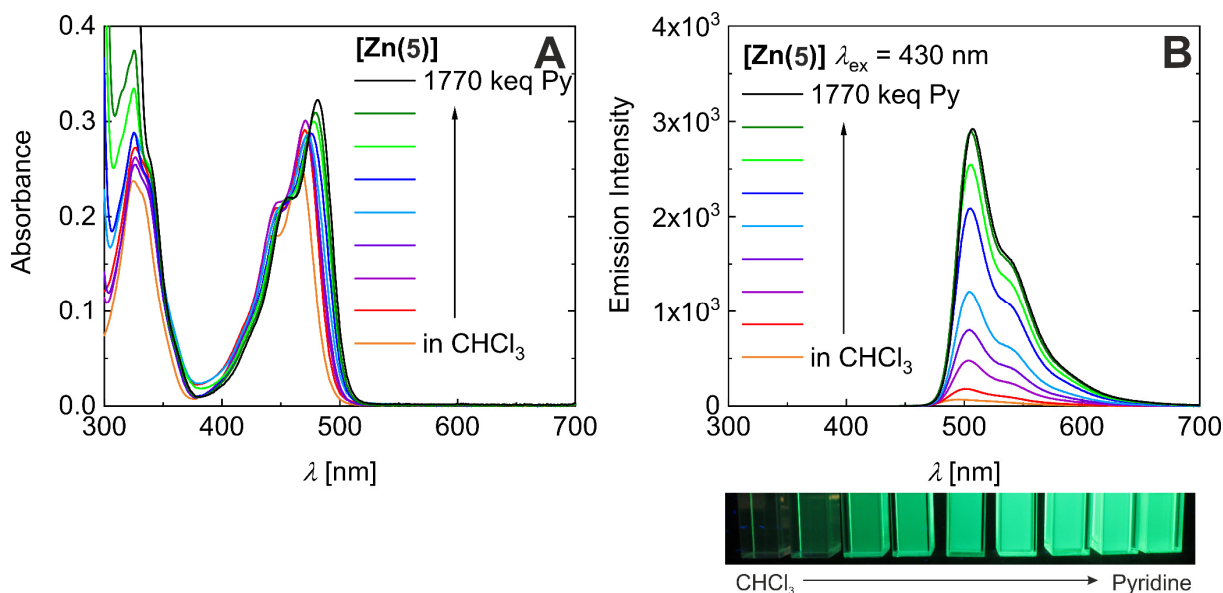


Figure 5: Absorbance (A) and steady-state emission spectra (B) of a chloroform/pyridine series of **[Zn(5)]**. Photograph of the respective solutions under light irradiation ($\lambda_{\text{ex}} = 365$ nm).

The aptitude of **[Zn(5–7)]** as photoluminescent sensor materials was investigated in CHCl_3 /pyridine series. While only minor changes were observed in the absorbance spectra upon addition of pyridine, the emission properties were strongly affected. A turn-on sensor emission behavior was observed for all three complexes as shown exemplary for **[Zn(5)]** in Figure 5. The increased acidity of CF_3 -equipped **[Zn(7)]** leads to a higher sensitivity towards donors relative to **[Zn(5,6)]**. This finding is not only experimentally reflected by a saturation of the absorption changes at lower pyridine equivalents, but also in DFT calculations considering the reaction energies. Both experiments and calculations showed that **[Zn(5–7)]** and the close

congener **[Zn(sal)]**, which was studied in detail by Di Bella *et al.*, behave in a similar manner and show striking emission turn-on behavior upon coordination.² However, the pyridine equivalents required to achieve these emission changes differ significantly. While the coordination-induced changes of **[Zn(sal)]** already saturate at 2-10 eq of pyridine, a massive excess of pyridine of $\gg 10^4$ eq is required to obtain these changes for **[Zn(5-7)]**. This seemingly reduced Lewis acidity of **[Zn(5-7)]**, though, is not reflected in the calculated Lewis base affinity, as **[Zn(5-7)]** feature an even higher Lewis acidity compared to **[Zn(sal)]**.

In literature, the lack of emission of **[Zn(sal)]** in non-coordinating solvents is attributed to stacking into dimers or oligomers. The formation of these dimers consisting of $[\text{Zn}_2\text{O}_2]$ cores was experimentally and theoretically confirmed and the emission increase was attributed to the coordination-induced destacking of the zinc(II) complexes.² It seems likely that similar stacking processes are involved for **[Zn(5-7)]** as well. The stability of a similar dimer of **[Zn(5)]**₂ based on the $[\text{Zn}_2\text{O}_2]$ stacking motif was determined by DFT calculations and similar stabilities were obtained compared to **[Zn(sal)]**₂. However, DFT calculations revealed an alternative stacking motif for **[Zn(5-7)]** based on $(\text{ZnO})_2$ macrocycles, that features a drastically increased stability (see Figure 6B). Indeed, DLS measurements confirm the presence of huge aggregates (≈ 100 nm) in non-coordinating solvents that dissolve upon addition of pyridine. This formation of strongly stabilized oligomers results in the quenched Lewis acidity of **[Zn(5-7)]**.

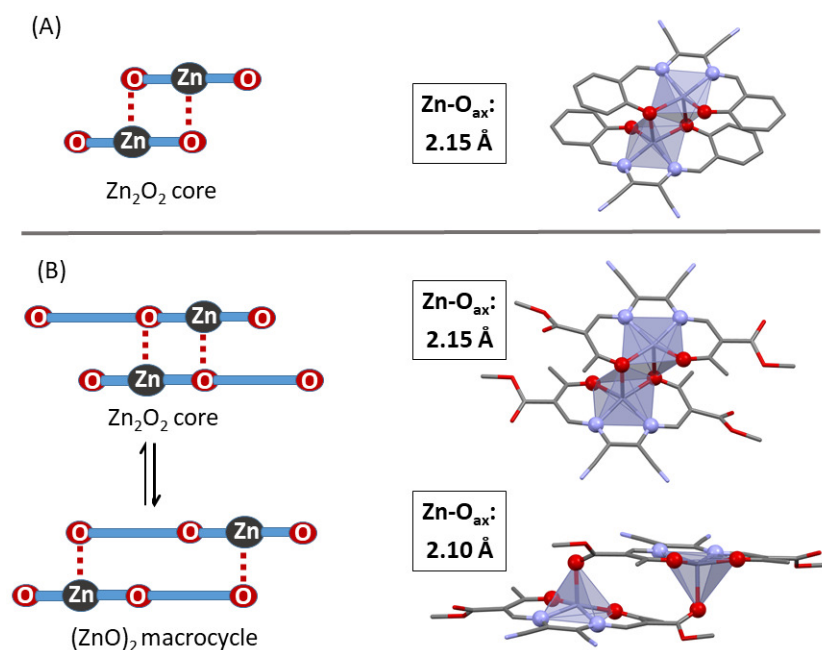
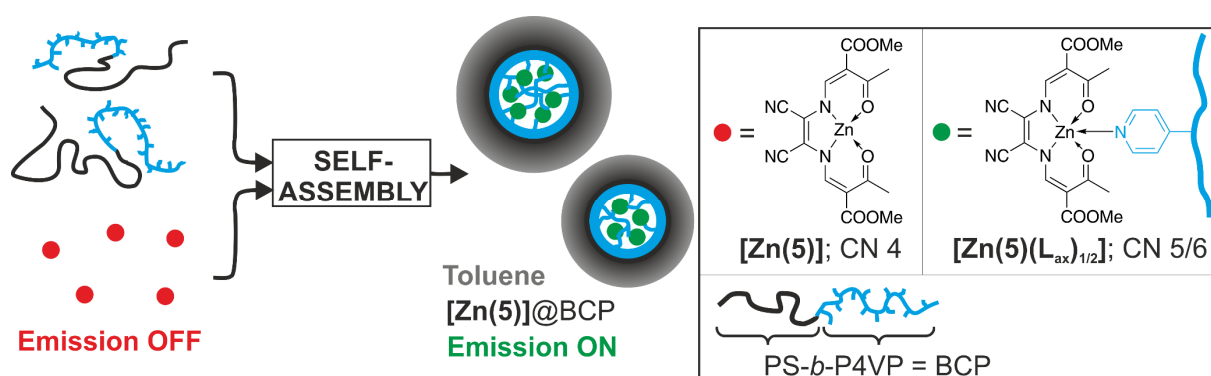


Figure 6: Dimer speciation of **[Zn(sal)]**₂ (left) and its DFT-optimized structures with pertinent metrics (right) (A). Dimer speciation of the $[\text{Zn}_2\text{O}_2]$ and the $[\text{ZnO}]_2$ motif of **[Zn(5-7)]**₂ (left) and its DFT-optimized structures with pertinent metrics (right) (B).

Chapter 7 deals with the encapsulation of **[Zn(5)]**, that features coordination-induced emission, into polystyrene-*block*-poly(4-vinylpyridine) (PS-*b*-P4VP) block copolymer (BCP) micelles to obtain fluorescent self-assembled micelles as shown in Scheme 3. Three different block copolymers with varying block ratios were used for this purpose, namely S₅₈V₄₂¹⁵⁷, S₆₅V₃₅¹³¹, and S₈₅V₁₅¹⁵⁴ (subscripts give the fraction of the respective block in wt%; superscript denotes the number average molecular weight in kg mol⁻¹). In toluene, BCP micelles composed of a PS shell and a P4VP block form through self-assembly. Weber *et al.* previously reported on the ability of the pyridine substituents of the P4VP block to function as axial ligands for iron(II) and zinc(II) metal complexes based on Schiff base-like ligands.³ We encapsulated the zinc(II) complex **[Zn(5)]** into these micelles, to investigate the effect on the optical properties. DLS and TEM measurements confirm the formation of spherical micelles of all neat BCP and **[Zn(5)]@BCP** compounds in toluene. The hydrodynamic diameter D_h varies only slightly in between 150 to 170 nm. In contrast, the core diameter D_{core} differs drastically and can be correlated to the ratio of the P4VP block. D_{core} values between approximately 30 nm for S₈₅V₁₅¹⁵⁴ and 60 nm for S₅₈V₄₂¹⁵⁷ were obtained. Interestingly, encapsulation of **[Zn(5)]** does not significantly alter neither D_h nor D_{core} .

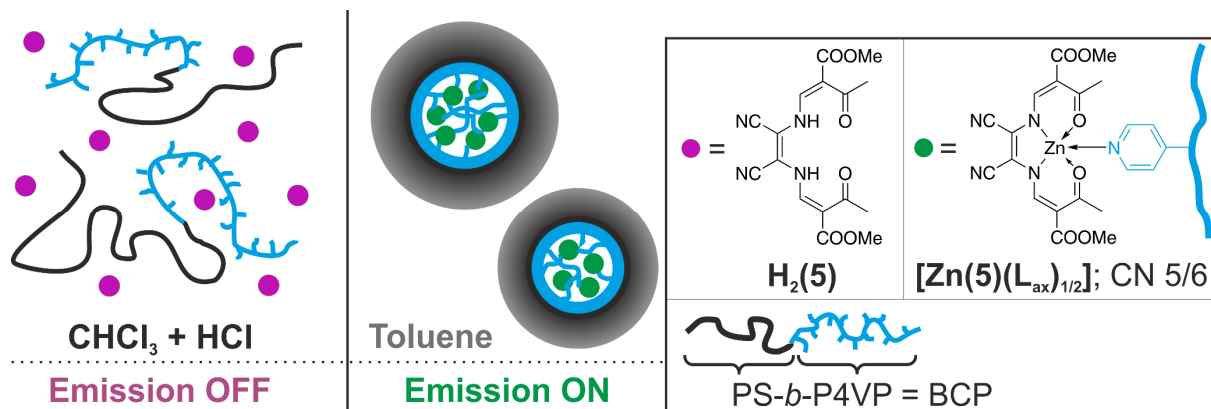


Scheme 3: Representation of the self-assembly of **[Zn(5)]** and BCP in toluene into fluorescent micelles composed of **[Zn(5)]@BCP**.

All three self-assembled **[Zn(5)]@BCP** micelles feature a strong green emission in toluene. The absorbance and emission spectra of the **[Zn(5)]@BCP** micelles clearly reflect the optical behavior of **[Zn(5)]** in pyridine. This indicates that the zinc(II) complex is coordinated by the pyridine substituents of the P4VP block and therefore must be located within the micelle core. Although the absorbance and emission wavelengths are very similar for all three **[Zn(5)]@BCP** compounds, they differ strongly in their quantum yields and excited state lifetimes. Thereby, an increase of the P4VP ratio results in an enhanced quantum yield, that is reflected as well in increased excited state lifetimes determined from the biexponential decays. **[Zn(5)]@S₈₅V₁₅**¹⁵⁴,

for instance, features a quantum yield of 16% in toluene, while a drastically enhanced quantum yield of 33% is obtained for $[\text{Zn}(\mathbf{5})]@\text{S}_{58}\text{V}_{42}$ ¹⁵⁷. Interestingly, all $[\text{Zn}(\mathbf{5})]@\text{BCP}$ compounds feature higher quantum yields and excited state lifetimes compared to neat $[\text{Zn}(\mathbf{5})]$ in pyridine. The prevention of non-radiative decays upon encapsulation can be nicely seen in temperature-dependent excited state lifetime measurements of $[\text{Zn}(\mathbf{5})]@\text{BCP}$ in toluene and $[\text{Zn}(\mathbf{5})]$ in pyridine, too. Here, increasing the temperature results in a drastic reduction of the excited state lifetime of $[\text{Zn}(\mathbf{5})]$ in pyridine, while the effect on the incorporated $[\text{Zn}(\mathbf{5})]$ in the P4VP core is much weaker, indicating the oppression of dynamic quenching processes.

In the next step, a photoluminescent sensor material was investigated that is based on medium-dependent micelle formation. In contrast to the previous study, where the concentration of the pyridine was changed directly in a chloroform/pyridine series, the overall pyridine concentration is not altered in this approach. However, upon successively changing the medium from chloroform to toluene, the induced micelle formation results in an increase of the effective pyridine concentration due to a smaller effective volume. Simplified calculations of the respective vinylpyridine equivalents in the molecularly dissolved and the micelle form indicate a significant change of the effective concentration upon micelle formation. Nevertheless, the calculations imply as well that the amount of potent pyridine units in the molecularly dissolved form is still rather high and prevails the formation of an emission off-state in chloroform. For this reason, the chloroform was acidified with HCl to induce protonation of the complex resulting in the non-emissive ligand $\text{H}_2(\mathbf{5})$ in chloroform (see Scheme 4). The effects of the micelle formation and the acidification on the optical properties was studied in $\text{CHCl}_3/\text{toluene}$ and acidified $\text{CHCl}_3(\text{acidic})/\text{toluene}$ series of $[\text{Zn}(\mathbf{5})]@\text{S}_{58}\text{V}_{42}$ ¹⁵⁷. DLS measurements confirm that micelle formation occurs for all series in between 20 to 33 vol% toluene, regardless of the presence of $[\text{Zn}(\mathbf{5})]$ or hydrochloric acid.



Scheme 4: Representation of the medium-dependent off-on sensor material based on the self-assembly of $[\text{Zn}(\mathbf{5})]@\text{BCP}$ into fluorescent micelles.

As suspected, a non-negligible emission can be observed in the non-acidified CHCl_3 /toluene series even below 33 vol% toluene, where micelle formation occurs. Fluorescence excitation spectra confirm that this emission is based on the coordinated $[\text{Zn}(\mathbf{5})]$ species due to potent pyridine donors of the P4VP block in the molecularly dissolved form of the BCP. Nevertheless, an emission enhancement upon increasing the toluene ratio can be observed. This finding reflects on the one hand the increased effective pyridine concentration inside the micelles, and on the other hand the lower degree of dynamic quenching processes through encapsulation.

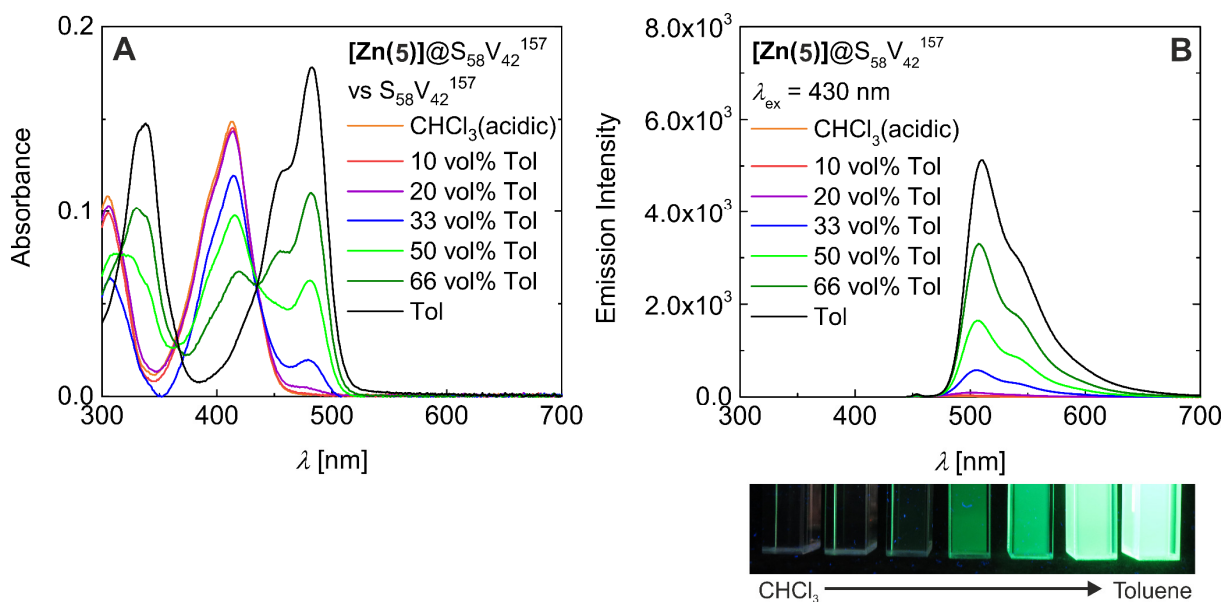


Figure 7: Absorbance (A) and steady-state emission spectra (B) of the CHCl_3 (acidic)/toluene series of $[\text{Zn}(\mathbf{5})]@S_{58}V_{42}^{157}$. Photograph of the respective solutions under light irradiation ($\lambda_{\text{ex}} = 365$ nm).

Absorbance and emission spectra of CHCl_3 / CHCl_3 (acidic) series of neat $[\text{Zn}(\mathbf{5})]$ and $[\text{Zn}(\mathbf{5})]@S_{58}V_{42}^{157}$ confirm the successful formation of the ligand $\text{H}_2(\mathbf{5})$ through acidification of the chloroform. Moreover, formation of the non-emissive ligand can be obtained as well in toluene through addition of the organic acid AcOH, while maintaining the micelle form. In the absorbance spectra of the CHCl_3 (acidic)/toluene series of $[\text{Zn}(\mathbf{5})]@S_{58}V_{42}^{157}$ drastic changes can be observed as shown in Figure 7A. The characteristic main band of the ligand at $\lambda = 414$ nm decreases upon increasing the toluene ratio, while a new band at approximately $\lambda = 480$ nm increases, which can be associated with the axially coordinated zinc(II) complex $[\text{Zn}(\mathbf{5})]$. These drastic changes take place from 33 vol% toluene on, where micelle formation occurs. Remarkably, a close-to-zero emission was observed up to 20 vol% toluene, while further increase of the toluene ratio results in a drastic emission enhancement (see Figure 7B and photograph). Plotting the integrated emission intensity vs the toluene fraction reveals a

linear progression that, in agreement with DLS measurements, indicates that micelle formation occurs at around 25 vol% toluene. These results confirm the successful design of a turn-on emission sensor based on medium-dependent micelle formation.

References

- (1) Lochenie, C.; Wagner, K. G.; Karg, M.; Weber, B. Modulation of the ligand-based fluorescence of 3d metal complexes upon spin state change. *J. Mater. Chem. C* **2015**, *3* (30), 7925–7935. DOI: 10.1039/c5tc00837a.
- (2) Di Bella, S. Lewis acidic zinc(II) salen-type Schiff-base complexes: sensing properties and responsive nanostructures. *Dalton Trans.* **2021**, *50* (18), 6050–6063. DOI: 10.1039/D1DT00949D.
- (3) Göbel, C.; Hils, C.; Drechsler, M.; Baabe, D.; Greiner, A.; Schmalz, H.; Weber, B. Confined Crystallization of Spin-Crossover Nanoparticles in Block-Copolymer Micelles. *Angew. Chem. Int. Ed.* **2020**, *59* (14), 5765–5770. DOI: 10.1002/anie.201914343.

4 Individual Contributions to Joint Publications

The results presented in the thesis were obtained in collaboration with other researchers. In this chapter, the respective contributions of each co-author to the manuscripts will be specified. The corresponding author is stressed by an asterisk. The publication state (published, submitted, to be submitted) is given below.

Chapter 5

This work was published in *Journal of the American Chemical Society (J. Am. Chem. Soc.)* **2021**, *143*, 9, 3466–3480; DOI: 10.1021/jacs.0c12568) with the title:

“A Fluorescence-Detected Coordination-Induced Spin State Switch”

Hannah Kurz, Konstantin Schötz, Ilias Papadopoulos, Frank W. Heinemann, Harald Maid, Dirk M. Guldi, Anna Köhler, Gerald Hörner, and Birgit Weber*

I synthesized the ligands and complexes, carried out most of the experiments, and wrote the first draft of the manuscript. Konstantin Schötz measured the temperature-dependent UV-vis and emission spectra in acetone and determined the PLQYs as well as the PL lifetimes using TCSPC. Dr. Gerald Hörner performed the DFT calculations, corrected the manuscript, and contributed to the overall scientific discussion. Ilias Papadopoulos measured the temperature-dependent UV-vis spectra in DCM/pyridine mixtures. Dr. Frank W. Heinemann measured and solved the X-ray structures. Dr. Harald Maid measured the temperature-dependent NMR spectra. Prof. Dr. Dirk M. Guldi and Prof. Dr. Anna Köhler gave scientific advice and corrected the manuscript. Prof. Dr. Birgit Weber supervised the work, gave scientific advice, and corrected the manuscript.

Chapter 6

This work was published in *Chemistry – A European Journal (Chem. Eur. J.)* **2021**, *27*, 15159-15171; DOI: 10.1002/chem.202102086) with the title:

“Quenched Lewis acidity: Studies on the Medium Dependent Fluorescence of Zinc(II) Complexes”

Hannah Kurz, Gerald Hörner, Oskar Weser, Giovanni Li Manni, Birgit Weber*

I synthesized the ligands and complexes, carried out most of the experiments, solved the crystal structures, and wrote the first draft of the manuscript. Dr. Gerald Hörner performed the (KS/TD)-DFT calculations, measured the crystal structures, corrected the manuscript, and contributed to the overall scientific discussion. Oskar Weser performed the MC-PDFT calculations and wrote the MC-PDFT part in the manuscript. Dr. Giovanni Li Manni gave scientific advice and corrected the manuscript. Prof. Dr. Birgit Weber supervised the work, gave scientific advice, and corrected the manuscript.

Chapter 7

This work was published in *Angewandte Chemie International Edition (Angew. Chem. Int. Ed.)* **2022**, *61*, e202117570; DOI: 10.1002/anie.202117570) with the title:

“Self-Assembled Fluorescent Block Copolymer Micelles with Responsive Emission”

Hannah Kurz, Christian Hils, Jana Timm, Gerald Hörner, Andreas Greiner, Roland Marschall, Holger Schmalz, Birgit Weber*

I synthesized the complexes and the nanocomposite samples, carried out most of the experiments, analysed the DLS and TEM data, and wrote the first draft of the manuscript. Christian Hils performed the TEM measurements. Dr. Jana Timm gave support with the determination of the quantum yield and excited state lifetimes. Dr. Gerald Hörner and Prof. Dr. Roland Marschall were involved in scientific discussions and corrected the manuscript. Prof. Dr. Andreas Greiner was involved in scientific discussions. Dr. Holger Schmalz synthesised the block copolymer, characterised the block copolymer by GPC, DSC, NMR, and MALDI-ToF, was involved in scientific discussions, and corrected the manuscript. Prof. Dr. Birgit Weber supervised this work, was involved in scientific discussions, and corrected the manuscript.

5 A Fluorescence-Detected Coordination-Induced Spin State Switch

Hannah Kurz, Konstantin Schötz, Ilias Papadopoulos, Frank W. Heinemann, Harald Maid, Dirk M. Guldi, Anna Köhler, Gerald Hörner, Birgit Weber*

Hannah Kurz, Dr. Gerald Hörner, Prof. Dr. Birgit Weber – Inorganic Chemistry IV, University of Bayreuth, Universitätsstraße 30, NW I, 95447 Bayreuth, Germany

Konstantin Schötz, Prof. Dr. Anna Köhler – Soft Matter Optoelectronics and Bayreuth Institute of Macromolecular Research (BIMF) and Bavarian Polymer Institute (BPI), University of Bayreuth, Universitätsstraße 30, NW I, 95447 Bayreuth, Germany

Ilias Papadopoulos, Prof. Dr. Dirk M. Guldi – Department of Chemistry and Pharmacy & Interdisciplinary Center for Molecular Materials (ICMM), Physical Chemistry I, Friedrich-Alexander-University Erlangen-Nürnberg (FAU), Egerlandstraße 3, 91058 Erlangen, Germany

Dr. Frank W. Heinemann – Inorganic Chemistry, Friedrich-Alexander-University Erlangen-Nürnberg (FAU), Egerlandstraße 1, 91058 Erlangen, Germany

Dr. Harald Maid – Organic Chemistry II, Friedrich-Alexander-University Erlangen-Nürnberg (FAU), Nikolaus-Fiebiger-Straße 10, 91058 Erlangen, Germany

Published in *J. Am. Chem. Soc.* **2021**, *143*, 9, 3466–3480 (DOI: 10.1021/jacs.0c12568).

Reprinted with permission from Hannah Kurz, Konstantin Schötz, Ilias Papadopoulos, Frank W. Heinemann, Harald Maid, Dirk M. Guldi, Anna Köhler, Gerald Hörner, Birgit Weber*, *J. Am. Chem. Soc.* **2021**, *143*, 9, 3466–3480. Copyright 2021 American Chemical Society.

<http://pubs.acs.org/articlesonrequest/AOR-NUFK3IC69CB3XRT7KF99>

Abstract: The response of the spin state to *in situ* variation of the coordination number (CISSS) is a promising and viable approach to smart sensor materials, yet it suffers to date from insensitive detection. Herein, we present the synthetic access to a family of planar nickel(II)

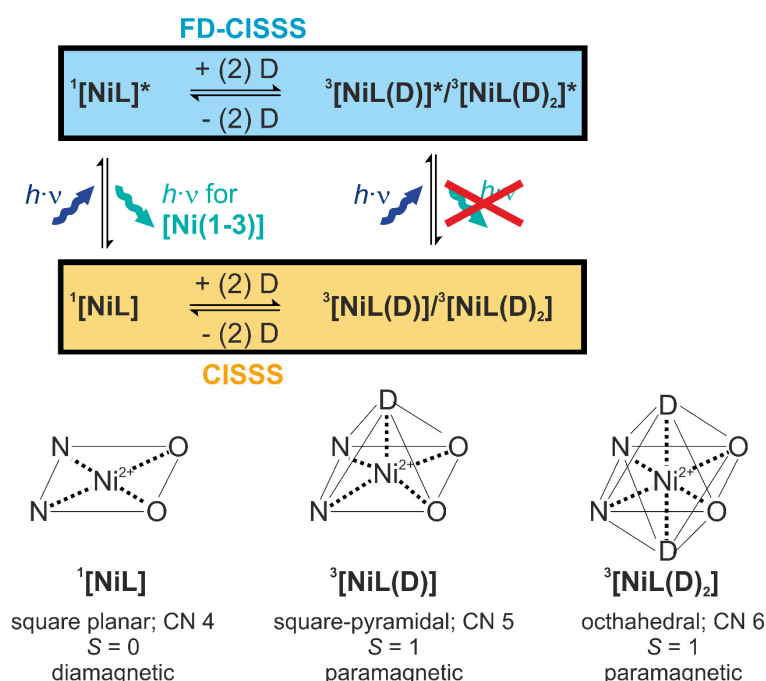
complexes, whose CISSS is sensitively followed by means of fluorescence detection. For this purpose, nickel(II) complexes with four phenazine-based Schiff base-like ligands were synthesized and characterized through solution-phase spectroscopy (NMR and UV–vis), solid-state structure analysis (single-crystal XRD), and extended theoretical modeling. All of them reveal CISSS in solution through axial ligating a range of N- and O-donors. CISSS correlates nicely with the basicity of the axial ligand and the substitution-dependent acidity of the nickel(II) coordination site. Remarkably, three out of the four nickel(II) complexes are fluorescent in noncoordinating solvents but are fluorescence-silent in the presence of axial ligands such as pyridine. As these complexes are rare examples of fluorescent nickel(II) complexes, the photophysical properties with a coordination number of 4 were studied in detail, including temperature-dependent lifetime and quantum yield determinations. Most importantly, fluorescence quenching upon adding axial ligands allows a “black or white”, i.e. digital, sensing of spin state alternation. Our studies of fluorescence-detected CISSS (FD-CISSS) revealed that absorption-based CISSS and FD-CISSS are super proportional with respect to the pyridine concentration: FD-CISSS features a higher sensitivity. Overall, our findings indicate a favored ligation of these nickel(II) complexes in the excited state in comparison to the ground state.

4.1 Introduction

Multifunctional, externally switchable molecular building blocks are interesting and promising for their application as molecular sensors.^{1–6} The coordination chemistry community has focused mostly on iron(II) spin crossover (SCO) complexes in an octahedral ligand environment. Spin crossover denotes a phenomenon that a spin transition from a high-spin (HS) to a low-spin (LS) state and *vice versa* is induced by physical external stimuli such as a temperature change, a pressure change, or light irradiation, while the coordination number is maintained. Iron(II) complexes are particularly interesting in this context, as the spin transition is accompanied by a qualitative magnetic change from a diamagnetic LS state to a paramagnetic HS state enabling “black-or-white”, i.e. digital, recording.^{7–9}

Iron(II) complexes based on Schiff base-like ligands are well-known for their versatile SCO features.^{10–15} One major drawback of iron(II) SCO complexes is their high air sensitivity, which impedes their use as sensor materials. Notably, the broader access to SCO in the 3d alternatives manganese(II/III)^{16,17} and cobalt(II)¹⁸ is limited by the specific ligand-field requirements in octahedral coordination. However, nickel(II) offers ready access to spin state variation, termed

a coordination-induced spin state switch (CISSS). In contrast to the more common SCO mechanism, for CISSS the spin transition is triggered by a chemical impact, as the spin transition appears upon (de)coordination of additional guest molecules. Thus, singlet–triplet crossover which is usually synchronized to axial ligation (CN 4 \rightarrow CN 5) is followed by a second axial ligation (CN 5 \rightarrow CN 6) (Scheme 1). Research on CISSS has focused mainly on porphyrin-based nickel(II) complexes^{19–23} for the following reasons. First, for nickel(II) (d^8) the switch from a square-planar to square-pyramidal/octahedral coordination sphere is accompanied by a qualitative magnetic change from diamagnetic to paramagnetic. Second, porphyrins serve as synthetically versatile and structurally rigid strong-field ligand platforms. These are required to stabilize the diamagnetic square-planar over the paramagnetic tetrahedral coordination sphere.^{21,24}



Scheme 1. Representation of the coordination-induced spin state switch (CISSS) for nickel(II) complexes (where D = donor; CN = coordination number).^a

^aThe properties dependent on the coordination number and the readout of the magnetic status are realized via a change of fluorescence. Here two different possibilities are differentiated: the CISSS in the ground state and the CISSS in the excited state detected via fluorescence (FD-CISSS).

These physically and/or chemically induced spin transitions need to be coupled to a readout to enable a functional molecular sensor material. An optical readout such as photoluminescence is highly sought after, as it offers the advantage of easy detectability even at low concentrations. The coupling of SCO/CISSS with photoluminescence has been demonstrated via two approaches:²⁵ the synthesis of composite materials^{26–29} or a combination of both functionalities

in one molecule by covalently linking a photoluminescent unit to a SCO/CISSS unit.^{12,27,30–33} The combination of both functionalities in one molecule offers the advantage of a (mostly) concentration-independent sensor material. However, this approach turned out to be challenging, as in most cases the insertion of open-shell 3d metals results in a complete quenching of the photoluminescence independent of the coordination number.^{34–36}

It is due to the rapid quenching within an open *d* shell that only a few examples of nickel(II)-containing fluorophores have been reported so far. It is furthermore noted that in the vast majority of such systems the coordination site for nickel(II) and the fluorophore are electronically uncoupled. Examples of luminescent nickel(II) complexes with electronic coupling between nickel and the fluorophore are extremely rare.^{30,37,38} In very recent work, Yam et al. reported the first nickel(II) C[^]N[^]N pincer complex, which shows metal-based phosphorescence.³⁸ To the best of our knowledge, metal-based fluorescence from nickel(II) complexes has remained completely elusive; in particular, the well-studied nickel(II) porphyrin systems are notorious for being nonfluorescent.

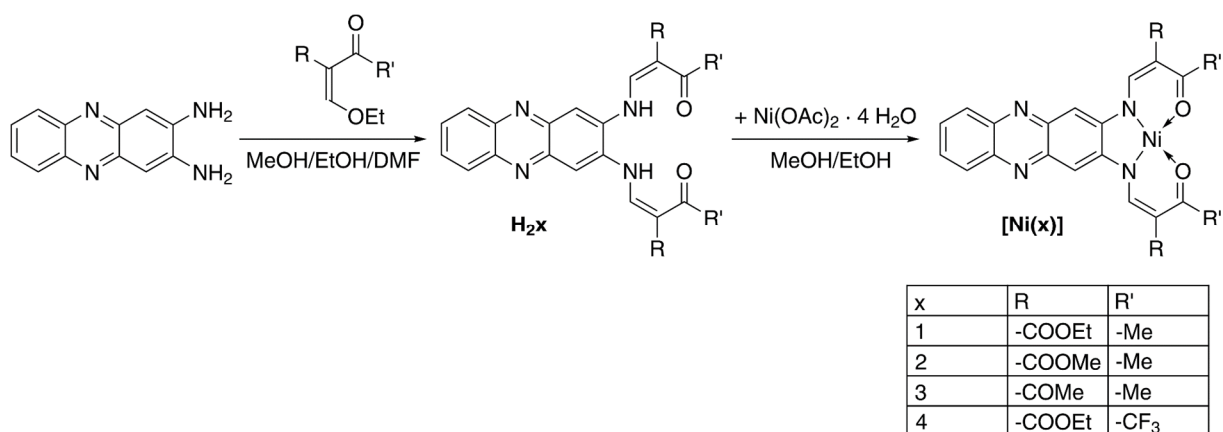
A single notable exception of a fluorescent nickel(II) complex has been communicated in a preliminary study by Weber et al. Therein, the fluorescence of a phenazine-based N₂O₂-coordinated nickel(II) complex was detected (see Scheme 2; [Ni(**1**)]). Intriguingly, the emission was quenched upon adding additional ligands.³⁹ Overall, the quenching was tentatively attributed to CISSS of the nickel(II) center. At that time, the nature of the emission was not investigated in detail by experimental and/or computational methods and was rationalized as ligand based. In this work, we greatly extend the experimental and theoretical fundament of this switchable fluorescence and provide synthetic access to a family of nickel(II) complexes with different substituent patterns, where most, but not all, of the complexes show this effect. The effect of the metal center on the CISSS not only in the ground state but also in the excited state and on the fluorescence properties will be discussed.

4.2 Results and Discussion

Synthesis

Nickel(II) complexes were synthesized in two steps as shown in Scheme 2. In the first step, 2,3-diaminophenazine was converted in a condensation reaction with the respective keto-enol ether to the Schiff base-like ligands **H21–4**. The identity and purity of the ligands was confirmed by ¹H ¹³C NMR and IR spectroscopy, mass spectrometry, and elemental analysis (¹H NMR spectra are given in Figures S1, S4, S6, and S8 in the Supporting Information). While **H21–3** give

almost coinciding signal pattern in ^1H NMR spectra, CF_3 -appended **H₂4** clearly deviates, as the NH signal is shifted to high field. In a second step, the ligands were converted with an excess of $\text{Ni}(\text{OAc})_2 \cdot 4\text{H}_2\text{O}$ to the respective orange-red nickel(II) complexes, with acetate as the source of base equivalents. **[Ni(1–3)]** were obtained solvent free in good yields of >75% as orange solids. Poorer yields of 55% prevailed for dark red **[Ni(4)]** due to its substantially enhanced solubility; it is noted that elemental analysis also identifies **[Ni(4)]** as a solvent-free complex. The identity and purity of the nickel(II) complexes were confirmed by ^1H NMR and IR spectroscopy, mass spectrometry, and elemental analysis.



Scheme 2. Synthesis of the ligands **H₂1–4** and the respective diamagnetic nickel(II) complexes **[Ni(1–4)]**.

^1H NMR spectra in CDCl_3 give narrow lines and unexceptional chemical shifts for all nickel(II) complexes, supporting diamagnetic electronic singlet ground states and planar coordination under these conditions (^1H NMR spectra are given in Figure S2, S5, S7, and S9 in the Supporting Information). ^{13}C NMR spectra and assignments of the signal of **[Ni(1)]** and **[Ni(4)]** are shown in Figures S3 and S10 in the Supporting Information. In the ^{13}C NMR spectra of **[Ni(4)]** a splitting of the CF_3 carbon signals is observed due to fluorine coupling.

Complex Structures: Single-Crystal XRD and DFT Modelling

Orange plate-like crystals of **[Ni(4)(H₂O)₂]·H₂O·DMF** suitable for X-ray structure analyses were obtained from a vapor-vapor slow diffusion setup of a dimethylformamide solution and water. The crystallographic data were collected at 100 K and are summarized in Table S1 in the Supporting Information. **[Ni(4)(H₂O)₂]·H₂O·DMF** crystallizes in the monoclinic space group $P2_1/c$. The asymmetric unit contains one hexacoordinate **[Ni(4)(H₂O)₂]** complex and two additional solvent molecules: namely, water and dimethylformamide. Dimethylformamide and one ethyl arm of one ester substituent of the equatorial ligand are strongly disordered. An illustration of the molecular structure of **[Ni(4)(H₂O)₂]** is shown in Figure 1A (see Figure S11A

in Supporting Information for a fully labeled asymmetric unit). Selected bond lengths and angles are given in Table S2 in the Supporting Information. The nickel(II) center is enclosed in a slightly distorted N_2O_4 coordination sphere, consisting of N_2O_2 of the equatorial ligand and O_2 of two axial water ligands. The equatorial bond lengths are all close to 2.0 Å, while the axial bond lengths are slightly elongated at 2.1 Å, which is consistent with a triplet ground state electronic configuration, centered at nickel. The bond angles within the chelate cycle differ only slightly from the expected values of 90 or 180°, which are needed for cis and trans angles in a perfectly octahedral coordination sphere to support an unstrained coordination. A DFT structure optimization of $[Ni(4)(H_2O)_2]$ gives close agreement with experimental metrics (see Table S2, in italics), supporting the triplet-state assignment. Similar metrics have been reported in the topologically related case of axially N-ligated nickel porphyrins.^{21,22}

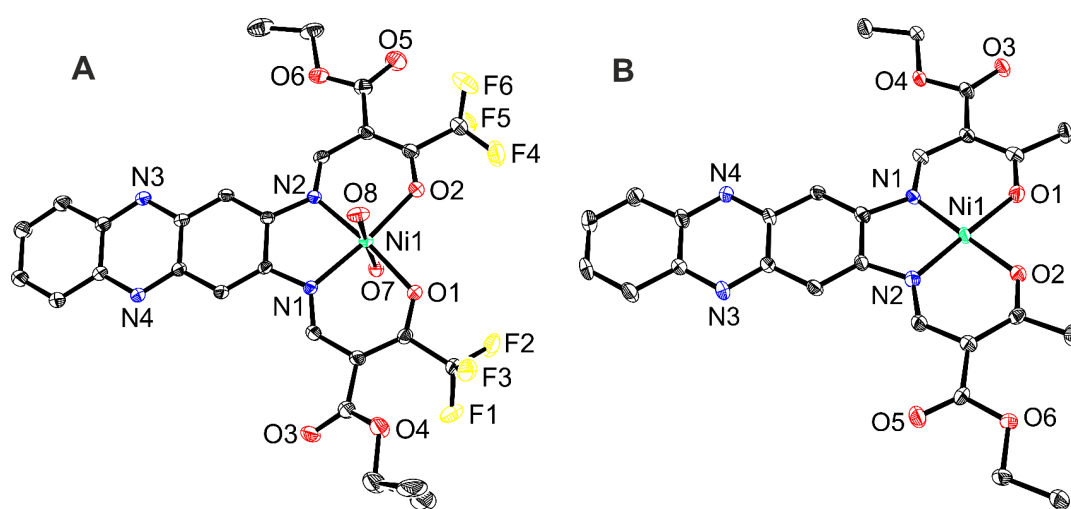


Figure 1. Representation of the molecular structure of $[Ni(4)(H_2O)_2]$ (A) and $[Ni(1)]$ (B). Hydrogen atoms and additional solvent molecules are omitted for clarity. Ellipsoids are drawn at the 50% probability level.

Figure 2 shows the crystal packing of $[Ni(4)(H_2O)_2] \cdot H_2O \cdot DMF$ along $[100]$ (Figure 2A) and $[010]$ (Figure 2B). Details of the hydrogen bonds are given in Table S3 in the Supporting Information. In contrast to other common phenazine systems,^{39,40} $[Ni(4)(H_2O)_2] \cdot H_2O \cdot DMF$ lacks stacking effects among the extended π planes. On one hand, the CF_3 substituents feature a higher steric demand in comparison to the CH_3 substituents.⁴¹ On the other hand, the axial water ligands, which give first indication of the high acidity of the nickel(II) center, hinder a stacking of the phenazines as well. Both aspects are supportive for the substantially enhanced solubility of $[Ni(4)]$ in many common solvents.

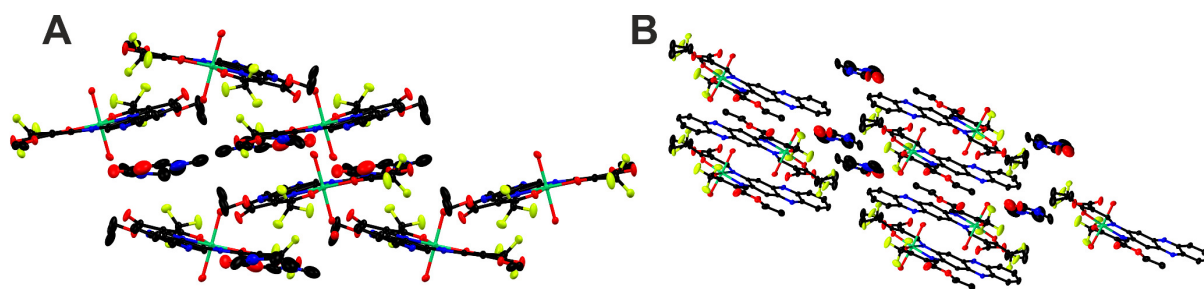


Figure 2. Molecular packing of $[\text{Ni}(\mathbf{4})(\text{H}_2\text{O})_2]\cdot\text{H}_2\text{O}\cdot\text{DMF}$ along $[100]$ (A) and $[010]$ (B). Hydrogen atoms are omitted for clarity.

The expanded coordination sphere of $[\text{Ni}(\mathbf{4})]$ is in stark contrast to the preference of $[\text{Ni}(\mathbf{1})]$ for planar coordination, irrespective of the crystallization medium. In previous work planar $[\text{Ni}(\mathbf{1})]$ prevailed in crystals obtained from a chloroform/ethanol diffusion setup.³⁹ In this work, we now obtained identical orange needlelike crystals of $[\text{Ni}(\mathbf{1})]$ from a pyridine/water diffusion setup, despite the presence of potent donors in high concentrations. For the sake of comparison, complex metrics of $[\text{Ni}(\mathbf{1})]$ from single-crystal XRD analysis and DFT optimization are given in Table S2 in the Supporting Information. In brief, the asymmetric unit of $[\text{Ni}(\mathbf{1})]$ consists of one complex molecule, in which the nickel(II) metal center is enclosed in a N_2O_2 square-planar coordination sphere (see Figure 1B and Figure S11B in the Supporting Information). π - π interactions between the aromatic rings and metal-aromatic interactions between the nickel(II) center and the chelate rings lead to the formation of columns along $[100]$ (see Table S4 in the Supporting Information). In comparison to $[\text{Ni}(\mathbf{4})(\text{H}_2\text{O})_2]\cdot\text{H}_2\text{O}\cdot\text{DMF}$, $[\text{Ni}(\mathbf{1})]$ shows low solubility in many common solvents, which is likely due to these stacking effects. Comprehensive metrical data of DFT optimized structures of $[\text{Ni}(\mathbf{1-4})]$ are given in the Tables S5–8 in the Supporting Information; variable coordination numbers and spin states were considered.

The powder diffraction patterns of all measured complexes differ significantly, as the variation of substituents results in a change in the molecular packing. PXRD patterns of bulk samples of $[\text{Ni}(\mathbf{1})]$ are in good agreement with the data calculated from the crystal structure (Figure S12; in the Supporting Information). While this agreement indicates conserved molecular structure and packing in samples of $[\text{Ni}(\mathbf{1})]$, the calculated and recorded powder patterns of $[\text{Ni}(\mathbf{4})]$ differ significantly. This finding reflects the varied formulations of solvent-free bulk material gained from EtOH and the single crystals gained from DMF/water, which consist of $[\text{Ni}(\mathbf{4})(\text{H}_2\text{O})_2]\cdot\text{H}_2\text{O}\cdot\text{DMF}$.

Photophysics of the Planar Complexes and their Ligands

Steady-state UV-vis absorption and fluorescence spectra were recorded of the ligands **H21–4** and the planar complexes **[Ni(1–4)]** in noncoordinating chloroform solutions (3.7×10^{-6} M; $T = 293$ K; spectra for ligands in Figure S13 in the Supporting Unit and complexes in Figure 3). All ligands are photoluminescent not only in chloroform but also in pyridine solution and share in chloroform similar optical behavior, apart from an approximately 4-fold lower emission intensity of **H24** in comparison to **H21–3**.

Figure 3 gives the absorbance and emission spectra of all nickel(II) complexes in chloroform. Intense absorption bands ($\epsilon_{\max} > 10^4 \text{ cm}^{-1} \text{ M}^{-1}$; $410 \text{ nm} < \lambda_{\max} < 445 \text{ nm}$) dominate the low-wavelength visible region, in agreement with the orange-red color of the nickel(II) complexes.

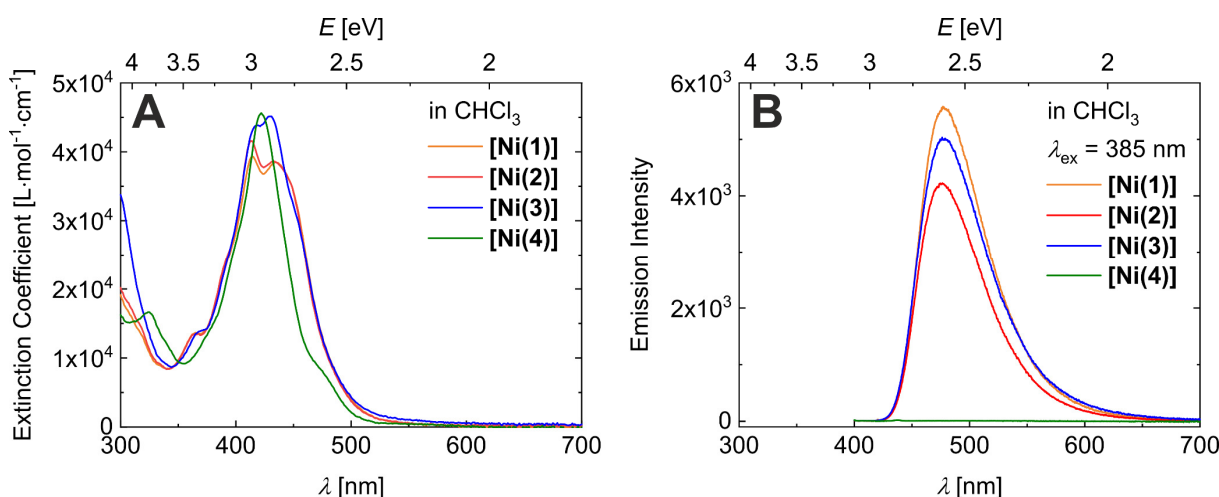


Figure 3. Steady-state UV-vis absorption spectra of **[Ni(1–4)]** in chloroform ($(3.7 \pm 0.1) \times 10^{-6}$ M) (A). Steady-state emission spectra of **[Ni(1–4)]** in chloroform (3.7×10^{-6} M; $\lambda_{\text{exc}} = 385$ nm) (B).

Table 1. Photophysical Data of the Complexes **[Ni(1–4)]**.

	$\lambda_{\text{abs,max}}$ (nm)	ϵ_{max} ($\text{L mol}^{-1} \text{ cm}^{-1}$)	$\lambda_{\text{em,max}}$ (nm)	PLQY (%)	$\lambda_{\text{exc,max}}$ (nm)
[Ni(1)]	415	39000	477	4.8	431
	434	38000			
[Ni(2)]	414	42000	476	3.6 ^a	430
	433	39000			
[Ni(3)]	419	44000	476	3.9 ^a	430
	430	45000			
[Ni(4)]	422	46000	^b	^b	^b

^a Calculated from the ratio of the measured emission intensities of all complexes relative to the measured quantum yield of **[Ni(1)]**. ^b No emission could be observed upon irradiation with $\lambda_{\text{exc}} = 385$ nm.

The presence of two distinct maxima for **[Ni(1–3)]** (but not for **[Ni(4)]**) and significant tailing toward the low-energy end indicate an overlay of several individual transitions. All complexes, except for **[Ni(4)]**, show emission. Pertinent photophysical data are summarized in Table 1.

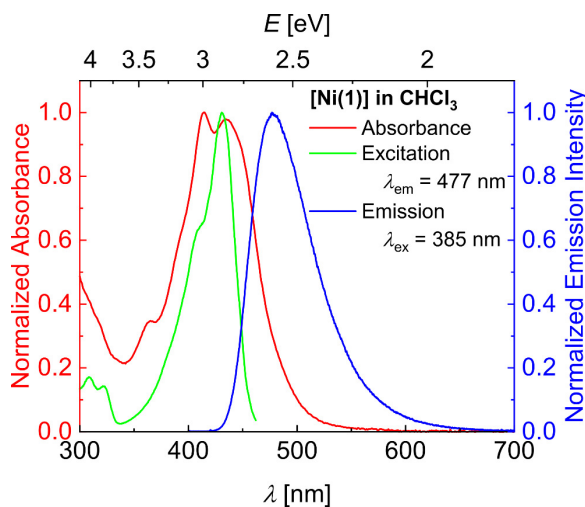


Figure 4. Normalized absorbance, excitation ($\lambda_{em} = 477$ nm), and emission spectra ($\lambda_{exc} = 385$ nm) of **[Ni(1)]** in chloroform.

As an example, a comparison of excitation and emission spectra recorded for chloroform solutions of **[Ni(1)]** ($\lambda_{exc} = 385$ nm; 3.7×10^{-6} M) is shown in Figures 4 (see Figure S14 in the Supporting Information for **[Ni(2)]** and **[Ni(3)]**). The emission is unstructured with a moderate Stokes shift of ca. 2000 cm^{-1} , which closely mimics the emission of the free ligands (see Figure S13 in the Supporting Information). Excitation spectra ($\lambda_{em} = 477$ nm) of the nickel(II) complexes identify a specific emissive state, which is kinetically isolated from nonemissive states at both higher and lower energies. The nature of the optical transitions has been addressed with methods of time-dependent DFT (TD-DFT), using the TPSSh functional. These settings previously served to adequately mimic the optical spectra of planar nickel(II) complexes.^{42,43} Frontier orbital energies of **[Ni(1–4)]** and frontier orbital landscapes of **[Ni(1)]** and **[Ni(4)]** are summarized in Figures S15–S17 in the Supporting Information. Irrespective of the substitution pattern, the HOMO and LUMO are largely phenazine centered with a conserved HOMO-LUMO gap; it is noted that the presence of CF_3 in **[Ni(4)]** similarly stabilizes both donor and acceptor MOs. Furthermore, the electron-withdrawing effect of the CF_3 substituent is reflected in the LUMO character, which now carries significant contributions of the $[\text{NiN}_2\text{O}_2]$ core. This subtle effect translates into opposite directions of the transition dipoles of relevant optical transitions in **[Ni(1–3)]** and **[Ni(4)]**, as shown in Figure 5.

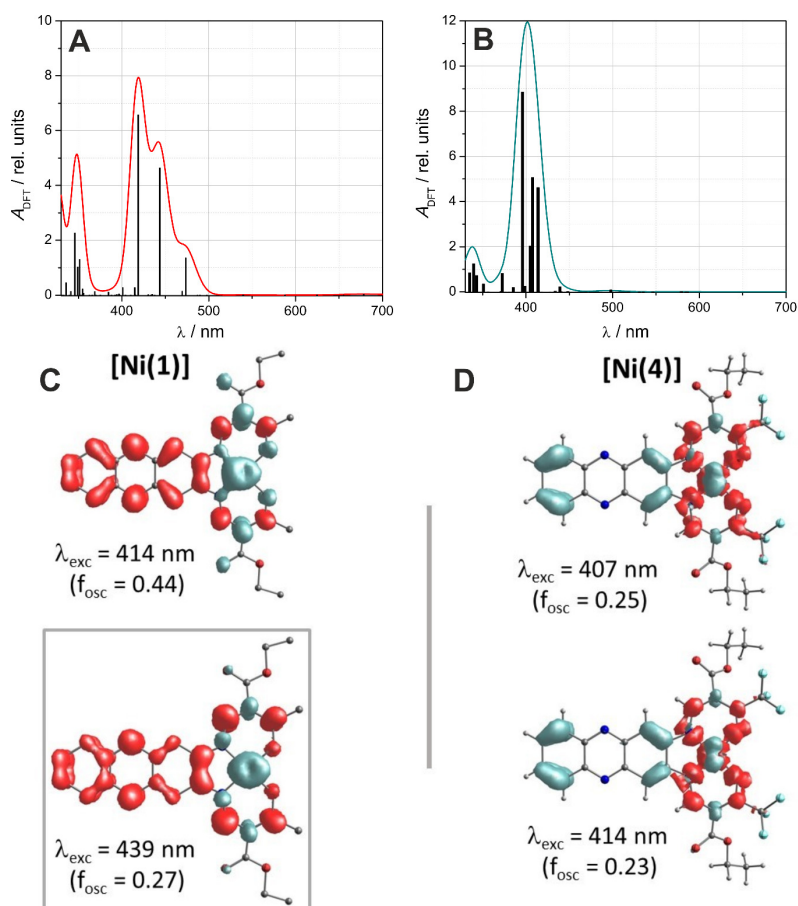


Figure 5. Computed line spectra and convoluted and broadened optical spectra of [Ni(1)] (A) and [Ni(4)] (B). Graphical representations of the difference densities of selected diagnostic visible transitions in [Ni(1)] (C) and [Ni(4)] (D). Color code: source, dark cyan; sink, red.

The lowest 70 vertical transitions have been computed, covering the entire UV-NIR range. The obtained line spectra and convoluted and broadened TD-DFT spectra of [Ni(1)] and [Ni(4)] are shown in Figure 5; the corresponding spectra of [Ni(2,3)] are given in Figures S18–S20 in the Supporting Information. In fact, the predicted spectra match the experimental data very well with respect to energy, (relative) intensity, and overall shape except for the experimentally observed shoulder at 475 nm for [Ni(4)] that is not predicted by the theory. In particular, we note that the double-peak structure of the intense band at 420 nm for [Ni(1–3)] is found also in the calculations, whereas TD-DFT correctly predicts two nearly coinciding transitions in [Ni(4)]. The difference densities of the two leading visible transitions of [Ni(1)] and [Ni(4)] are shown in Figures 5C,D, respectively (see Figures S21 and S22 in the Supporting Information for graphical representations of the single orbital contributions of the leading visible transitions of [Ni(1)] and [Ni(4)]; see Table S9 and S10 in the Supporting Information for summaries of the TD-DFT results for [Ni(1)] and [Ni(4)]). In [Ni(1)] (and [Ni(2,3)]) both transitions indicate a charge-transfer from the [NiN₂O₂] core to the electron-accepting phenazine. Significant

contributions of nickel(II)-based d orbitals render the transitions MLCT-like. Evidently, the direction of the charge shift is inverted in the leading transition of CF₃-appended **[Ni(4)]**; quite surprisingly, the electron source is largely phenazine centered, whereas **[NiN₂O₂]** acts as the charge sink. Although the transitions are partially d-d like, the dominating pathway is assigned as an LMCT. That is, the dominant vertical excited singlet states take on formal nickel(III) and nickel(I) character in **[Ni(1)]** and **[Ni(4)]**, respectively. As a matter of fact, the qualitative difference in electronic structure extends to the relaxation of the excited states: while **[Ni(1–3)]** all show significant emission in many different media, **[Ni(4)]** is nonemissive (see Figure 3B). It is noted that the excited state obtained via metal to ligand CT can be best described as nickel(III) coupled to a phenazine radical anion, **[Ni^{III}(1)^{•-}]**, largely akin to the well-established ruthenium polypyridine photosensitizers.⁴⁴ In contrast to nickel(II), nickel(III) is a much stronger Lewis acid and, thus, fast coordination of a Lewis base is very likely. As was seen later in fluorescence quenching studies, axial ligation indeed is highly favored in excited **[Ni(1)]** (see below). In contrast, excited **[Ni(4)]** is rather formulated as **[Ni^I(4)⁺]** with an oxidized phenazine moiety. It is tempting to associate its lacking fluorescence with secondary electron relaxation to yield a d-d excited singlet state, prone to rapid intersystem crossing to a nonemissive triplet state. We expect deeper insights here from the application of advanced wave-functional methods.⁴⁵

The mere observation of luminescent nickel(II) complexes is remarkable, as there are only two reported cases so far.³⁸ Typically, low-lying d-d states of a nonclosed d electronic shell result in a complete photoluminescence quenching due to effective deactivation paths. As a matter of fact, the quantum yield of the photoluminescence of **[Ni(1)]** ($5 \pm 1\%$) almost equals the one of the ligand **H₂1** ($6 \pm 1\%$), pointing to only minor spin-orbit coupling effects. The relative quantum yields of **[Ni(2)]** and **[Ni(3)]** which were determined from the measured emission intensities at $\lambda_{\text{exc}} = 405$ nm are on the same order of magnitude (see Figure S23A for Φ vs T plot of **H₂1** and **[Ni(1)]**); the T dependence of absorption was taken into account). Time-correlated single-photon counting (TCSPC) gave a long fluorescence lifetime of $\tau = 1.0$ ns for **[Ni(1)]** at room temperature. Deactivation of competitive nonradiative relaxation paths leads to further increased lifetimes at lower temperatures, reaching $\tau = 1.8$ ns at 218 K (see Figure S23B,C for VT-TCSPC detected monoexponentially fluorescence decays of **[Ni(1)]** and a lifetime vs T plot for **[Ni(1)]**; Table S11 for T -dependent lifetimes). The natural radiative rate constant amounts to a mean value of $(5.2 \pm 0.2) \times 10^7$ s⁻¹, which is equivalent to an intrinsic lifetime of 19 ± 1 ns (see Figure S23D for a k_r/k_{nr} vs T plot of **[Ni(1)]**).

Coordination-Induced Spin State Switch (CISSS)

Planar nickel(II) complexes of strong-field ligands can expand their coordination sphere through ligation of additional axial donors, giving rise to diagnostic shifts in the UV-vis spectra.²¹ Accordingly, the response of the optical spectra of dilute solutions of **[Ni(1–4)]** toward the nature and the amount of external donors was recorded. Steady-state UV-vis measurements were first performed in chloroform/pyridine mixtures of variable mixing ratios. The corresponding absorption spectra of **[Ni(1)]** and **[Ni(4)]** are shown in Figure 6 (photographs of the solutions of **[Ni(1)]** and **[Ni(4)]** upon irradiation are given in Figure S24 in the Supporting Information; corresponding spectra of **[Ni(2,3)]** are given in Figure S25 in the Supporting Information).

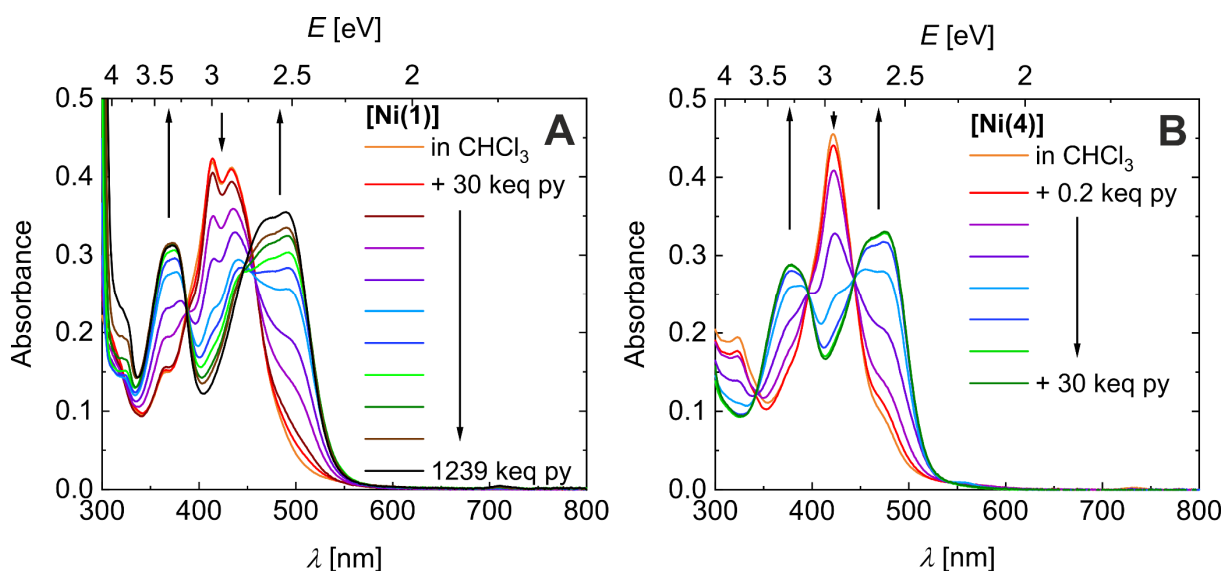


Figure 6. Absorbance measurements of **[Ni(1)]** (A) and **[Ni(4)]** (B) in varying chloroform/pyridine ratios at room temperature; $[\text{Ni(1/4)}] = 1.0 \times 10^{-5}$ M. The increments are given in the Supporting Information.

The coinciding response of **[Ni(1–3)]** to the amount of pyridine points to a very mild influence of the nature of the substituents on the chelate cycle (ester or ketone). The spectra of these complexes remain unaffected by the presence of pyridine up to a threshold concentration, which corresponds to a molar excess of pyridine relative to **[Ni(1–3)]** of approximately 30.000:1. Even higher amounts of pyridine, that is, >100 kequiv, are necessary to significantly bleach the diagnostic double-peak band of the planar species at 430 nm. Its subspectrum is then successively replaced by two strong bands centered at 370 and 510 nm. The growth of a subspectrum is safely associated with five- and/or six-coordinate nickel(II) species and thus in line with our preliminary results on **[Ni(1)]**,³⁹ a CISSS takes place. TD-DFT computed vertical spectra of triplet-configured **[Ni(1)py]** and **[Ni(1)(py)₂]** likewise feature intense transitions in the UV and the visible regimes (see Figure S26 in the Supporting Information) at 360/480 nm

and 360/500 nm, respectively; a distinction between CN 5 and CN 6 in the experimental spectra on the basis of just the DFT results appears nonviable due to the spectral overlap.

If the substituents on the ligand can strongly influence the acidity of the metal center through electron-withdrawing effects, the sensitivity of the complex toward CISSS is expected to increase. Accordingly, fluorine-persubstituted tetraphenylporphyrin derivatives have been found to produce highly electron deficient coordination platforms.⁴⁶ This effect can be likewise seen with **[Ni(4)]**, carrying electron-withdrawing CF₃ groups. The main absorption band of **[Ni(4)]** in chloroform at 422 nm disappears completely upon addition of pyridine, to be replaced by three intense absorbance bands at 375, 455, and 471 nm. Notably, these massive CISSS-related changes take place upon addition of much smaller amounts of pyridine for **[Ni(4)]** than are seen with **[Ni(1–3)]**. **[Ni(4)]** shows a threshold value for CISSS of only a few hundred equivalents and saturates in the presence of ca. 6 kequiv: that is, [py]₀ = 60 mM.

A detailed look at the set of spectra allows insight into nickel speciation as a function of pyridine concentration. For **[Ni(4)]**, only a single set of isosbestic points can be observed at 396 and 443 nm, pointing to significant amounts of only two absorbing species. This observation is in agreement with previous studies. It is generally assumed that five-coordinate nickel(II) does not accumulate due to unfavorable thermodynamics.^{23,48–50} Nevertheless, when preorganized ligands are used five-coordinate nickel(II) complexes can be obtained.^{21,51} Alternatively, the similarity between the computed spectra of CN 5 and CN 6 species **[Ni(4)(py)]** and **[Ni(4)(py)₂]** in Figure S27 in the Supporting Information may be indicative of coinciding experimental spectra. For **[Ni(1)]**, however, two sets of isosbestic points can be observed in the visible region, one at low pyridine concentrations and a second at high concentrations. The shift from the low-concentration regime with $\lambda_{\text{isp}} = 463$ nm to the high-concentration regime with $\lambda_{\text{isp}} = 445$ nm is at odds with the implications of only two absorbing species. This finding indicates the presence of three different nickel(II) complexes upon addition of pyridine, most likely CN 4, CN 5, and CN 6. The two bands at around 430 nm and 480 nm are thus convenient indicators on the relative weights of the diamagnetic and paramagnetic states, respectively, and their associated coordination complexes.

As the spectral changes are due to Lewis acid-base interactions, they also reflect the basicity of the external donor. In order to investigate the influence of the basicity of the axial ligands, chloroform solutions with a molar concentration of 1.0×10^{-5} M of **[Ni(1)]** and **[Ni(4)]** were treated with variable amounts of the pyridine derivatives 4-cyanopyridine (4-CN-Py; pK_b = 12.1), pyridine (Py; pK_b = 8.83) and 4-dimethylaminopyridine (DMAP; pK_b = 7.91).

Uncompensated dilution effects through nonadditive volumes inhibit the observation of isosbestic points in these experiments. 4-CN-Py is sparingly soluble in chloroform, and therefore, only up to 10 kequiv 4-CN-Py was added to the chloroform solutions: that is, $[4\text{-CN-Py}]_{\text{max}} = 0.10\text{ M}$.

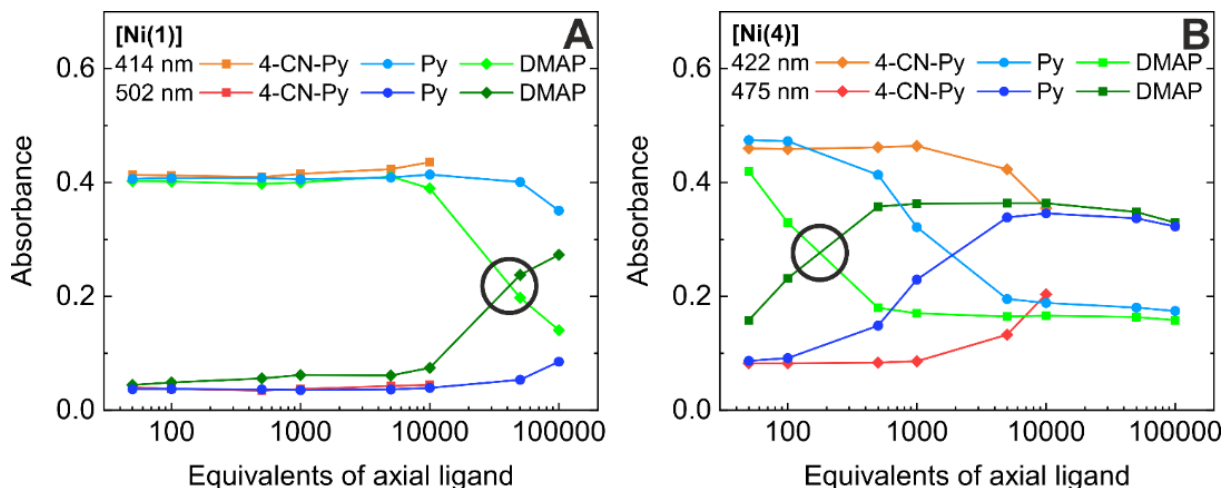


Figure 7. Plot of the absorbance at characteristic wavelengths vs donor concentration for $[\text{Ni}(\text{1})]$ (A) and $[\text{Ni}(\text{4})]$ (B) at $T = 293\text{ K}$ ($1.0 \times 10^{-5}\text{ M}$). The observation wavelengths are given in the captions; crossing points are highlighted for DMAP, indicating half-step concentrations $[\text{DMAP}]_{1/2}$.

Table 2. CISSS for $[\text{Ni}(\text{1})]$ and $[\text{Ni}(\text{4})]$ at $T = 293\text{ K}$.

	pK_b^a	donor no.	$[\text{Ni}(\text{1})]$	$[\text{Ni}(\text{4})]$
Titration in Chloroform, $[\text{CN6}]/[\text{CN4}] \approx 1.0$				
4-CN-Py	12.1			20 kequiv
Py	8.83	33	ca. 1000 kequiv	2 kequiv
DMAP	7.91		40 kequiv	200 equiv
Neat solvent, 1/1 Mixture with CHCl_3				
toluene		0.1	no CISSS / no CISSS	no CISSS
chloroform		4	no CISSS / no CISSS	no CISSS
MeCN		14	insoluble / no CISSS	no CISSS
Acetone		17	insoluble / no CISSS	no CISSS
MeOH		19	insoluble / no CISSS	CISSS
EtOH		19	insoluble / no CISSS	CISSS
DMF		27	no CISSS / no CISSS	CISSS

^a From ref 47.

In Figure 7 the effect of donor concentration on spectral evolution at selected wavelengths is plotted as a function of donor concentration (given in molar equivalents of the external donor relative to $[\text{Ni}(\text{1})]_0$ or $[\text{Ni}(\text{4})]_0$).

Wavelengths have been chosen so as to be diagnostic of the concentrations of CN 4 and CN 6: $\lambda = 414$ nm (**[Ni(1)]**) and 422 nm (**[Ni(4)]**) for CN 4 and $\lambda = 502$ nm (**[Ni(1)]**) and 475 nm (**[Ni(4)]**) for CN 5/6. Table 2 summarizes the donor amounts required to induce CISSS for 50% of the nickel(II) centers, denoted as critical concentration $[L_{ax}]_{1/2}$. This point defines **[Ni(1/4)] = [Ni(1/4)(py)₂]**: that is, it is approximated as the crossing points in the plots of Figure 7. The absorbance spectra of all measurements are shown in Figure S28 in the Supporting Information.

As required for an acid/base reaction, CISSS scales with the strength of the base. This fact can be readily seen in the donor-concentration-dependent absorbance data of **[Ni(4)]** (Figure 7B). Therein, the step concentration is reduced with an increasing strength of the base, giving $[DMAP]_{1/2} \ll [py]_{1/2} \ll [4-CN-Py]_{1/2}$. The variance in Brønsted basicity of the pyridines of $\Delta pK_b = 4.19$ translates into a variation of step concentrations by a factor of 100. As expected, the weaker acidity of **[Ni(1)]** hinders CISSS. The step concentrations of **[Ni(1)]** are ca. 200–500 times greater than those of **[Ni(4)]**, pointing to significant differences in the thermodynamics. In combination with the weakest base, 4-CN-Py axial ligation is not even observed within the solubility limits.

At the step concentrations, $[py]_{1/2}$, the formation constants of the six-coordinate species are simply $K_{eq} = ([py]_{1/2})^{-2}$. In other words, the equilibrium constants are directly extractable from the plots in Figure 7. For DMAP, this treatment gives $K_{eq} \approx (2 \text{ mM})^{-2} = 2.5 \times 10^5 \text{ M}^{-2}$ and $K_{eq} \approx (0.4 \text{ M})^{-2} = 6.2 \text{ M}^{-2}$ for **[Ni(4)]** and **[Ni(1)]**, respectively. Such a difference in K_{eq} translates into a remarkable difference of CISSS Gibbs energies: $\Delta\Delta_{CISSS}G = 26 \text{ kJ mol}^{-1}$ (for parent pyridine a slightly larger difference of $\Delta\Delta_{CISSS}G = 30 \text{ KJ mol}^{-1}$ is calculated). DFT computation of the pyridine ligation thermodynamics helps in the differential analysis of the three elementary steps associated with the CISSS (eqs 1–3): that is, (i) singlet-triplet crossover in CN 4, (ii) axial ligation in CN 4 \rightarrow CN 5, and (iii) axial ligation in CN 5 \rightarrow CN 6. It is found that the implementation of CF₃ in **[Ni(4)]** favors CISSS by an overall increase in the driving force ($\Delta\Delta_{CISSS}G(\text{DFT})$) of 37 kJ mol^{-1} , which is well in line with the experiments. Interestingly, CF₃ substitution not only enhances ligation due to increased acidity but also reduces the thermal singlet/triplet gap.



Molecules lacking significant Brønsted basicity likewise coordinate to metal centers due to their action as Lewis bases. **[Ni(1)]** lacks any CISSS in different neat solvents apart from pyridine, as shown in Figure 8A. Due to the low solubility in most solvents and therefore the limited solvent range, 1/1 solvent mixtures with chloroform were investigated, which also showed no CISSS apart from the pyridine-containing mixture (see Figure 13A). In contrast, CISSS is recorded for **[Ni(4)]** in some neat solvents such as methanol, ethanol, and DMF at $T = 293$ K (Figure 8B). Thereby, a clear “black-or-white” behavior was observed: i.e., we observed the absorption spectrum of either CN 4 or CN 5/6. The trend is qualitatively referred to the donor number (DN) of the solvents (see Table 2), which is a measure for the Lewis basicity of the respective solvents.⁵² Acetone and methanol are the two borderline cases: acetone (DN 17) is CISSS-silent at room temperature, whereas methanol (DN 19) is CISSS-active.

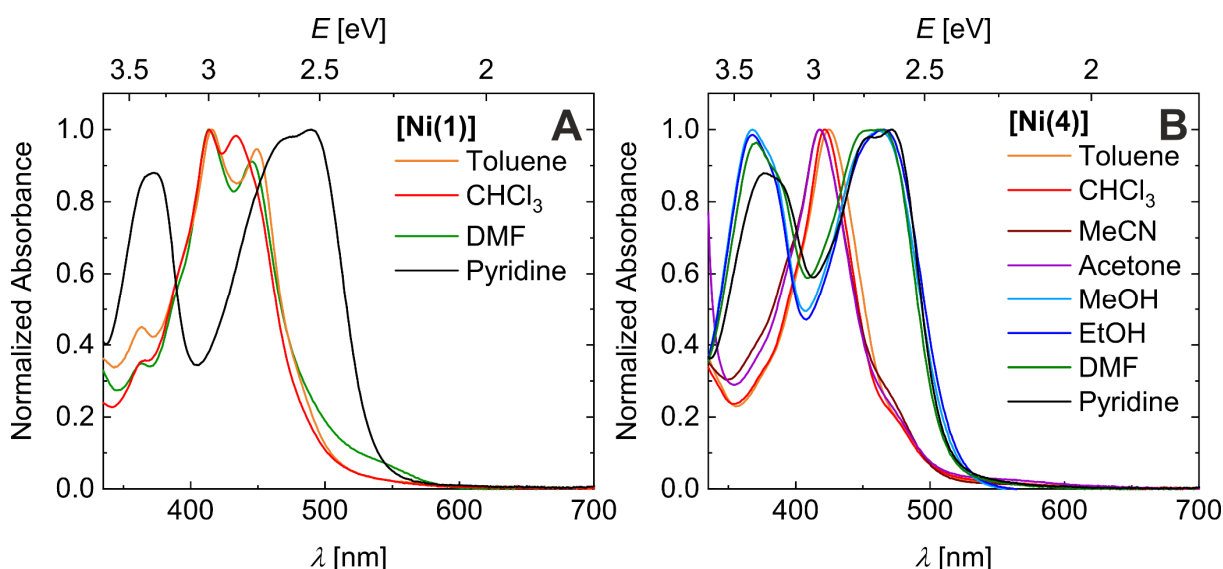


Figure 8. Normalized absorbance spectra of **[Ni(1)]** (A) and **[Ni(4)]** (B) in different solvents (for the respective donor numbers see Table 2).

Temperature Dependence of CISSS

The spin state switch from the singlet to the triplet state, as such, is driven by entropy and is therefore favored at elevated temperature. In contrast, the ligand-association steps to five- and six-coordinate triplet species are entropically disfavored and therefore require a low temperature. Previous examples have shown that commonly the entropic requirements of ligand association dominate, favoring high coordination numbers at low temperatures.²⁴ Temperature scans of diluted solutions of **[Ni(1)]** and **[Ni(4)]** in the presence of pyridine as a potential axial donor have been followed by means of UV-vis and ^1H NMR measurements. For the UV-vis T scans with pyridine, a DCM/pyridine mixture was used in order to widen the liquid temperature range. For **[Ni(1)]**, a DCM/Py mixing ratio of 2/1 was used (see Figure 9A,B), whereas **[Ni(4)]**

required a much higher mixing ratio of 2000/1 (see Figure 9C,D). Under these conditions, the room-temperature spectra show significant contributions of both species, four-coordinate and six-coordinate; the dominating species are ligated $[\text{Ni}(\mathbf{1})(\text{py})_2]$ and native $[\text{Ni}(\mathbf{4})]$, respectively. The spectral evolution in both systems indicates ligand decoordination and coordination for heating and cooling scans, respectively. Clean isosbestic points at 392 and 436 nm were observed in the cooling scans of $[\text{Ni}(\mathbf{1})]$ (see Figure 9A), whereas heating gives rise to a second set of isosbestic points at 390 and 452 nm, akin to the aforementioned isothermal titrations (see Figure 9B and Figure 6A).

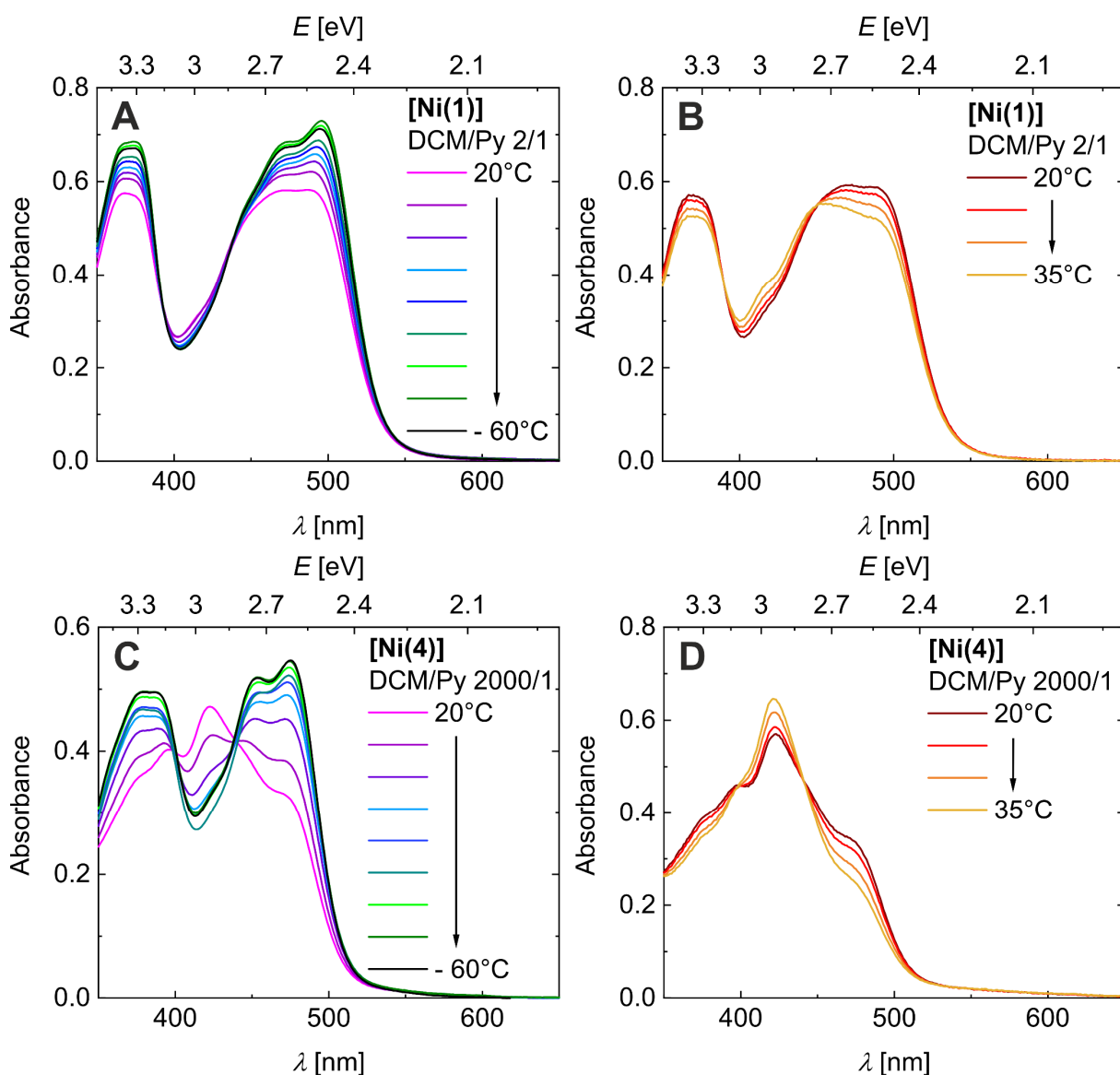


Figure 9. Temperature-dependent UV-vis spectra of $[\text{Ni}(\mathbf{1})]$ upon cooling (A) and heating (B) and of $[\text{Ni}(\mathbf{4})]$ upon cooling (C) and heating (D).

As the wealth of data is in full accordance with the concentration-dependent and T -dependent series, the simultaneous presence of coordination numbers 4, 5, and 6 in the spectra can be

safely concluded. It is noted that speciation of **[Ni(1)]** varies only moderately with temperature. For instance, the transition CN 5 \rightarrow CN 4 is far from complete at 35 °C, as the diagnostic band at 414 nm only begins to increase at 35 °C. *T*-dependent (de)coordination of pyridine is more clearly traceable in ^1H NMR measurements. The ^1H NMR spectra of **[Ni(1)]** in (D₅)pyridine show massive spectral evolution in the temperature range from 30 to 110 °C (Figure S29 in the Supporting Information). Around room temperature, the spectral range of the ^1H NMR spectra and the line widths of some of the signals are clearly indicative of a paramagnetic species. Accordingly, the Bohr magneton number of **[Ni(1)]** in (D₅)pyridine at room temperature was determined to 2.81 (2.92 for **[Ni(4)]**). Upon heating, a sharpening of the signals and a high-field shift is observed, indicating decoordination of pyridine. The speciation changes much more rapidly and completely with temperature in the case of **[Ni(4)]**. Remarkably, the spectral evolution indicates that almost the complete CISSS between CN 4 and CN 6 takes place in the narrow temperature range of only 95 K (CN 4 still has some minor residual contribution at about 485 nm, cf. Figure 8). When similar entropic effects are assumed, the deviation among the complexes reflects the favorable enthalpic contributions in the case of **[Ni(4)]** as mentioned previously. Similarly, to the isothermal titrations, only a single set of isosbestic points at approximately 400 and 440 nm was observed in the heating and cooling measurements (see Figure 9C,D).

The two frontier cases in Figure 8B, that is, **[Ni(4)]** in acetone and in MeOH, were likewise investigated in more detail by temperature-dependent UV-vis and NMR measurements (see Figures 10 and Figures S30, S33, and S34 in the Supporting Information). As shown in Figure S30 in the Supporting Information, heating of the MeOH solutions fails to induce any significant spectra evolution, which would be indicative for a ligand cleavage of the solvent molecule(s) in the recorded temperature range. The absence of CISSS in acetone at room temperature is somewhat surprising, because a DFT analysis of the CISSS thermodynamics predicted a reasonable driving force in favor of CISSS. Indeed, acetone solutions of **[Ni(4)]**, which are CISSS-inactive at room temperature, undergo a massive absorption change upon cooling (see Figure 10A). The spectral evolution in acetone fully matches the spectral changes observed for **[Ni(4)]** in the presence of pyridine in both the isothermal titrations and the iso-concentration *T* scans (see Figures 6B and 9C,D). At room temperature, just a 419 nm maximum is discernible, which decreases upon cooling. In addition, new features at approximately 382, 454, and 472 nm appear. To illustrate this effect, the absorbance intensities at 418 nm (λ_{max} of CN 4) and at 472 nm (λ_{max} of CN 5/6) were plotted versus temperature in Figure 10B.

The plot of the T -dependent association/dissociation equilibrium of **[Ni(4)]** in acetone and a $\text{CHCl}_3/\text{pyridine}$ (2000/1) mixture shows a similar progression for both solvents (see Figure S31 in the Supporting Information).

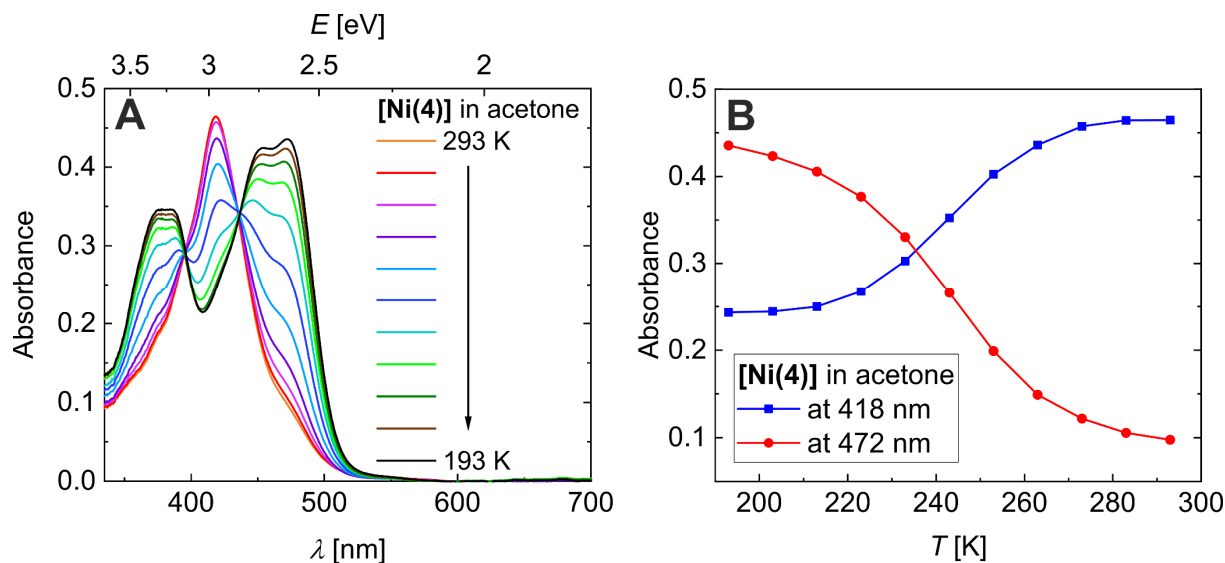


Figure 10. Temperature-dependent absorbance spectra of **[Ni(4)]** in acetone (A). Plot of the absorbance intensity vs T at 418 nm and 472 nm for **[Ni(4)]** (B).

Thermodynamic analyses of the underlying (de)coordination equilibrium in acetone afford values of $(-37.9 \pm 1.0) \text{ kJ mol}^{-1}$ and $(-158.0 \pm 4.0) \text{ J K}^{-1} \text{ mol}^{-1}$ for $\Delta_{\text{CISSS}}H$ and $\Delta_{\text{CISSS}}S$, respectively (see Figure S32 in the Supporting Information). The large negative entropy change echoes previous CISSS studies and reflects the entropically demanding association steps. CISSS upon cooling of an acetone solution is supported by temperature-dependent $^{19}\text{F}^{53}$ and ^1H NMR studies in the range from 0 to 50 °C (see Figures S33 and S34 in the Supporting Information). Thereby, drastic broadenings and low-field shifts were observed upon cooling for both NMR nuclei due to CISSS. The method-dependent concentration ranges and the stronger sensitivity of NMR toward paramagnetism in comparison to UV-vis result in slightly different switching temperatures while the trend is retained.

Fluorescence-Detected CISSS

Static fluorescence quenching through CISSS had been communicated by Weber et al. to rationalize the lack of emission in pyridine-containing chloroform solutions of **[Ni(1)]**. As **[Ni(1)]** is the rare example of photoluminescent nickel(II) complexes, we will herein discuss the emission behavior in more detail. Additional results for **[Ni(1)]** and **[Ni(2,3)]** identify all these complexes to be potent fluorescence sensors, active in the static and dynamic quenching by Lewis bases. Importantly, these complexes constitute the first examples of fluorescence-

detected CISSS, FD-CISSS, as we will illustrate in the following. To rule out inner filter effects, low concentrations of the ligand and complex solutions were chosen for the fluorescence measurements.^{54,55} To allow for a quantitative comparison iso-concentrated solutions (3.7×10^{-6} M) were used. The emission intensity was corrected against the absorbance intensity at the excitation wavelength. The observation that **H21–4** are emissive, albeit with different bands, in chloroform and pyridine rules out ligand-based quenching in pyridine due to intermolecular interactions (see Figure S13 in the Supporting Information).

The phenomenon of a fluorescence-detected CISSS can be realized across the series of nickel(II) complexes [**Ni(1–3)**], as is shown in fluorescence titration experiments with pyridine (Figure 11C,D and Figure S35B in the Supporting Information for [**Ni(1)**]). Upon pyridine addition, the single-band emission at 477/478 nm (see Table 1) drastically deintensifies, reaching close to zero emission in pure pyridine solution. The intensity loss is accompanied by a slight red shift of the emission, giving a residual peak at about 580 nm, due to minor contamination with the free ligand (absent for [**Ni(1)**]), see Figure S35B, SI). As shown in Figure 11E/F (see Figure S35C in the Supporting Information for [**Ni(1)**]), for all solutions the same fluorescence excitation spectrum is recorded, irrespective of the pyridine concentration, giving just one sharp feature at 430/431 nm. Accordingly, fluorescence is solely derived from the residual fraction of four-coordinate native [**Ni(1–3)**].

Absorption spectra of [**Ni(2)**] and [**Ni(3)**] (Figure 11 A,B) fully echo the observations made with [**Ni(1)**] (Figure 6 and S35A in the Supporting Information). Consistent with a pyridine-induced CISSS the major visible envelope of CN4 nickel(II) is replaced by a red-shifted band of conserved intensity. As emission is solely due to the diamagnetic four-coordinate species, both the UV-vis spectra and the steady-state emission spectra are expected to scale with the concentration of native four-coordinate [**Ni(1–3)**] and, in turn, with the pyridine concentration. A comparison of the pyridine-dependent quenching with the pyridine-dependent dynamics of the absorption spectra indeed is suggestive of a common molecular origin of both effects. As is shown in Figure 12A, however, FD-CISSS of [**Ni(1)**] is more sensitive to the pyridine concentration in comparison to CISSS; the fraction of [**Ni(1)**] in CN4 is defined as $c_{\text{CN4}}/c_0 = (A(\lambda) - A(\lambda)_\infty)/(A(\lambda)_0 - A(\lambda)_\infty)$ (with $A(\lambda)_\infty$ = absorbance of pure CN6 at λ , $A(\lambda)_0$ = absorbance of pure CN4 at λ , and $A(\lambda)$ = absorbance at $\lambda = 414 \text{ nm}/433 \text{ nm}$).

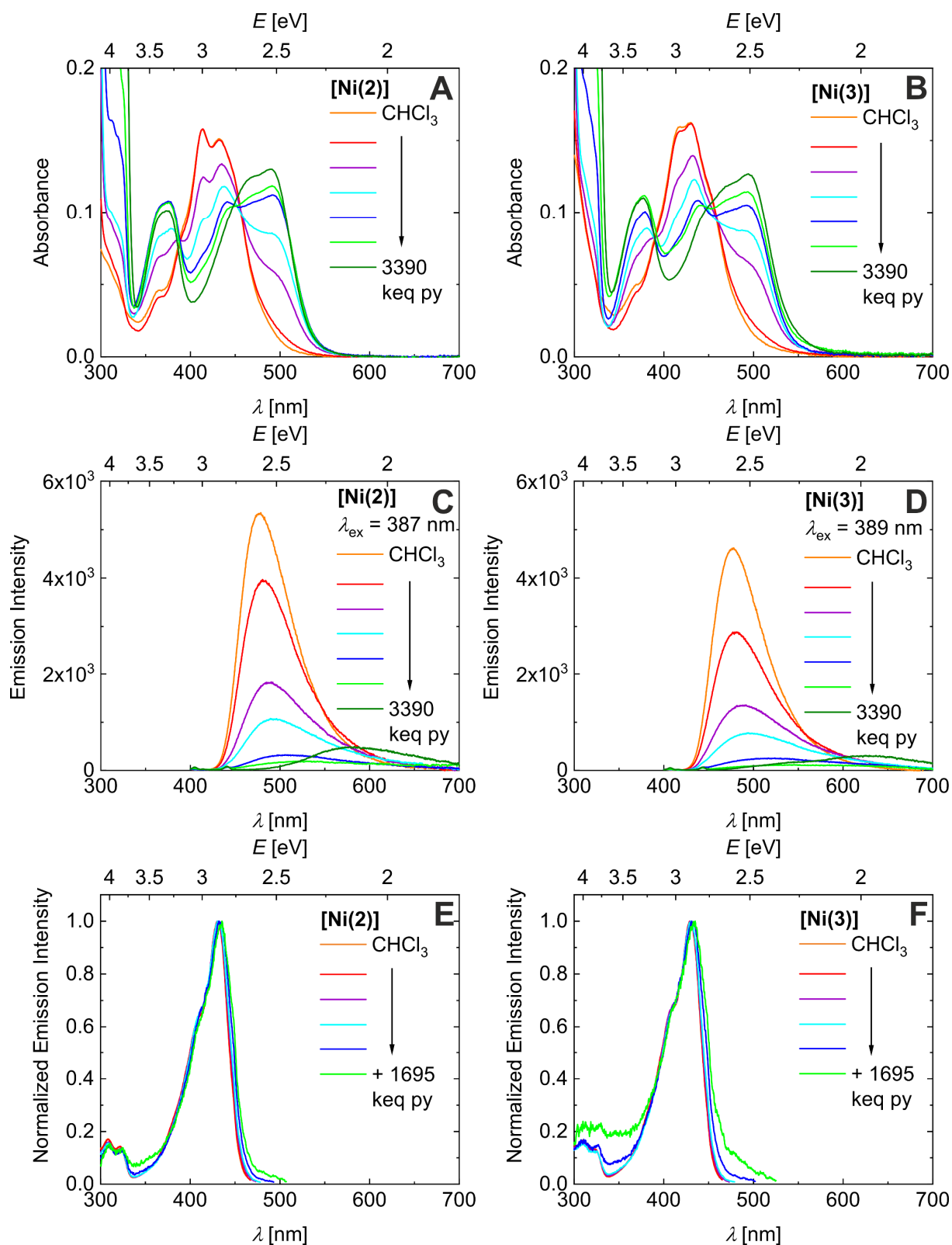


Figure 11. FD-CISSS of $[\text{Ni}(2)]$ and $[\text{Ni}(3)]$ in various chloroform/pyridine mixtures ($3.7 \times 10^{-6} \text{ M}$): absorption spectra of $[\text{Ni}(2)]$ (A) and $[\text{Ni}(3)]$ (B); emission spectra of $[\text{Ni}(2)]$ ($\lambda_{\text{exc}} = 387 \text{ nm}$; C) and $[\text{Ni}(3)]$ ($\lambda_{\text{exc}} = 389 \text{ nm}$; D); fluorescence excitation spectra of $[\text{Ni}(2)]$ ($\lambda_{\text{em}} = \lambda_{\text{exc,max}}$; E) and $[\text{Ni}(3)]$ ($\lambda_{\text{em}} = \lambda_{\text{exc,max}}$; F).

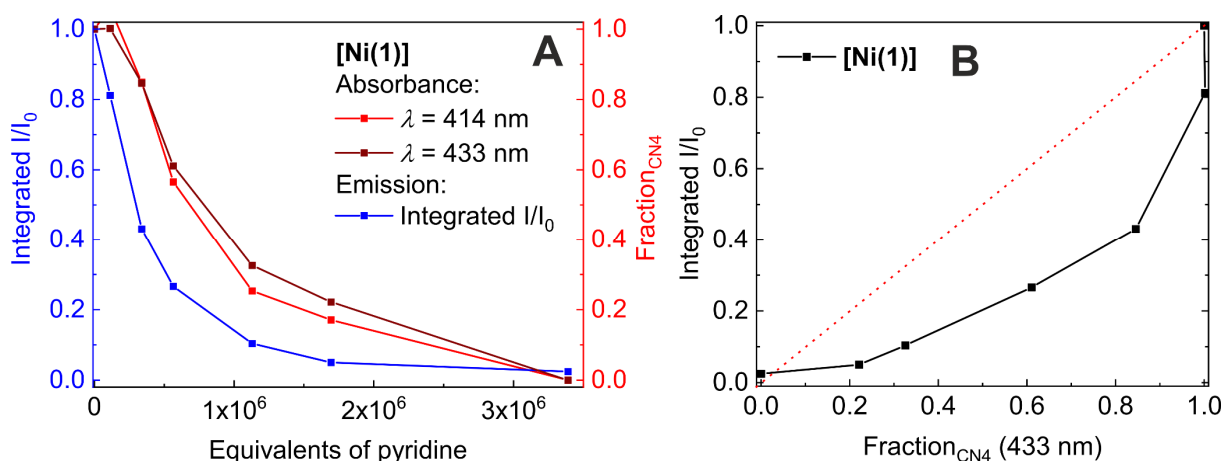


Figure 12. CISSS in absorption and emission. Pyridine-dependent CN4 molar fraction (red) and normalized integrated emission intensity (blue) of [Ni(1)] (A). Plot of the normalized integrated emission intensity vs the CN4 molar fraction of [Ni(1)] (B). $\text{Fraction}_{\text{CN4}} = c_{\text{CN4}}/c_0 = (A(\lambda) - A(\lambda)_\infty)/(A(\lambda)_0 - A(\lambda)_\infty)$.

A plot of the normalized integrated emission intensity versus the CN4 fraction is strongly bent upward and distinctly deviates from a 1/1 proportionality (Figure 12B). This finding denies that emission quenching is fully derived from static pathways in terms of the thermal depletion of CN4 species. In contrast, we suggest that quenching is partially derived from interactions of excited [Ni(1)] with potent axial ligands. The mere importance of this additional *dynamic* quenching pathway is seen in the high efficiency at rather low quencher concentrations. In keeping with this hypothesis, the Stern-Volmer plot of emission quenching of [Ni(1)] by pyridine, which is shown in Figure S36A in the Supporting Information, is likewise strongly bent upward.

In contrast, donors such as acetone and DMF (Figure 13) are found to selectively quench fluorescence via dynamic pathways. Accordingly, the finding that excited [Ni(1)] is quenched via axial ligand coordination is not limited to the chloroform/pyridine prototype. Rather, it is broadly applicable to different donor types. This conclusion stems from the comparison of the absorbance and emission spectra recorded of [Ni(1)] in various coordinating and noncoordinating solvents (Figure 13; 1/1 chloroform/solvent mixtures for solubility reasons). Except the mixture consisting of chloroform/pyridine, all mixtures feature identical absorption spectra attributable to CN 4 (see Figure 13A). That is, different from [Ni(4)], CISSS requires very potent donors in the case of [Ni(1)]. However, the lack of CISSS does not interfere with fluorescence quenching: the emission of [Ni(1)] is nearly quantitatively quenched not only in the presence of CISSS-*active* pyridine but also in the presence of CISSS-*inactive* acetonitrile,

acetone, methanol, ethanol, and DMF. In contrast, with the noncoordinating base triethylamine no quenching was observed.³⁹

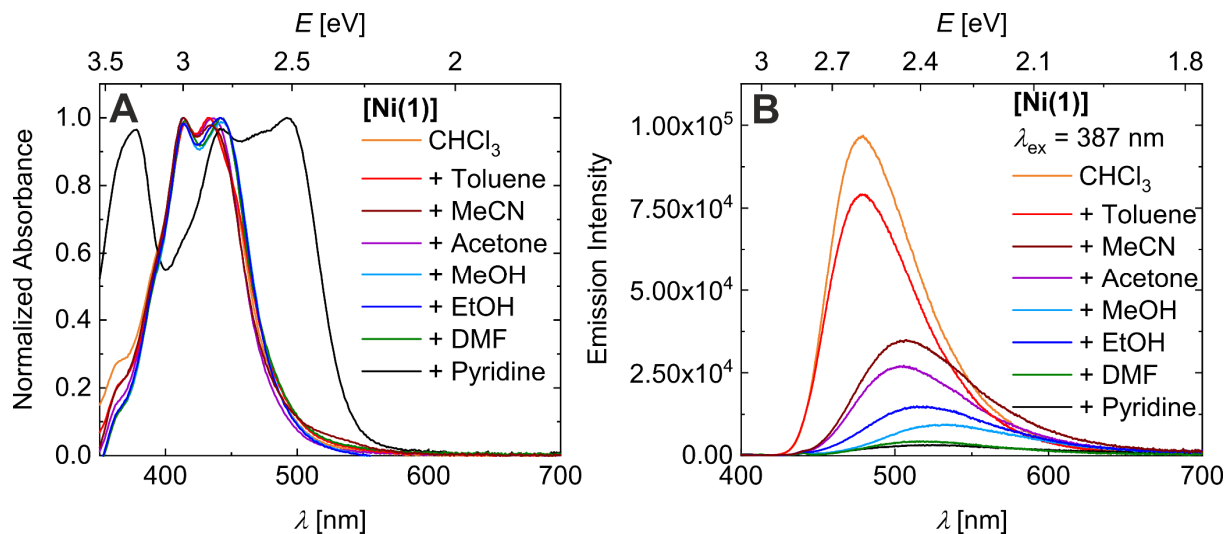
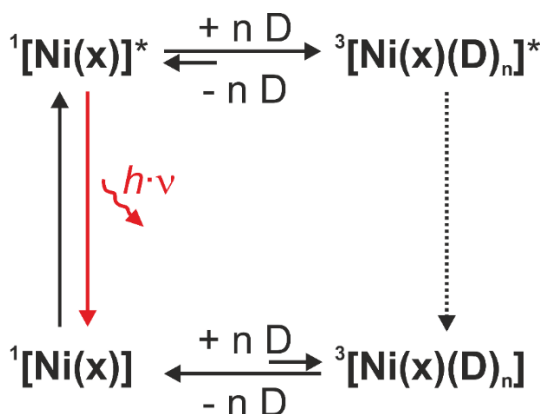


Figure 13. Normalized absorbance spectra of [Ni(1)] in different 1/1 solvent mixtures with CHCl₃ (A). Respective donor numbers (DN): toluene DN, 0.1; CHCl₃ DN, 4; MeCN DN, 14; acetone DN, 17; MeOH DN, 19; EtOH DN, 19; DMF DN, 27; pyridine DN, 33. Emission spectra of these [Ni(1)] solutions (B).

Both the emission intensity at λ_{\max} and the Stokes shift follow the donor number of the respective solvent (see Figure S36B in the Supporting Information). The increase in Stokes shifts with solvent donor number points to enhanced stabilization of a polar excited state by a polar medium. As the relative intensity of the emission scales inversely with the Lewis basicity of the solvent (given as donor number in terms of Gutmann's definition, DN), we assign the quenching to be due to Lewis acid-base interactions in the singlet excited state. Dynamic emission quenching via bimolecular diffusive pathways is by no means exceptional for organic fluorescent dyes.⁵⁵ Our observation of dynamic quenching of fluorescence in nickel(II) complexes via axial coordination (Scheme 3), however, deserves some additional comments: most importantly, quenching through Lewis bases of excited [Ni(1)] *must* have occurred in the excited singlet state! This observation is in stark contrast with what is known for the related nickel(II) porphyrin systems. This contrasting behavior of [Ni(1)] (and [Ni(2,3)], see below) renders spin-state changes recordable via fluorescence methods in terms of fluorescence-detected CISSS, FD-CISSS.

Previous experimental and theoretical studies on nickel(II) porphyrins have discussed the ability for ligation of singlet-based ¹B_{1g} states⁵⁶ but did not provide any evidence for its involvement in the ligation process. In particular, a thorough investigation of the excited-state

dynamics of nickel(II) porphyrins revealed ultrafast intersystem crossing in the 10-15 ps range from the singlet to the triplet excited state, rendering any axial ligation entirely triplet-based.⁵⁷⁻⁶⁰



Scheme 3. FD-CISSS as complementary static and dynamic fluorescence quenching pathways in planar nickel(II) complexes through ground-state CISSS (bottom line) and CISSS in the singlet excited state (upper line).

This value should be compared to the singlet excited state lifetime of ca. 1.0 ns recorded for **[Ni(1)]**. Obviously, the lifetime of the excited singlet state in **[Ni(1)]** is much longer than in the respective nickel(II) porphyrins, rendering emission kinetically competitive with intersystem crossing. Indeed, TCSPC results of **[Ni(1)]** in acetone/chloroform and dimethylformamide/chloroform 1/1 mixtures both yield distinctly faster fluorescence decays at room temperature; i.e., lifetimes amount to 0.27 and 0.07 ns in acetone/chloroform and DMF/chloroform, respectively (see Figure S37 in the Supporting Information). With a view to these striking divergences in behavior, our finding of a dynamic emission quenching via axial ligation is as exciting a finding as the mere observation of emissive nickel(II) complexes is.

4.3 Conclusion

Smart molecular sensor materials are highly sought after especially for the applications as biosensors. An applicable sensor should feature, on one hand, a high sensitivity toward specific molecules and, on the other hand, an easy and directly detectable readout such as a change in the photoluminescence behavior. In this study, we report on three rare examples of nickel(II) complexes that are emissive with a coordination number of 4 and, most importantly, nonemissive upon CISSS. To this end, the optical properties of **[Ni(1)]** are discussed in detail on basis of a (temperature-dependent) solvent scan of the steady-state UV-vis absorption and emission. In order to address the nature of the emissive state(s), temperature-dependent lifetimes and quantum yields are reported for **[Ni(1)]**. The experimental work is supplemented

by (TD-)DFT modeling of the nickel(II) speciation with respect to coordination number, geometry, spin state, and UV-vis spectra. FD-CISSS has been proven to tolerate lateral substitution of the ligand backbone through the synthesis and in-depth spectroscopic analysis of the new **[Ni(2)]** and **[Ni(3)]**. In parallel, the electron-withdrawing CF₃ substituents in **[Ni(4)]** enhance the CISSS sensitivity. This method of enhanced CISSS has been demonstrated by Tuzek et al. with a salpn-based Schiff base ligand system.⁶¹ As a matter of fact, an enhanced sensitivity goes hand in hand with a quenched emission, irrespective of the coordination number. A likely rationale is based on the character of the dominant absorption. This is best described as LMCT for **[Ni(4)]** but as MLCT for **[Ni(1–3)]**. The finding of long-lived MLCT states of nickel(II) complexes promises applications in base-metal light energy conversion processes. Most importantly, the fluorescence of **[Ni(1–3)]** is quenched in noncoordinating solvents upon addition of axial ligands, allowing an easy readout of the CISSS through fluorescence spectroscopy (FD-CISSS). Thereby, FD-CISSS is found to be active at lower pyridine concentrations in comparison to CISSS, which indicates greatly favored coordination of axial ligands in the singlet excited state in comparison to the ground state. Accordingly, efficient quenching in FD-CISSS is observed in a number of CISSS-inactive media, which follows nicely the donor number of the solvent. In summary, our study provides a detailed insight into the radiative nature of phenazine-based nickel(II) complexes and their CISSS. These findings might help in the design of new nickel(II)-based molecular sensors based on fluorescence-detected CISSS.

4.4 Notes and References

Associated Content

The Supporting Information is available free of charge at <https://pubs.acs.org/doi/10.1021/jacs.0c12568>.

Experimental section, ¹H and ¹³C NMR spectra X-ray crystal structure determinations, metrics of the optimized complexes based on DFT powder X-ray diffraction patterns, optical spectra of the ligands and **[Ni(2)]** and **[Ni(3)]**, computed frontier orbital energies and landscapes, computed line spectra and difference density plots, photophysical measurements of **H₂1** and **[Ni(1)]**, photographs of **[Ni(1)]** and **[Ni(4)]** chloroform/pyridine solutions, absorbance measurements of **[Ni(2)]** and **[Ni(3)]** chloroform/pyridine solutions, computed line spectra of **[Ni(1)]** and **[Ni(4)]** in CN 5 and 6, absorbance measurements of **[Ni(1)]** and **[Ni(4)]** with various axial ligands, temperature-dependent ¹H NMR spectra of **[Ni(1)]** in (D₅)pyridine, temperature-

dependent absorbance spectra of [Ni(4)] in MeOH, analysis of the association/dissociation equilibrium of [Ni(4)], temperature-dependent ^{19}F and ^1H NMR spectra of [Ni(4)] in (D6)acetone, optical spectra and analysis of the data of [Ni(1)] in chloroform/pyridine solutions (PDF)

Cartesian coordinates of the calculated structures (PDF)

Accession Codes

CCDC 2042261 and 2042264 contain the supplementary crystallographic data for this paper. These data can be obtained free of charge via www.ccdc.cam.ac.uk/data_request/cif, or by emailing data_request@ccdc.cam.ac.uk, or by contacting The Cambridge Crystallographic Data Center, 12 Union Road, Cambridge CB2 1EZ, UK; fax: +44 1223 336033.

Author Contributions

H.K. synthesized the ligands and complexes, carried out most of the experiments, and wrote the first draft of the manuscript. K.S. measured the T-dependent UV–vis and emission spectra in acetone and determined the PLQYs as well as the PL lifetimes using TCSPC. G.H. did the electronic structure calculations and contributed to the overall scientific discussion. I.P. measured the T-dependent UV–vis spectra in DCM/pyridine. F.W.H. determined the X-ray structures. H.M. measured the T-dependent NMR spectra. D.M.G., A.K., and B.W. gave scientific advice and helped in writing the manuscript. All authors have given approval to the final version of the manuscript.

Funding Sources

Financial supports from the Fonds der Chemischen Industrie (Kekulé-Stipendium), MINT Lehramt Plus, German Research foundation (SFB840; project A10), the BayNAT program, ENB Elite Network of Bavaria, and the University of Bayreuth are gratefully acknowledged. K.S. acknowledges financial support from the German National Science Foundation (Project KO 3973/2-1 and GRK 1640). I.P., A.K. and D.M.G. gratefully acknowledge funding from “Solar Technologies Go Hybrid (SolTech)”, an initiative of the Bavarian State Ministry for Science, Research, and Art.

Notes

The authors declare no competing financial interest.

Acknowledgement

We thank Dr. Ulrike Lacher for the measurement of the mass spectra and Florian Puchtler for the measurement of the PXRD patterns.

Abbreviations

CISSS, coordination-induced spin state switch; FD-CISSS, fluorescence-detected coordination-induced spin state switch; CN, coordination number; SCO, spin crossover; HS, high-spin; LS, low-spin; kequiv, kiloequivalents; (TD-)DFT, time-dependent density functional theory; MLCT, metal to ligand charge-transfer; LMCT, ligand to metal charge-transfer; PLQY, photoluminescence quantum yield; TCSPC, time-correlated single photon counting

References

- (1) Coronado, E. Molecular magnetism: from chemical design to spin control in molecules, materials and devices. *Nature Rev. Mater.* **2020**, *5* (2), 87–104. DOI: 10.1038/s41578-019-0146-8.
- (2) Senthil Kumar, K.; Ruben, M. Emerging trends in spin crossover (SCO) based functional materials and devices. *Coord. Chem. Rev.* **2017**, *346*, 176–205. DOI: 10.1016/j.ccr.2017.03.024.
- (3) Brooker, S. Spin crossover with thermal hysteresis: practicalities and lessons learnt. *Chem. Soc. Rev.* **2015**, *44* (10), 2880–2892. DOI: 10.1039/c4cs00376d.
- (4) Enriquez-Cabrera, A.; Rapakousiou, A.; Piedrahita Bello, M.; Molnár, G.; Salmon, L.; Bousseksou, A. Spin crossover polymer composites, polymers and related soft materials. *Coord. Chem. Rev.* **2020**, *419*, 213396. DOI: 10.1016/j.ccr.2020.213396.
- (5) Halcrow, M. A. Manipulating metal spin states for biomimetic, catalytic and molecular materials chemistry. *Dalton Trans.* **2020**, *49*, 15560. DOI: 10.1039/d0dt01919d.
- (6) Boillot, M.-L.; Weber, B. Mononuclear ferrous and ferric complexes. *C. R. Chim.* **2018**, *21* (12), 1196–1208. DOI: 10.1016/j.crci.2018.01.006.
- (7) Halcrow, M. A., Ed. *Spin-Crossover Materials*; John Wiley & Sons Ltd, 2013.
- (8) Gütllich, P.; Goodwin, H., Eds. *Spin Crossover in Transition Metal Compounds I-III*; Topics in Current Chemistry, 233-235; Springer Berlin / Heidelberg, 2004.
- (9) Sieklucka, B.; Pinkowicz, D., Eds. *Molecular Magnetic Materials*; Wiley-VCH Verlag GmbH & Co. KGaA, 2017. DOI: 10.1002/9783527694228.
- (10) Göbel, C.; Hils, C.; Drechsler, M.; Baabe, D.; Greiner, A.; Schmalz, H.; Weber, B. Confined Crystallization of Spin-Crossover Nanoparticles in Block-Copolymer Micelles. *Angew. Chem. Int. Ed.* **2020**, *59* (14), 5765–5770. DOI: 10.1002/anie.201914343.
- (11) Weihermüller, J.; Schlamp, S.; Milius, W.; Puchtler, F.; Breu, J.; Ramming, P.; Hüttner, S.; Agarwal, S.; Göbel, C.; Hund, M.; Papastavrou, G.; Weber, B. Amphiphilic iron(ii) spin crossover coordination polymers: Crystal structures and phase transition properties. *J. Mater. Chem. C* **2019**, *7*, 1151–1163. DOI: 10.1039/c8tc05580g.
- (12) Lochenie, C.; Schötz, K.; Panzer, F.; Kurz, H.; Maier, B.; Puchtler, F.; Agarwal, S.; Köhler, A.; Weber, B. Spin-Crossover Iron(II) Coordination Polymer with Fluorescent Properties: Correlation between Emission Properties and Spin State. *J. Am. Chem. Soc.* **2018**, *140* (2), 700–709. DOI: 10.1021/jacs.7b10571.
- (13) Weber, B. Spin crossover complexes with N4O2 coordination sphere – The influence of covalent linkers on cooperative interactions: Deutsche Forschungsgemeinschaft Molecular

- Magnetism Research Report. *Coord. Chem. Rev.* **2009**, 253 (19-20), 2432–2449. DOI: 10.1016/j.ccr.2008.10.002.
- (14) Senthil Kumar, K.; Bayeh, Y.; Gebretsadik, T.; Elemo, F.; Gebrezgiabher, M.; Thomas, M.; Ruben, M. Spin-crossover in iron(ii)-Schiff base complexes. *Dalton Trans.* **2019**, 48 (41), 15321–15337. DOI: 10.1039/c9dt02085c.
- (15) Harding, D. J.; Harding, P.; Phonsri, W. Spin crossover in iron(III) complexes. *Coord. Chem. Rev.* **2016**, 313, 38–61. DOI: 10.1016/j.ccr.2016.01.006.
- (16) Morgan, G. G.; Murnaghan, K. D.; Müller-Bunz, H.; McKee, V.; Harding, C. J. A Manganese(III) Complex That Exhibits Spin Crossover Triggered by Geometric Tuning. *Angew. Chem. Int. Ed.* **2006**, 45 (43), 7192–7195. DOI: 10.1002/anie.200601823.
- (17) Sim, P. G.; Sinn, E. First manganese(III) spin crossover, first d4 crossover. Comment on cytochrome oxidase. *J. Am. Chem. Soc.* **1981**, 103 (1), 241–243. DOI: 10.1021/ja00391a067.
- (18) Graf, M.; Wolmershäuser, G.; Kelm, H.; Demeschko, S.; Meyer, F.; Krüger, H.-J. Temperature-Induced Spin-Transition in a Low-Spin Cobalt(II) Semiquinonate Complex. *Angew. Chem. Int. Ed.* **2010**, 49 (5), 950–953. DOI: 10.1002/anie.200903789.
- (19) Venkataramani, S.; Jana, U.; Dommaschk, M.; Sonnichsen, F. D.; Tucek, F.; Herges, R. Magnetic Bistability of Molecules in Homogeneous Solution at Room Temperature. *Science* **2011**, 331 (6016), 445–448. DOI: 10.1126/science.1201180.
- (20) Thies, S.; Sell, H.; Schütt, C.; Bornholdt, C.; Näther, C.; Tucek, F.; Herges, R. Light-induced spin change by photodissociable external ligands: a new principle for magnetic switching of molecules. *J. A. Chem. Soc.* **2011**, 133 (40), 16243–16250. DOI: 10.1021/ja206812f.
- (21) Gutzeit, F.; Dommaschk, M.; Levin, N.; Buchholz, A.; Schaub, E.; Plass, W.; Näther, C.; Herges, R. Structure and Properties of a Five-Coordinate Nickel(II) Porphyrin. *Inorg. Chem.* **2019**, 58, 12542. DOI: 10.1021/acs.inorgchem.9b00348.
- (22) Dommaschk, M.; Peters, M.; Gutzeit, F.; Schütt, C.; Näther, C.; Sönnichsen, F. D.; Tiwari, S.; Riedel, C.; Boretius, S.; Herges, R. Photoswitchable Magnetic Resonance Imaging Contrast by Improved Light-Driven Coordination-Induced Spin State Switch. *J. Am. Chem. Soc.* **2015**, 137 (24), 7552–7555. DOI: 10.1021/jacs.5b00929.
- (23) Thies, S.; Bornholdt, C.; Köhler, F.; Sönnichsen, F. D.; Näther, C.; Tucek, F.; Herges, R. Coordination-Induced Spin Crossover (CISCO) through Axial Bonding of Substituted Pyridines to Nickel–Porphyrins: σ -Donor versus π -Acceptor Effects. *Chem. Eur. J.* **2010**, 16 (33), 10074–10083. DOI: 10.1002/chem.201000603.
- (24) Klaß, M.; Kraemer, J.; Näther, C.; Tucek, F. Design, synthesis, and evaluation of nickel dipyridylmethane complexes for Coordination-Induced Spin State Switching (CISSS). *Dalton Trans.* **2018**, 47 (4), 1261–1275. DOI: 10.1039/C7DT03952B.
- (25) Shepherd, H. J.; Quintero, C. M.; Molnár, G.; Salmon, L.; Bousseksou, A. Luminescent Spin-Crossover Materials. In *Spin-Crossover Materials*; Halcrow, M. A., Ed.; John Wiley & Sons Ltd, 2013; pp 347–373. DOI: 10.1002/9781118519301.ch13.
- (26) Matsuda, M.; Kiyoshima, K.; Uchida, R.; Kinoshita, N.; Tajima, H. Characteristics of organic light-emitting devices consisting of dye-doped spin crossover complex films. *Thin Solid Films* **2013**, 531, 451–453. DOI: 10.1016/j.tsf.2013.01.094.
- (27) Wang, C.-F.; Li, R.-F.; Chen, X.-Y.; Wei, R.-J.; Zheng, L.-S.; Tao, J. Synergetic spin crossover and fluorescence in one-dimensional hybrid complexes. *Angew. Chem. Int. Ed.* **2015**, 54 (5), 1574–1577. DOI: 10.1002/anie.201410454.
- (28) Salmon, L.; Molnár, G.; Zitouni, D.; Quintero, C.; Bergaud, C.; Micheau, J.-C.; Bousseksou, A. A novel approach for fluorescent thermometry and thermal imaging purposes using spin crossover nanoparticles. *J. Mater. Chem.* **2010**, 20 (26), 5499. DOI: 10.1039/c0jm00631a.

- (29) Titos-Padilla, S.; Herrera, J. M.; Chen, X.-W.; Delgado, J. J.; Colacio, E. Bifunctional Hybrid SiO₂ Nanoparticles Showing Synergy between Core Spin Crossover and Shell Luminescence Properties. *Angew. Chem. Int. Ed.* **2011**, *50* (14), 3290–3293. DOI: 10.1002/anie.201007847.
- (30) Engeser, M.; Fabbrizzi, L.; Licchelli, M.; Sacchi, D. A fluorescent molecular thermometer based on the nickel(II) high-spin/low-spin interconversion. *Chem. Commun.* **1999** (13), 1191–1192. DOI: 10.1039/a901931f.
- (31) Garcia, Y.; Robert, F.; Naik, A. D.; Zhou, G.; Tinant, B.; Robeyns, K.; Michotte, S.; Piriaux, L. Spin transition charted in a fluorophore-tagged thermochromic dinuclear iron(II) complex. *J. Am. Chem. Soc.* **2011**, *133* (40), 15850–15853. DOI: 10.1021/ja205974q.
- (32) Schafer, B.; Bauer, T.; Faus, I.; Wolny, J. A.; Dahms, F.; Fuhr, O.; Lebedkin, S.; Wille, H.-C.; Schlage, K.; Chevalier, K.; Rupp, F.; Diller, R.; Schunemann, V.; Kappes, M. M.; Ruben, M. A luminescent Pt₂Fe spin crossover complex. *Dalton Trans.* **2017**, *46* (7), 2289–2302. DOI: 10.1039/C6DT04360G.
- (33) Ge, J.-Y.; Chen, Z.; Zhang, L.; Liang, X.; Su, J.; Kurmoo, M.; Zuo, J.-L. A Two-Dimensional Iron(II) Coordination Polymer with Synergetic Spin-Crossover and Luminescent Properties. *Angew. Chem. Int. Ed.* **2019**, *58* (26), 8789–8793. DOI: 10.1002/anie.201903281.
- (34) Förster, C.; Heinze, K. Photophysics and photochemistry with Earth-abundant metals - fundamentals and concepts. *Chem. Soc. Rev.* **2020**, *49* (4), 1057–1070. DOI: 10.1039/c9cs00573k.
- (35) Wenger, O. S. Photoactive Complexes with Earth-Abundant Metals. *J. Am. Chem. Soc.* **2018**, *140* (42), 13522–13533. DOI: 10.1021/jacs.8b08822.
- (36) Wenger, O. S. Is Iron the New Ruthenium? *Chem. Eur. J.* **2019**, *25* (24), 6043–6052. DOI: 10.1002/chem.201806148.
- (37) Chai, L.-Q.; Liu, G.; Zhang, Y.-L.; Huang, J.-J.; Tong, J.-F. Synthesis, crystal structure, fluorescence, electrochemical property, and SOD-like activity of an unexpected nickel(II) complex with a quinazoline-type ligand. *J. Coord. Chem.* **2013**, *66* (22), 3926–3938. DOI: 10.1080/00958972.2013.857016.
- (38) Wong, Y.-S.; Tang, M.-C.; Ng, M.; Yam, V. W.-W. Toward the Design of Phosphorescent Emitters of Cyclometalated Earth-Abundant Nickel(II) and Their Supramolecular Study. *J. Am. Chem. Soc.* **2020**, *142* (16), 7638–7646. DOI: 10.1021/jacs.0c02172.
- (39) Lochenie, C.; Wagner, K. G.; Karg, M.; Weber, B. Modulation of the ligand-based fluorescence of 3d metal complexes upon spin state change. *J. Mater. Chem. C* **2015**, *3* (30), 7925–7935. DOI: 10.1039/C5TC00837A.
- (40) Sarma, B.; Reddy, L. S.; Nangia, A. The Role of π -Stacking in the Composition of Phloroglucinol and Phenazine Cocrystals. *Cryst. Growth Des.* **2008**, *8* (12), 4546–4552. DOI: 10.1021/cg800585d.
- (41) Kurz, H.; Sander, J.; Weber, B. Influence of CF₃ Substituents on the Spin Crossover Behavior of Iron(II) Coordination Polymers with Schiff Base-like Ligands. *Z. Anorg. Allg. Chem.* **2020**, *646* (13), 800–807. DOI: 10.1002/zaac.201900354.
- (42) Berkefeld, A.; Fröhlich, M.; Kordan, M.; Hörner, G.; Schubert, H. Selective metalation of phenol-type proligands for preparative organometallic chemistry. *Chem. Commun.* **2020**, *56* (28), 3987–3990. DOI: 10.1039/d0cc01254h.
- (43) Kletsch, L.; Hörner, G.; Klein, A. Cyclometalated Ni(II) Complexes [Ni(NACAN)X] of the Tridentate 2,6-di(2-pyridyl)phen-ide Ligand. *Organometallics* **2020**, *39* (15), 2820–2829. DOI: 10.1021/acs.organomet.0c00355.
- (44) McCusker, J. K. Femtosecond absorption spectroscopy of transition metal charge-transfer complexes. *Acc. Chem. Res.* **2003**, *36* (12), 876–887. DOI: 10.1021/ar030111d.

- (45) Li Manni, G.; Alavi, A. Understanding the Mechanism Stabilizing Intermediate Spin States in Fe(II)-Porphyrin. *J. Phys. Chem. A* **2018**, *122* (22), 4935–4947. DOI: 10.1021/acs.jpca.7b12710.
- (46) DiMaggio, S. G.; Williams, R. A.; Therien, M. J. Facile Synthesis of meso-Tetrakis(perfluoroalkyl)porphyrins: Spectroscopic Properties and X-ray Crystal Structure of Highly Electron-Deficient 5,10,15,20-Tetrakis(heptafluoropropyl)porphyrin. *J. Org. Chem* **1994**, *59* (23), 6943–6948. DOI: 10.1021/jo00102a017.
- (47) Hawe, G. I.; Alkorta, I.; Popelier, P. L. A. Prediction of the basicities of pyridines in the gas phase and in aqueous solution. *J. Chem. Inf. Model.* **2010**, *50* (1), 87–96. DOI: 10.1021/ci900396k.
- (48) Kruglik, S. G.; Ermolenkov, V. V.; Orlovich, V. A.; Turpin, P.-Y. Axial ligand binding and release processes in nickel(II)-tetraphenylporphyrin revisited: a resonance Raman study. *Chem. Phys.* **2003**, *286* (1), 97–108. DOI: 10.1016/S0301-0104(02)00906-0.
- (49) Rodriguez, J.; Holten, D. Ultrafast photodissociation of a metalloporphyrin in the condensed phase. *J. Chem. Phys.* **1990**, *92* (10), 5944–5950. DOI: 10.1063/1.458364.
- (50) Hoshino, M. Laser photolysis studies of nickel(II) tetraphenylporphyrin in a mixed solvent of pyridine and toluene in the temperature range 180–300 K. *Inorg. Chem.* **1986**, *25* (14), 2476–2478. DOI: 10.1021/ic00234a041.
- (51) Katovic, V.; Taylor, L. T.; Busch, D. H. Application of the coordination template effect to prepare five-coordinate nickel(II) and copper(II) complexes containing a "basket-like" polycyclic ligand. *J. Am. Chem. Soc* **1969**, *91* (8), 2122–2123. DOI: 10.1021/ja01036a050.
- (52) Cataldo, F. A Revision of the Gutmann Donor Numbers of a Series of Phosphoramides Including TEPA. *Eur. Chem. Bull.* **2015**, *4* (2), 92–97. DOI: 10.17628/ECB.2015.4.92-97.
- (53) Xie, D.; Yu, M.; Xie, Z.-L.; Kadakia, R. T.; Chung, C.; Ohman, L. E.; Javanmardi, K.; Que, E. L. Versatile Nickel(II) Scaffolds as Coordination-Induced Spin-State Switches for ¹⁹F Magnetic Resonance-Based Detection. *Angew. Chem. Int. Ed.* **2020**, *59*, 22523–22530. DOI: 10.1002/anie.202010587.
- (54) Lewandowska-Andralojc, A.; Marciniak, B. Five Major Sins in Fluorescence Spectroscopy of Light-Harvesting Hybrid Materials. *ACS Energy Lett.* **2019**, *4* (8), 1898–1901. DOI: 10.1021/acsenergylett.9b01146.
- (55) Lakowicz, J. R. *Principles of Fluorescence Spectroscopy*, 3rd ed.; Springer, 2006.
- (56) Patchkovskii, S.; Kozlowski, P. M.; Zgierski, M. Z. Theoretical analysis of singlet and triplet excited states of nickel porphyrins. *J. Chem. Phys.* **2004**, *121* (3), 1317–1324. DOI: 10.1063/1.1762875.
- (57) Kim, D.; Kirmaier, C.; Holten, D. Nickel porphyrin photophysics and photochemistry. A picosecond investigation of ligand binding and release in the excited state. *Chem. Phys.* **1983**, *75* (3), 305–322. DOI: 10.1016/0301-0104(83)85199-4.
- (58) Kim, D.; Holten, D. Picosecond measurements on the binding and release of basic ligands by excited states of Ni(II) porphyrins. *Chem. Phys. Lett.* **1983**, *98* (6), 584–589. DOI: 10.1016/0009-2614(83)80247-4.
- (59) Shelby, M. L.; Lestrangle, P. J.; Jackson, N. E.; Haldrup, K.; Mara, M. W.; Stickrath, A. B.; Zhu, D.; Lemke, H. T.; Chollet, M.; Hoffman, B. M.; Li, X.; Chen, L. X. Ultrafast Excited State Relaxation of a Metalloporphyrin Revealed by Femtosecond X-ray Absorption Spectroscopy. *J. Am. Chem. Soc.* **2016**, *138* (28), 8752–8764. DOI: 10.1021/jacs.6b02176.
- (60) Chen, L. X.; Zhang, X.; Wasinger, E. C.; Lockard, J. V.; Stickrath, A. B.; Mara, M. W.; Attenkofer, K.; Jennings, G.; Smolentsev, G.; Soldatov, A. X-ray snapshots for metalloporphyrin axial ligation. *Chem. Sci.* **2010**, *1* (5), 642. DOI: 10.1039/C0SC00323A.
- (61) Brandenburg, H.; Kraemer, J.; Fischer, K.; Schwager, B.; Flöser, B.; Näther, C.; Tuczek, F. Coordination-Induced Spin-State Switching with Nickel(II) salpn Complexes:

Electronic versus Steric Effects and Influence of Intermolecular Interactions. *Eur. J. Inorg. Chem.* **2018**, 2018 (5), 576–585. DOI: 10.1002/ejic.201701281.

4.6 Supporting Information

Table of contents

Experimental Section

Synthesis

^1H and ^{13}C NMR spectra

Complex Structures: Single-crystal XRD and DFT modelling

X-Ray crystal structure determinations

Metrics of the optimized complexes based on DFT

Powder X-ray diffraction patterns

Photophysics of the Planar Complexes and their Ligands

Optical spectra of the ligands, [Ni(2)], and [Ni(3)]

Computed frontier orbital energies and landscapes

Computed line spectra and difference density plots

Photophysical measurements of H₂I and [Ni(1)]

Coordination-Induced Spin State Switch (CISSS)

Photographs of [Ni(1)] and [Ni(4)] chloroform/pyridine solutions

Absorbance measurements of [Ni(2)] and [Ni(3)] chloroform/pyridine solutions

Computed line spectra of [Ni(1)] and [Ni(4)] in CN 5 and 6

Absorbance measurements of [Ni(1)] and [Ni(4)] with various axial ligands

Temperature-dependent CISSS

Temperature-dependent ^1H NMR spectra of [Ni(1)] in (D₅)pyridine

Temperature-dependent absorbance spectra of [Ni(4)] in MeOH

Analysis of the association/dissociation equilibrium of [Ni(4)]

Temperature-dependent ^{19}F and ^1H NMR spectra of [Ni(4)] in (D₆)acetone

Fluorescence-detected CISSS

Optical spectra and analysis of the data of [Ni(1)] in chloroform/pyridine solutions

Experimental Section

Synthesis

Ethoxymethylene-ethylacetoacetate, methoxymethyleneacetylacetone, methoxymethylene-methylacetoacetate, **H₂1**, and [Ni(1)] were synthesized to a similar procedure as described in literature.¹⁻³ 2,3-Diaminophenanzine (90%, Sigma Aldrich), ethyl-2-(ethoxymethylen)-4,4,4-trifluoro-3-oxobutyrat (>96%, TCI), and nickel(II) acetate tetrahydrate (99%, Fluka) were used without further purification. Ethanol, methanol, and dimethylformamide was of analytical grade and used without further purification. Oxygen was removed in the TCSPC and quantum yield experiments by degassing with Argon 5.0 for 10 min. In the steady-state measurements oxygen was not removed. Room-temperature ¹H NMR spectra were recorded with a 500 MHz Avance III HD NMR spectrometer from Bruker. The Bohr magneton numbers were determined upon measurement on a 400 MHz Varian INOVA NMR with toluene as reference. Temperature-dependent ¹H and ¹⁹F NMR spectra were recorded with a 500 MHz Avance NEO from Bruker operating at 500.34 MHz equipped with a triple resonance probehead (PATBO500S1BB-H/F-D-05ZFB) double tuned for H/F. ¹³C and 2D NMR spectra were recorded on a 600 MHz Avance NEO from Bruker operating at 600.7 MHz equipped with a cryoprobe (CPDCH600S3 C/H-D-05Z). CHN analyses were measured with an Unicube from Elementar Analysen Systeme. The samples were prepared in a tin boat, sulfanilamide was used as standard and the samples measured at least twice. Mass spectra were recorded with a Finnigan MAT 8500 with a data system MASPEC II. IR spectra were recorded with a Perkin Elmer Spectrum 100 FT-IR spectrometer.

X-ray Crystal Structure Determinations. The single crystal X-ray structure determinations of [Ni(1)] and [Ni(4)(H₂O)₂·H₂O·DMF] were performed at 100 K using MoK α radiation ($\lambda = 0.71073$ Å). Intensity data were collected on a Bruker Kappa PHOTON 2 *I* μ S Duo diffractometer equipped with QUAZAR focusing Montel optics. Data were corrected for Lorentz and polarization effects semi-empirical absorption corrections were performed on the basis of multiple scans using SADABS.⁴ The structures were solved by direct methods using SHELX XT 2014/5⁵ and refined on F^2 by full-matrix least-squares techniques (SHELXL 2018/3). All non-hydrogen atoms were refined with anisotropic displacement parameters. The hydrogen atoms of [Ni(1)] were placed in positions of optimized geometry; their isotropic displacement parameters were tied to those of their corresponding carrier atoms by a factor of

1.2 or 1.5. In $[\text{Ni}(\mathbf{4})(\text{H}_2\text{O})_2]\cdot\text{H}_2\text{O}\cdot\text{DMF}$ one of the terminal methyl groups of the complex was disordered. Two orientations were refined and resulted in site occupancies of 76(4) and 24(4) % for the atoms C19 and C19A. The compound crystallized with one molecule of water and one molecule of DMF, the latter one being disordered. Two different orientations were refined and resulted in site occupancies of 70.4(5) and 29.6(5)% for the atoms O10, N5, C27 – C29 and O10A, N5A, C27A – C29A, respectively. Similarity restraints were applied to the anisotropic displacement parameters of the disordered atoms. There was one significant residual density maximum in the region of the disordered dimethylformamide solvent molecule which might indicate further disorder. However, no reasonable orientation or position of this solvent molecule other than the two refined could be resolved. The positions of the oxygen bound hydrogen atoms were derived from a difference Fourier synthesis. These hydrogen atoms were subsequently treated with fixed distance restraints. All other hydrogen atoms were placed in positions of optimized geometry. The isotropic displacement parameters of all hydrogen atoms were tied to those of their corresponding carrier atoms by a factor of 1.2 or 1.5. ORTEP-III⁶⁻⁷ was used for the structure representation, Mercury-3.10⁸ to illustrate molecule packing.

X-ray Powder Diffraction. Powder diffractograms were recorded with a STOE StadiP diffractometer using Cu $K\alpha 1$ radiation with a Ge monochromator, and a Mythen 1K Stripdetector in transmission geometry.

Optical measurements. Room temperature absorbance spectra were obtained using an Agilent UV-vis spectrophotometer Cary 60 (Agilent Technologies, USA) operating in a spectral range of 190–1100 nm. Temperature dependent steady-state absorption measurements were performed with a Varian Cary 5000 double-beam UV-vis-NIR spectrometer, using a FK2 thermostat from Haake for high temperature and an Optistat DN2 cryostat from Oxford Instruments for low temperature measurements, respectively. Steady-state room temperature PL measurements were performed on a FP-8600 fluorescence spectrometer (JASCO) equipped with a Xe lamp as excitation source. The absorbance and emission spectra were measured at 298 K in quartz cells with 1 cm lightpath (Hellma, Germany). The temperature dependent PL and absorption spectra were measured in a home-built setup. For transmission measurements, a tungsten halogen lamp (LOT Oriel) served as a white light source. For PL measurements, the sample was excited using a 405 nm diode laser (Coherent COMPASS 405-50 CW). The sample was placed in an electrically heatable continuous flow cryostat (Oxford Instruments). The signal (either the PL or the transmitted light) was collected into a spectrograph (Andor Technology Shamrock SR303i) coupled to a CCD camera (Andor iDus DU420a-OE). All PL spectra were corrected for the efficiency of the setup, self-absorption effects and changing optical density at

the excitation wavelength. Time-resolved PL was measured using a commercial TCSPC setup (Pico Harp 300 PicoQuant), using a 405 nm diode laser for excitation (PicoQuant LDH-P-C-405 controlled by the PDL 800-D PicoQuant laser driver). PLQE at room temperature was measured following the approach by de Mello *et al.*⁹ using an integrating sphere and a 405 nm diode laser (PicoQuant LDH-P-C-405 controlled by the PDL 800-D PicoQuant laser driver). All spectra were conducted in quartz cells with 1 cm lightpath (Hellma, Germany).

H21. 2,3-Diaminophenazine (1.00 g, 4.76 mmol, 1 eq), and ethoxymethylene-ethylacetoacetate (2.21 g, 11.89 mmol, 2.5 eq) were dissolved in 50 mL ethanol. The solution was heated to reflux for 1 h. After cooling to room temperature the orange solid was filtered and recrystallized in 40 mL ethanol. The orange precipitate was filtered off and washed with ethanol. Yield: 1.03 g (44%). ¹H NMR (500 MHz, CDCl₃, 25°C): δ = 13.47, 13.59 (ee, zz) (d, ³J(NH–NCH) = 12.0 Hz, 2 H, –NH); 8.70, 8.66 (ee, zz) (d, ³J(NH–NCH) = 12.0 Hz, 2 H, NC–H); 8.23, 8.20 (ee,zz) (m, 2 H, H_{Ar}); 8.06, 8.04 (ee, zz) (s, 2 H, H_{Ar}); 7.86, 7.82 (ee, zz) (m, 2 H, H_{Ar}); 4.40, 4.32 (ee, zz) (q, ³J(CH₂–CH₃) = 7.0 Hz, 4 H, –CH₂); 2.66, 2.62 (ee, zz) (s, 6 H, –CH₃); 1.44, 1.39 (ee, zz) (t, ³J(CH₂–CH₃) = 7.0 Hz, 6 H, –CH₃) ppm. ¹³C NMR (500 MHz, CDCl₃, 25°C, jmod): δ = 201.66, 166.15, 152.07, 143.72, 142.00, 135.91, 131.09, 129.52, 116.30, 106.78, 60.61, 31.43, 14.70 ppm. MS (DEI(+), 70 eV): m/z = 490 (M⁺, 7%). C₂₆H₂₆N₄O₆ (490.52 g/mol); C 63.12 (calc. 63.66); H 5.84 (5.34); N 11.50 (11.42)%. IR: $\tilde{\nu}$ = 3250 (s, N–H), 1708 (s, C=O), 1625 (s, C=O) cm⁻¹.

[Ni(1)]. H21. (0.50 g, 1.02 mmol, 1 eq) and nickel(II) acetate tetrahydrate (0.30 g, 1.22 mmol, 1.2 eq) were dissolved in 50 mL ethanol. The solution was heated under reflux for 1 h. After cooling to room temperature the orange precipitate was filtered and washed with ethanol. Yield: 0.43 g (77%). ¹H NMR (500 MHz, CDCl₃, 25°C): δ = 8.67 (s, 2 H, NC–H); 8.22 (s, 2 H, H_{Ar}); 8.15 (m, 2 H, H_{Ar}); 7.81 (m, 2 H, H_{Ar}); 4.32 (q, ³J(CH₂–CH₃) = 7.0 Hz, 4 H, –CH₂); 2.63 (s, 6 H, –CH₃); 1.41 (t, ³J(CH₂–CH₃) = 7.0 Hz, 6 H, CH₃) ppm. ¹³C NMR (600 MHz, CDCl₃, 25°C): δ = 191.73, 166.48, 153.77, 147.63, 143.21, 141.64, 130.47, 129.34, 110.90, 106.83, 60.64, 28.53, 14.82 ppm. MS (DEI(+), 70 eV): m/z = 546 (M⁺, 100%). C₂₆H₂₄N₄NiO₆ (547.19 g/mol); C 57.34 (calc. 57.07); H 4.47 (4.42); N 9.93 (10.24)%. IR: $\tilde{\nu}$ = 1707 (s, C=O), 1685 (s, C=O) cm⁻¹.

H22. 2,3-Diaminophenazine (1.00 g, 4.76 mmol, 1 eq), and methoxymethylene-methylacetoacetate (1.88 g, 11.89 mmol, 2.5 eq) were dissolved in 150 mL methanol. The solution was heated to reflux for 1 h. After cooling to room temperature the yellow precipitate was filtered off, and washed with methanol. Yield: 0.92 g (41%). ¹H NMR (500 MHz, CDCl₃,

25°C): $\delta = 13.26$ (d, $^3J(\text{NH-NCH}) = 12.0$ Hz, 2 H, -NH); 8.69 (d, $^3J(\text{NH-NCH}) = 12.0$ Hz, 2 H, NC-H); 8.20 (m, 2 H, H_{Ar}); 8.08 (s, 2 H, H_{Ar}); 7.87 (m, 2 H, H_{Ar}); 3.85 (s, 6 H, -CH₃); 2.66 (s, 6 H, -CH₃) ppm. ^{13}C NMR (500 MHz, CDCl₃, 25°C, jmod): $\delta = 201.61, 166.52, 152.22, 143.78, 141.98, 135.77, 131.12, 129.56, 116.29, 106.46, 51.72, 31.36$ ppm. MS (DEI(+), 70 eV): $m/z = 462$ (M⁺, 23%). C₂₄H₂₂N₄O₆ (462.46 g/mol); C 62.41 (calc. 62.33); H 4.69 (4.80); N 12.90 (12.12)%. IR: $\tilde{\nu} = 3176$ (s, N-H), 1718 (s, C=O), 1633 (s, C=O) cm⁻¹.

[Ni(2)]. H₂ (0.30 g, 0.65 mmol, 1 eq) and nickel(II) acetate tetrahydrate (0.19 g, 0.78 mmol, 1.2 eq) were dissolved in 100 mL methanol. The solution was heated under reflux for 1 h. After cooling to room temperature the orange precipitate was filtered and washed with methanol. The orange solid was recrystallized from methanol. Yield: 0.33 g (98%). ^1H NMR (500 MHz, CDCl₃, 25°C): $\delta = 8.68$ (s, 2 H, NC-H); 8.24 (s, 2 H, H_{Ar}); 8.14 (m, 2 H, H_{Ar}); 7.81 (m, 2 H, H_{Ar}); 3.84 (s, 6 H, -CH₃); 2.63 (s, 6 H, -CH₃) ppm. ^{13}C NMR (500 MHz, CDCl₃, 25°C, jmod): $\delta = 191.83, 166.80, 153.86, 147.58, 143.31, 141.68, 130.58, 129.39, 111.00, 106.46, 51.75, 28.44$ ppm. MS (DEI(+), 70 eV): $m/z = 518$ (M⁺, 100%); 503 (M⁺-CH₃, 25%). C₂₄H₂₀N₄NiO₆ (519.14 g/mol); C 54.19 (calc. 55.53); H 4.12 (3.88); N 11.19 (10.79)%. IR: $\tilde{\nu} = 1721$ (s, C=O), 1694 (s, C=O) cm⁻¹.

H₂3. 2,3-Diaminophenazine (1.00 g, 4.76 mmol, 1 eq), and methoxymethylene-acetylacetone (1.69 g, 11.89 mmol, 2.5 eq) were dissolved in 100 mL methanol. The solution was heated to reflux for 1 h. After cooling to room temperature the brown precipitate was filtered off, and washed with methanol. Yield: 0.69 g (34%). ^1H NMR (500 MHz, CDCl₃, 25°C): $\delta = 13.30$ (d, $^3J(\text{NH-NCH}) = 12.0$ Hz, 2 H, -NH); 8.39 (d, $^3J(\text{NH-NCH}) = 12.0$ Hz, 2 H, NC-H); 8.21 (m, 2 H, H_{Ar}); 8.04 (s, 2 H, H_{Ar}); 7.89 (m, 2 H, H_{Ar}); 2.65 (s, 6 H, -CH₃); 2.47 (s, 6 H, -CH₃) ppm. ^{13}C NMR (500 MHz, CDCl₃, 25°C, jmod): $\delta = 202.59, 195.01, 151.67, 143.77, 141.94, 135.99, 131.32, 129.52, 116.72, 116.24, 32.26, 27.56$ ppm. MS (DEI(+), 70 eV): $m/z = 430$ (M⁺, 18%). C₂₄H₂₂N₄O₄ (430.46 g/mol); C 65.10 (calc. 66.97); H 5.05 (5.15); N 13.91 (13.02)%. IR: $\tilde{\nu} = 3169$ (s, N-H), 1622 (s, C=O), 1586 (s, C=O) cm⁻¹.

[Ni(3)]. H₂3 (0.20 g, 0.46 mmol, 1 eq) and nickel(II) acetate tetrahydrate (0.14 g, 0.56 mmol, 1.2 eq) were dissolved in 20 mL methanol. The solution was heated under reflux for 1.5 h. After cooling to room temperature the orange precipitate was filtered and washed with methanol. Yield: 0.20 g (89%). ^1H NMR (500 MHz, CDCl₃, 25°C): $\delta = 8.49$ (s, 2 H, NC-H); 8.19 (s, 2 H, H_{Ar}); 8.18 (m, 2 H, H_{Ar}); 7.84 (m, 2 H, H_{Ar}); 2.63 (s, 6 H, -CH₃); 2.52 (s, 6 H, -CH₃) ppm. ^{13}C NMR (500 MHz, CDCl₃, 25°C, jmod): $\delta = 195.17, 192.85, 153.03, 147.63, 143.38, 141.65, 130.83, 129.38, 116.83, 110.58, 29.50, 29.01$ ppm. MS (DEI(+), 70 eV): $m/z = 486$ (M⁺, 34%).

$C_{24}H_{20}N_4NiO_4$ (487.14 g/mol); C 58.99 (calc. 59.17); H 4.42 (4.14); N 12.60 (11.50)%. IR: $\tilde{\nu} = 1652$ (s, C=O), 1580 (s, C=O) cm^{-1} .

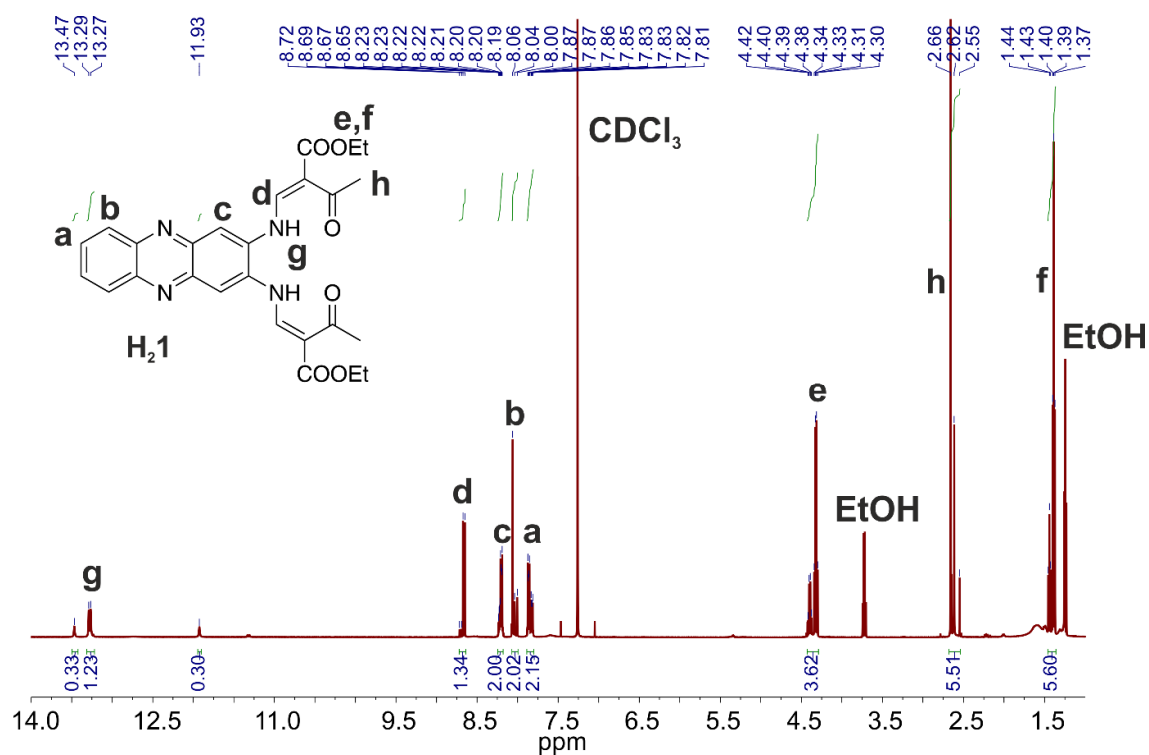
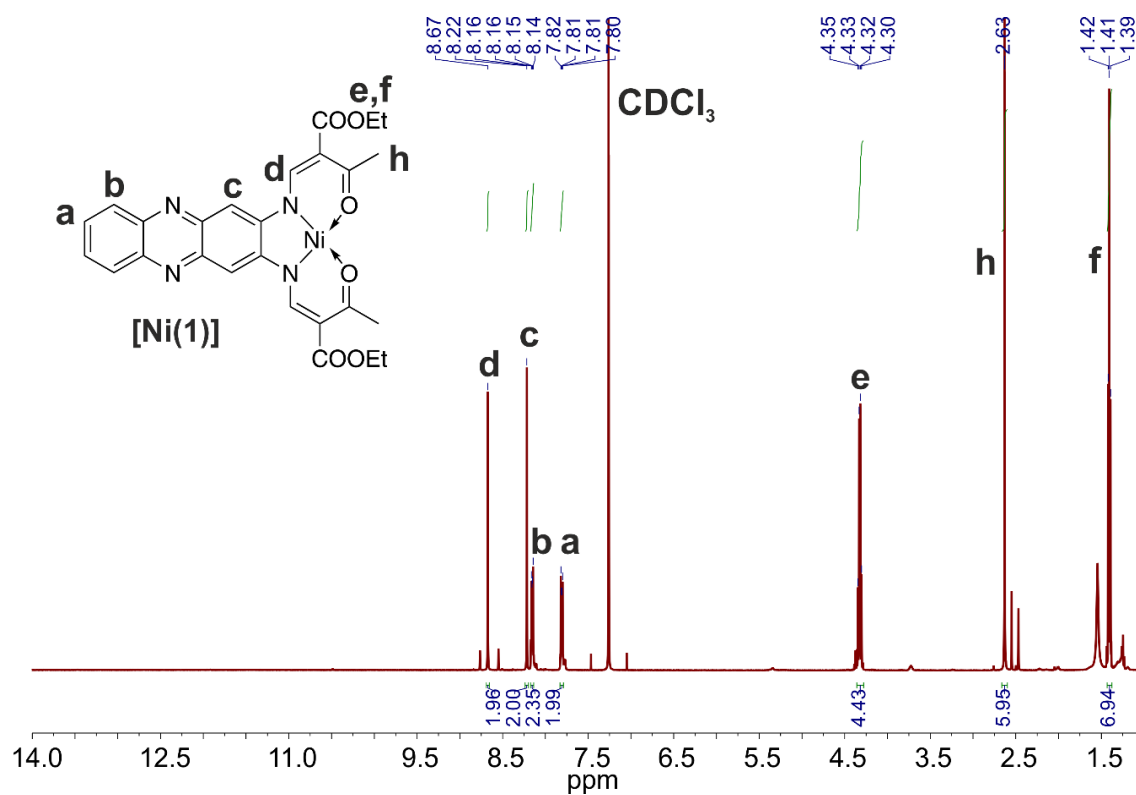
H24. 2,3-Diaminophenazine (0.50 g, 2.38 mmol, 1 eq), and ethyl-2-(ethoxymethylen)-4,4,4-trifluoro-3-oxobutyrat (1.71 g, 7.13 mmol, 3 eq) were dissolved in 50 mL dimethylformamide. The solution was heated to 75°C for 2 h. After cooling to room temperature 25 mL distilled water was added dropwise. The brown precipitate was filtered off, and washed with H_2O . Yield: 0.69 g (48 %). 1H NMR (500 MHz, $CDCl_3$, 25°C): $\delta = 12.30, 11.92, 11.78$ (ee, ez, zz) (d, $^3J(NH-NCH) = 12.5$ Hz, 2 H, -NH); 8.76, 8.59, 8.58 (ee, ez, zz) (d, $^3J(NH-NCH) = 12.5$ Hz, 2 H, NC-H); 8.23 (m, 2 H, H_{Ar}); 8.22, 8.14, 8.13 (ee, ez, zz) (s, 2 H, H_{Ar}); 7.91 (m, 2 H, H_{Ar}); 4.38 (m, 4 H, -CH₂); 1.40 (m, 6 H, -CH₃) ppm. ^{13}C NMR (500 MHz, $CDCl_3$, 25°C, jmod): $\delta = 167.65, 164.15, 165.90/156.58/154.87/154.60$ (ee, ez, ze, zz; fluorine coupling), 144.34/144.32/144.17/144.12 (ee, ez, ze, zz; fluorine coupling), 142.17/141.95/141.89/141.67 (ee, ez, ze, zz; fluorine coupling), 134.47/134.24, 131.93/131.84/131.73/131.65 (ee, ez, ze, zz; fluorine coupling), 129.78/129.72, 119.68/119.56/118.22/117.87 (ee, ez, ze, zz; fluorine coupling), 103.80/103.70/103.51/103.13 (ee, ez, ze, zz; fluorine coupling), 62.10/61.89/61.74/61.69 (ee, ez, ze, zz; fluorine coupling), 14.24/14.21/13.97/13.90 (ee, ez, ze, zz; fluorine coupling) ppm. MS (DEI(+), 70 eV): $m/z = 598$ (M^+ , 17%). $C_{26}H_{20}F_6N_4O_6$ (598.46 g/mol); C 52.05 (calc. 52.18); H 3.63 (3.37); N 9.59 (9.36)%. IR: $\tilde{\nu} = 3394$ (s, N-H), 1697 (s, C=O), 1639 (s, C=O), 1137 (s, C-F) cm^{-1} .

[Ni(4)]. H24 (0.30 g, 0.50 mmol, 1 eq) and nickel(II) acetate tetrahydrate (0.15 g, 0.60 mmol, 1.2 eq) were dissolved in 20 mL ethanol. The solution was heated under reflux for 1.5 h. After three days at -20°C the dark-red crystalline precipitate was filtered and washed with ethanol. Yield: 0.18 g (55%). 1H NMR (500 MHz, $CDCl_3$, 25°C): $\delta = 8.69$ (s, 2 H, NC-H); 8.38 (s, 2 H, H_{Ar}); 8.20 (m, 2 H, H_{Ar}); 7.88 (m, 2 H, H_{Ar}); 4.38 (q, $^3J(CH_2-CH_3) = 7.0$ Hz, 4 H, -CH₂); 1.40 (t, $^3J(CH_2-CH_3) = 7.0$ Hz, 6 H, -CH₃) ppm. ^{13}C NMR (600 MHz, $CDCl_3$, 25°C): $\delta = 169.49, 164.47, 157.09, 145.39, 144.03, 141.53, 131.64, 129.65, 116.64, 113.06, 106.77, 62.05, 14.17$ ppm. ^{19}F NMR (500 MHz, $CDCl_3$, 25°C): $\delta = -68.00$ ppm. MS (DEI(+), 70 eV): $m/z = 654$ (M^+ , 100%). $C_{26}H_{18}F_6N_4NiO_6$ (655.14 g/mol); C 47.00 (calc. 47.67); H 2.76 (2.77); N 8.54 (8.55)%. IR: $\tilde{\nu} = 1722$ (s, C=O), 1703 (s, C=O), 1156 (s, C-F) cm^{-1} .

Computational Details

Electronic structure calculations on the complexes have been performed through density-functional theory (DFT) methods using the ORCA program package.¹⁰ For all optimizations triple- ξ -valence TZVP¹¹ basis sets were used with the generalized gradient approximated

functional BP86.¹² Optimized complexes were verified as stationary points through the absence of imaginary modes in numerical frequency calculations. Molecular orbitals and electronic properties were extracted from single-point calculations in the optimized positions with the global hybrid functional TPSSH¹³ and triple- ξ -valence TZVP basis sets. Grimme's third generation D3 correction of dispersion was used;^{14,15} medium effects were approximated in a dielectric continuum approach (COSMO), parameterized for MeCN.¹⁶ Coordinates of the computed structures are assembled in the SI file COORDINATES, frontier orbital landscapes are shown in Figures S15-S20. For each complex the 70-80 lowest optical electronic transitions were assessed with ORCA implemented TD-DFT methods within the Tamm-Dancoff approximation.

^1H and ^{13}C NMR spectraFigure S1: ^1H NMR spectrum of $\text{H}_2\text{1}$ in CDCl_3 measured at room temperature.Figure S2: ^1H NMR spectrum of $[\text{Ni}(\text{1})]$ in CDCl_3 measured at room temperature.

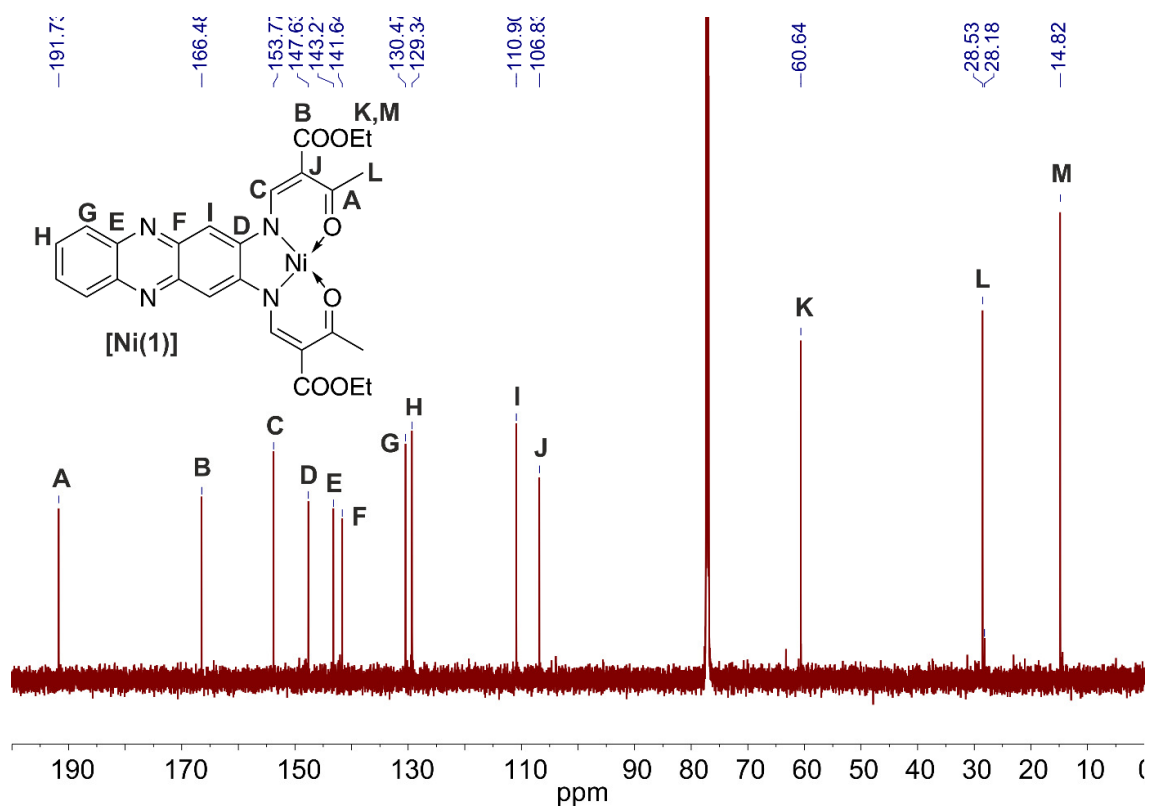


Figure S3: ^{13}C NMR spectrum of **[Ni(1)]** in CDCl_3 measured at room temperature.

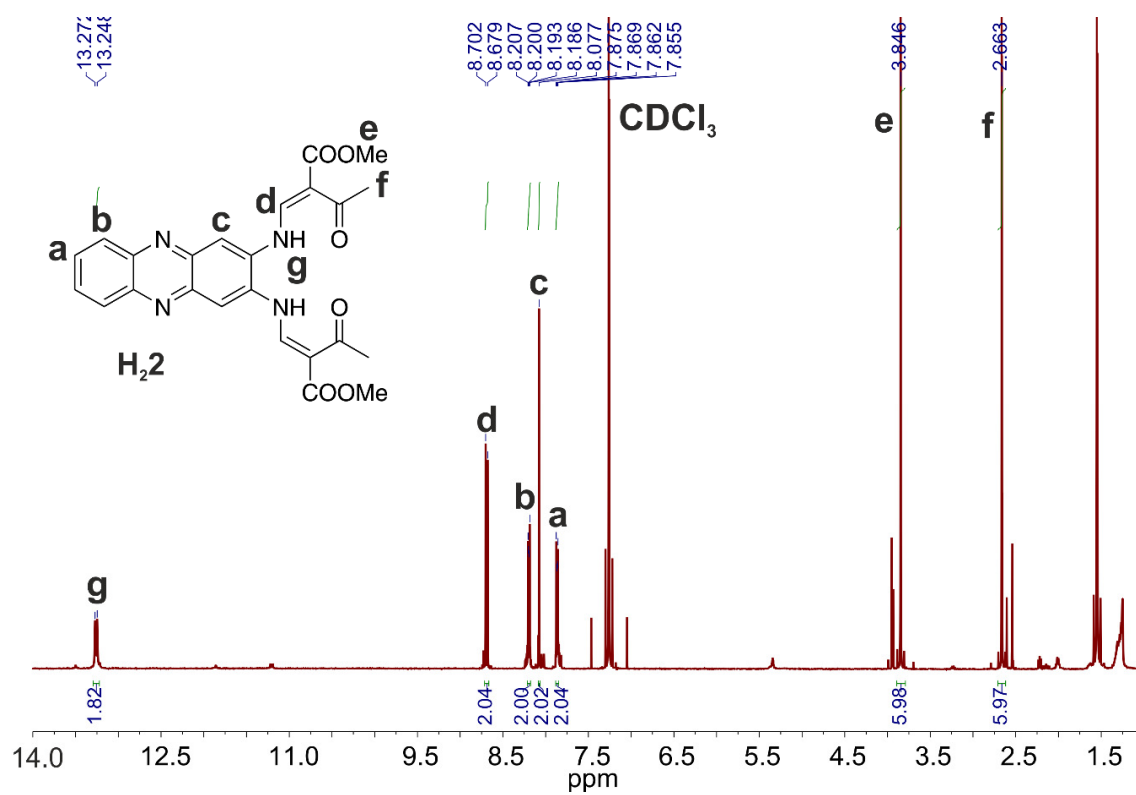


Figure S4: ^1H NMR spectrum of **H₂2** in CDCl_3 measured at room temperature.

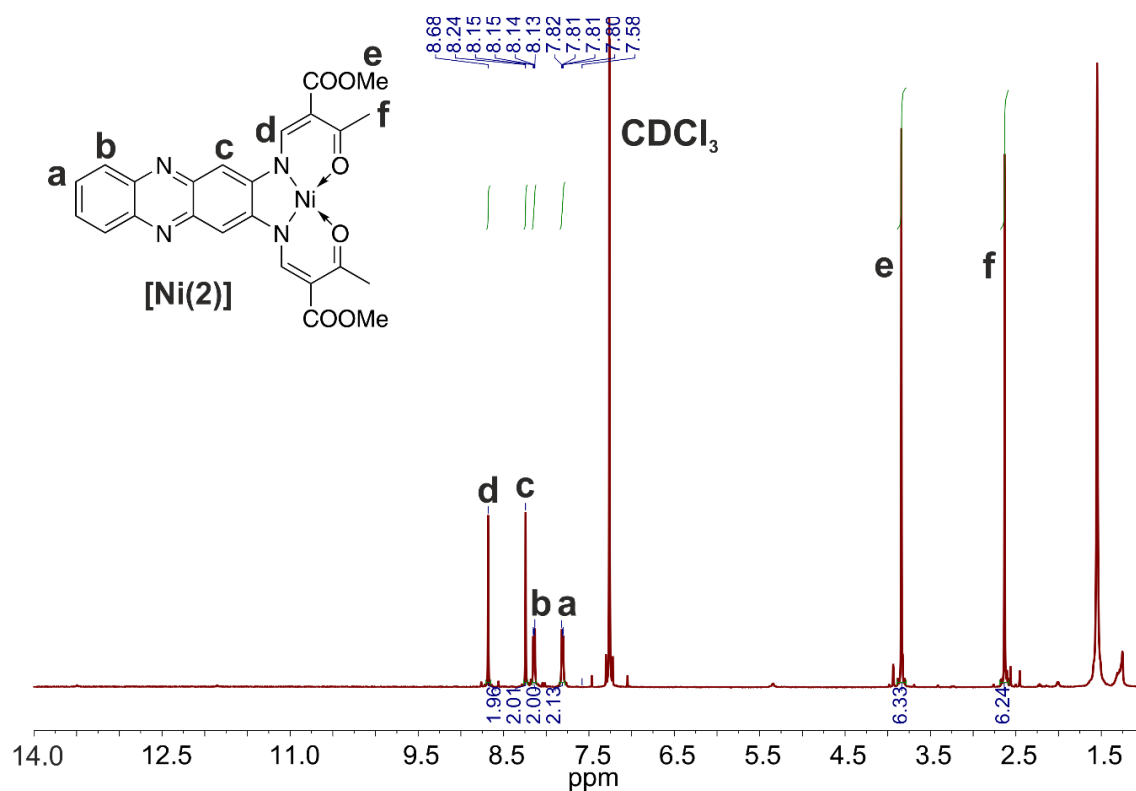


Figure S5: ¹H NMR spectrum of [Ni(2)] in CDCl₃ measured at room temperature.

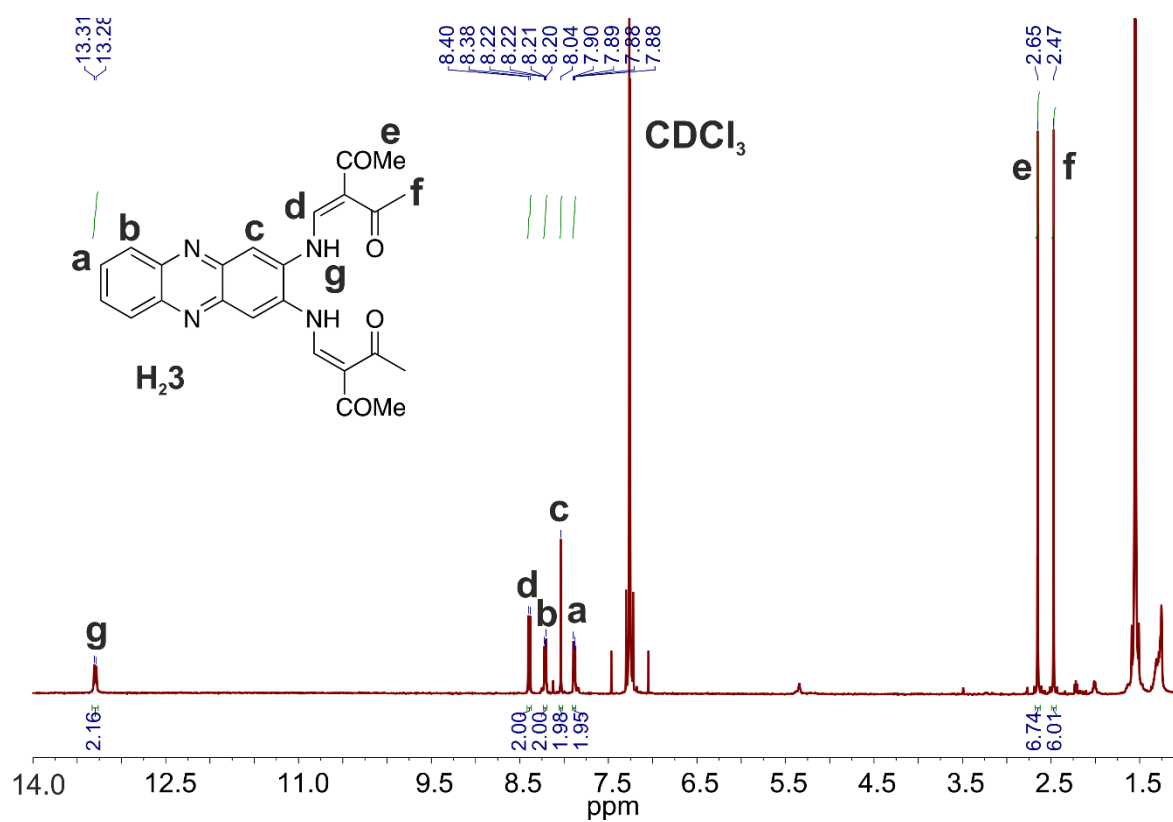


Figure S6: ¹H NMR spectrum of H₂3 in CDCl₃ measured at room temperature.

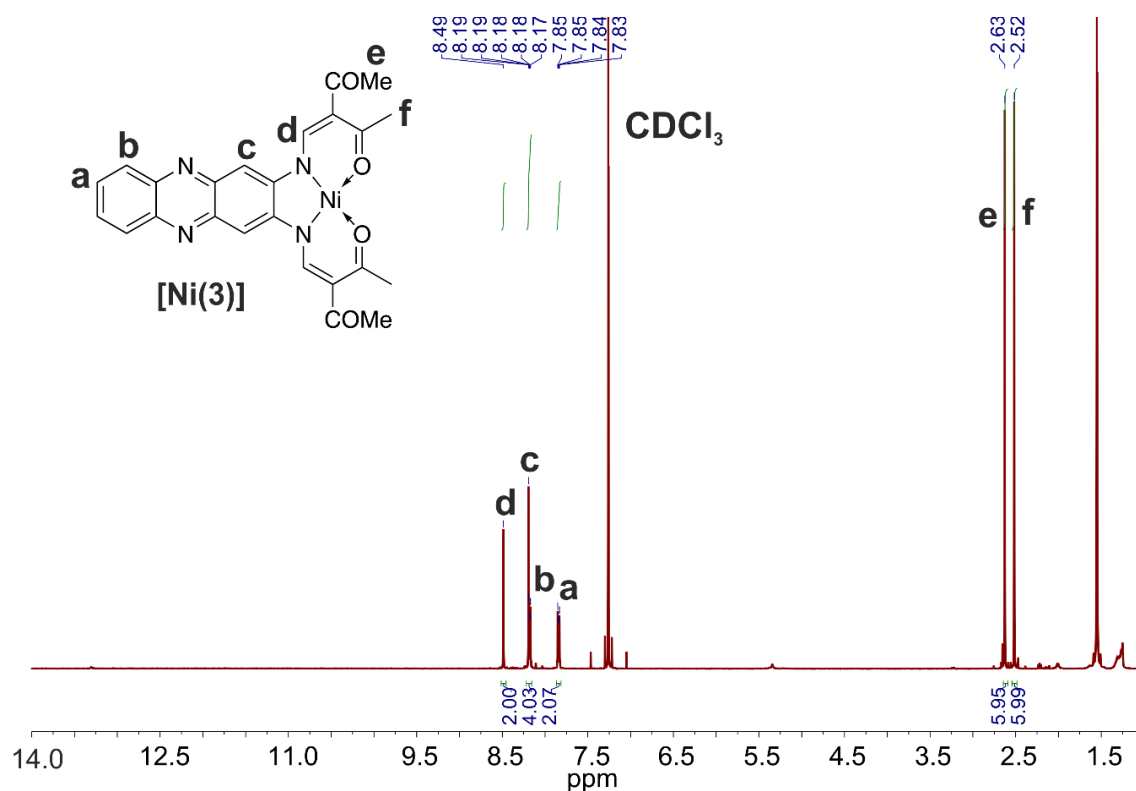


Figure S7: ¹H NMR spectrum of [Ni(3)] in CDCl₃ measured at room temperature.

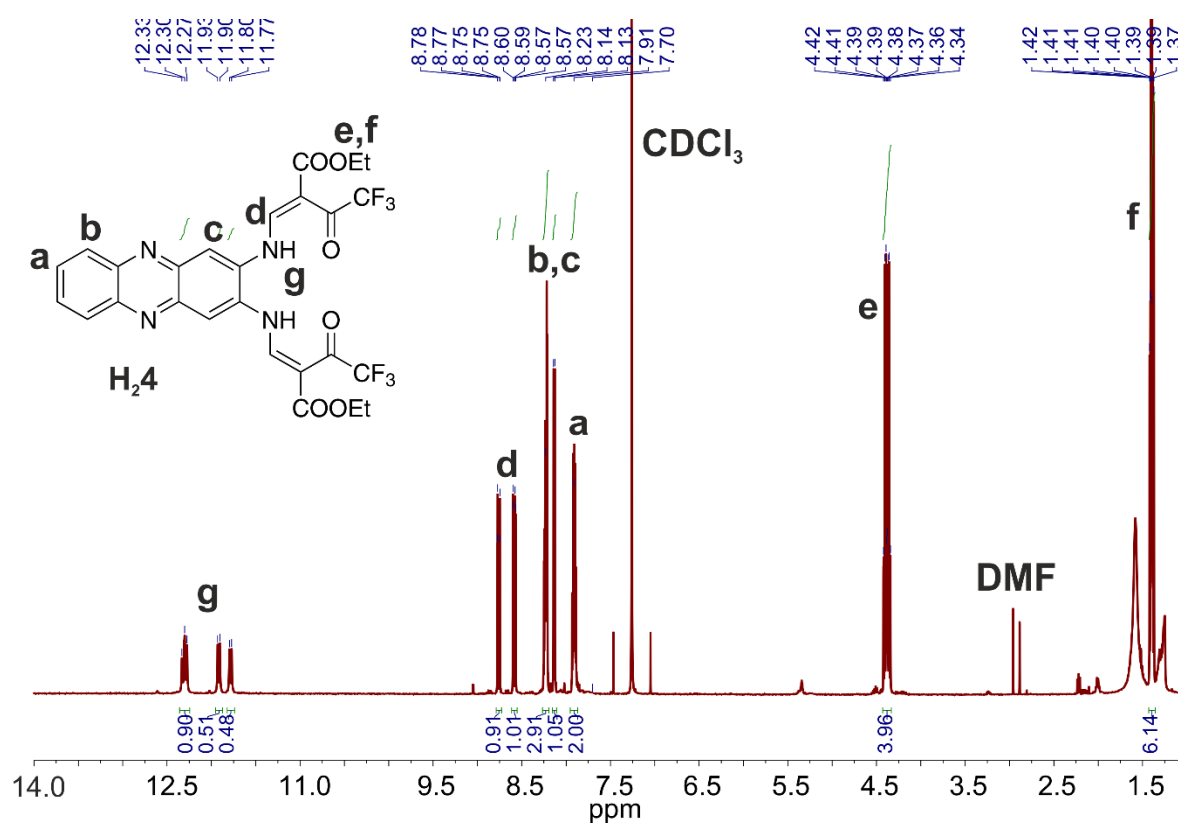


Figure S8: ¹H NMR spectrum of H₂4 in CDCl₃ measured at room temperature.

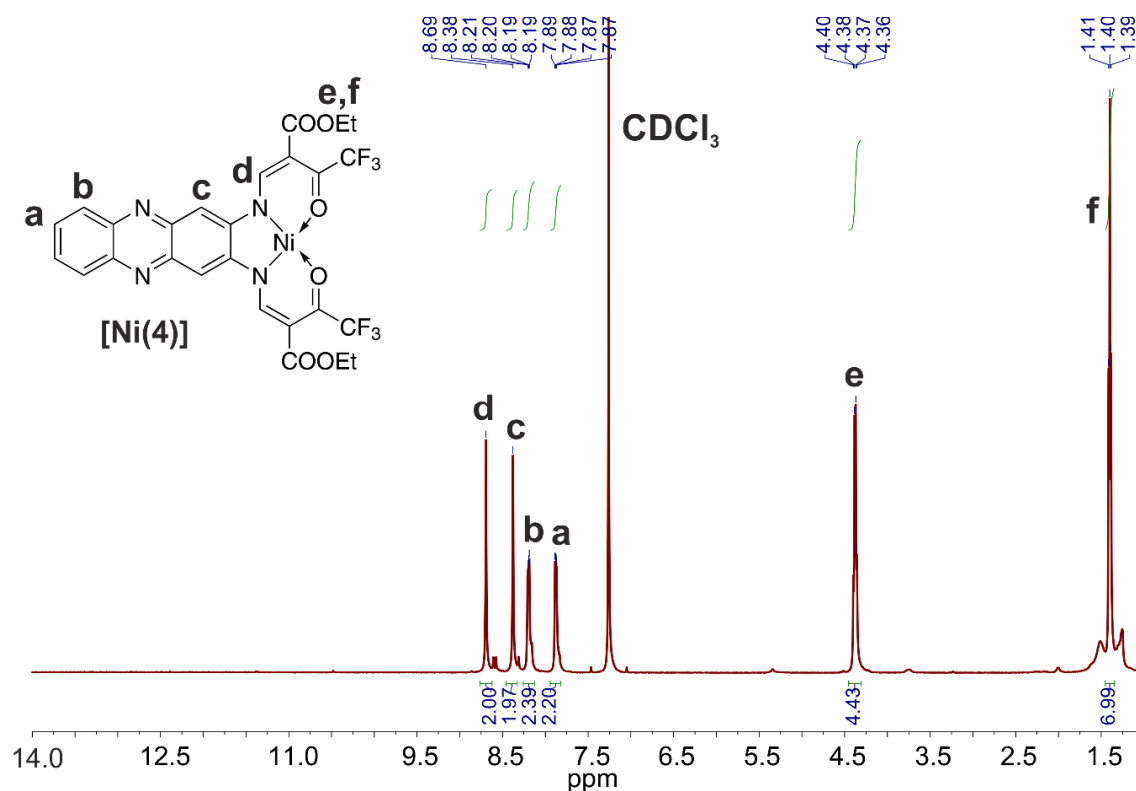


Figure S9: ^1H NMR spectrum of $[\text{Ni}(4)]$ in CDCl_3 measured at room temperature.

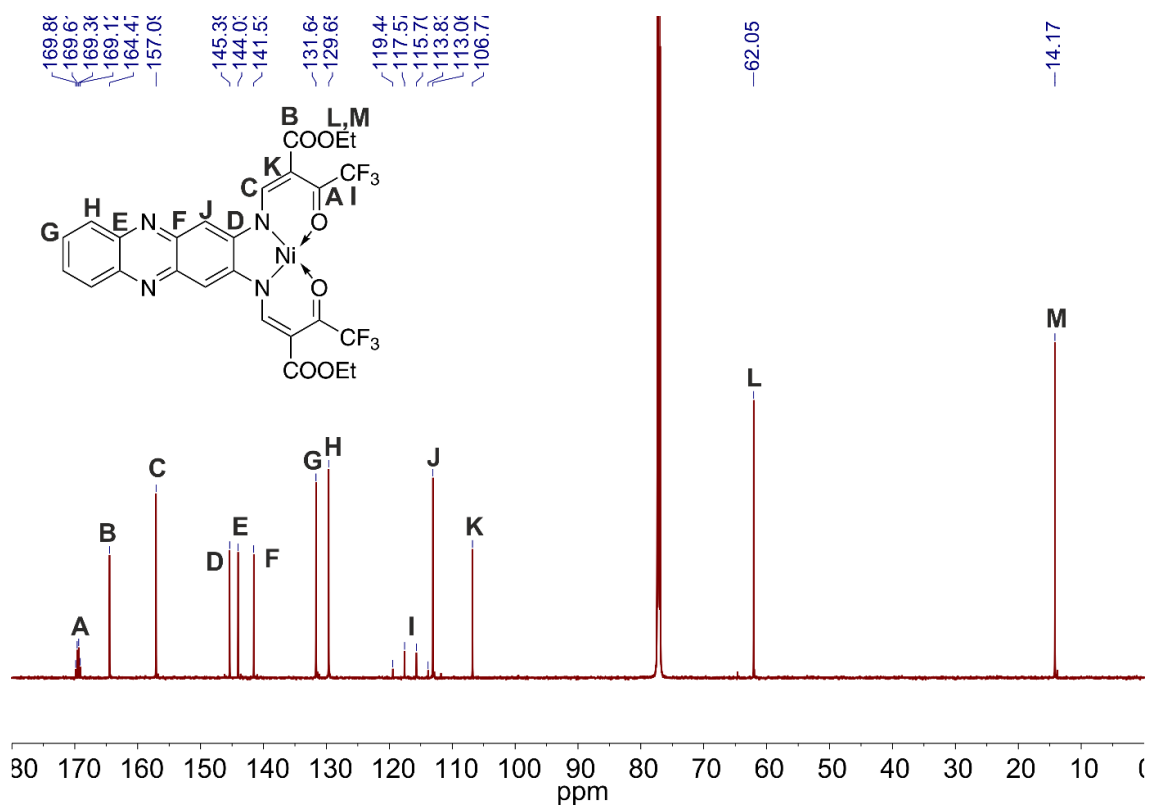


Figure S10: ^{13}C NMR spectrum of $[\text{Ni}(4)]$ in CDCl_3 measured at room temperature.

X-Ray crystal structure determinations

Crystallographic information: CCDC-2042264 (for $[\text{Ni}(\mathbf{4})(\text{H}_2\text{O})_2]\cdot\text{H}_2\text{O}\cdot\text{DMF}$) and 2042261 (for $[\text{Ni}(\mathbf{1})]$) contain the supplementary crystallographic data for this paper. The data can be obtained free of charge from The Cambridge Crystallographic Data Center via www.ccdc.cam.ac.uk/structures.

Crystallographic data, data collection, and structure refinement details are given in Table S1.

Table S1: Crystallographic data of $[\text{Ni}(\mathbf{4})(\text{H}_2\text{O})_2]\cdot\text{H}_2\text{O}\cdot\text{DMF}$ and $[\text{Ni}(\mathbf{1})]$.

compound (unit cell)	$[\text{Ni}(\mathbf{4})(\text{H}_2\text{O})_2]\cdot\text{H}_2\text{O}\cdot\text{DMF}$	$[\text{Ni}(\mathbf{1})]$
CCDC	2042264	2042261
description	orange plate	orange needle
sum formula	$\text{C}_{26} \text{H}_{22} \text{F}_6 \text{N}_4 \text{Ni} \text{O}_8 \cdot \text{H}_2\text{O} \cdot \text{C}_3 \text{H}_7 \text{N} \text{O}$	$\text{C}_{26} \text{H}_{24} \text{N}_4 \text{Ni} \text{O}_6$
$M/\text{g}\cdot\text{mol}^{-1}$	782.30	547.20
crystal system	monoclinic	triclinic
space group	$P2_1/c$	$P\bar{1}$
$a/\text{\AA}$	16.9955(10)	4.0771(5)
$b/\text{\AA}$	13.5987(8)	12.8739(17)
$c/\text{\AA}$	15.7979(9)	22.826(3)
$\alpha/^\circ$	90	101.899(4)
$\beta/^\circ$	111.157(2)	91.667(5)
$\gamma/^\circ$	90	93.798(5)
$V/\text{\AA}^3$	3405.1(3)	1168.7(3)
Z	4	2
$\rho/\text{g}\cdot\text{cm}^{-3}$	1.526	1.555
μ/mm^{-1}	0.664	0.883
crystal size/ mm	0.24 x 0.17 x 0.04	0.22 x 0.06 x 0.02
T/K	100	100
λ (MoK α)/ \AA	0.71073	0.71073
θ -range/ $^\circ$	2.0-28.3	1.8-27.1
reflns. collected	144517	32699
indep. reflns. (R_{int})	8429 (0.064)	5137 (0.110)
parameters	541	338
$R1$	0.0624	0.0673
$wR2$	0.1658	0.1226
$Goof$	1.091	1.153

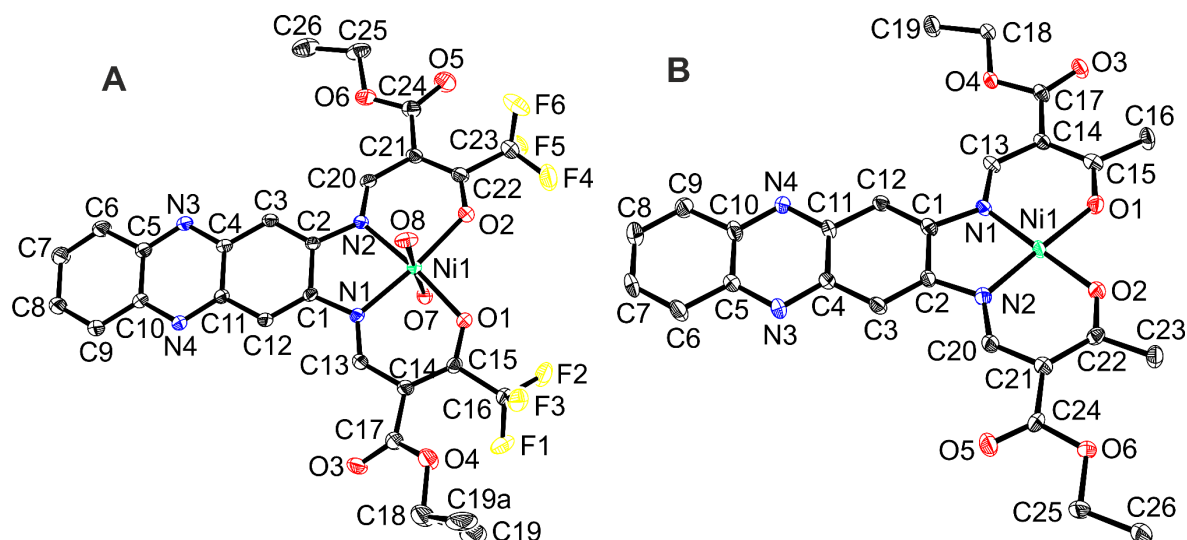


Figure S11: Thermal ellipsoid representation of the molecular structures with the applied numbering scheme of $[\text{Ni}(\mathbf{4})(\text{H}_2\text{O})_2]\cdot\text{H}_2\text{O}\cdot\text{DMF}$ (A) and $[\text{Ni}(\mathbf{1})]$ (B). Hydrogen atoms and additional solvent molecules are omitted for clarity. Ellipsoids are drawn at 50% probability.

Table S2: Selected bond lengths [\AA] and bond angles [$^\circ$] of $[\text{Ni}(\mathbf{1})]$ and $[\text{Ni}(\mathbf{4})(\text{H}_2\text{O})_2]\cdot\text{H}_2\text{O}\cdot\text{DMF}$; data in italics from DFT optimized structures.^a

$[\text{Ni}(\mathbf{1})]^b$				
	Bond length		Bond angles	
Ni1–N1	1.833(3)	<i>(1.846)</i>	O1–Ni1–O2	85.61(12) <i>(84.45)</i>
Ni1–N2	1.835(3)	<i>(1.846)</i>	N1–Ni1–N2	86.79(14) <i>(86.87)</i>
Ni1–O1	1.842(3)	<i>(1.862)</i>	O1–Ni1–N1	94.02(13) <i>(94.34)</i>
Ni1–O2	1.848(3)	<i>(1.861)</i>	O2–Ni1–N2	93.62(13) <i>(94.33)</i>
			O2–Ni1–N1	178.43(15) <i>(178.79)</i>
			O1–Ni1–N2	178.27(15) <i>(178.73)</i>
$[\text{Ni}(\mathbf{4})(\text{H}_2\text{O})_2]\cdot\text{H}_2\text{O}\cdot\text{DMF}$				
	Bond length		Bond angles	
Ni1–N1	1.989(3)	<i>(1.982)</i>	O1–Ni1–O2	95.96(9) <i>(94.97)</i>
Ni1–N2	1.995(3)	<i>(1.984)</i>	N1–Ni1–N2	83.62(10) <i>(83.47)</i>
Ni1–O1	2.023(2)	<i>(2.025)</i>	O1–Ni1–N1	90.71(10) <i>(90.86)</i>
Ni1–O2	2.026(2)	<i>(2.029)</i>	O2–Ni1–N2	89.62(10) <i>(90.69)</i>
Ni1–O7	2.102(2)	<i>(2.149)</i>	O1–Ni1–N2	173.94(10) <i>(174.12)</i>
Ni1–O8	2.079(3)	<i>(2.145)</i>	O2–Ni1–N1	172.95(10) <i>(174.32)</i>
			O7–Ni1–O8	177.19(10) <i>(174.83)</i>

^a BP86-D3/TZVP/COSMO(MeCN); $S = 0$ and $S = 1$ for $[\text{Ni}(\mathbf{1})]$ and $[\text{Ni}(\mathbf{4})(\text{H}_2\text{O})_2]$, respectively.

^b crystal structure from Ref.³⁹

Table S3: Hydrogen bonds and angles of $[\text{Ni}(\mathbf{4})(\text{H}_2\text{O})_2]\cdot\text{H}_2\text{O}\cdot\text{DMF}$.

Donor	Acceptor	D–H [\AA]	H \cdots A [\AA]	D \cdots A [\AA]	D–H \cdots A [$^\circ$]
O7–H7a [a]	N4	0.81(3)	1.98(3)	2.792(4)	176(5)
O7–H7B [b]	O9	0.79(3)	1.98(3)	2.762(4)	168(5)
O8–H8A [c]	N3	0.81(3)	2.02(3)	2.822(3)	174(5)

O8–H8B	O10	0.79(3)	1.93(3)	2.723(5)	172(5)
O8–H8B	O10A	0.79(3)	2.15(5)	2.74(2)	132(5)
O9–H9A	O5	0.90(3)	1.88(3)	2.774(4)	172(5)
O9–H9A	F5	0.90(3)	2.61(5)	3.123(4)	117(4)
O9–H9B [d]	O3	0.83(3)	2.10(3)	2.873(4)	155(5)

[a] $-x+1, y+1/2, -z+3/2$; [b] $-x+1, y-1/2, -z+3/2$; [c] $-x+1, -y+1, -z+1$; [d] $x, y+1, z$

Table S4: Selected distances [\AA] and angles [$^\circ$] of the π – π and M– π interactions of **[Ni(1)]**. Cg(I) is the centroid of the ring number I, α is the dihedral angle between the rings, β is the angle between the vector Cg(I)–Cg(J) and the normal to ring I, γ is the angle between the vector Cg(I)–Cg(J) and the normal to ring J.

Cg(I)	Cg(J)	Cg–Cg [\AA]	α [$^\circ$]	β [$^\circ$]	γ [$^\circ$]
Ni1–N1–C1–C2–N2	Ni1–N1–C1–C2–N2 (a)(b)	4.077(2)	0.03(16)	35.7	35.7
Ni1–N1–C1–C2–N2	Ni1–O1–C15–C14–C13–N1 (b)	3.7345(19)	2.53(15)	29.3	30.2
Ni1–N1–C1–C2–N2	Ni1–O2–C22–C21–C20–N2 (a)	3.647(2)	2.66(15)	26.7	24.9
Ni1–O1–C15–C14–C13–N1	Ni1–O1–C15–C14–C13–N1 (a)(b)	4.0771(19)	0.00(13)	38.2	38.2
Ni1–O1–C15–C14–C13–N1	Ni1–O2–C22–C21–C20–N2 (a)	3.4314(19)	2.80(14)	18.5	20.4
Ni1–O2–C22–C21–C20–N2	Ni1–O2–C22–C21–C20–N2 (a)(b)	4.077(2)	0.00(14)	36.9	36.9
N3–C4–C11–N4–C10–C5	N3–C4–C11–N4–C10–C5 (a)(b)	4.077(2)	0.00(18)	32.8	32.8
C1–C2–C3–C4–C11–C12	C1–C2–C3–C4–C11–C12 (a)(b)	4.077(2)	0.00(18)	33.3	33.3
C5–C6–C7–C8–C9–C10	C5–C6–C7–C8–C9–C10 (a)(b)	4.077(3)	0.0(2)	32.6	32.6
Ni1–O1–C15–C14–C13–N1	Ni1 (a)	3.298	-	12.84	-
Ni1–O2–C22–C21–C20–N2	Ni1 (b)	3.320	-	11.48	-

a = $-1+X, Y, Z$; b = $1+X, Y, Z$

Metrics of the optimized complexes based on DFT

Table S5: Metrics of optimized complexes **[Ni(1)(py)_n]** in the singlet and triplet state.

	$S = 0$ $n = 0$	$S = 1$ $n = 0$	$S = 1$ $n = 1$	$S = 1$ $n = 2$
Ni–N _{eq}	1.846	1.927	1.970	1.992
Ni–N _{eq}	1.846	1.927	1.971	1.992
Ni–O	1.862	1.948	2.000	2.046
Ni–O	1.861	1.948	1.999	2.047
Ni–N _{ax}	--	--	2.008	2.109

Ni-N _{ax}	--	--	--	2.115
N _{eq} -Ni-O	178.8	177.6	164.4	172.3
N _{eq} -Ni-O	178.7	177.4	164.4	172.4
O-Ni-O	84.4	90.4	90.7	97.9
N _{ax} -Ni-N _{ax}	--	--	--	176.3

Table S6: Metrics of optimized complex [Ni(2)] in the singlet state.

	[Ni(2)]
Ni-N _{eq}	1.846
Ni-N _{eq}	1.846
Ni-O	1.862
Ni-O	1.861
N _{eq} -Ni-O	178.7
N _{eq} -Ni-O	178.7
O-Ni-O	84.5

 Table S7: Metrics of optimized complexes [Ni(3)(py)_n] in the singlet and triplet state.

	<i>S</i> = 0 <i>n</i> = 0	<i>S</i> = 1 <i>n</i> = 0	<i>S</i> = 1 <i>n</i> = 1	<i>S</i> = 1 <i>n</i> = 2
Ni-N _{eq}	1.844	1.928	1.968	1.988
Ni-N _{eq}	1.845	1.921	1.968	1.993
Ni-O	1.861	1.935	1.999	2.046
Ni-O	1.859	1.950	1.996	2.051
Ni-N _{ax}	--	--	2.005	2.112
Ni-N _{ax}	--	--	--	2.108
N _{eq} -Ni-O	178.7	173.7	164.2	171.7
N _{eq} -Ni-O	178.6	172.9	163.4	171.6
O-Ni-O	84.6	91.6	90.9	99.3
N _{ax} -Ni-N _{ax}	--	--	--	176.1

 Table S8: Metrics of optimized complexes [Ni(4)(py)_n] in the singlet and triplet state.

	<i>S</i> = 0 <i>n</i> = 0	<i>S</i> = 1 <i>n</i> = 0	<i>S</i> = 1 <i>n</i> = 1	<i>S</i> = 1 <i>n</i> = 2
Ni-N _{eq}	1.848	1.932	1.974	1.995
Ni-N _{eq}	1.849	1.932	1.974	1.996
Ni-O	1.862	1.949	2.008	2.061
Ni-O	1.861	1.952	2.004	2.064
Ni-N _{ax}	--	--	2.007	2.108
Ni-N _{ax}	--	--	--	2.101
N _{eq} -Ni-O	178.7	177.7	164.1	171.7
N _{eq} -Ni-O	178.4	177.7	165.0	171.7
O-Ni-O	84.4	89.8	90.6	98.8
N _{ax} -Ni-N _{ax}	--	--	--	175.6

Powder X-ray diffraction patterns

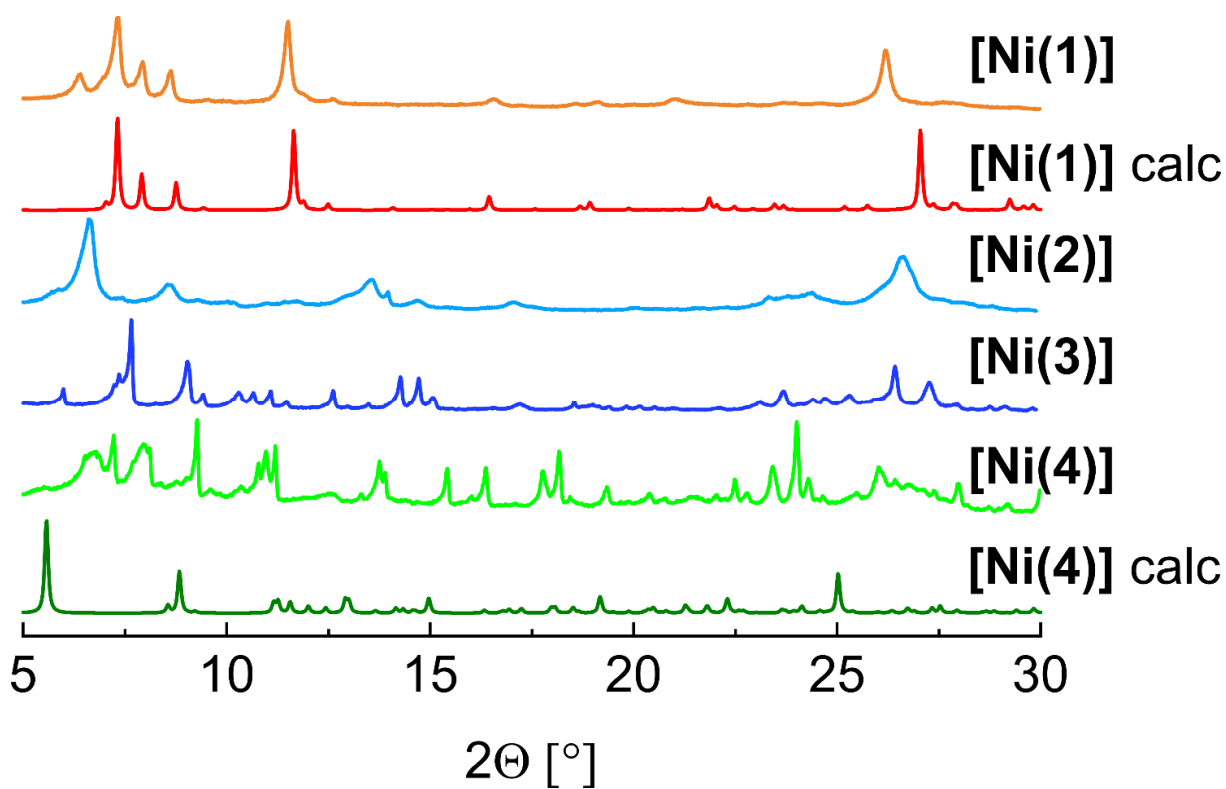


Figure S12: PXRD pattern of [Ni(1-4)] the range of 5–30° 2θ at room temperature and the calculated PXRD pattern of the single crystal of [Ni(1)] and [Ni(4)(H₂O)₂·H₂O·DMF] measured at 100 K.

Optical spectra of the ligands

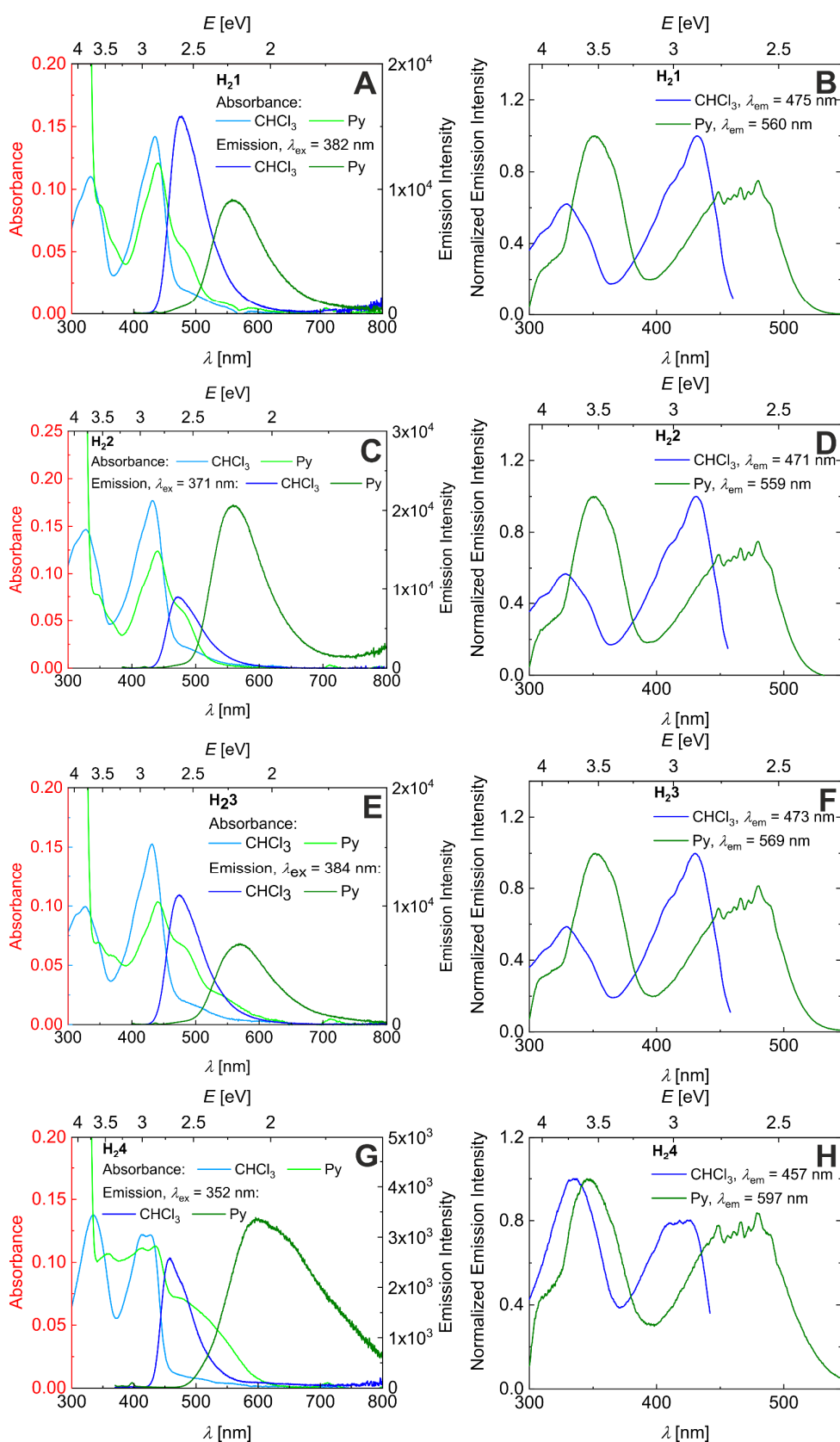


Figure S13: Absorbance and emission spectra of the ligands **H₂1–4** in CHCl_3 and pyridine (A, C, E, G). Excitation spectra of the ligands **H₂1–4** in CHCl_3 and pyridine (B, D, F, H).

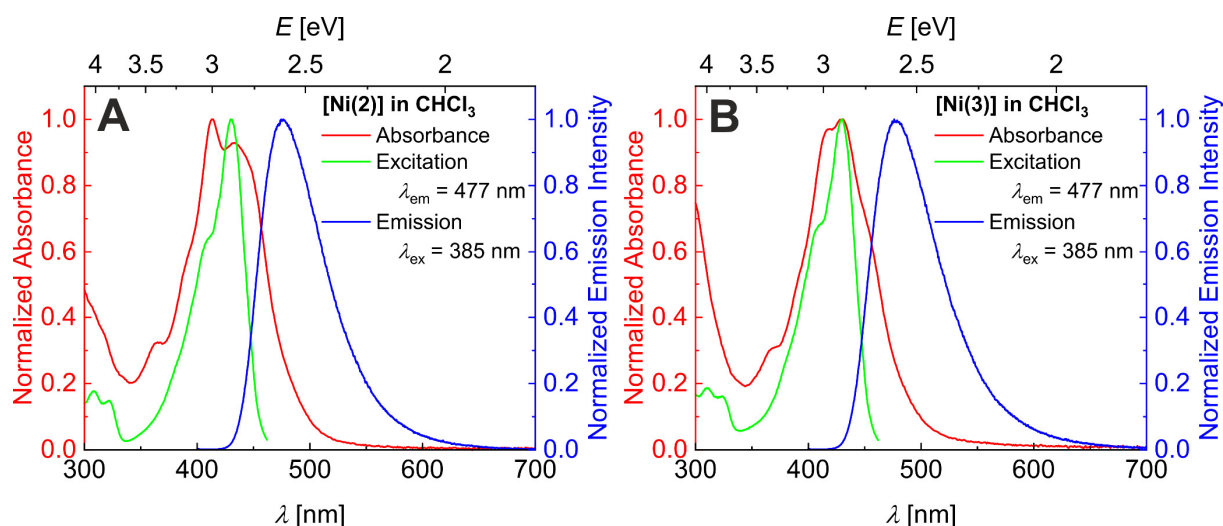


Figure S14: Normalized absorbance, excitation ($\lambda_{em} = 477$ nm), and emission spectra ($\lambda_{exc} = 385$ nm) of [Ni(2)] in chloroform (A) and [Ni(3)] in chloroform (B).

Computed frontier orbital energies and landscapes

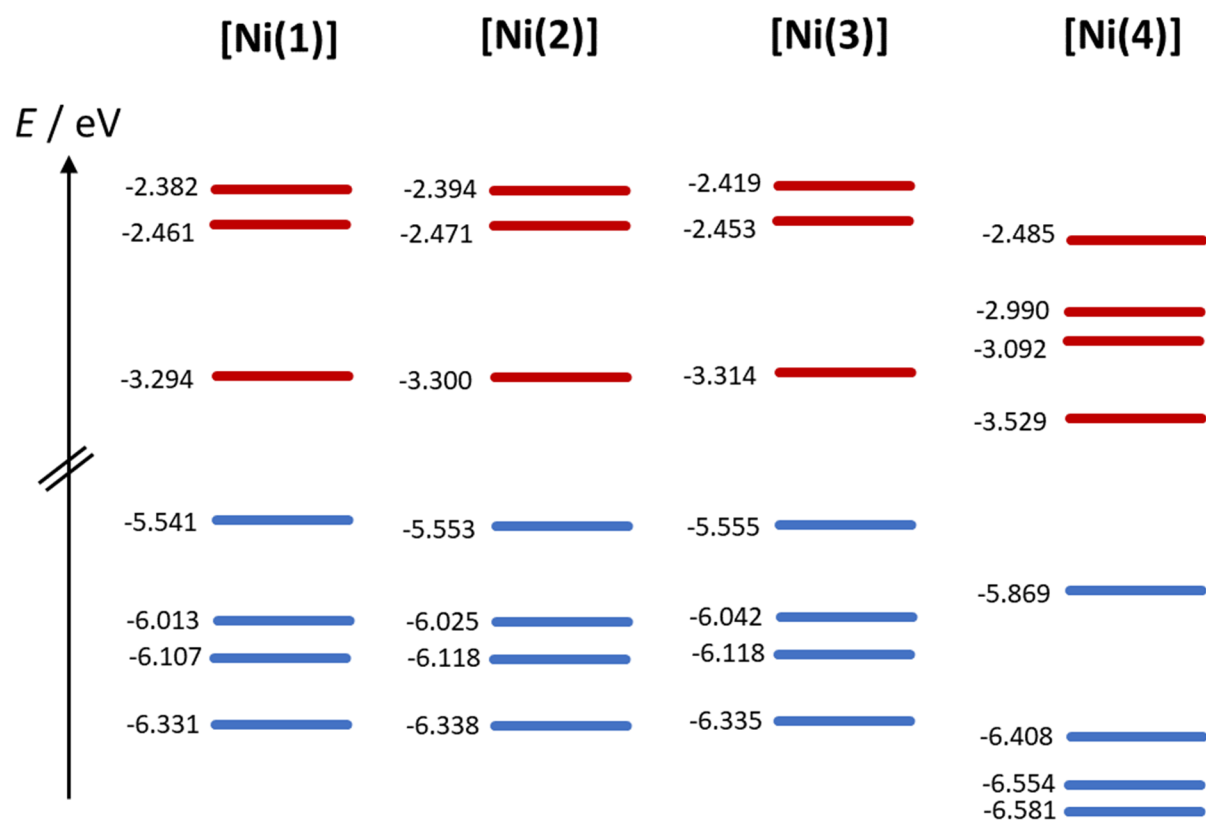


Figure S15: Frontier orbital energies of [Ni(1-4)]; TPSSh-D3/TZVP/COSMO(MeCN) level of theory.

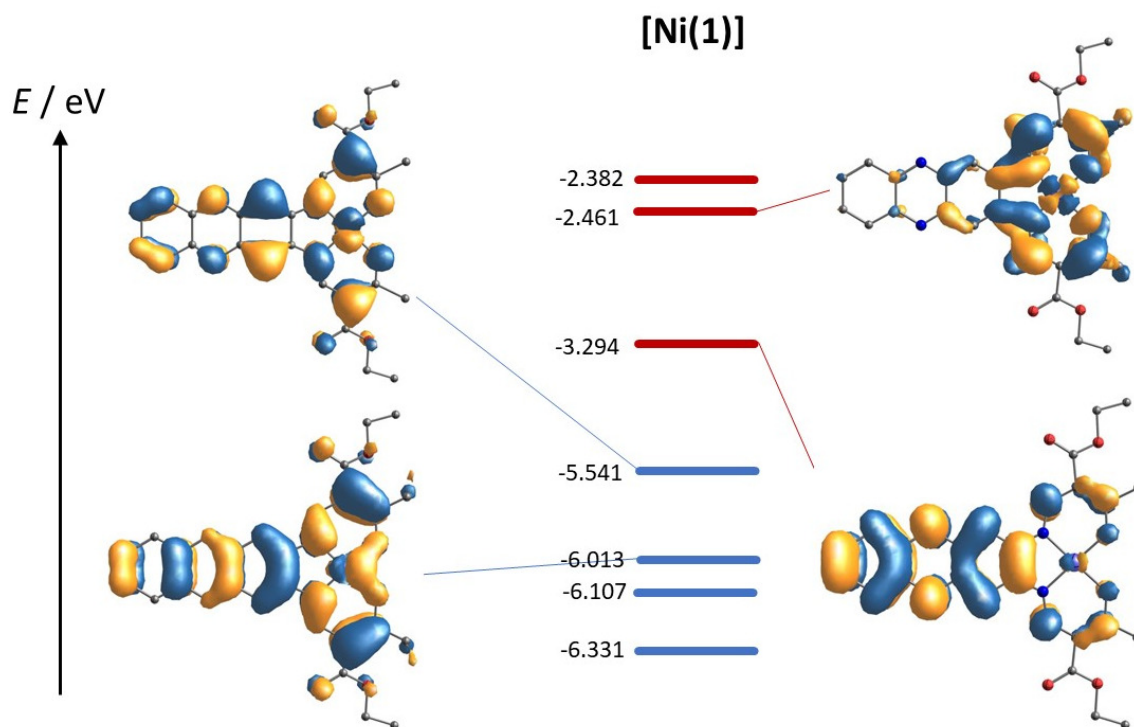


Figure S16: Frontier orbital landscape of [Ni(1)]; TPSSh-D3/TZVP/COSMO(MeCN) level of theory.

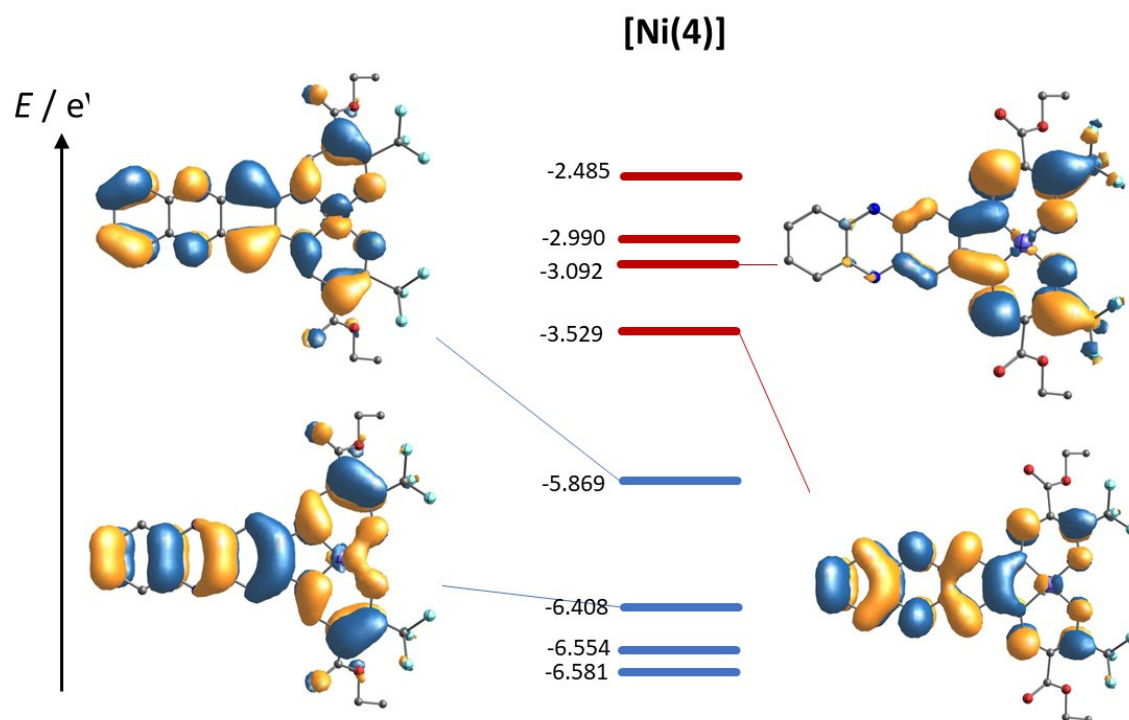


Figure S17: Frontier orbital landscape of [Ni(4)]; TPSSh-D3/TZVP/COSMO(MeCN) level of theory.

Computed line spectra and difference density plots

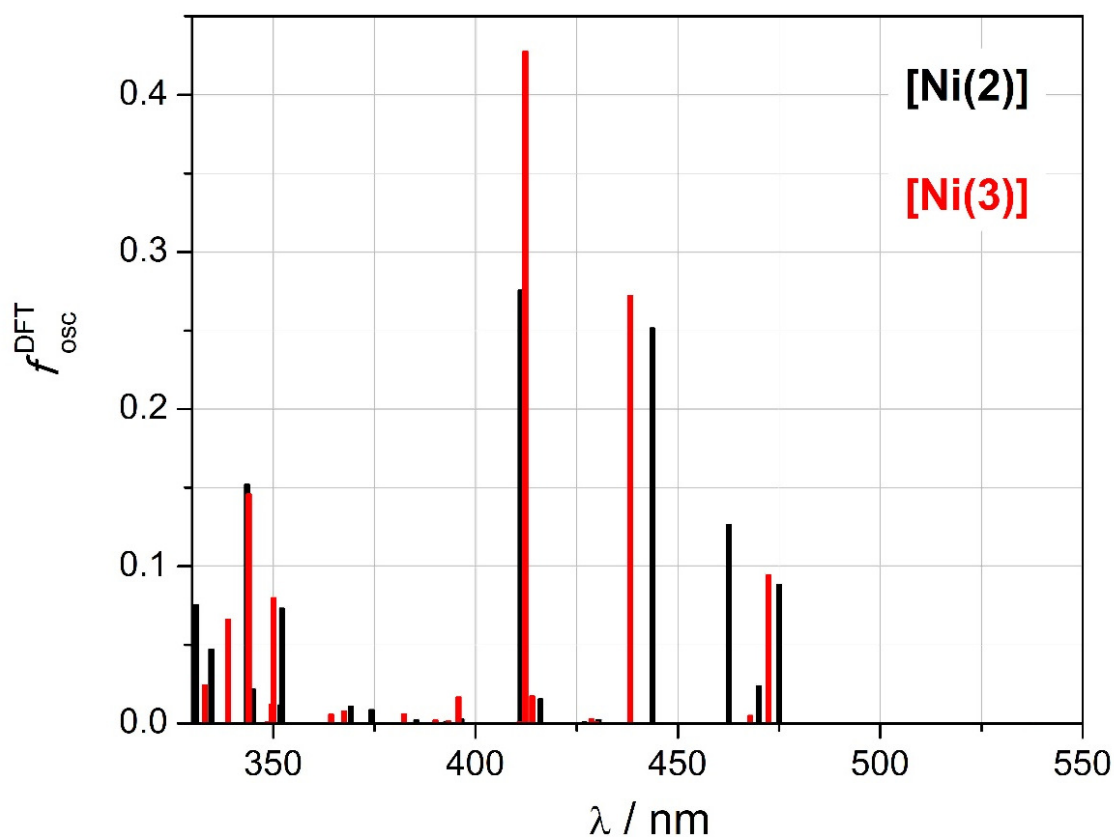


Figure S18: Computed line spectra of [Ni(2)] (black) and [Ni(3)] (red); TPSSh-D3/TZVP/COSMO(MeCN).

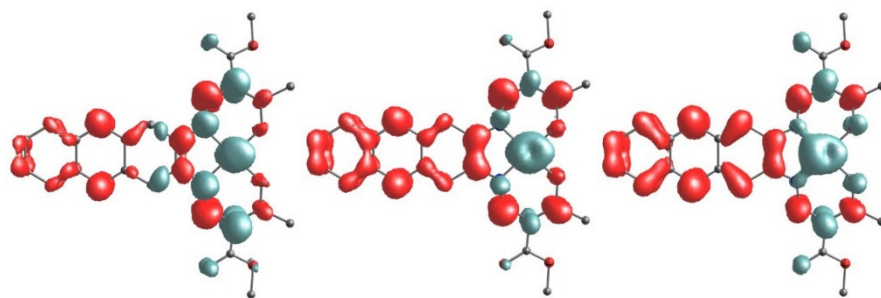


Figure S19: Computed difference density plot of the leading Vis-transitions, T15/20/28 in [Ni(2)]; from left: $\lambda_{15} = 473$ nm; $f_{\text{osc}} = 0.09$; $\lambda_{20} = 439$ nm; $f_{\text{osc}} = 0.27$; $\lambda_{28} = 413$ nm; $f_{\text{osc}} = 0.43$; dark cyan: source; red: sink.

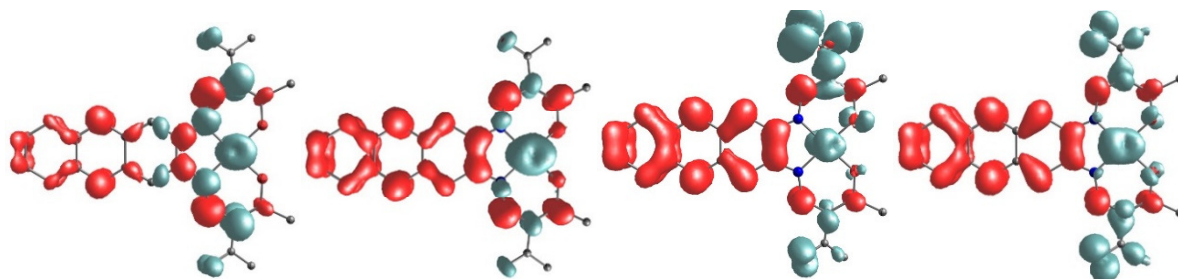


Figure S20: Computed difference density plot of the leading Vis-transitions, T14/20/23/33 in **[Ni(3)]**; from left: $\lambda_{14} = 474$ nm; $f_{osc} = 0.09$; $\lambda_{20} = 443$ nm; $f_{osc} = 0.25$; $\lambda_{23} = 463$ nm; $f_{osc} = 0.12$; $\lambda_{33} = 411$ nm; $f_{osc} = 0.28$; dark cyan: source; red: sink.

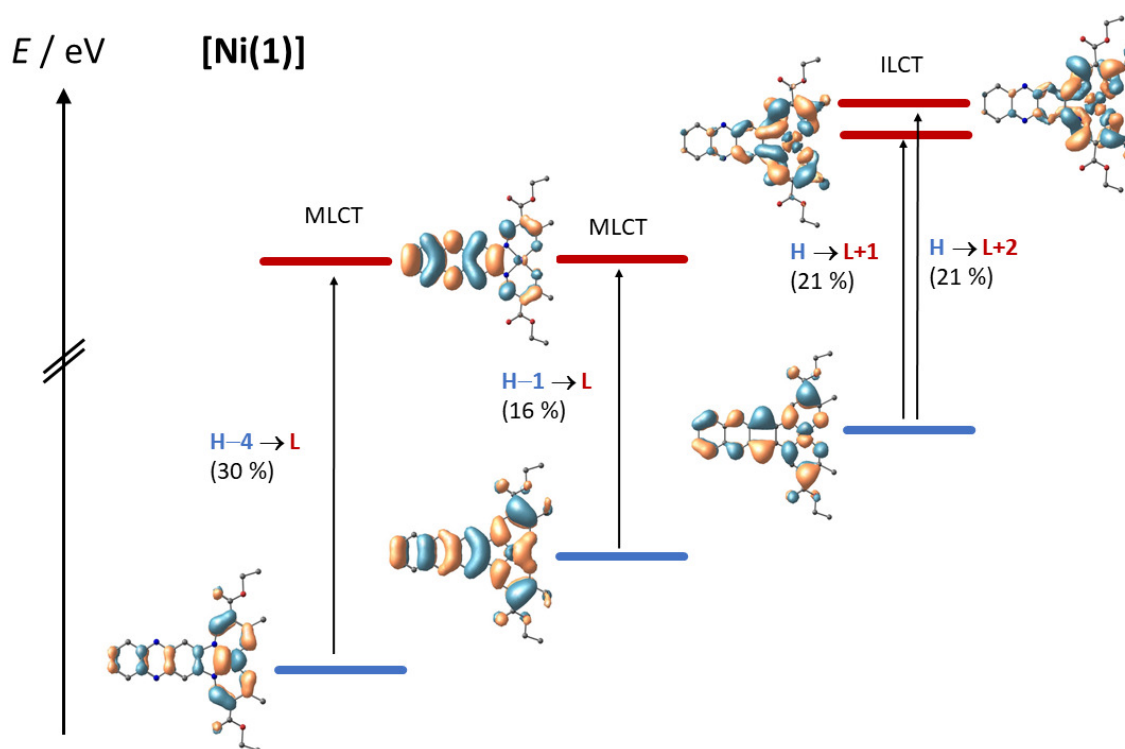


Figure S21: Graphical representations of the single orbital contributions of the leading Vis transition of **[Ni(1)]**.

Table S9: Summary of TD-DFT results obtained for **[Ni(1)]**; transitions with vanishing probability ($f_{osc} < 0.001$) have been omitted; mixed character applies to transitions with maximum orbital-transition coefficients $< 10\%$.

T	ν [cm^{-1}]	λ [nm]	f_{osc}	Character of the transition
5	14975.8	667.7	0.002	H \rightarrow L (89%)
14	21148.4	472.8	0.082	H-1 \rightarrow L (47%)
15	21331.9	468.8	0.022	H-2 \rightarrow L+1/L+2 (35% / 33%)
19	23332.8	428.6	0.004	H-5 \rightarrow L (97%)
20	22786.7	438.9	0.268	mixed , see Figure S21
21	24147.5	414.1	0.017	H-3 \rightarrow L (86%)
23	25391.7	393.8	0.001	mixed

28	24180.7	413.6	0.436	H-4 → L (62%)
30	26135.3	382.6	0.006	H-1/H-4 → L+1 (37% / 23%)
32	27158.2	368.2	0.008	H → L+3 (66%)
33	25335.5	394.7	0.016	H-3 → L+1/L+2 (36% / 33%)
38	28459.4	351.4	0.077	H-6 → L (38%) // H-1 → L+2 (30%)
39	25659.6	389.7	0.003	H-7 → L (90%)
42	29123	343.4	0.131	H-3 → L+1/L+2 (33% / 29%)
43	29100.5	343.6	0.071	H-6 → L (41%)
44	28557	350.2	0.010	H-2 → L+3 (76%)
45	29108.6	343.5	0.005	H-8 → L (78%)
48	29969.6	333.7	0.026	H-4 → L+1/L+2 (45% / 45%)
49	30720.5	325.5	0.192	H-9 → L (42%)
53	30980.2	322.8	0.038	H-10 → L (57%)
57	31426.3	318.2	0.051	H-11 → L (80%)
59	32533.2	307.4	0.071	mixed

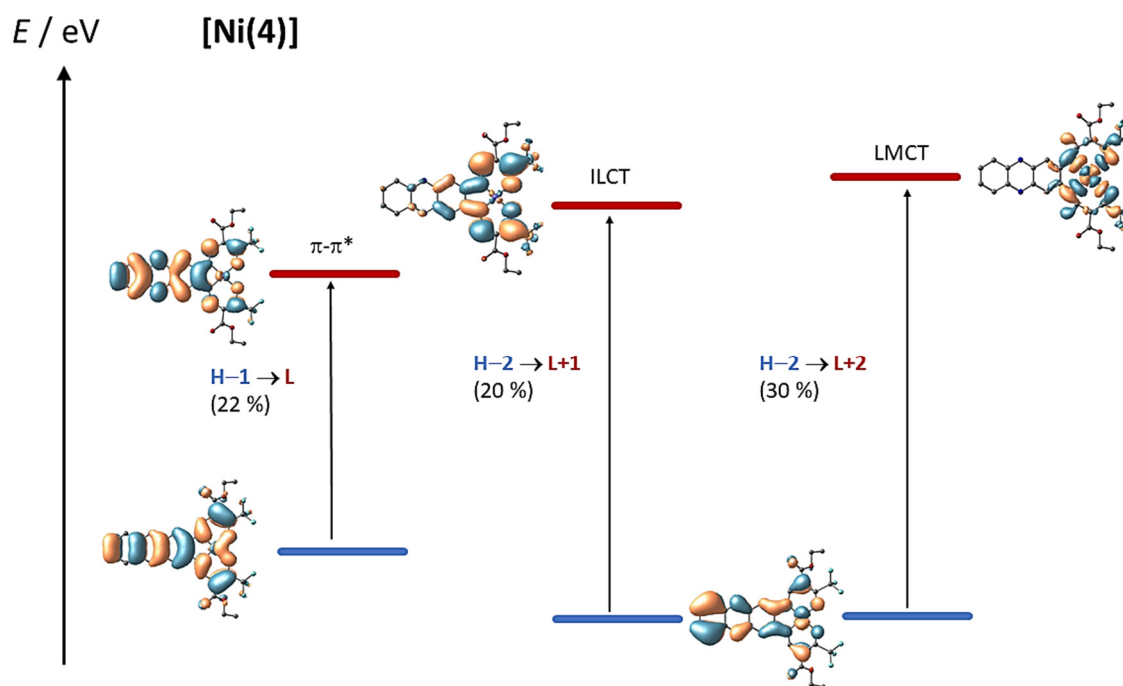


Figure S22: Graphical representations of the single orbital contributions of the leading Vis transition of **[Ni(4)]**.

Table S10: Summary of TD-DFT results obtained for **[Ni(4)]**; transitions with vanishing probability ($f_{\text{osc}} < 0.001$) have been omitted; mixed character applies to transitions with maximum orbital-transition coefficients $< 10\%$.

T	ν [cm^{-1}]	λ [nm]	f_{osc}	Character of the transition
12	20086.2	497.9	0.004	H → L+1 (76%)
17	23058.4	433.7	0.002	H-5/H-1 → L+2 (46% / 47%)
18	22313	448.2	0.001	H-4 → L (99%)

20	22776.1	439.1	0.011	H-2 → L (80%)
26	24151	414.1	0.002	H-5/H-1 → L+2 (44% / 32%)
28	24157.8	413.9	0.231	mixed , see Figure S22
29	24538.7	407.5	0.253	H-2 → L+2 (40%)
31	25092.7	398.5	0.012	mixed
32	25953	385.3	0.009	mixed
34	25264.7	395.8	0.443	H-2 → L+1 (60%)
36	26847.6	372.5	0.041	H-1 → L+1 (43%)
37	24690.3	405	0.102	H-5 → L (89%)
45	26947.8	371.1	0.001	H-3 → L+3 (91%)
47	29155.5	343	0.036	H-5 → L+1 (43%)
49	29460	339.4	0.062	H-7 → L+1 (66%)
51	29861.4	334.9	0.042	H-6 → L (46%)
52	28506.1	350.8	0.017	H-8 → L (83%)
53	30614.8	326.6	0.004	H-9 → L (46%)
57	30914	323.5	0.032	H-2 → L+3 (84%)

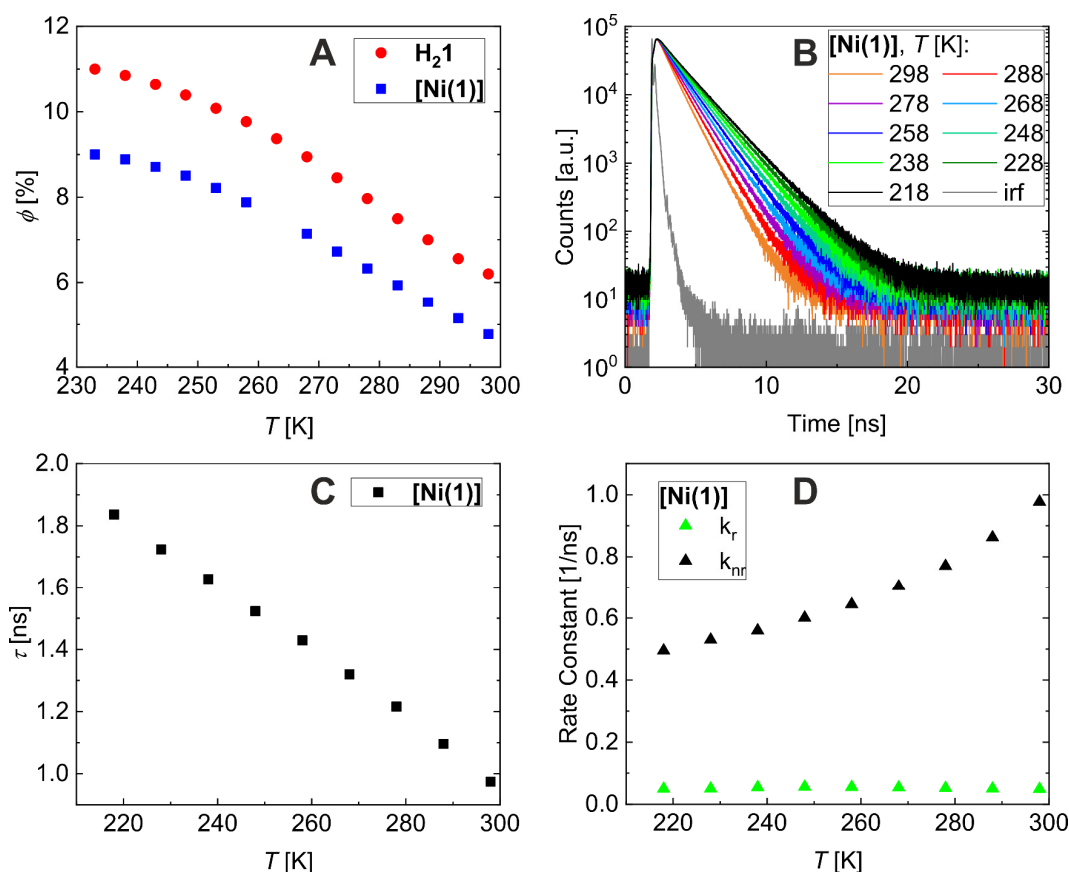
Photophysical measurements of H₂1 and [Ni(1)]


Figure S23: Plot of the extrapolated photoluminescence quantum yield vs T of the ligand **H₂1** and **[Ni(1)]** in chloroform (A). VT-TCSPC detected fluorescence decays of **[Ni(1)]** in chloroform (B). Lifetime vs T plot of **[Ni(1)]** in chloroform (C). Plot of the radiative and non-radiative rate constants of **[Ni(1)]** in chloroform vs T (D).

The temperature-dependent PL quantum yields of **H₂1** and **[Ni(1)]** were estimated by multiplying the temperature dependent PL intensities, normalized to the value at room temperature, with the measured PLQYs at room temperature, that is, $\phi(T) \approx \phi(\text{RT}) \{I_{\text{int}}(T) / I_{\text{int}}(\text{RT})\}$. Data was corrected for temperature-dependent changes in absorption at the excitation wavelength. As PL intensity, we considered the spectral integral of the PL signal, I_{int} . The quantum yields were determined as $\phi(\mathbf{H}_2\mathbf{1}) = 6.2\%$ (at room temperature, $\lambda_{\text{exc}} = 405$ nm) and $\phi(\mathbf{[Ni(1)]}) = 4.8\%$ (at room temperature, $\lambda_{\text{exc}} = 405$ nm). The quantum yields of **[Ni(2)]** and **[Ni(3)]**, which were determined from the measured emission intensities at $\lambda_{\text{exc}} = 405$ nm relative to the measured PLQY of **[Ni(1)]**, are in the same order of magnitude compared to **[Ni(1)]**.

The PL decays were recorded via time-correlated single photon counting (TCSPC), showing a mono-exponentially decay at all temperatures. From these measurements, the radiative rate constants k_r and the non-radiative rate constants k_{nr} were calculated according to

$$k_r = \phi/\tau,$$

$$k_{\text{nr}} = (1-\phi)/\tau.$$

Table S11: Lifetime τ determined from lifetime measurements of **[Ni(1)]** at different temperatures.

T [K]	298	288	278	268	258	248	238	228	218
τ [ns]	0.975	1.096	1.216	1.320	1.429	1.523	1.628	1.724	1.836

Coordination Induced Spin State Switch (CISSS)

Equimolar stock solutions (1.0×10^{-5} M) of [Ni(1–4)] were prepared in the non-coordinating solvent chloroform and the coordinating solvent pyridine. In a second step, binary mixtures of varying chloroform/pyridine ratio but iso-concentrated in the respective nickel(II) complex were obtained through mixing defined volumes of the stock solutions.

Photographs of [Ni(1)] and [Ni(4)] chloroform/pyridine solutions

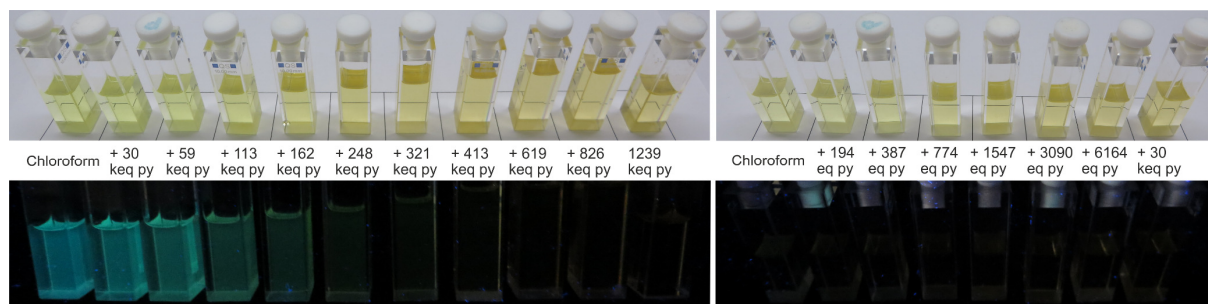


Figure S24: Photographs of the chloroform/pyridine measurements series of [Ni(1)] (left) and [Ni(4)] (right) at room light (top) and upon irradiation with 365 nm (bottom).

Absorbance measurements of [Ni(2)] and [Ni(3)] chloroform/pyridine solutions

Increments for the titration experiments:

[Ni(4)]: 0.2 keq, 0.4 keq, 0.8 keq, 1.5 keq, 3.1 keq, 6.2 keq, 30.2 keq

[Ni(1–3)]: 30 keq, 59 keq, 113 keq, 162 keq, 248 keq, 321 keq, 413 keq, 619 keq, 826 keq, 1239 keq

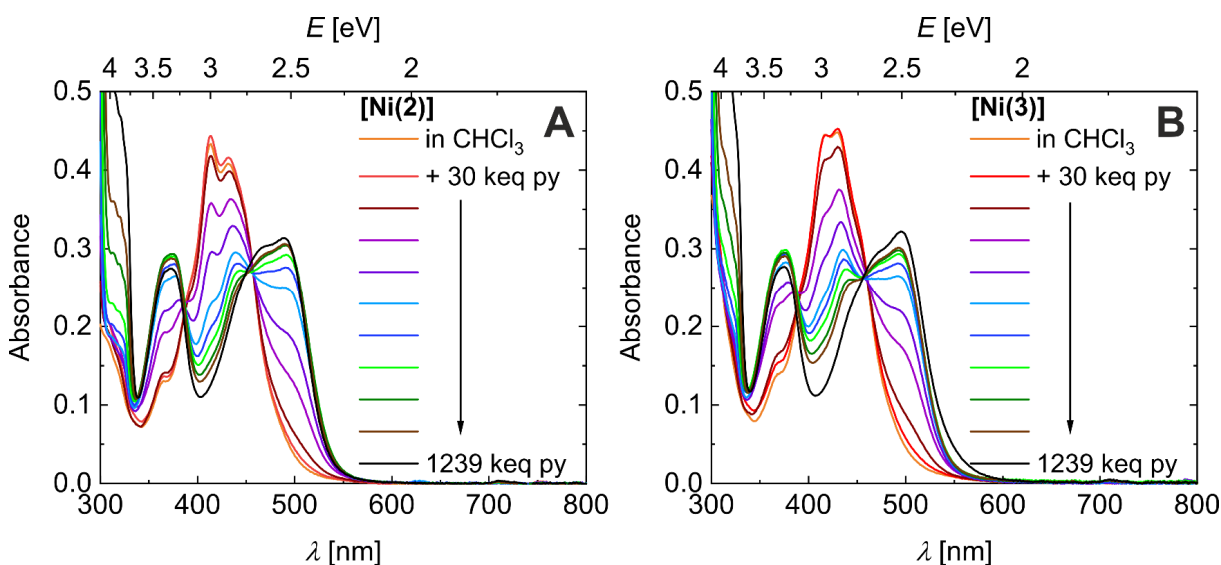


Figure S25: Absorbance measurements of [Ni(2)] (left) and [Ni(3)] (right) in varying chloroform/pyridine ratios.

Computed line spectra of [Ni(1)] and [Ni(4)] in CN 5 and 6

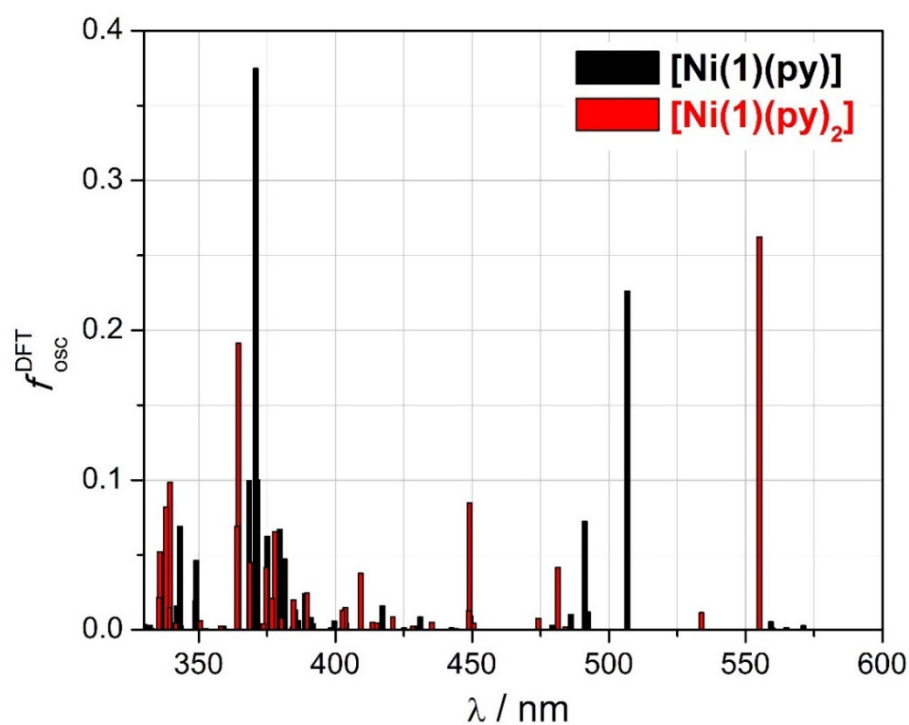


Figure S26: Computed line spectra of [Ni(1)(py)] (black) and [Ni(1)(py)₂] (red); TPSSh-D3/TZVP/COSMO(MeCN).

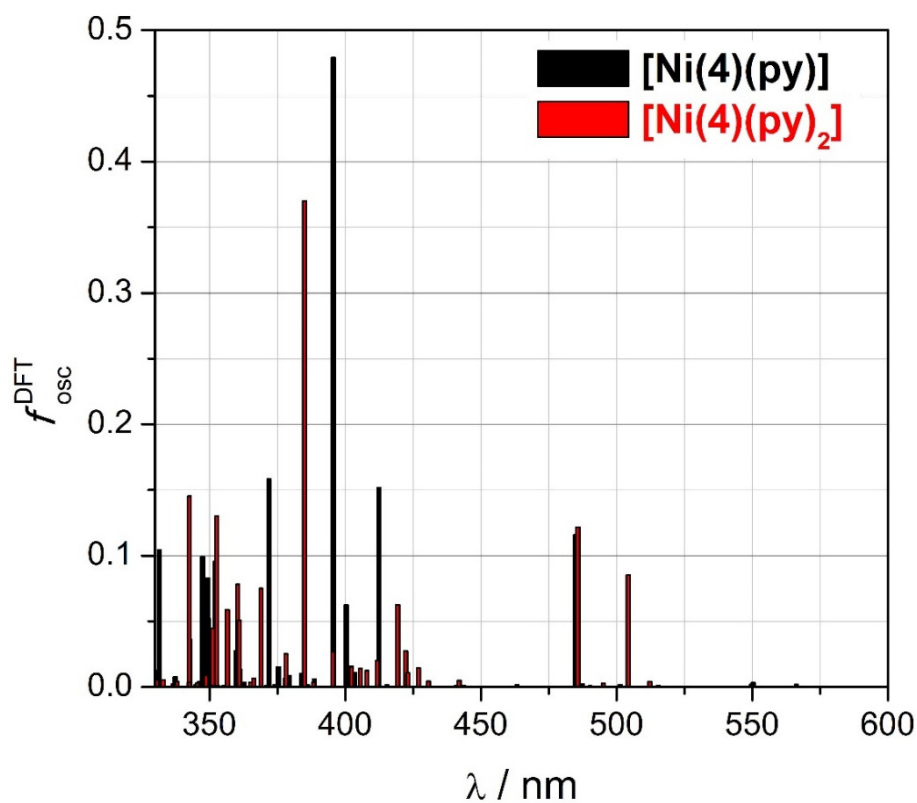


Figure S27: Computed line spectra of [Ni(4)(py)] (black) and [Ni(4)(py)₂] (red); TPSSh-D3/TZVP/COSMO(MeCN).

Absorbance measurements of [Ni(1)] and [Ni(4)] with various axial ligands

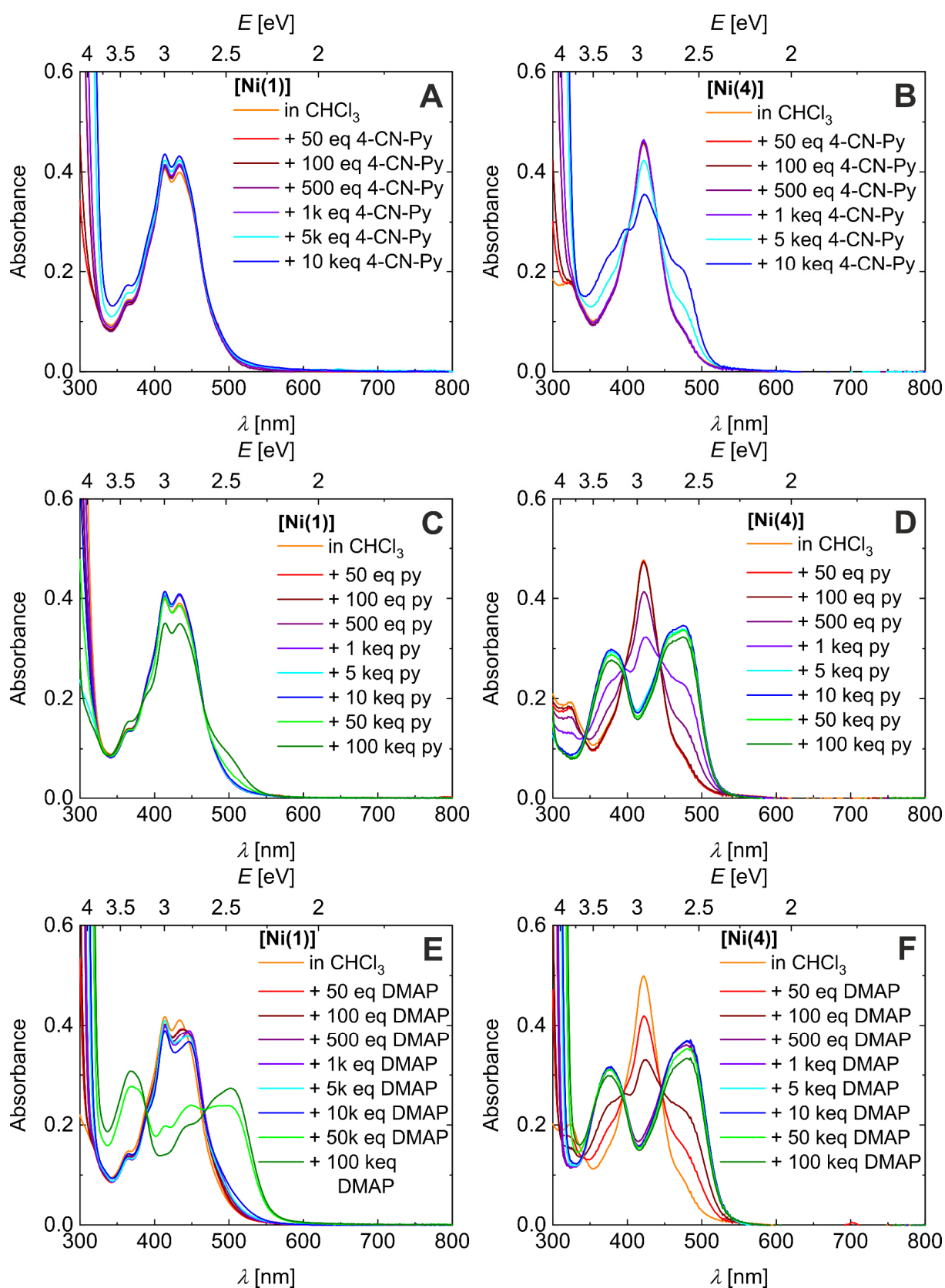
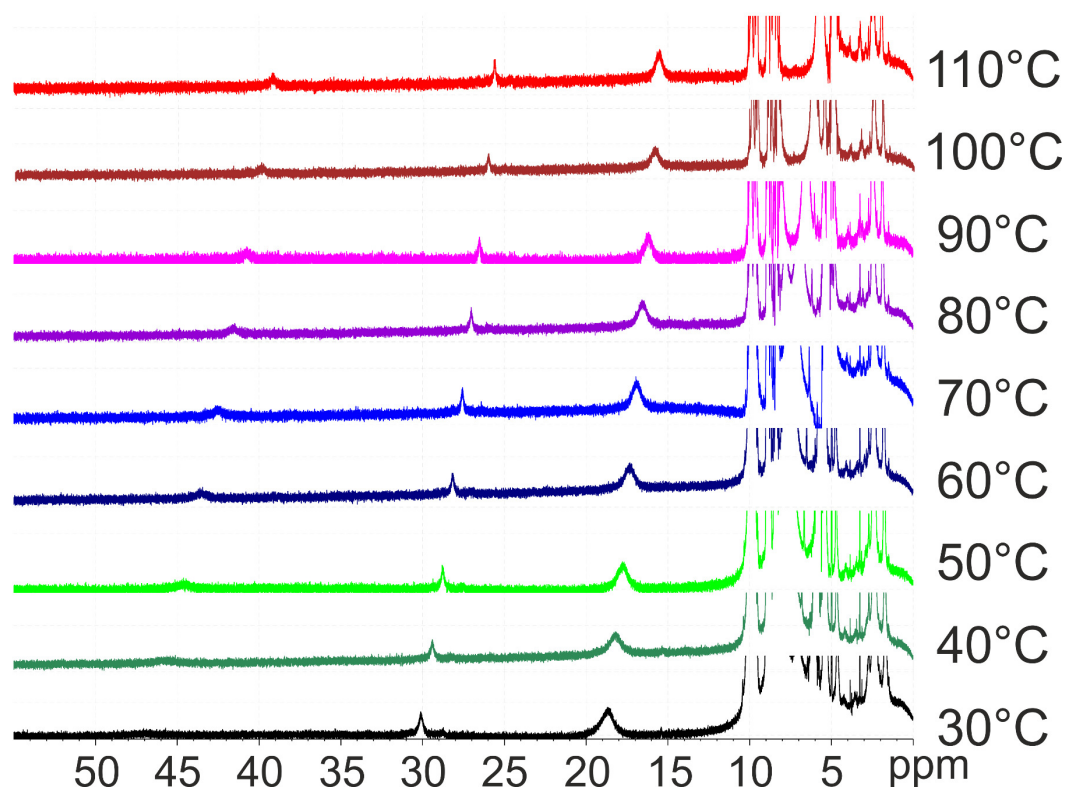
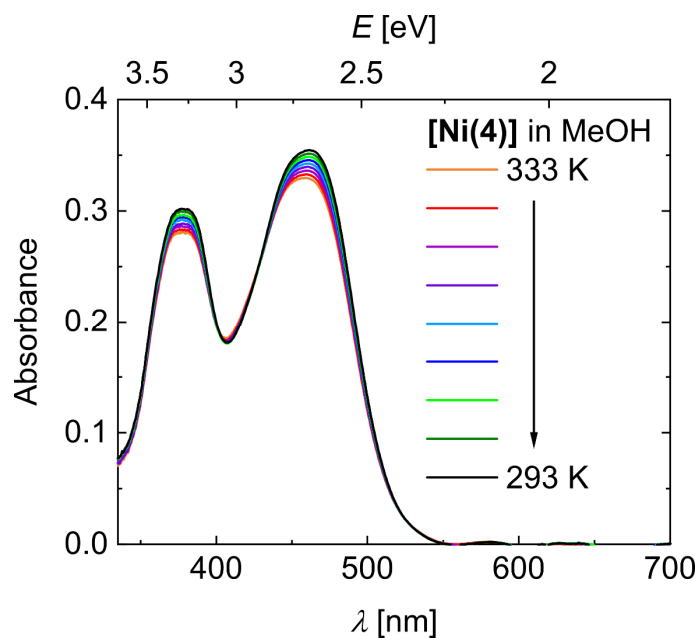


Figure S28: Absorbance measurements of [Ni(1)] (A, C, E) and [Ni(4)] (B, D, F) in chloroform upon addition of different axial ligands (4-cyanopyridine = 4-CN-Py (A, B); pyridine = Py (C, D); 4-dimethylaminopyridine = DMAP (E, F)).

Temperature-dependent ^1H NMR spectra of $[\text{Ni}(\mathbf{1})]$ in $(\text{D}_5)\text{pyridine}$ Figure S29 ^1H NMR spectra of $[\text{Ni}(\mathbf{1})]$ in $(\text{D}_5)\text{pyridine}$ measured at different temperatures.Temperature-dependent absorbance spectra of $[\text{Ni}(\mathbf{4})]$ in MeOHFigure S30: Temperature-dependent absorbance spectra of $[\text{Ni}(\mathbf{4})]$ in MeOH.

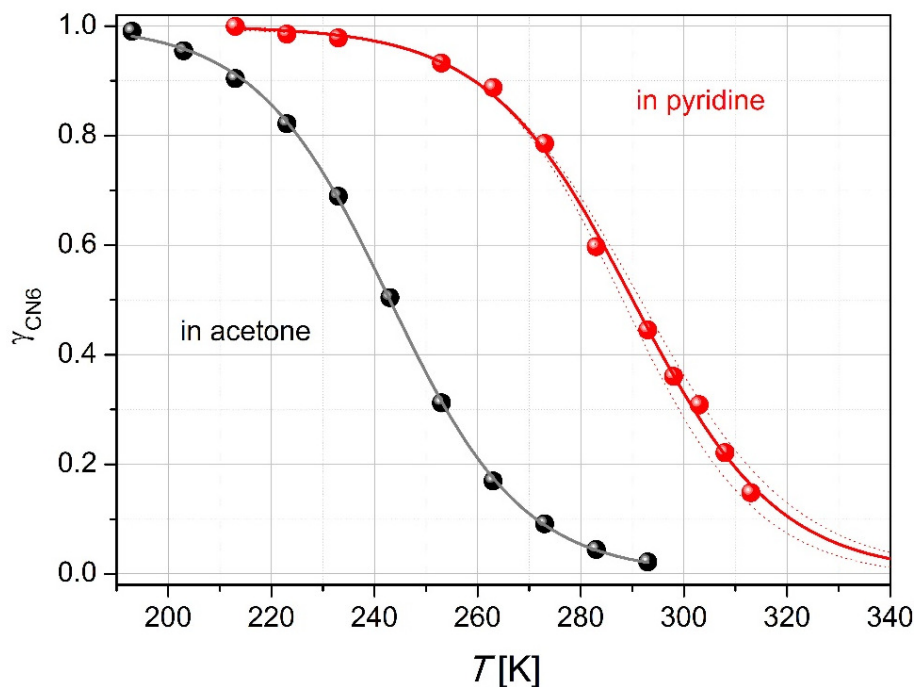
Analysis of the association/dissociation equilibrium of [Ni(4)]


Figure S31: Association/dissociation equilibrium of [Ni(4)] in acetone (black) and pyridine (1:2000 with CHCl₃; red); dashed red lines reflect the uncertainty in the high-temperature extrapolation.

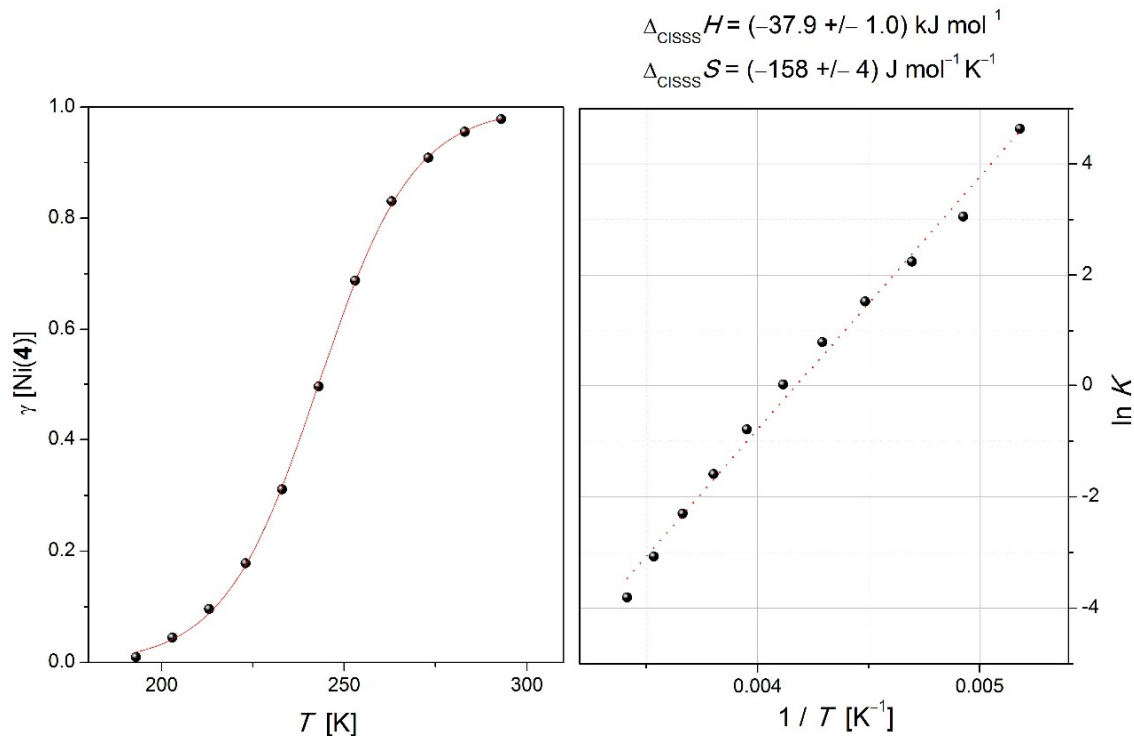
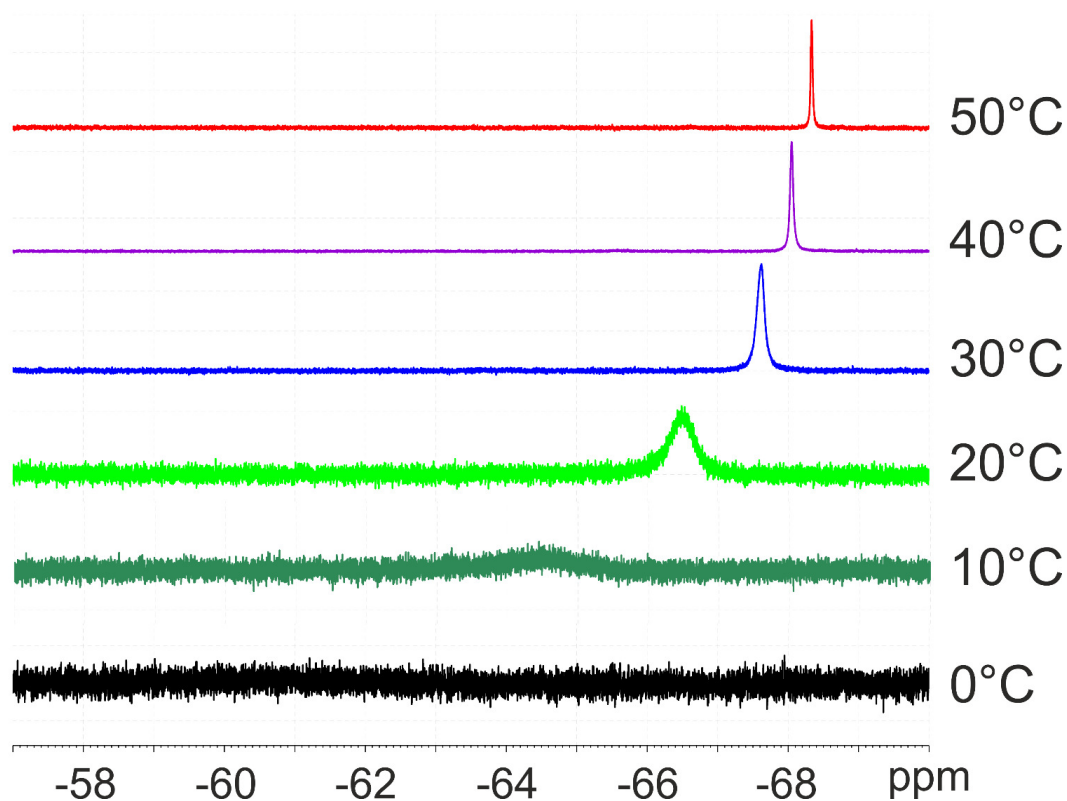
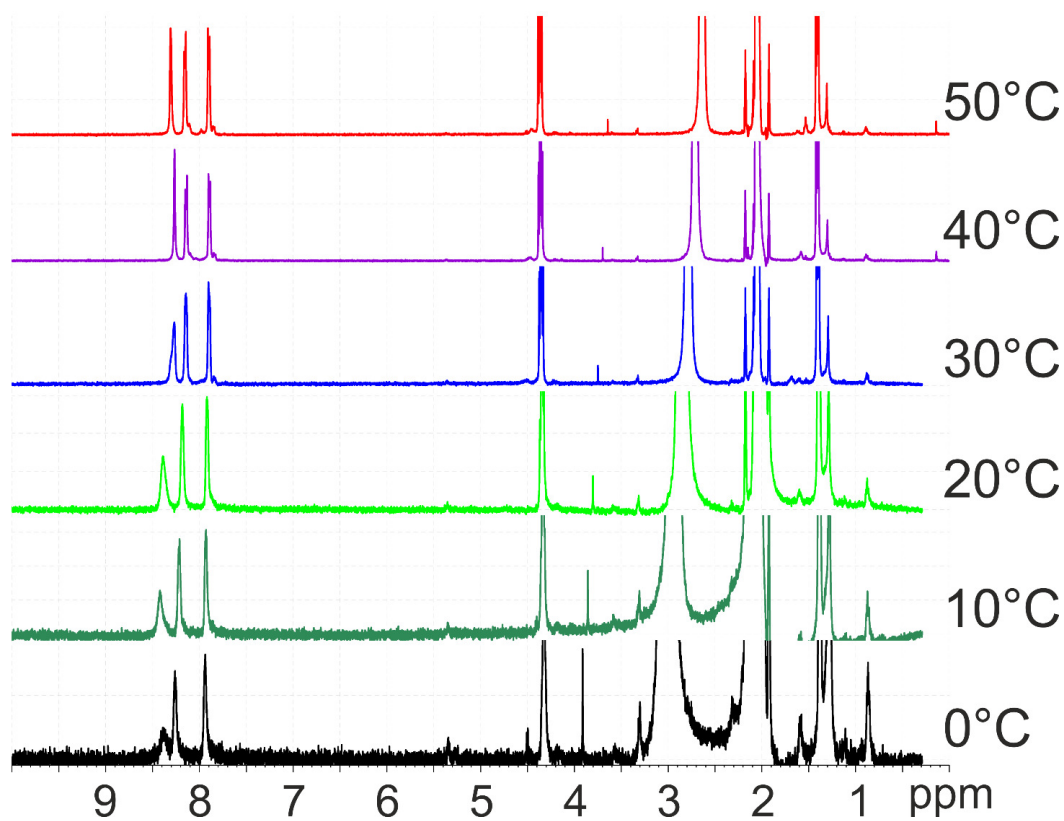


Figure S32: Thermodynamic analysis of the association/dissociation equilibrium of [Ni(4)] in acetone (data from Fig. 10 in the manuscript); (left) temperature dependent fraction of native [Ni(4)] (line: Boltzmann fit); van't Hoff analysis.

Temperature-dependent ^{19}F and ^1H NMR spectra of [Ni(4)] in (D_6) acetoneFigure S33: ^{19}F NMR spectra of [Ni(4)] in (D_6) acetone measured at different temperatures.Figure S34: ^1H NMR spectra of [Ni(4)] in (D_6) acetone measured at different temperatures.

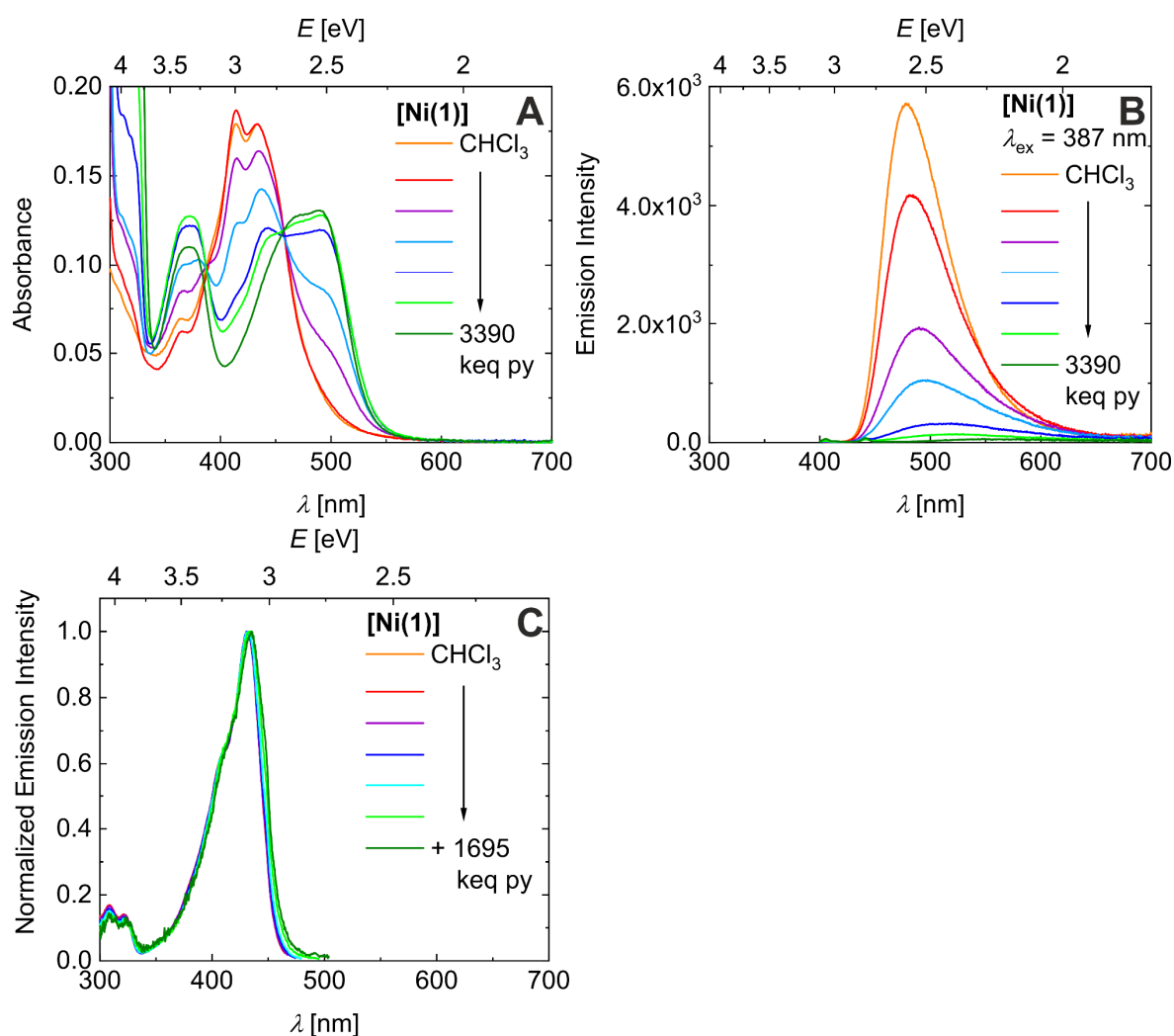
Optical spectra and analysis of the data of [Ni(1)] in chloroform/pyridine solutions


Figure S35: FD-CISSS of [Ni(1)] in various chloroform/pyridine mixtures (3.7×10^{-6} M); Absorption spectra (A); Emission spectra ($\lambda_{\text{exc}} = 387$) (B). Fluorescence excitation spectra ($\lambda_{\text{em}} = \lambda_{\text{exc,max}}$) (C).

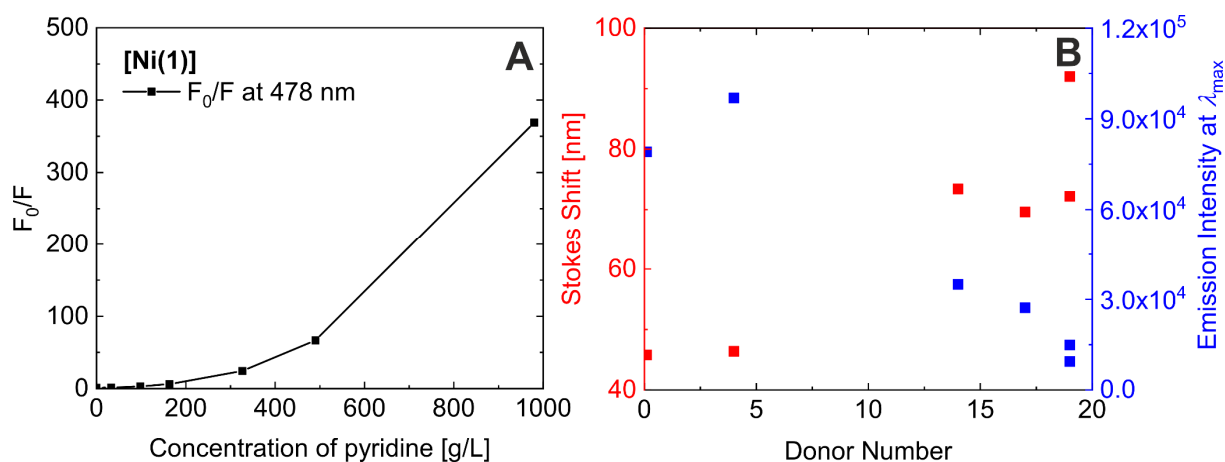


Figure S36: Stern-Vollmer plot of fluorescence quenching of [Ni(1)] (A). Plot of the Stokes shift and the emission intensity of λ_{max} vs. the donor number of the additional solvent in the CHCl_3 :solvent 1:1 mixtures of [Ni(1)] (B).

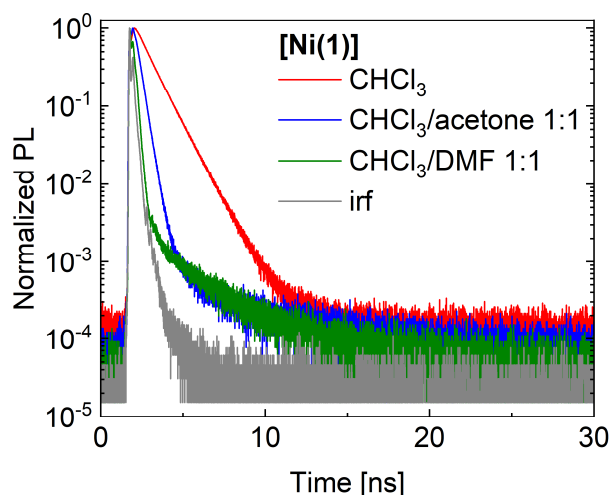


Figure S37: TCSPC detected fluorescence decays of [Ni(1)] in chloroform, a CHCl₃/acetone 1:1 mixture, and a CHCl₃/DMF 1:1 mixture.

References

- (1) Lochenie, C.; Wagner, K. G.; Karg, M.; Weber, B. Modulation of the ligand-based fluorescence of 3d metal complexes upon spin state change. *J. Mater. Chem. C* **2015**, *3* (30), 7925–7935. DOI: 10.1039/C5TC00837A.
- (2) Claisen, L. Untersuchungen über die Oxymethylenverbindungen. (Zweite Abhandlung.). *Justus Liebigs Ann. Chem.* **1897**, *297* (1-2), 1–98. DOI: 10.1002/jlac.18972970102.
- (3) Bauer, W.; Osslander, T.; Weber, B. A Promising New Schiff Base-like Ligand for the Synthesis of Octahedral Iron(II) Spin Crossover Complexes. *Z. Naturforsch. B* **2010**, *2010* (65b), 323–328. DOI: 10.1515/znb-2010-0315.
- (4) Bruker. *SADABS*; Bruker AXS Inc., **2014**.
- (5) Sheldrick, G. M. Crystal structure refinement with SHELXL. *Acta Cryst. C* **2015**, *71* (Pt 1), 3–8. DOI: 10.1107/S2053229614024218.
- (6) Farrugia, L. ORTEP-3 for Windows - a version of ORTEP-III with a Graphical User Interface (GUI). *J. Appl. Cryst.* **1997**, *30* (5), 565.
- (7) Johnson, C. K.; Burnett, M. N. *ORTEP-III*; Oak-Ridge National Laboratory, **1996**.
- (8) Macrae, C. F.; Edgington, P. R.; McCabe, P.; Pidcock, E.; Shields, G. P.; Taylor, R.; Towler, M.; van de Streek, J.; Macrae, C. F.; Edgington, P. R.; McCabe, P.; Pidcock, E.; Shields, G. P.; Taylor, R.; Towler, M.; van de Streek, J. Mercury: Visualization and analysis of crystal structures. *J. Appl. Cryst.* **2006**, *39* (3), 453–457. DOI: 10.1107/S002188980600731X.
- (9) Mello, J. C. de; Wittmann, H. F.; Friend, R. H. An improved experimental determination of external photoluminescence quantum efficiency. *Adv. Mater.* **1997**, *9* (3), 230–232. DOI: 10.1002/adma.19970090308.
- (10) Neese, F. The ORCA program system. *WIREs Comput. Mol. Sci.* **2012**, *2* (1), 73–78. DOI: 10.1002/wcms.81.
- (11) Schäfer, A.; Horn, H.; Ahlrichs, R. Fully optimized contracted Gaussian basis sets for atoms Li to Kr. *J. Chem. Phys.* **1992**, *97* (4), 2571–2577. DOI: 10.1063/1.463096.
- (12) Becke. Density-functional exchange-energy approximation with correct asymptotic behavior. *Phys. Rev. A* **1988**, *38* (6), 3098–3100. DOI: 10.1103/PhysRevA.38.3098.
- (13) Staroverov, V. N.; Scuseria, G. E.; Tao, J.; Perdew, J. P. Comparative assessment of a new nonempirical density functional: Molecules and hydrogen-bonded complexes. *J. Chem. Phys.* **2003**, *119* (23), 12129–12137. DOI: 10.1063/1.1626543.

- (14) Grimme, S.; Antony, J.; Ehrlich, S.; Krieg, H. A consistent and accurate ab initio parametrization of density functional dispersion correction (DFT-D) for the 94 elements H-Pu. *J. Chem. Phys.* **2010**, *132* (15), 154104. DOI: 10.1063/1.3382344.
- (15) Grimme, S.; Ehrlich, S.; Goerigk, L. Effect of the damping function in dispersion corrected density functional theory. *J. Comput. Chem.* **2011**, *32* (7), 1456–1465. DOI: 10.1002/jcc.21759.
- (16) Klamt, A.; Schüürmann, G. COSMO: a new approach to dielectric screening in solvents with explicit expressions for the screening energy and its gradient. *J. Chem. Soc., Perkin Trans. 2* **1993** (5), 799–805. DOI: 10.1039/P29930000799.

6 Quenched Lewis Acidity: Studies on the Medium Dependent Fluorescence of Zinc(II) Complexes

Hannah Kurz, Gerald Hörner, Oskar Weser, Giovanni Li Manni, Birgit Weber*

Hannah Kurz, Dr. Gerald Hörner, Prof. Dr. Birgit Weber – Inorganic Chemistry IV, University of Bayreuth, Universitätsstraße 30, NW I, 95447 Bayreuth, Germany. E-mail: weber@uni-bayreuth.de

O. Weser, Dr. G. Li Manni, Max-Planck-Institute for Solid State Research, Heisenbergstraße 1, 70569 Stuttgart, Germany.

Published in: *Chem. Eur. J.* **2021**, 27, 15159-15171 (DOI: [10.1002/chem.202102086](https://doi.org/10.1002/chem.202102086)).

Reproduced by permission from WILEY-VCH GmbH.

Abstract: Three new zinc(II) coordination units **[Zn(1–3)]** based on planar-directing tetradentate Schiff base-like ligands **H₂(1–3)** were synthesized. Their solid-state structures were investigated by single crystal X-ray diffraction, showing the tendency to overcome the square-planar coordination sphere by axial ligation. Affinity in solution towards axial ligation has been tested by extended spectroscopic studies, both in the absorption and emission mode. The electronic spectrum of the pyridine complex **[Zn(1)(py)]** has been characterized by MC-PDFT to validate the results of extended TD-DFT studies. Green emission of non-emissive solutions of **[Zn(1–3)]** in chloroform could be switched on in the presence of potent Lewis bases. While interpretation in terms of an equilibrium of stacked/non-fluorescent and destacked/fluorescent species is in line with precedents from literature, the sensitivity of **[Zn(1–3)]** was greatly reduced. Results of a computation-based structure search allow to trace the hidden Lewis acidity of **[Zn(1–3)]** to a new stacking motif, resulting in a strongly enhanced stability of the dimers.

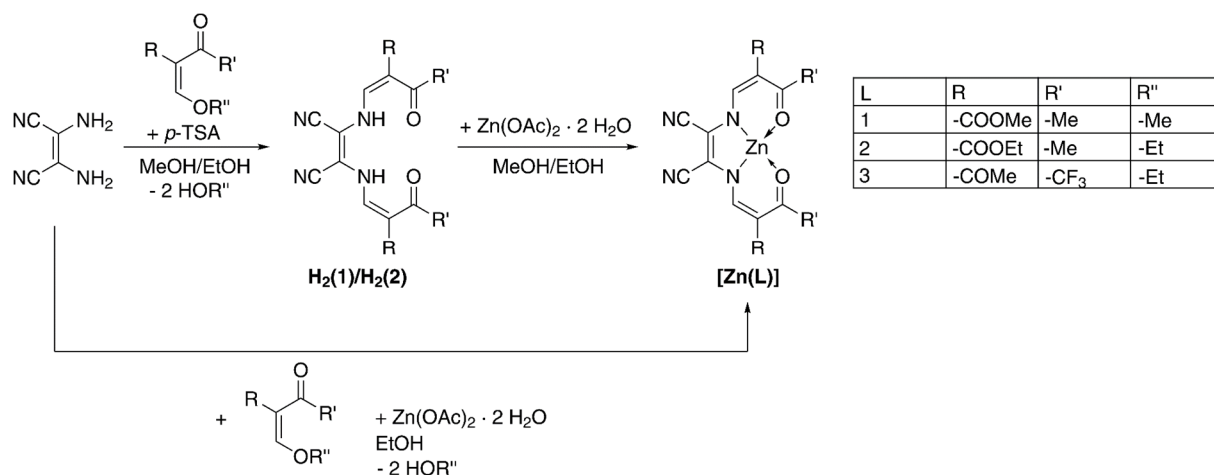
5.1 Introduction

Switchable materials are of great interest for applications as molecular sensor materials.¹ These materials need to combine a high sensitivity toward external physical or chemical stimuli with an easily detectable change of discrete properties such as photoluminescence. For this purpose, metal complexes with photoluminescent ligands are an interesting class of materials, as they can combine an easily tunable photoluminescence based on the ligand with a switching behavior based on the metal center. Various switching processes are possible that depend on the metal center and its electronic configuration. One possibility is the switching based on externally induced spin transitions. Two well-known phenomena are *spin crossover*, which is mostly investigated for iron(II) complexes,^{2,3} and *coordination-induced spin state switching* that can be observed with nickel(II) complexes.^{4,5} In recent years, many workgroups focused on combining one of these two switching mechanisms with a photoluminescent ligand to obtain emissive sensor materials.⁶⁻⁸ However, electronic coupling of metal and ligand often results in predominant non-radiative excited-state decay into low-lying *d-d* states, independent of the spin state.⁹⁻¹¹

Due to these drawbacks, recently much emphasis was put on metal centers with closed d^0 or d^{10} shells such as Zr(IV), Cu(I), or Zn(II). As the *d* orbitals of the metal center are not directly electronically involved in the photophysical processes, the emission is not quenched and a wide range of photoluminescent complexes has been reported.^{10,12-15} Especially, zinc(II) complexes are interesting for the application as molecular sensor materials, as their emission is often medium dependent. In the last decade many zinc(II) complexes have been reported that show aggregation-induced emission enhancement (AIEE).^{16,17}

Interestingly, the opposite case – an emission quenching due to stacking – has been observed as well with zinc(II) complexes. Many studies focus on zinc(II) complexes based on a Schiff base tetradentate ligand equipped with nitrile substituents.¹⁸⁻²⁴ Coordination of additional ligands resulted in a strong increase of the emission intensity. Experimental and computational studies suggested that the zinc(II) complexes stack into dimers or oligomers in solvents that do not support axial coordination.^{21,23} The high emission intensity increase in coordinating solvents was assigned to de-stacking of the zinc(II) complexes.^{19,21} This effect was used previously for bioimaging and biosensing in living cells.^{20,24,25} Furthermore, derivatives of this zinc(II) complex type were investigated for their mechanochromic luminescence behavior, and as emitters for optical temperature sensing via thermally activated delayed fluorescence (TADF).²⁶⁻²⁸

Herein, we present a concerted experiment-theory approach to investigate the influence of the molecular structure on the fluorescence of zinc(II) complexes. A family of neutral complexes of Schiff base-like ligands with appended nitrile groups $[\text{Zn}(\text{L})\text{X}]$ (for the nature of **L**, see Scheme 1; **X** = H_2O , EtOH, THF, py) was synthesized. Please note that the simplified notation $[\text{Zn}(\mathbf{1-3})]$ is used whenever the nature of the axial ligand cannot be specified. In agreement with the established stacking/destacking hypothesis put forward by Di Bella and others for analogue Schiff-base derived complexes,^{21,23} turn-on emission behavior is observed in spectroscopic titrations with Lewis bases, but requires much higher base loads. The seemingly weakened Lewis base affinity of $[\text{Zn}(\text{L})\text{X}]$ was found to be due to quenched Lewis-acidity based on the formation of highly stable dimers in solvents that do not support axial coordination. Results from (time-dependent) density functional theory are benchmarked through complete active space self-consistent field methods. CASSCF, followed by the multi-configurational pair-density functional theory correction (MC-PDFT) accurately captures correlation effects for the relevant states involved in the diagnostic ILCT process.



Scheme 1: Synthetic pathway toward the reported zinc(II) coordination units $[\text{Zn}(\mathbf{1-3})]$.

5.2 Results and Discussion

Complex syntheses and characterization

The zinc(II) coordination units $[\text{Zn}(\mathbf{1})]$ and $[\text{Zn}(\mathbf{2})]$ were synthesized in two steps as shown in Scheme 1; $[\text{Zn}(\mathbf{3})]$ was synthesized in a one-pot reaction as the synthesis of the free ligand $\text{H}_2(\mathbf{3})$ failed. In the case of $\text{H}_2(\mathbf{1})$ and $\text{H}_2(\mathbf{2})$ the free Schiff base-like ligands were obtained directly through reaction of diaminomaleonitrile with the respective keto-enol ether in the presence of *p*-toluenesulfonic acid (*p*-TSA); $\text{H}_2(\mathbf{2})$ has been reported previously.²⁹ $\text{H}_2(\mathbf{1})$ was received from MeOH as an orange solid in 44% yield. The identity and purity of the ligands

was confirmed by ^1H NMR spectroscopy, mass spectrometry, and elemental analysis. It is noted that resonances of the NH hydrogen atom could not be observed spectroscopically, neither in IR nor ^1H NMR. This finding indicates fast exchange in solution and strong involvement of the NH hydrogen atoms in a hydrogen bond network in the solid.

From the ligands the respective zinc(II) complexes were obtained through conversion with stoichiometric amounts of $\text{Zn}(\text{OAc})_2 \cdot 2 \text{H}_2\text{O}$ in alcohol media. Thereby, acetate provides the required base equivalents. In this manner $\{\{\text{Zn(1)}\}(\text{H}_2\text{O})(\text{MeOH})\}$ and $\{\{\text{Zn(2)}\}_2(\text{H}_2\text{O})_3\}$ were obtained as a red crystalline (70 %) and an orange solid (47%), respectively. $\{\{\text{Zn(3)}\}(\text{H}_2\text{O})(\text{EtOH})\}$ was received as an orange solid (66%) in a zinc-templated three-component reaction in EtOH (diaminomaleonitrile, keto-enol ether, $\text{Zn}(\text{OAc})_2 \cdot 2 \text{H}_2\text{O}$; 1:2.2:1.3). Sample homogeneity and purity was established by ^1H NMR spectroscopy and mass spectrometry. Elemental analysis indicated the presence of stoichiometrically defined amounts of solvent molecules in the samples as indicated by the above empirical formulae. X-ray diffraction of single-crystalline samples indeed identified the complexes to be five (N_2O_3) and six-coordinate (N_2O_4) in the solid, besides additional solvent molecules in the lattice.

X-ray diffraction analysis

Molecular structures and packing pattern were addressed by single-crystal X-ray diffraction. The crystallographic data of all crystal structures are summarized in Table S1/S2 in the SI. Orange block-like crystals of $[\text{Zn(1)}(\text{MeOH})] \cdot \text{MeOH}$ were obtained directly from the mother liquor. The material crystallizes in the orthorhombic space group *Pbca*. The asymmetric unit consists of the five-coordinate zinc(II) complex and one solvent MeOH molecule as shown in Figure 1A (see Figure S1 for a fully labelled representation of the asymmetric unit). The zinc(II) center is enclosed in a close-to-ideal tetragonal pyramidal N_2O_3 coordination sphere ($S_p(\text{SqPy}) = 1.18$),³⁰ wherein an axial methanol ligand adds to the N_2O_2 chelate of the Schiff base-like ligand. Selected bond lengths are given in Table 1. The average bond lengths within the chelate cycle are 1.99 Å ($\text{Zn1}-\text{O}_{\text{eq}}$), 2.06 Å ($\text{Zn1}-\text{N}_{\text{eq}}$), and 2.01 Å ($\text{Zn1}-\text{O}_{\text{ax}}$). The *cis*-angles including the zinc(II) metal center are in the range of 97–104°, which indicates an almost ideal square-pyramidal coordination sphere.

Yellow plate-like crystals of $[\text{Zn(1)}(\text{py})]$ were obtained by adding deuterated pyridine to a solution of $\{\{\text{Zn(1)}\}(\text{H}_2\text{O})(\text{MeOH})\}$ in deuterated acetonitrile. In the triclinic space group $P\bar{1}$, the asymmetric unit consists of one five-coordinate zinc(II) complex as shown in Figure 1B (see Figure S2 for a fully labelled representation of the asymmetric unit). The zinc(II) center is enclosed in a N_3O_2 coordination sphere due to an axially coordinating pyridine molecule. The

bond lengths (2.01 Å (Zn1–O_{eq}), 2.06 Å (Zn1–N_{eq}), 1.99 Å (Zn1–N_{ax}) are very similar to the ones of [Zn(1)(MeOH)]·MeOH. However, the square-pyramidal coordination sphere features a slightly higher distortion with bond angles of 94–110° ($S_p(\text{SqPy}) = 2.07$).³⁰ A very similar asymmetric unit with five-coordinate zinc(II) complexes could be obtained by crystallization from wet acetonitrile. Thereby, orange rhombohedral-like crystals of [Zn(1)(H₂O)] were obtained that crystallize in the triclinic space group $P\bar{1}$. The asymmetric unit consists of a five-coordinate zinc(II), where one water molecule acts as the axial ligand leading to a N₂O₃ coordination sphere (see Figure 1C and Figure S3 in the Supporting Information for a fully labelled representation of the asymmetric unit). The average bond lengths are with 2.00 Å (Zn1–O_{eq}), 2.06 Å (Zn1–N_{eq}), and 2.06 Å (Zn1–O_{ax}) very similar to the ones of [Zn(1)(MeOH)]·MeOH. However, similar to [Zn(1)(py)], the square-pyramidal coordination sphere shows a slightly higher degree of distortion ($S_p(\text{SqPy}) = 1.97$).³⁰

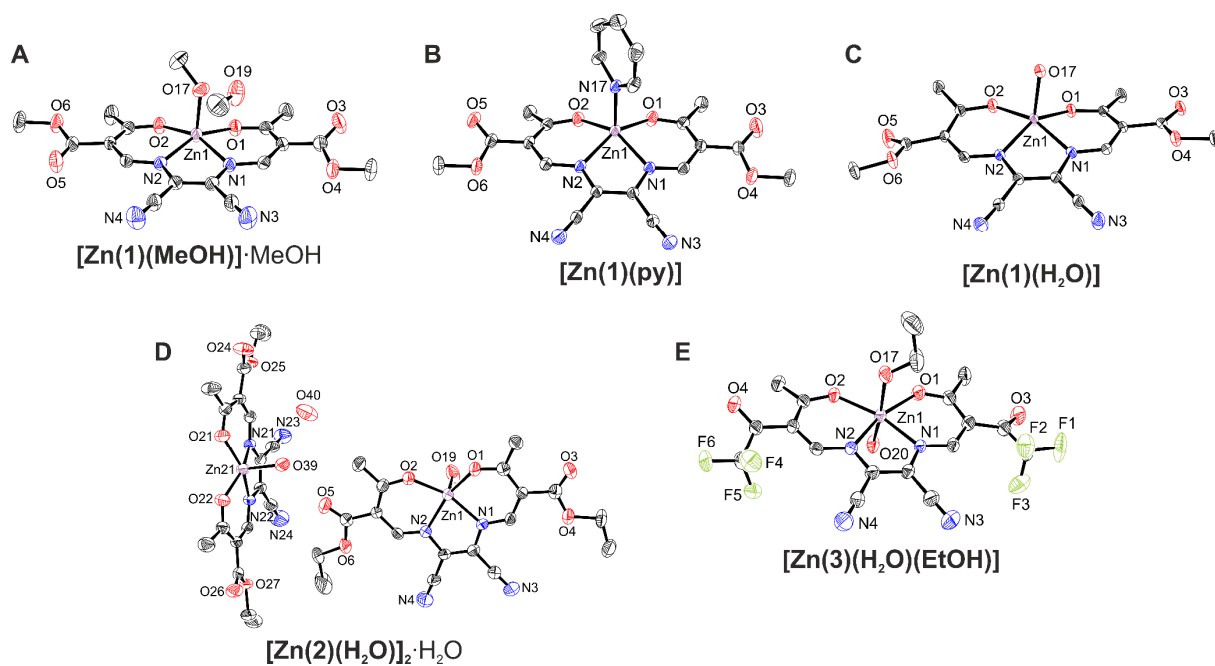


Figure 1: Structures of the asymmetric units of [Zn(1)(MeOH)]·MeOH (A), [Zn(1)(py)] (B), [Zn(1)(H₂O)] (C), [Zn(2)(H₂O)]₂·H₂O (D), and [Zn(3)(H₂O)(EtOH)] (E). Hydrogen atoms are omitted for clarity. Ellipsoids are shown at 50% probability level.

Similar to [Zn(1)(MeOH)]·MeOH, the zinc(II) center in [Zn(2)(H₂O)]₂·H₂O is enclosed in a N₂O₃ coordination sphere where water ligates axially. Orange block-like single crystals of [Zn(2)(H₂O)]₂·H₂O obtained from the mother liquor were analysed in the triclinic space group $P\bar{1}$. The asymmetric unit consists of two five-coordinate zinc(II) complexes and one water solvent molecule (see Figure 1D and Figure S4 for a fully labelled representation of the asymmetric unit). The bond lengths and angles (2.00 Å (Zn1–O_{eq}), 2.06 Å (Zn1–N_{eq}), 1.99 Å

(Zn1–O_{ax}), 99–104°) of the largely undistorted square-pyramidal coordination sphere ($S_p(SqPy) = 1.28/1.36$)³⁰ closely match the data of [Zn(1)(MeOH)]·MeOH. Interestingly, the metrics of all these complexes closely mimic structures which have been reported of five-coordinate zinc(II) complexes deriving from *salmant* (2,2'-[(1,2-Dicyanoethene-1,2-diyl)bis(nitrilomethanylylidene)]-diphenol)³¹ and *salophen* (2,2'-[1,2-phenylenebis(nitrilomethanylylidene)]diphenol) ligands.³²

Table 1: Selected bond lengths [Å] and bond angles [°] of [Zn(1)(MeOH)]·MeOH, [Zn(1)(py)], [Zn(1)(H₂O)], [Zn(2)(H₂O)]₂·H₂O, and [Zn(3)(H₂O)(EtOH)].

Compound	Bond	Bond length	Bonds	Bond angle
[Zn(1)(MeOH)]·MeOH	Zn1-O _{eq}	1.9925(15) 1.9909(15)	O _{eq} -Zn1-O _{eq}	99.21(6)
	Zn1-N _{eq}	2.0562(18) 2.0572(18)	N _{eq} -Zn-O _{ax}	97.78(7) 103.77(7)
	Zn1-O _{ax}	2.0091(19)	O _{eq} -Zn-O _{ax}	97.15(7) 103.34(7)
[Zn(1)(py)]	Zn1-O _{eq}	2.0060(18) 2.0074(16)	O _{eq} -Zn1-O _{eq}	93.86(7)
	Zn1-N _{eq}	2.0708(18) 2.0576(19)	N _{eq} -Zn1-N _{ax}	110.08(7) 108.28(8)
	Zn1-N _{ax}	2.0480(18)	O _{eq} -Zn1-N _{ax}	99.31(7) 101.00(7)
[Zn(1)(H ₂ O)]	Zn1-O _{eq}	2.0117(11) 1.9866(11)	O _{eq} -Zn1-O _{eq}	98.92(4)
	Zn1-N _{eq}	2.0577(12) 2.0624(12)	N _{eq} -Zn-O _{ax}	102.68(5) 112.45(5)
	Zn1-O _{ax}	2.0555(12)	O _{eq} -Zn-O _{ax}	96.41(5) 97.30(5)
[Zn(2)(H ₂ O)] ₂ ·H ₂ O	Zn1-O _{eq}	2.000(3) 2.003(3)	O _{eq} -Zn1-O _{eq}	99.36(12)
	Zn1-N _{eq}	2.062(3) 2.055(3)	N _{eq} -Zn-O _{ax}	102.30(15) 103.35(16)
	Zn1-O _{ax}	1.991(5)	O _{eq} -Zn-O _{ax}	99.19(15) 100.36(15)
[Zn(3)(H ₂ O)(EtOH)]	Zn1-O _{eq}	2.057(3) 2.043(3)	O _{eq} -Zn1-O _{eq} O _{ax} -Zn1-O _{ax}	111.90(12) 166.53(16)
	Zn1-N _{eq}	2.090(4) 2.098(4)	O _{eq} -Zn- O _{ax} ,EtOH	87.12(13) 86.91(14)
	Zn1-O _{ax}	2.129(4) 2.108(4)	O _{eq} -Zn- O _{ax} ,H ₂ O	85.91(13) 85.02(14)

Finally, red block-like crystals of [Zn(3)(H₂O)(EtOH)] were obtained from the mother liquor. Different from [Zn(1/2)], fragment [Zn(3)] exhibits electron withdrawing CF₃ substituents. This increase in Lewis acidity of the zinc(II) metal center is directly reflected in a coordination

of two axial ligands leading to a six-coordinate zinc(II) complex. In the monoclinic space group $P2_1/c$, the asymmetric unit consists of one mononuclear six-coordinate zinc(II) complex, where the axial positions are occupied by one water and one EtOH ligand (see Figure 1E and Figure S5 in the Supporting Information for a fully labelled representation of the asymmetric unit). This coordination results in an N_2O_4 coordination sphere. The average bond lengths (2.05 Å (Zn1–O_{eq}), 2.09 Å (Zn1–N_{eq}), 2.12 Å (Zn1–O_{ax})) are significantly longer than in the five-coordinate congeners **[Zn(1)(MeOH)]** and **[Zn(2)(H₂O)]**. The O_{ax}–Zn1–O_{ax} *trans*-angle of 166.53(16) and *cis*-angles of 85–87° indicate a distorted octahedral coordination sphere ($S_p(O_h) = 1.83$).³⁰

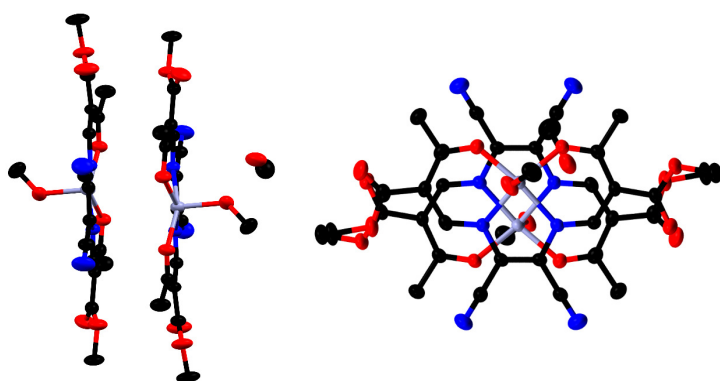


Figure 2: Side view and top view of the stacked dimers in **[Zn(1)(MeOH)]·MeOH**. Hydrogen bonds are omitted for clarity. Ellipsoids are shown at 50% probability level.

In the crystal, π - π interactions between the chelate Zn1–N1–C4–C5–N2 of neighboring complexes and towards the zinc(II) metal center result into stacked dimers, in **[Zn(1)(MeOH)]**, **[Zn(1)(H₂O)]**, **[Zn(2)(H₂O)]₂·H₂O** (see Figure 2 and Figure S6 and S9 in the Supporting Information; Table S3 in the SI for distances and angles of the π - π and M- π interactions). These stacked dimers interact with neighboring molecules through a hydrogen bond network (see Figure S7, S8, and S10 in the SI; Table S4 in the Supporting Information for hydrogen bonds and angles). The supramolecular packing in **[Zn(1)py]** clearly differs from the above cases, as no stacked dimers are observed due to the coordination of pyridine. The packing is similar to the above described cases dominated by non-classical hydrogen bonds forming columns (see Figure S11 in the SI; Table S3/4 in the Supporting Information). In the case of **[Zn(3)(H₂O)(EtOH)]**, where the zinc(II) metal centers are six-coordinated, the packing is likewise dominated by hydrogen bonds resulting in a 3D hydrogen bond network (see Figure S12 in the SI; Table S4 in the Supporting Information for hydrogen bond and angles).

Powder X-ray diffraction patterns of the zinc(II) complexes [**Zn(2/3)**] at RT are matched by the calculated patterns of [**Zn(2/3)**] based on the single-crystals data (Figure S13 in the Supporting Information), indicating conserved formulations of bulk and crystalline samples. In contrast, the calculated pattern of [**Zn(1)**] clearly differs from the experimental data, as could be expected from the different constitution of bulk powder and single crystal.

Optical properties of the zinc(II) complexes

Steady-state absorption and emission. Due to the closed shell character and a large net nuclear charge, zinc(II) centers are usually not directly involved in optical processes such as absorption or emission. In particular, radiative transitions with predominating MLCT character that are the basis of the rich photophysics and photochemistry of copper(I) are prohibited in isoelectronic zinc complexes. Instead, optical excitation and relaxation are largely dominated by the ligand. Nevertheless, coordination of zinc(II) by the ligands **H₂(1)** and **H₂(2)** after deprotonation clearly affects the optical properties in solution as they are strongly red-shifted going from a yellow to an orange solution.

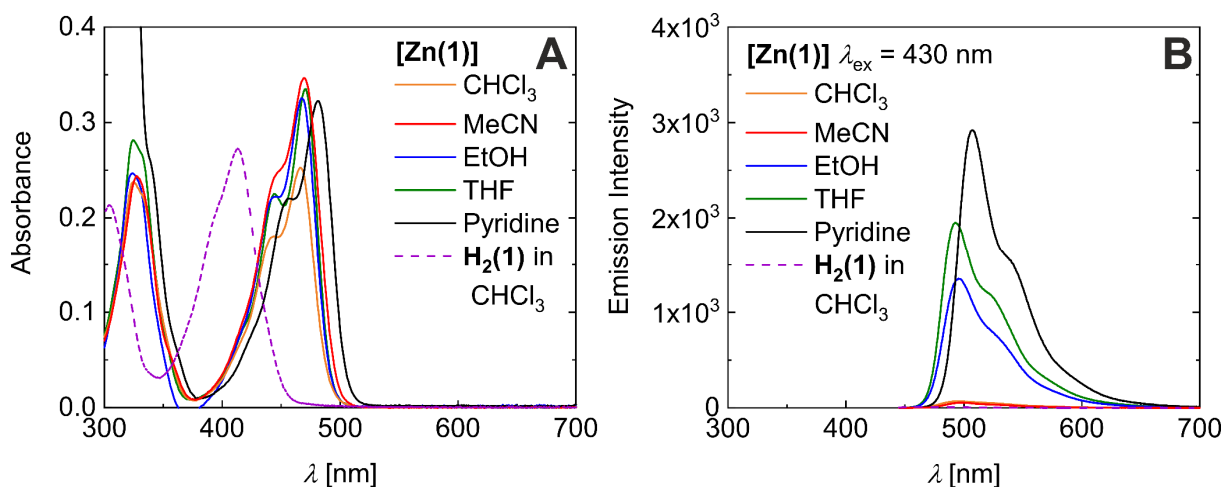


Figure 3: Absorbance (A) and emission (B) spectra of [**Zn(1)**] in CHCl₃, MeCN, EtOH, THF, and pyridine (7×10^{-6} M).

Accordingly, the optical spectra are dominated by intense absorption bands centered at 413 nm ($\epsilon_M = 3.9/3.6 \cdot 10^4 \text{ M}^{-1}\text{cm}^{-1}$) and 467 nm ($\epsilon_M = 3.6 \cdot 10^4 \text{ M}^{-1}\text{cm}^{-1}$) for dilute solutions in chloroform ($c = 7 \cdot 10^{-6}$ M) of the ligands **H₂(1/2)** and the zinc complexes [**Zn(1/2)**], respectively. The leading absorption in [**Zn(3)**] bearing CF₃ substituents is located at 451 nm (see Figure 3A and Figure S14/15 in the Supporting Information). Exemplarily, this distinct red shift upon coordination by $\Delta\nu = 2800 \text{ cm}^{-1}$ is shown for ligand **H₂(1)** and [**Zn(1)**] in Figure 3A; similar observations hold for **H₂(2)**/[**Zn(2)**] (Fig. S14B and S15A in the Supporting

Information). The strong UV band in the ligand spectrum at 305 nm is likewise shifted to smaller energy by $\Delta\nu = 2100 \text{ cm}^{-1}$. Spectral shifts of ligand-centered bands upon coordination are not unique. For a topologically related couple deriving from salicylic aldehyde, a coordination-dependent red shift has been recorded from 374 nm (in acetonitrile) for the ligand³³ to 560 nm for the zinc complex (in DMSO)³⁴; that is, excitation energy shifts by as much as $\Delta\nu = 8800 \text{ cm}^{-1}$.

[Zn(1)] shows weak fluorescence in CHCl_3 , that is in a non-coordinating environment ($\lambda_{\text{Em}} = 495 \text{ nm}$; $\Phi_{\text{F}} \approx 0.004$; all reported quantum yields are relative to [Zn(1)] in pyridine by the comparison of the absorbance corrected integrated emission intensity). Similar observations hold for [Zn(2)] and [Zn(3)], with somewhat smaller quantum yield Φ_{F} of the latter. By contrast the free ligands are essentially non-emissive under the same conditions ($\Phi_{\text{Em}} \approx 10^{-4}$); it is noted that the salicylic analogue of ligand H₂(1) supports fluorescence with $\Phi_{\text{Em}} = 0.017$.³³ The spectra of all zinc(II) complexes indicate partly resolved vibrational structure, both in absorption and in emission. An energy spacing of the vibrational progression by $\Delta_{\text{vib}}E \approx 1100 \text{ cm}^{-1}$ points to a leading role of chelate skeletal modes. This assignment is supported by analysis of DFT-derived harmonic frequencies (see Fig. S16 in the Supporting Information and animated gif).

Quite generally zinc complexes of planar-directing N_2O_2 ligands show significant solvatochromism in both, absorption and emission.^{19,22} Different from these literature precedents, a solvent scan shows that the absorption spectra of unit [Zn(1)] are largely indifferent to solvent variation with respect to energy and band shape (Fig. 3A). It is only in neat pyridine that absorption is affected. Notwithstanding the almost invariant absorption spectra, however, emission properties of [Zn(1)] vary substantially with solvent (see Figure 3B). While emission is very weak in chloroform and acetonitrile ($\Phi_{\text{Em}}(\text{CHCl}_3) = \Phi_{\text{Em}}(\text{MeCN}) \approx 0.004$), it is greatly enhanced in EtOH and THF ($\Phi_{\text{Em}}(\text{EtOH}) \approx 0.07$ and $\Phi_{\text{Em}}(\text{THF}) \approx 0.10$) and reaches its maximum in neat pyridine ($\Phi_{\text{Em}}(\text{Py}) \approx 0.15$). As a matter of fact, fluorescence of [Zn(1)] which is silent in acetonitrile, can be increased successively through addition of water (see Figure S17 in the SI). Increasing the water content up to 50 vol-% results in a quantum yield increase up to $\Phi_{\text{Em}}(\text{MeCN}/\text{H}_2\text{O} 1/1) \approx 0.013$. Coordination of Lewis-basic solvent molecules to the Lewis-acidic zinc center must be considered as the underlying molecular factor that switches on fluorescence in [Zn(1)]. This notion is supported by the continuous increase of Φ_{Em} with the donor number of the solvent (see Figure S18 in the Supporting Information).

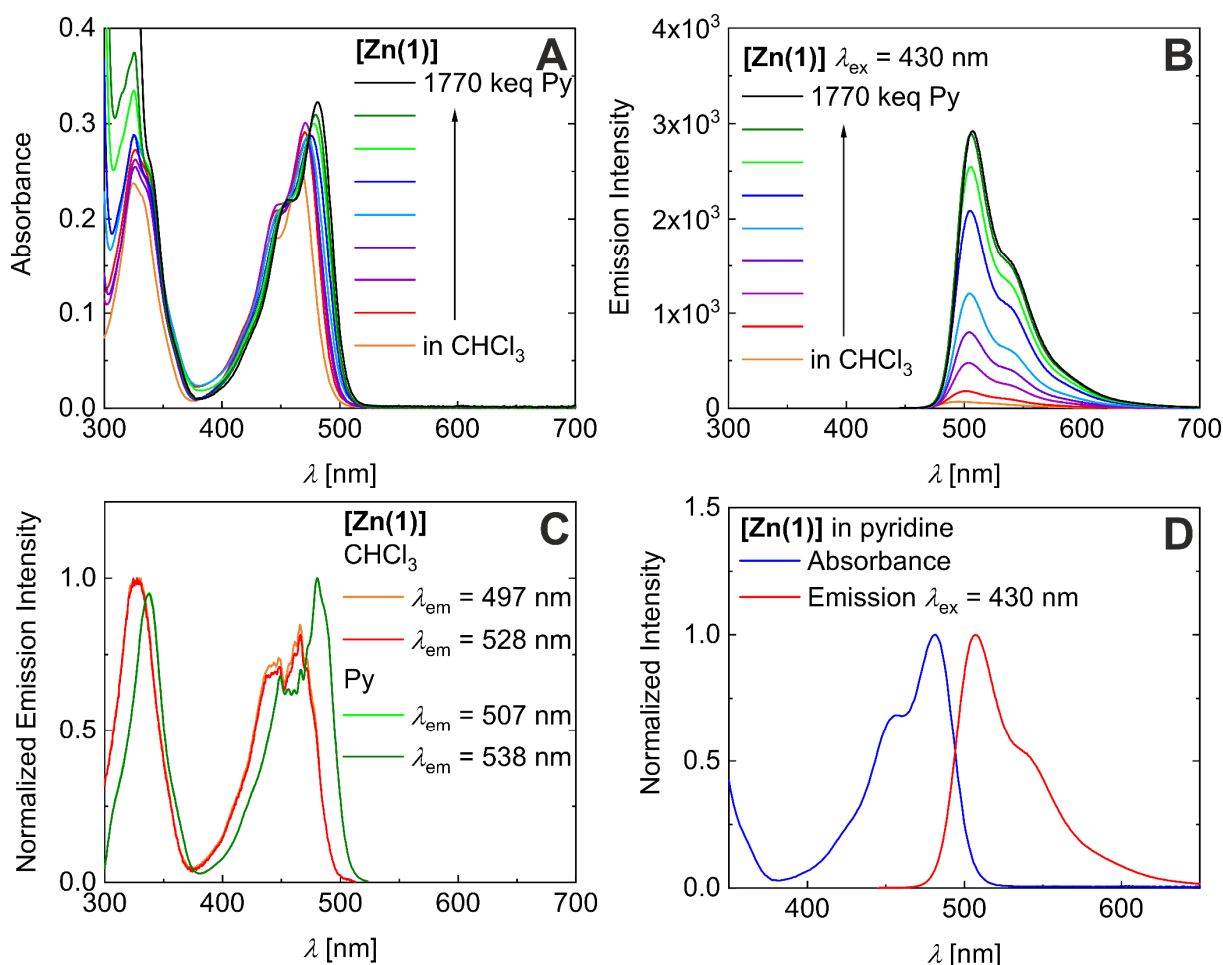


Figure 4: Chloroform/pyridine series: Absorption spectra of [Zn(1)] (A). Emission spectra of [Zn(1)] ($\lambda_{exc} = 430$ nm; B). Fluorescence excitation spectra of [Zn(1)] (C). Absorbance and emission spectra of [Zn(1)] in pyridine (D).

Shown in Figure 4A is a titration of equally concentrated solutions in CHCl₃ of [Zn(1)] with pyridine which yields a continuous red-shift by up to 15 nm (see Fig. S15A/B in the Supporting Information for titrations of [Zn(2)] and [Zn(3)], see Figure S19 for photographs), coupled to an intensity variation between $3.6 \times 10^4 \text{ cm}^{-1} \text{ M}^{-1} < \epsilon_M < 4.6 \times 10^4 \text{ cm}^{-1} \text{ M}^{-1}$. (see Fig. 4A). Fluorometric titration with pyridine shows a continuously enhanced emission for [Zn(1)] and [Zn(2)] which saturates only at the highest pyridine loads, which equals neat pyridine (see Fig. 4B and Figs. S15C in the Supporting Information). Fluorescence excitation spectra are indifferent to the observation wavelength and qualitatively map the absorption spectrum across the entire UV-vis range (red in Fig. 4C, Figure S15E/F in the Supporting Information). Thereby, the pyridine-dependent red shift in absorption is compensated by a parallel red shift in emission so that the Stokes-shift of $\Delta_{Stokes}E \approx 1100 \text{ cm}^{-1}$ is preserved. Likewise, the coincidence of absorption and fluorescence excitation spectra (deviation at $\lambda < 330$ nm is due to uncompensated absorption by excess pyridine) and the vibrational structure of the diagnostic

bands are maintained nearly constant (see Fig. 4D and Figure S15E in the Supporting Information).

Table 2: Medium dependence of the $S_0 \rightarrow S_1$ transition of **[Zn(1)]** from experiment and theoretical modelling (λ_{\max} [nm]; ϵ_{\max} [$10^4 \text{ M}^{-1} \text{ cm}^{-1}$]).

Medium	Experimental		Theoretical [a]		
	λ_{\max}	ϵ_{\max}	λ_{\max}	f_{osc}	Nature
chloroform	466	3.4	414 (487) [b]	0.784 [b]	H \rightarrow L (34%); H \rightarrow L (59%)
			433 [c]	1.244 [c]	H \rightarrow L+1 (44%); H \rightarrow L (39%)
MeCN	469	5.0	430 [d]	0.782 [d]	H \rightarrow L (92%)
MeCN/water (1:1)	467	4.4	426 [d]	0.791 [d]	H \rightarrow L (92%)
EtOH/MeOH	467	4.6	427 [d]	0.746 [d]	H \rightarrow L (90%)
THF	471	4.8	430 [d]	0.726 [d]	H \rightarrow L (90%)
pyridine	481	4.6	440 (512) [d]	0.673 [d]	H \rightarrow L (91%)

[a] On the TPSSh/TZVP level of theory; in parentheses: $S_0 \rightarrow S_1$ transition as predicted by MC-PDFT. [b] *hypothetic* monomeric CN 4 species. [c] dimeric species, **[Zn(1)]₂**. [d] monomeric CN 5 species with axial solvent.

DFT and wave-function theory analysis of the electronic structure. The nature of the leading optical transition of the zinc complexes has been addressed by means of (time-dependent) density-functional theory and wave function-based approaches. Complete active space self-consistent field, CASSCF, calculations were performed for the **[Zn(1)py]** complex, with an active space comprising the entire system of π -orbitals and their electrons, CAS(18,16). This represents the main set of orbitals responsible for the luminescence process. The lowest two singlet spin states (S_0 and S_1 states) and the lowest triplet spin state (T_1) wave functions have been optimized at the CASSCF level of theory, followed by a multiconfiguration pair-density functional theory approach (MC-PDFT) for treating dynamic correlation effects outside the chosen active space.³⁵⁻³⁷ The singlet state calculations were performed at the DFT optimized geometry (pertinent metrics in Tables S5/6, Supporting Information). Triplet spin state calculations were performed both at the optimized triplet geometry (*adiabatic excitation*) and at the singlet geometry (*vertical excitation*).

According to theory, the photophysics of **[Zn(1)X]** is invariably centered at the chelate ligand. Variation of the axial ligand, X, does not considerably affect the transition frequency, neither in experiment nor theory (see Table 2). MC-PDFT calculations on **[Zn(1)py]** predict the $S_0 \rightarrow S_1$

transition at 512 nm, while DFT predicts the same transition at 440 nm, both in fair agreement with the experimental value (481nm) (see Table 2). TD-DFT tends to systematically overestimate the energy of the leading Vis transition in the entire ligand-substitution series $[\text{Zn}(\mathbf{1})\text{X}]$ (X: H_2O ; ROH; pyridine; average deviation over five-coordinate complexes, $\Delta\nu = 1700 \text{ cm}^{-1}$), while MC-PDFT underestimates the transition energy for $[\text{Zn}(\mathbf{1})\text{py}]$. Nonetheless, our theoretical predictions match the overall pattern and intensities in the experimental data.

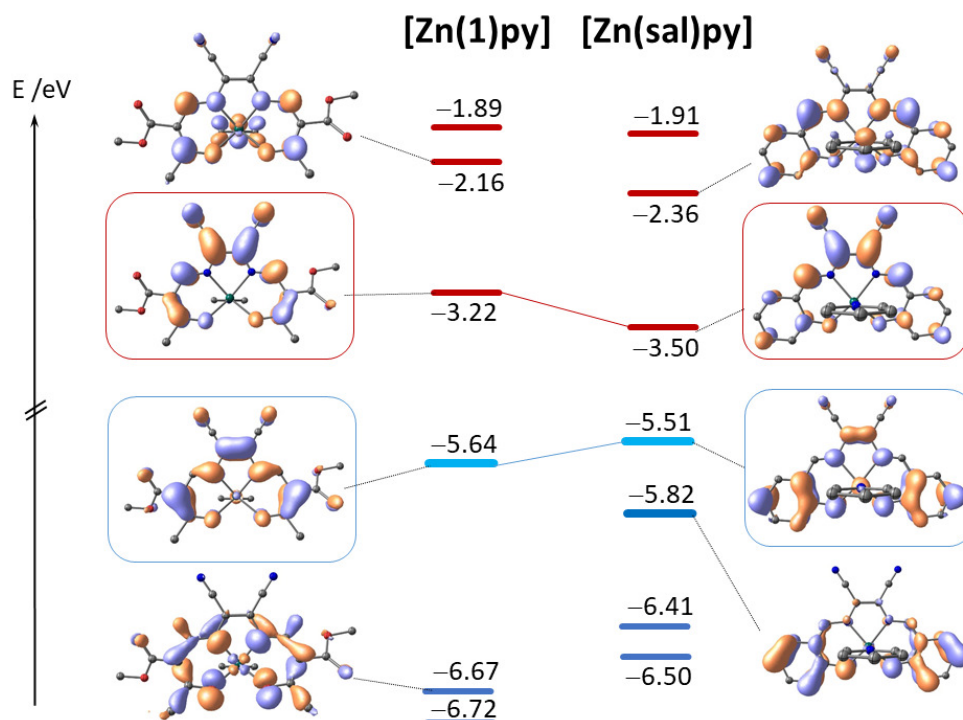


Figure 5: DFT-derived frontier MOs of five-coordinate zinc complexes ($[\text{Zn}(\text{sal})\text{py}]$ denotes an analogue derived from salicylic aldehyde; blue: occupied; red: virtual; HOMO and LUMO are highlighted).

Both at DFT and CASSCF level of theory, the HOMO and the LUMO are residing predominantly on the ligand (only at DFT level a very slight contribution of zinc d_{z^2} features in the HOMO), yet with distinctly different local weights. The HOMO subsumes contributions of the ligand π -backbone and the σ -bound donors, whereas the LUMO is more localized on the dinitrile moiety. As a consequence, optical excitation in $[\text{Zn}(\mathbf{1})\text{py}]$ leads to a charge shift toward the dinitrile site, rendering the excited state intra-ligand CT-like. Similar conclusions had been drawn previously in studies of the closely related congener $[\text{Zn}(\text{sal})\text{py}]$, which derives from an enole/imine ligand based on salicylic aldehyde. In keeping with conserved transition energies, the axial ligand X does not feature significantly in the frontier molecular orbitals, as exemplarily shown in Figure 5 for $[\text{Zn}(\mathbf{1})\text{py}]$ (data of the entire X-series is summarized in Fig. S20 in the Supporting Information). The optimized CASSCF natural orbitals for all states are similar to

each other and to the Kohn-Sham (KS) orbitals derived from DFT. They are reported in Figure S21 in the Supporting Information. As for the KS-orbitals, the CAS natural orbitals do not show any significant admixture from the axial pyridine ligand. This indifference is reflected by a small decrease in the transition energies upon axial coordination. MC-PDFT and TD-DFT predict a red-shift of $\sim 1000\text{ cm}^{-1}$ and $\sim 1400\text{ cm}^{-1}$, respectively, of the $S_0 \rightarrow S_1$ transition upon adding pyridine to the hypothetical four-coordinate model system $[\text{Zn}(\mathbf{1})]$, with no axial ligands. Even smaller red-shifts of $700 - 900\text{ cm}^{-1}$ are induced by the weaker Lewis bases (see Table 2). N_2O_3 coordination inherent to the dimeric complexes $[\text{Zn}(\mathbf{1})]_2$ likewise results in a red-shifted $S_0 \rightarrow S_1$ transition. It is predicted at $\approx 430\text{ nm}$, irrespective of dimer structure (see also Discussion below).

Overall, both methods yield consistent results concerning the nature and energies of electronic states and transitions in the five-coordinate species. It is not uncommon that KS-DFT and the subsequent TD-DFT are able to describe excited states (here, the S_1 state) with a reasonable level of accuracy. Neither a bi-configurational wave function nor spin-adaptation is enforced by the method often leading to unphysical eigensolutions to the Schrödinger equation (not spin eigenstates). Nonetheless, KS-DFT can predict accurate energies of electronic states, in virtue of the fact that DFT relies on correct local spin-densities and not to the detailed structure of the wave function. Given the widespread utilization of KS-DFT also beyond its inherent single-reference limits, this aspect is discussed in the following. A more detailed treatment is given in Reference ³⁷.

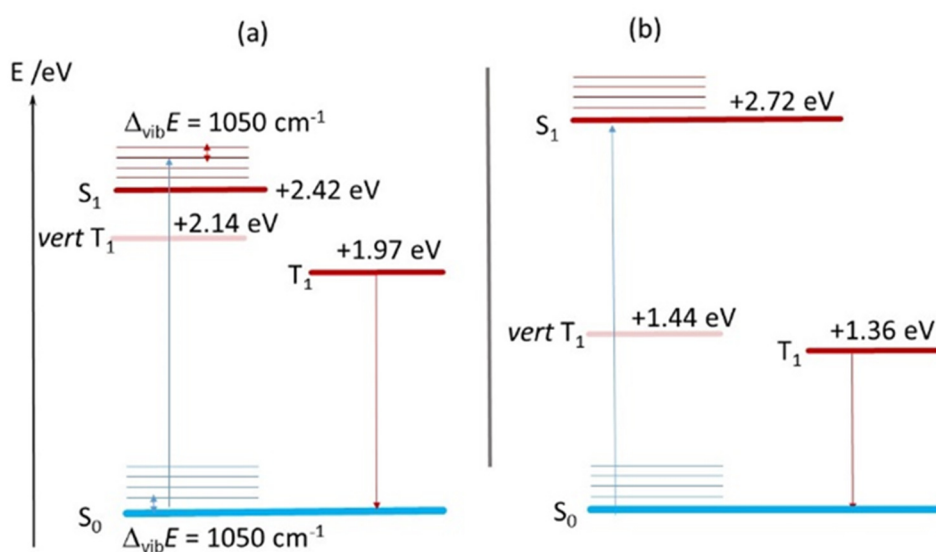


Figure 6: Jablonski diagrams of $[\text{Zn}(\mathbf{1})\text{py}]$; (a) data from MC-PDFT (ANO-RCC-VDZP); vibrational splitting $\Delta_{\text{vib}} E$ from experiment; (b) data from KS-DFT and TD-DFT ($S_0 \rightarrow S_1$) (TPSSH/TZVP).

Inspection of the CAS wave functions of the S_0 and S_1 states of **[Zn(1)py]** clearly corroborates the ILCT nature of the $S_0 \rightarrow S_1$ transition involving a HOMO to LUMO single excitation, adding value to our DFT computations. Both S_0 and S_1 wave functions are predominantly single-reference. The leading contribution to the S_0 state (79% weight) is the closed-shell configuration (single-reference) found also by KS-DFT for the same state. In the lowest excited singlet state an electronic configuration corresponding to the HOMO-to-LUMO one-electron excitation dominates with a weight of 73%. It is important to point out here that while the S_1 wave function is predominantly single-configurational (in terms of spin-adapted configuration state functions, CSFs), it is inherently bi-configurational. That is, the two unpaired electrons residing in the HOMO and the LUMO are precisely coupled to a singlet spin state, $(a_H^\alpha)^\dagger (a_L^\beta)^\dagger - (a_H^\beta)^\dagger (a_L^\alpha)^\dagger$ (here H and L refer to HOMO and LUMO respectively). Thus, while both states can be considered single-reference, the S_1 excited state requires a more careful theoretical treatment, to ensure the correct spin-symmetry and to correctly capture electron correlation effects. These aspects are explicitly considered in the CASSCF/MCPDFT methodology, due to the multi-configurational character of the method, and their formulation in a spin-adapted basis (via the graphical unitary group approach, GUGA, algorithm).³⁸⁻⁴¹

The MC-PDFT-derived vertical and adiabatic singlet-triplet gaps of **[Zn(1)py]**, $\Delta_{S/T}E$, are reported in the Jablonski diagram in Figure 6a; they are given in terms of the $S_0 \rightarrow T_1$ transition energies at the relaxed geometry of S_0 (vertical excitation) and T_1 (adiabatic excitation). Closely lying excited singlet and triplet states are generally taken as a basic requirement of rapid and efficient intersystem crossing, which would competitively limit the fluorescence quantum yield. A vertical gap of $\Delta_{S/T}E = 2.14$ eV places the triplet state only 0.28 eV below the computed energy of the Franck-Condon state, that is, relative to S_1 in an excited vibronic state. In the relaxed geometry of T_1 the somewhat smaller adiabatic gap of $\Delta_{S/T}E = 1.97$ eV arises, concomitant with a slightly widening gap between S_1 and T_1 . Nevertheless, these calculations indicate an efficient ISC to the triplet state as the reducing factor of the fluorescence quantum yield. In the related zinc(II) system **[ZnTPP]** (TPP: tetraphenylporphine), fluorescence and phosphorescence have been recorded at 600 nm and ca. 780 nm (77 K), respectively, giving an upper limit for the S_1 - T_1 gap of 0.48 eV.^{42,43} In keeping with the narrow S_1 - T_1 gap, a large triplet quantum yield of 0.88 was observed.

For comparison we plot in Figure 6b the data that derive from KS-DFT and TD-DFT. These are in qualitative agreement with the MC-PDFT values, but indicate larger S_1 - T_1 splitting. We believe that a gap of 1.3 eV is hardly in agreement with efficient intersystem crossing.

In agreement with experiment the Vis transition of **[Zn(sal)py]** ($\lambda_{\text{DFT}} = 565 \text{ nm}$; $\lambda_{\text{exp}} = 560 \text{ nm}$ ³⁴) is predicted at significantly smaller energy than in **[Zn(1)py]** ($\lambda_{\text{DFT}} = 440 \text{ nm}$; $\lambda_{\text{exp}} = 481 \text{ nm}$). This tendency is maintained in the (hypothetical, see discussion) planar CN 4 species and is reflected by the shrinking HOMO-LUMO gap of **[Zn(sal)py]**. The presence of additional phenolate-borne π -donor states in the latter gives rise to further Vis transitions at higher energy that are clearly absent in **[Zn(1)py]**. Nevertheless, both complex families share similar optoelectronic properties, in a qualitative sense; that is, conserved nature and intensity of the leading excitation and significant CT-state emission with minor Stokes-shift. As is detailed below, however, they differ substantially in quantitative terms, with respect to their affinity for Lewis bases.

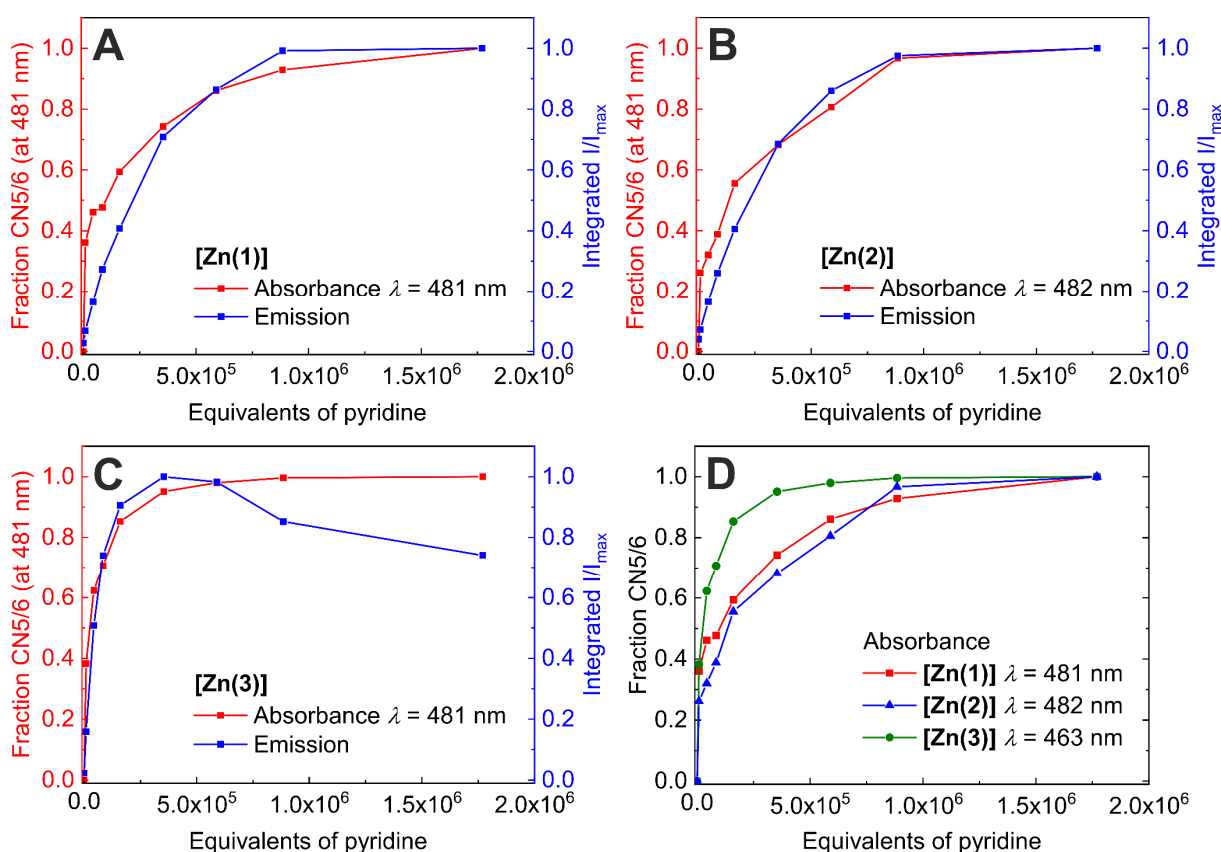


Figure 7: Fraction $\gamma(\text{CN5/6})$ of **[Zn(1–3)]** and integrated emission intensity I/I_{max} vs equivalents of pyridine (A: **[Zn(1)]**; B: **[Zn(2)]**; C: **[Zn(3)]**). $\text{Fraction}_{\text{CN5/6}} = (A - A_0)/(A_{\text{max}} - A_0)$ with A: Absorbance at $\lambda = 481 \text{ nm}$, A_0 : Absorbance in neat CHCl_3 at $\lambda = 481 \text{ nm}$, and A_{max} : Absorbance in neat pyridine at $\lambda = 481 \text{ nm}$. D: Comparison of fractions $\gamma(\text{CN5/6})$ of **[Zn(1–3)]**.

Quenched Lewis-acidity and Emission Properties. To discuss the optical phenomena in more quantitative terms, the concentration dependence in the spectroscopic titrations with pyridine has been analyzed. Plots of the integrated emission intensity and the differential changes of

absorptivity (abstracted in terms of speciation; that is, reporting the fraction CN 5/6) as a function of pyridine concentration are shown in Figure 7.

As a first result, the above Lewis base hypothesis is corroborated by the higher affinity for pyridine expressed by **[Zn(3)]**. Bearing electron withdrawing CF₃ substituents, **[Zn(3)]** is set apart quantitatively of the other zinc complexes in this study. With respect to **[Zn(1/2)]** the absorbance and emission bands of **[Zn(3)]** are all blue-shifted by approximately 15 nm (see Figure S15B/D/F in the Supporting Information). These shifts to larger energy reflect the stabilized Schiff-base borne donor levels (see MO diagram in Fig. S22 in the Supporting Information). They further support the ILCT character of the underlying transitions. As a more diagnostic effect of enhanced Lewis acidity, the pyridine-dependent spectral evolution of **[Zn(3)]** saturates above approximately 590 keq, whereas much larger amounts are necessary with **[Zn(1/2)]** (see Figure 7D). Similarly, enhanced affinity for Lewis bases has been recently reported for nickel(II) complexes of CF₃-decorated ligands.⁴⁴ The experimentally observed order of affinity is well captured by DFT model calculations. Reaction energies of the Lewis acid-base association of pyridine with (*hypothetical*) planar monomeric zinc complexes (CN 4) are all highly negative, indicating a significant thermodynamic driving force even if unfavorable entropies are considered (eq 1-3). Association is predicted to be more exothermic in **[Zn(3)]** than in **[Zn(1)]** by ca. 8 kJ mol⁻¹.



It is of particular importance for the following argumentation to note that computed Lewis base affinities of **[Zn(1)]** and **[Zn(3)]** are *larger* than that of the known system **[Zn(sal)]**, $\Delta\Delta_{\text{LBE}} = \Delta_{\text{LBE}}(\mathbf{[Zn(1)]}) - \Delta_{\text{LBE}}(\mathbf{[Zn(sal)]}) \approx -9 \text{ kJ mol}^{-1}$ (for X = MeCN, pyridine, THF). That is, according to the chemistry indicated in eq 1-3 we must expect **[Zn(1)]** and **[Zn(3)]** to be more potent Lewis acids than **[Zn(sal)]**.

In clear contrast with this statement is the drastically smaller affinity of **[Zn(1)]** and **[Zn(3)]** toward axial ligation observed in experiment. Whereas ligation of mononuclear **[Zn(sal)]** and derivatives thereof has been reported to saturate already at slightly super-stoichiometric doses of pyridine (2-10 eq),¹⁹ *all* complexes **[Zn(1-3)]** in the present study require pyridine doses that are higher by a factor of $\gg 10^4$! Therefore, the central premises of our analysis must be called into question. As we discuss in the following, speciation in solution of **[Zn(sal)]** and **[Zn(1-3)]**

is not identical, as it has been silently assumed. There is general agreement that four-coordinate planar monomeric zinc complexes (CN 4) will add one or two additional axial ligands to saturate the Lewis-acidic center as is implied by eq 1-3. In the absence of potent donors self-complementary stacking of such zinc(II) units occurs to yield dimers with a Zn₂O₂ core.¹⁸⁻²⁴ Crystal structures including stacked dimers with a Zn₂O₂ core have been reported for several derivatives of the *salophen* type and dimers have been generally suggested as the dominant species in solution under non-coordinating conditions. Such dimeric structures are generally found to have reduced fluorescence quantum yields, whereas the on-switch of fluorescence in the presence of Lewis bases has been interpreted in terms of base-induced de-aggregation. Stacking into dimers in non-coordinated media was likewise suggested to reduce fluorescence in *malnant* derivatives with maleodinitrile backbones.²¹ The ligation equilibria of **[Zn(sal)]** could be convincingly treated in terms of a theoretical three-component model, yielding very large equilibrium constants for both, the dimerization step and the ligation of the sub-coordinate monomer (eq 4-5).^{45,46} Alluding to this model, speciation successively moves from one *single* non-fluorescent species, dimeric (**[Zn(sal)]₂**), to one *single* fluorescent species, monomeric (**[Zn(sal)py]**) (CN 5), with only vanishing contributions of four-coordinate **[Zn(sal)]**.



Different from **[Zn(sal)]**, there is no such simple correlation for **[Zn(1-3)]**. Closer inspection of the low-concentration sections of the plots in Figure 7A/B reveals that the concentration dependence of the absorption and the emission is not identical. In particular, the plot in Figure 8 of the normalized integrated emission intensity vs the CN 5/6 molar fraction of **[Zn(1-3)]** reflects pyridine-dependent transformations among (at least) four different species, from which (at least) the first two are non-emissive. The close similarity of **[Zn(1-3)]** in the plot of Figure 8 points to an overall conserved phenomenology among all three compounds.

The first chemical step connects two non-fluorescent species; notably almost one third of the overall absorption change is involved in this step, whereas there is hardly any increase in emission. In accordance to previous findings of non-emissive stacked dimers,^{19,21} it appears reasonable to ascribe the lack of fluorescence to the dimeric or oligomeric nature of *both* non-fluorescent species. This assignment is supported by means of dynamic light scattering (DLS) in MeCN. Solutions in CHCl₃ are expected to behave similarly, but could not be studied by DLS due to limited solubility. Non-emitting, filtered solutions of **[Zn(1)]** in neat MeCN ($3 \cdot 10^{-4} \text{ M} < c < 1 \cdot 10^{-3} \text{ M}$) all contain nanoparticles with broad particle size distributions ($d_{\text{max}} \approx 120$

nm) (see Figure S23 in the Supporting Information). Mean particle size scales inversely with the concentration of the complex. The presence of pyridine drastically reduces the amount of nanoparticles, whereas in neat pyridine, DLS gives no response (see Figure S24 in the SI). In keeping with the destacking of the dimers/oligomers in the presence of pyridine, and concomitant formation of fluorescent monomeric **[Zn(1–3)py]**, emission enhancement and absorption changes during the spectroscopic titrations are proportional, once a threshold concentration is passed (rising branch in Figure 8). For **[Zn(3)]** emission decreases in presence of very high doses of pyridine. We associate this unique behavior with the enhanced Lewis-acidity of **[Zn(3)]** which allows for the formation of six-coordinate species as seen also in the solid state molecular structure of **[Zn(3)(H₂O)(EtOH)]** (Figure 1). While we cannot judge with absolute certainty, the decreased emission efficiency of six-coordinate species may be associated with the higher flexibility of the octahedral coordination sphere due to the intrinsically longer Zn-N/O bonds leading to a higher rate of non-radiative decays. The coordination of the second pyridine might also result in a decreased singlet-triplet gap leading to emission quenching, which was found indeed in DFT calculations (see Figure S25 in the Supporting Information).

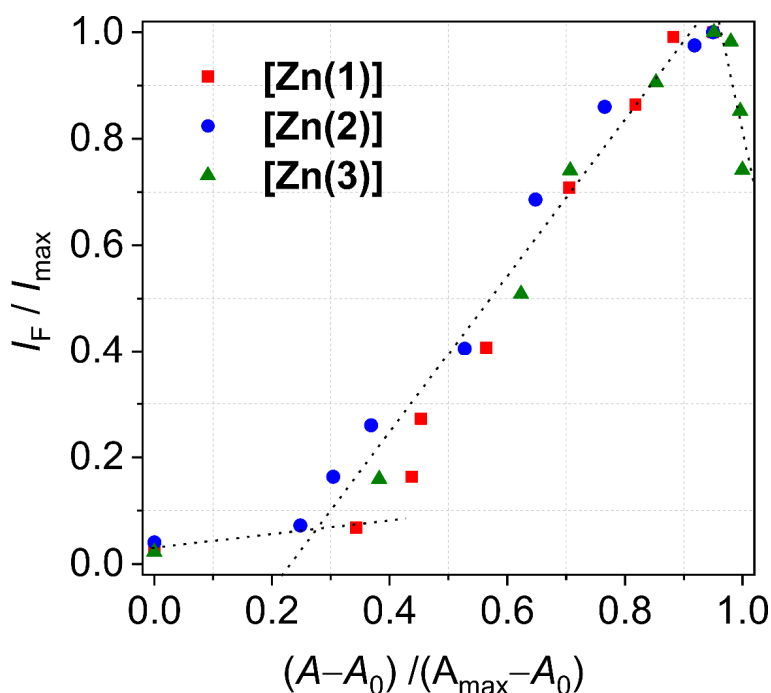


Figure 8: Correlation of pyridine-dependent absorption and emission changes. Plot of the normalized integrated emission intensity vs the CN5/6 molar fraction of **[Zn(1–3)]**. $\text{Fraction}_{\text{CN5/6}} = (A - A_0)/(A_{\text{max}} - A_0)$ with A: Absorbance at $\lambda = 481$ nm, A_0 : Absorbance in neat CHCl₃ at $\lambda = 481$ nm, and A_{max} : Absorbance in neat pyridine at $\lambda = 481$ nm. $\text{Fraction}_{5/6}$ of **[Zn(1/2)]** scaled by a factor of 0.95.

Kleij *et al.* had previously observed a diminished sensitivity toward Lewis bases of some dinuclear zinc(II) complexes.⁴⁷ Akin to our observations with **[Zn(1-3)]**, $> 10^5$ molar equivalents of pyridine were necessary to drive the destacking. The authors associated the markedly reduced sensitivity with strong stacking into large oligomers. Based on the observation of nanoparticles in dilute solutions via DLS, we likewise associate the *seemingly* reduced Lewis-acidity of **[Zn(1-3)]** with the formation of stable oligomers of unusual stability. That is, the strong Lewis-acidity of **[Zn(1-3)]** which is indicated by DFT calculations must be overridden by an additional ligand-borne effect not accessible to mononuclear *salophen* derivatives. Indeed, a DFT structure search served to identify plausible dimer structures of high stability for **[Zn(1)]₂**. For sake of comparison, stacked structures of **[Zn(sal)]₂** were studied on the same level of theory. The computed metrics of the Zn₂O₂ core of **[Zn(sal)]₂** shown in Figure 9A are similar to the reported crystal structures of *salophen*-type complexes.⁴⁵ Details of all optimized structures are summarized in Table S7 in the SI. In particular, the short axial Zn-O distance of 2.15 Å indicates tight binding within the dimers; electronic reaction energies of the dimerization equilibrium amount to -16 kJ mol⁻¹. Similar structures could be extracted from optimization of Zn₂O₂-bound dimers of **[Zn(1)]**, with similar energies of dimerization.

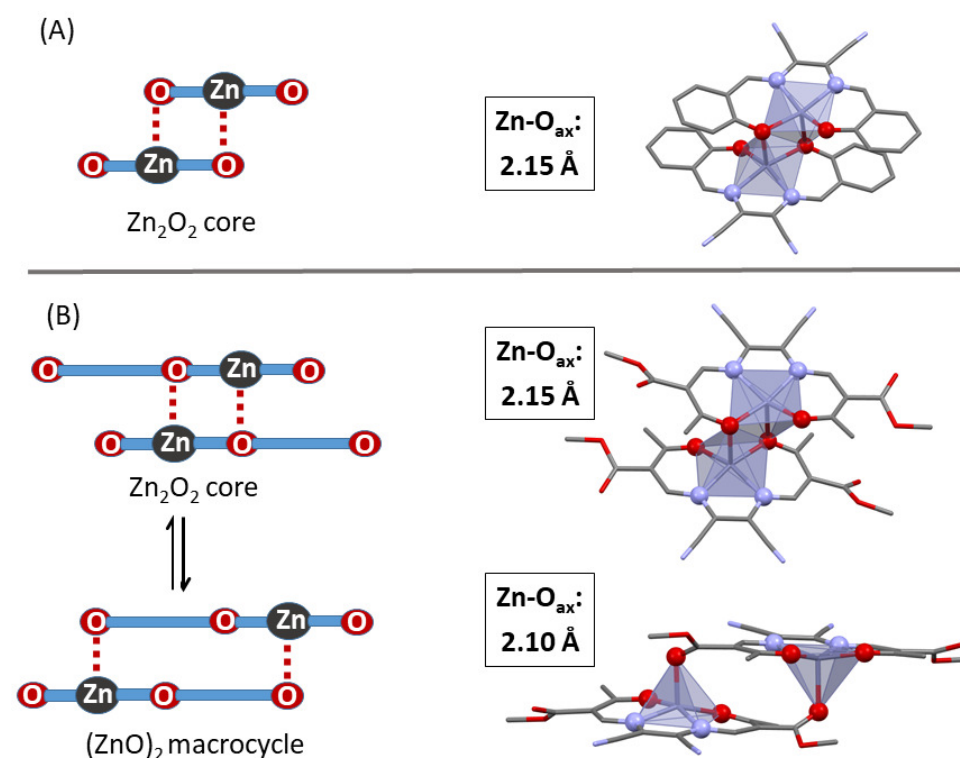


Figure 9: Dimer speciation of **[Zn(sal)]₂** (left) and its DFT-optimized structures with pertinent metrics (right). (B) Dimer speciation of **[Zn(1-3)]₂** (left) and its DFT-optimized structures with pertinent metrics (right).

Most importantly, however, these Zn_2O_2 -core dimers are not the minimum structures in the case of **[Zn(1–3)]**. By contrast, DFT calculations identify a completely different stacking motif at significantly lower energy, as shown in Figure 9B. In these $(ZnO)_2$ macrocycles, ligand-appended carbonyls saturate the N_2O_3 coordination sphere of zinc to establish fully relaxed square-pyramidal environments on both centers. A somewhat related constellation has been observed by Weber *et al.* in the solid-state structure of some iron(II) complexes of this general ligand type.⁴⁸ In the cited system, the axially arranged carbonyls rather assist coordination, given the long Fe-O distance of 2.70 Å. In **[Zn(1–3)]**, tight axial binding is indicated by short Zn-O_{ax} bond lengths of 2.10 Å, which are even shorter than in the reported and computed dimers of **[Zn(sal)]**. Favorable dispersive interactions between the chelate planes of the stacked complexes support the laterally shifted dimer structure. Both aspects sum up in a strongly increased stability compared to the Zn_2O_2 -core dimer. Computed energies of dimerization are in favor of the macrocyclic $(ZnO)_2$ dimer by -20 kJ mol^{-1} .

5.3 Conclusions

The family of planar zinc(II) complex platforms, **[Zn(1–3)]**, based on planar-directing tetradentate Schiff base-like ligands with appended nitrile groups supports *turn-on* fluorescence behavior, sensitive to axial ligation with potent Lewis bases. While the overall optical spectroscopic features of **[Zn(1–3)X]** comply with the established stacking/destacking hypothesis of zinc(II)-based fluorescence sensors in qualitative terms, a massive deviation is noticed in terms of a quantitative treatment. While only 2-3 equivalents of pyridine were reported to switch-on fluorescence in the closely related congener **[Zn(sal)]**, a large excess of $\gg 10^4$ equivalents is required in the case of **[Zn(1–3)]**. This enormous difference in sensitivity cannot be traced to a qualitative divergence in Lewis acidity of **[Zn(1–3)]** and **[Zn(sal)]**; in fact, KS-DFT calculations suggested an even stronger Lewis-acidity of **[Zn(1–3)]**. The higher intrinsic acidity of **[Zn(1–3)]** is quenched through formation of stable aggregates via axial Zn-O bonds. Qualitatively different from the established picture of a Zn_2O_2 core which prevails for **[Zn(sal)]** derivatives, KS-DFT calculations of dimeric species of **[Zn(1)]** support an alternative, very stable macrocyclic stacking motif which involves ligand-appended, remote carbonyl moieties. As the stability of the non-emissive dimers obviously controls the sensitivity of the sensor material, tuning through introduction of sterically demanding substituents might enable the design of sensor materials with consciously adjustable sensitivity areas.

5.4 Experimental Section

Methoxymethylenemethylacetoacetate, ethoxymethyleneethylaceto-acetate, ethoxymethylene-1,1,1-trifluoroacetylacetone, and **H₂(2)** were synthesised as described in literature.^{29,49,50} Diaminomaleonitril (98%, Sigma Aldrich), *p*-toluenesulfonic acid (98%, Merck), and Zn(OAc)₂·2 H₂O (97+%, Alfa Aesar) were used without further purification. Methanol, ethanol, THF, and pyridine were of analytical grade and used without further purification. Chloroform and acetonitrile were extracted with aqueous saturated NaHCO₃ solution and dried over CaCl₂. NMR spectra were recorded with a 500 MHz *Avance III HD* NMR spectrometer from Bruker. CHN analyses were measured with an Unicube from Elementar Analysen Systeme. The samples were prepared in a tin boat, sulfanilamide was used as standard and the samples measured at least twice. Mass spectra were recorded with a Finnigan MAT 8500 with a data system MASPEC II. IR spectra of the solid samples were recorded on a *Perkin Elmer Spectrum* 100 FT-IR spectrometer.

X-ray Structure Analysis. The X-ray analysis were performed with a Stoe StadiVari diffractometer using graphite-monochromated MoK_α radiation. The data were corrected for Lorentz and polarization effects. The structures were solved by direct methods (SIR-97)⁵¹ and refined by full-matrix least-square techniques against Fo²-Fc² (SHELXL-97).⁵² All hydrogen atoms were calculated in idealized positions with fixed displacement parameters. ORTEP-III was used for the structure representation,^{53,54} Mercury-3.10 to illustrate molecule packing.⁵⁵ Deposition Numbers 2086160 (for [**Zn(1)(MeOH)**]·MeOH), 2086684 (for [**Zn(1)(py)**]), 2086163 (for [**Zn(1)(H₂O)**]), 2086161 (for [**Zn(2)(H₂O)**]₂·H₂O), 2086162 (for [**Zn(3)(H₂O)(EtOH)**]) contain the supplementary crystallographic data for this paper. These data are provided free of charge by the joint Cambridge Crystallographic Data Center and Fachinformationszentrum Karlsruhe Access Structures service.

X-ray Powder Diffraction. Powder diffractograms were recorded with a STOE StadiP diffractometer using Cu K_α1 radiation with a Ge monochromator, and a Mythen 1K Stripdetector in transmission geometry.

Optical Measurements. Absorbance spectra were performed on a Cary 60 UV-vis spectrometer from Agilent Technologies. Steady-state PL measurements were performed on a FP-8600 fluorescence spectrometer from JASCO that is equipped with a Xe lamp as excitation source. Time-resolved measurements were performed on a FluoTime 300 fluorospectrometer from PicoQuant, using a 405 nm diode laser for excitation (Coherent COMPASS 405-50 CW), which was controlled by the PDL 820 PicoQuant laser driver. Quantum yields were determined at

room temperature using an integrating sphere and a Xe lamp as excitation source. All measurements were performed in quartz cells with a 1 cm lightpath from Hellma.

H₂(1). Diaminomaleonitrile (1.50 g, 13.88 mmol, 1 eq), methoxymethylene-methylacetoacetate (4.83 g, 30.53 mmol, 2.2 eq), and *p*-toluenesulfonic acid (0.13 g, 0.69 mmol, 0.05 eq) were dissolved in 37 mL MeOH. The red solution was heated under reflux for 5 h. After cooling at room temperature overnight the orange precipitate was filtered off and washed with MeOH. Yield: 2.18 g (44 %). ¹H NMR (500 MHz, DMSO, 25°C): δ = 8.11 (s, 2 H, NC–H); 3.74 (s, 6 H, –CH₃); 2.44 (s, 6 H, –CH₃) ppm. MS (DEI(+), 70 eV): m/z = 360 (M⁺, 36%). C₁₆H₁₆N₄O₆ (360.33 g/mol) found (calculated): C 53.18 (53.33); H 4.33 (4.48); N 15.31 (15.55)%. IR: $\tilde{\nu}$ = 2954 (s, C–H), 2228 (s, C≡N), 1719 (s, C=O), 1585 (s, C=O) cm⁻¹.

[Zn(1)(H₂O)(MeOH)]. H₂(1) (0.40 g, 1.11 mmol, 1 eq) and zinc(II) acetate dihydrate (0.32 g, 1.44 mmol, 1.3 eq) were dissolved in 40 mL MeOH. The solution was heated to reflux for 2 h. After cooling to room temperature and addition of 20 mL H₂O, the red crystalline precipitate was filtered off and washed with MeOH. Yield: 0.37 g (70%). ¹H NMR (500 MHz, DMSO, 25°C): δ = 8.51 (s, 2 H, NC–H); 3.69 (s, 6 H, –CH₃); 2.49 (s, 6 H, –CH₃) ppm. MS (DEI(+), 70 eV): m/z = 422 (M⁺, 58%). C₁₇H₂₀N₄O₈Zn (473.75 g/mol) found (calculated): C 42.97 (43.10); H 4.11 (4.26); N 11.98 (11.83)%. IR: $\tilde{\nu}$ = 3394 (b, O–H), 2954 (s, C–H), 2217 (s, C≡N), 1677 (s, C=O), 1574 (s, C=O) cm⁻¹.

[Zn(2)(H₂O)_{1.5}]. H₂(2) (0.40 g, 1.03 mmol, 1 eq) and zinc(II) acetate dihydrate (0.29 g, 1.34 mmol, 1.3 eq) were dissolved in 40 mL MeOH. The solution was heated to reflux for 2 h. After cooling to room temperature and addition of 20 mL H₂O, the orange precipitate was filtered off and washed with MeOH. Yield: 0.23 g (47%). ¹H NMR (500 MHz, DMSO, 25°C): δ = 8.53 (s, 2 H, NC–H); 4.16 (q, ³J(CH₂–CH₃) = 7.0 Hz, 4 H, –CH₂); 2.49 (s, 6 H, –CH₃); 1.25 (t, ³J(CH₂–CH₃) = 7.0 Hz, 6 H, –CH₃) ppm. MS (DEI(+), 70 eV): m/z = 450 (M⁺, 100%). C₁₈H₂₁N₄O_{7.5}Zn (478.77 g/mol) found (calculated): C 45.37 (45.16); H 4.24 (4.42); N 11.68 (11.70)%. IR: $\tilde{\nu}$ = 3311 (b, O–H), 2987 (s, C–H), 2217 (s, C≡N), 1674 (s, C=O), 1583 (s, C=O) cm⁻¹.

[Zn(3)(H₂O)(EtOH)]. Diaminomaleonitrile (0.05 g, 0.46 mmol, 1 eq), ethoxymethylene-1,1,1-trifluoroacetylacetone (0.21 g, 1.02 mmol, 2.2 eq), and zinc(II) acetate dihydrate (0.13 g, 0.60 mmol, 1.3 eq) were dissolved in 2.5 mL EtOH. The solution was heated to reflux for 2 h. After cooling to room temperature, 1 mL H₂O was added. After storing in the fridge overnight, the red precipitate was filtered off and washed with EtOH. Yield: 0.17 g (66%). ¹H NMR (500 MHz, DMSO, 25°C): δ = 8.35 (s, 2 H, NC–H); 2.54 (s, 6 H, –CH₃) ppm. MS (DEI(+), 70 eV):

$m/z = 498$ (M^+ , 30%), 429 ($M^+ - CF_3$, 53%). $C_{18}H_{16}F_6N_4O_6Zn$ (563.72 g/mol) found (calculated): C 38.32 (38.35); H 2.84 (2.86); N 9.98 (9.94)%. IR: $\tilde{\nu} = 3511$ (b, O–H), 3355 (b, O–H), 2987 (s, C–H), 2224 (s, C \equiv N), 1597 (s, C=O), 1538 (s, C=O), 1116 (s, C–F) cm^{-1} .

Computational Details

This section describes the most relevant details of DFT and CASSCF model calculations.

(TD-)DFT. Electronic structure calculations on the complexes have been performed through density-functional theory (DFT) methods using the ORCA program package.⁵⁶ For all optimizations triple- ξ -valence TZVP basis sets⁵⁷ were used with the generalized gradient approximated functional BP86.⁵⁸ Optimized complexes were verified as stationary points through the absence of imaginary modes in numerical frequency calculations. Molecular orbitals and electronic properties were extracted from single-point calculations in the optimized positions with the global hybrid functional TPSSh⁵⁹ and triple- ξ -valence TZVP basis sets. Grimme's third generation D3 correction of dispersion was used;^{60,61} medium effects were approximated in a dielectric continuum approach (COSMO), parameterized for MeCN.⁶² Coordinates of the computed structures are assembled in the SI file COORDINATES, frontier orbital landscapes are shown in Figures S19-S21/22 in the SI. For each complex the 70-80 lowest optical electronic transitions were assessed with ORCA implemented TD-DFT methods within the Tamm-Dancoff approximation.

CASSCF/MC-PDFT. Considering the marginal role of the closed-shell Zn(II) metal center in terms of correlation effect, as discussed above, the active space chosen for all CASSCF calculations contains MOs predominantly with character of the π -system of the tetra-dentate ligand, CAS(18,16), where the 16 orbitals are linear combinations of the 16 2p AOs on the conjugated system of the ligand. State-averaged calculations with 2 roots were performed for the singlet spin system (S_0 and S_1), while only the ground state for the triplet spin symmetry, T_1 .

MC-PDFT has been largely demonstrated a good and cheap alternative to CASPT2 and it has been utilized as main method of choice in this investigation to recover dynamic correlation outside the active space. Within MC-PDFT the tPBE translated functional has been chosen, that in our experience outperforms the other translated functional available to date.

A basis set of generally contracted atomic natural orbital (ANO-RCC) type has been used for all atoms, obtained from the C,N,O(14s,9p,4d), H(8s,4p) and Zn(21s,15p,10d,6f) primitive functions, contracted to C,N,O(3s,2p,1d), H(2s,1p), Zn(5s,4p,2d,1f) functions, giving a basis

set of split-valence double- ζ plus polarization quality (VDZP). This choice of basis set leads to a total of 577 basis functions for the [Zn(1)py] model system. Intermediate calculations in a minimal basis set (MB), with contraction scheme C,N,O(2s,1p), H(1s), Zn(4s,3p,1d), have been performed as aid in the choice of the active space for all model system and spin states. The basis set has been subsequently expanded to the VDZP and the MB optimized orbitals augmented and used as starting orbitals for the VDZP CASSCF(18,16) optimization. C1 point group symmetry has been utilized in line with the preceding DFT method. The evaluation of the electron repulsion integrals has been greatly simplified by means of the resolution-of-identity Cholesky decomposition technique, with a decomposition threshold of 10^{-4} a.u.

5.5 Notes and References

Acknowledgements

Financial supports from the Fonds der Chemischen Industrie (Kekulé-Stipendium), MINT-Lehramt Plus, German Research foundation (SFB840; project A10), the BayNAT program, the Max-Planck Society, and the University of Bayreuth are gratefully acknowledged. We thank Dr. Ulrike Lacher for the measurement of the mass spectra, Florian Puchtler for the measurement of the PXRD patterns. We thank Prof. Dr. Hans-Werner Schmidt for access to the fluorospectrometer for the steady-state measurements, Prof. Dr. Roland Marschall and Dr. Jana Timm for access to the FluoTime 300 fluorospectrometer for quantum yield determinations, and Armin Schuhmacher for the technical support on the local cluster used for the CASSCF/MC-PDFT simulations. Open Access funding enabled and organized by Project DEAL.

Keywords: CASSCF • Dimerization • Fluorescence • Schiff base • Zinc

References

- (1) Coronado, E. Molecular magnetism: from chemical design to spin control in molecules, materials and devices. *Nat. Rev. Mater.* **2020**, 5 (2), 87–104. DOI: 10.1038/s41578-019-0146-8.
- (2) Sieklucka, B.; Pinkowicz, D. *Molecular Magnetic Materials*; Wiley-VCH Verlag GmbH & Co. KGaA, **2017**. DOI: 10.1002/9783527694228.
- (3) Halcrow, M. A. *Spin-Crossover Materials*; John Wiley & Sons Ltd, **2013**. DOI: 10.1002/9781118519301.
- (4) Thies, S.; Sell, H.; Schütt, C.; Bornholdt, C.; Näther, C.; Tuzek, F.; Herges, R. Light-induced spin change by photodissociable external ligands: a new principle for magnetic switching of molecules. *J. Am. Chem. Soc.* **2011**, 133 (40), 16243–16250. DOI: 10.1021/ja206812f.

- (5) Dommaschk, M.; Schütt, C.; Venkataramani, S.; Jana, U.; Näther, C.; Sönnichsen, F. D.; Herges, R. Rational design of a room temperature molecular spin switch. The light-driven coordination induced spin state switch (LD-CISSS) approach. *Dalton Trans.* **2014**, 43 (46), 17395–17405. DOI: 10.1039/c4dt03048f.
- (6) Lochenie, C.; Schötz, K.; Panzer, F.; Kurz, H.; Maier, B.; Puchtler, F.; Agarwal, S.; Köhler, A.; Weber, B. Spin-Crossover Iron(II) Coordination Polymer with Fluorescent Properties: Correlation between Emission Properties and Spin State. *J. Am. Chem. Soc.* **2018**, 140 (2), 700–709. DOI: 10.1021/jacs.7b10571.
- (7) Senthil Kumar, K.; Ruben, M. Emerging trends in spin crossover (SCO) based functional materials and devices. *Coord. Chem. Rev.* **2017**, 346, 176–205. DOI: 10.1016/j.ccr.2017.03.024.
- (8) Lochenie, C.; Wagner, K. G.; Karg, M.; Weber, B. Modulation of the ligand-based fluorescence of 3d metal complexes upon spin state change. *J. Mater. Chem. C* **2015**, 3 (30), 7925–7935. DOI: 10.1039/C5TC00837A.
- (9) Förster, C.; Heinze, K. Photophysics and photochemistry with Earth-abundant metals - fundamentals and concepts. *Chem. Soc. Rev.* **2020**, 49 (4), 1057–1070. DOI: 10.1039/c9cs00573k.
- (10) Wenger, O. S. Photoactive Complexes with Earth-Abundant Metals. *J. Am. Chem. Soc.* **2018**, 140 (42), 13522–13533. DOI: 10.1021/jacs.8b08822.
- (11) Wenger, O. S. Is Iron the New Ruthenium? *Chem. Eur. J.* **2019**, 25 (24), 6043–6052. DOI: 10.1002/chem.201806148.
- (12) Zhang, Y.; Petersen, J. L.; Milsmann, C. A Luminescent Zirconium(IV) Complex as a Molecular Photosensitizer for Visible Light Photoredox Catalysis. *J. Am. Chem. Soc.* **2016**, 138 (40), 13115–13118. DOI: 10.1021/jacs.6b05934.
- (13) Förster, C.; Heinze, K. Preparation and Thermochromic Switching between Phosphorescence and Thermally Activated Delayed Fluorescence of Mononuclear Copper(I) Complexes. *J. Chem. Educ.* **2020**, 97 (6), 1644–1649. DOI: 10.1021/acs.jchemed.0c00171.
- (14) Zhang, Y.; Schulz, M.; Wächtler, M.; Karnahl, M.; Dietzek, B. Heteroleptic diimine–diphosphine Cu(I) complexes as an alternative towards noble-metal based photosensitizers: Design strategies, photophysical properties and perspective applications. *Coord. Chem. Rev.* **2018**, 356, 127–146. DOI: 10.1016/j.ccr.2017.10.016.
- (15) Xiong, J.; Li, K.; Teng, T.; Chang, X.; Wei, Y.; Wu, C.; Yang, C. Dinuclear ZnII Complexes Exhibiting Thermally Activated Delayed Fluorescence and Luminescence Polymorphism. *Chem. Eur. J.* **2020**, 26 (30), 6887–6893. DOI: 10.1002/chem.202000572.
- (16) Marafie, J. A.; Bradley, D. D. C.; Williams, C. K. Thermally Stable Zinc Disalphen Macrocycles Showing Solid-State and Aggregation-Induced Enhanced Emission. *Inorg. Chem.* **2017**, 56 (10), 5688–5695. DOI: 10.1021/acs.inorgchem.7b00300.
- (17) Cheng, J.; Li, Y.; Sun, R.; Liu, J.; Gou, F.; Zhou, X.; Xiang, H.; Liu, J. Functionalized Salen ligands linking with non-conjugated bridges: unique and colorful aggregation-induced emission, mechanism, and applications. *J. Mater. Chem. C* **2015**, 3 (42), 11099–11110. DOI: 10.1039/c5tc02555a.
- (18) Paul, M. K.; Dilipkumar Singh, Y.; Bedamani Singh, N.; Sarkar, U. Emissive bis-salicylaldiminato Schiff base ligands and their zinc(II) complexes: Synthesis, photophysical properties, mesomorphism and DFT studies. *J. Mol. Struct.* **2015**, 1081, 316–328. DOI: 10.1016/j.molstruc.2014.10.031.
- (19) Consiglio, G.; Failla, S.; Oliveri, I. P.; Purrello, R.; Di Bella, S. Controlling the molecular aggregation. An amphiphilic Schiff-base zinc(II) complex as supramolecular fluorescent probe. *Dalton Trans.* **2009** (47), 10426–10428. DOI: 10.1039/b914930a.

- (20) Xie, D.; Jing, J.; Cai, Y.-B.; Tang, J.; Chen, J.-J.; Zhang, J.-L. Construction of an orthogonal ZnSalen/Salophen library as a colour palette for one- and two-photon live cell imaging. *Chem. Sci.* **2014**, *5* (6), 2318. DOI: 10.1039/c3sc53299b.
- (21) Forte, G.; Oliveri, I. P.; Consiglio, G.; Failla, S.; Di Bella, S. On the Lewis acidic character of bis(salicylaldiminato)zinc(ii) Schiff-base complexes: a computational and experimental investigation on a series of compounds varying the bridging diimine. *Dalton Trans.* **2017**, *46* (14), 4571–4581. DOI: 10.1039/c7dt00574a.
- (22) Consiglio, G.; Oliveri, I. P.; Cacciola, S.; Maccarrone, G.; Failla, S.; Di Bella, S. Dinuclear zinc(ii) salen-type Schiff-base complexes as molecular tweezers. *Dalton Trans.* **2020**, *49* (16), 5121–5133. DOI: 10.1039/d0dt00494d.
- (23) Oliveri, I. P.; Malandrino, G.; Di Bella, S. Phase transition and vapochromism in molecular assemblies of a polymorphic zinc(II) Schiff-base complex. *Inorg. Chem.* **2014**, *53* (18), 9771–9777. DOI: 10.1021/ic5013632.
- (24) Strianese, M.; Guarnieri, D.; Lamberti, M.; Landi, A.; Peluso, A.; Pellecchia, C. Fluorescent salen-type Zn(II) Complexes as Probes for Detecting Hydrogen Sulfide and Its Anion: Bioimaging Applications. *Inorg. Chem.* **2020**, *59* (21), 15977–15986. DOI: 10.1021/acs.inorgchem.0c02499.
- (25) Yao, Y.; Yin, H.-Y.; Ning, Y.; Wang, J.; Meng, Y.-S.; Huang, X.; Zhang, W.; Kang, L.; Zhang, J.-L. Strong Fluorescent Lanthanide Salen Complexes: Photophysical Properties, Excited-State Dynamics, and Bioimaging. *Inorg. Chem.* **2019**, *58* (3), 1806–1814. DOI: 10.1021/acs.inorgchem.8b02376.
- (26) Yan, X.; Song, X.; Mu, X.; Wang, Y. Mechanochromic luminescence based on a phthalonitrile-bridging salophen zinc(ii) complex. *New J. Chem.* **2019**, *43* (40), 15886–15891. DOI: 10.1039/c9nj03704g.
- (27) Borisov, S. M.; Pommer, R.; Svec, J.; Peters, S.; Novakova, V.; Klimant, I. New red-emitting Schiff base chelates: promising dyes for sensing and imaging of temperature and oxygen via phosphorescence decay time. *J. Mater. Chem. C* **2018**, *6* (33), 8999–9009. DOI: 10.1039/c8tc02726a.
- (28) Steinegger, A.; Borisov, S. M. Zn(II) Schiff Bases: Bright TADF Emitters for Self-Referenced Decay Time-Based Optical Temperature Sensing. *ACS Omega* **2020**, *5* (13), 7729–7737. DOI: 10.1021/acsomega.0c01062.
- (29) Kurz, H.; Hörner, G.; Weber, B. An Iron(II) Spin Crossover Complex with a Maleonitrile Schiff base-like Ligand and Scan Rate-dependent Hysteresis above Room Temperature. *Z. Anorg. Allg. Chem.* **2021**, *647* (8), 896–904. DOI: 10.1002/zaac.202000407.
- (30) Alvarez, S.; Alemany, P.; Casanova, D.; Cirera, J.; Llunell, M.; Avnir, D. Shape maps and polyhedral interconversion paths in transition metal chemistry. *Coord. Chem. Rev.* **2005**, *249* (17-18), 1693–1708. DOI: 10.1016/j.ccr.2005.03.031.
- (31) Wang, Z.-C.; Chu, J.; Zhan, S.-Z. {2,2'-(1,2-Di-cyano-ethene-1,2-di-yl)bis-(nitrilo-methanylyl-idyne)diphenolato-κ(4) O,N,N',O'}(methanol-κO)zinc. *Acta Crystallogr. Sect. E* **2013**, *69* (Pt 7), m419. DOI: 10.1107/S1600536813016863.
- (32) Ouari, K.; Ourari, A.; Weiss, J. Synthesis and Characterization of a Novel Unsymmetrical Tetradentate Schiff Base Complex of Zinc(II) Derived from N,N-bis (5-Bromosalicylidene) 2,3-Diaminopyridine (H₂L): Crystal Structure of [Zn(II)L]Pyridine. *J. Chem. Crystallogr.* **2010**, *40* (10), 831–836. DOI: 10.1007/s10870-010-9749-z.
- (33) Cheng, J.; Wei, K.; Ma, X.; Zhou, X.; Xiang, H. Synthesis and Photophysical Properties of Colorful Salen-Type Schiff Bases. *J. Phys. Chem. C* **2013**, *117* (32), 16552–16563. DOI: 10.1021/jp403750q.
- (34) Dumur, F.; Contal, E.; Wantz, G.; Gimes, D. Photoluminescence of Zinc Complexes: Easily Tunable Optical Properties by Variation of the Bridge Between the Imido Groups of Schiff Base Ligands. *Eur. J. Inorg. Chem.* **2014**, *2014* (25), 4186–4198. DOI: 10.1002/ejic.201402422.

- (35) Gagliardi, L.; Truhlar, D. G.; Li Manni, G.; Carlson, R. K.; Hoyer, C. E.; Bao, J. L. Multiconfiguration Pair-Density Functional Theory: A New Way to Treat Strongly Correlated Systems. *Acc. Chem. Res.* **2017**, *50* (1), 66–73. DOI: 10.1021/acs.accounts.6b00471.
- (36) Hoyer, C. E.; Ghosh, S.; Truhlar, D. G.; Gagliardi, L. Multiconfiguration Pair-Density Functional Theory Is as Accurate as CASPT2 for Electronic Excitation. *J. Phys. Chem. Lett.* **2016**, *7* (3), 586–591. DOI: 10.1021/acs.jpcclett.5b02773.
- (37) Li Manni, G.; Carlson, R. K.; Luo, S.; Ma, D.; Olsen, J.; Truhlar, D. G.; Gagliardi, L. Multiconfiguration Pair-Density Functional Theory. *J. Chem. Theory Comput.* **2014**, *10* (9), 3669–3680. DOI: 10.1021/ct500483t.
- (38) Paldus, J. Group theoretical approach to the configuration interaction and perturbation theory calculations for atomic and molecular systems. *J. Chem. Phys.* **1974**, *61* (12), 5321–5330. DOI: 10.1063/1.1681883.
- (39) Paldus, J. Matrix elements of unitary group generators in many-fermion correlation problem. I. tensorial approaches. *J. Math. Chem.* **2021**, *59* (1), 1–36. DOI: 10.1007/s10910-020-01172-9.
- (40) Shavitt, I. Graph theoretical concepts for the unitary group approach to the many-electron correlation problem. *Int. J. Quantum Chem.* **1977**, *12* (S11), 131–148. DOI: 10.1002/qua.560120819.
- (41) Shavitt, I. Matrix element evaluation in the unitary group approach to the electron correlation problem. *Int. J. Quantum Chem.* **1978**, *14* (S12), 5–32. DOI: 10.1002/qua.560140803.
- (42) Harriman, A. Luminescence of porphyrins and metalloporphyrins. Part 1. –Zinc(II), nickel(II) and manganese(II) porphyrins. *J. Chem. Soc., Faraday Trans. 1* **1980**, *76* (0), 1978. DOI: 10.1039/f19807601978.
- (43) Quimby, D. J.; Longo, F. R. Luminescence studies on several tetraarylporphyrins and their zinc derivatives. *J. Am. Chem. Soc.* **1975**, *97* (18), 5111–5117. DOI: 10.1021/ja00851a015.
- (44) Kurz, H.; Schötz, K.; Papadopoulos, I.; Heinemann, F. W.; Maid, H.; Guldi, D. M.; Köhler, A.; Hörner, G.; Weber, B. A Fluorescence-Detected Coordination-Induced Spin State Switch. *J. Am. Chem. Soc.* **2021**, *143* (9), 3466–3480. DOI: 10.1021/jacs.0c12568.
- (45) Martínez Belmonte, M.; Wezenberg, S. J.; Haak, R. M.; Anselmo, D.; Escudero-Adán, E. C.; Benet-Buchholz, J.; Kleij, A. W. Self-assembly of Zn(salphen) complexes: steric regulation, stability studies and crystallographic analysis revealing an unexpected dimeric 3,3'-t-Bu-substituted Zn(salphen) complex. *Dalton Trans.* **2010**, *39* (19), 4541–4550. DOI: 10.1039/b925560e.
- (46) Oliveri, I. P.; Maccarrone, G.; Di Bella, S. A Lewis basicity scale in dichloromethane for amines and common nonprotogenic solvents using a zinc(II) Schiff-base complex as reference Lewis acid. *J. Org. Chem.* **2011**, *76* (21), 8879–8884. DOI: 10.1021/jo2016218.
- (47) Salassa, G.; Coenen, M. J. J.; Wezenberg, S. J.; Hendriksen, B. L. M.; Speller, S.; Elemans, J. A. A. W.; Kleij, A. W. Extremely strong self-assembly of a bimetallic salen complex visualized at the single-molecule level. *J. Am. Chem. Soc.* **2012**, *134* (16), 7186–7192. DOI: 10.1021/ja3030802.
- (48) Weber, B.; Käßplinger, I.; Görls, H.; Jäger, E.-G. The Relationship between the Structure and Magnetic Properties of Bioinspired Iron(ii/iii) Complexes with Schiff-Base-Like Chelate Ligands, Part I: Complexes with Dianionic [N4] Macrocycles. *Eur. J. Inorg. Chem.* **2005**, *2005* (14), 2794–2811. DOI: 10.1002/ejic.200400759.
- (49) Singh, S. P.; Kumar, D. A Facile Synthesis of 5-Methyl-1-(phenyl/heterocyclyl)-4-trifluoroacetylpyrazoles†. *J. Chem. Res.* **1997** (4), 142–143. DOI: 10.1039/A606444B.
- (50) L. Claisen. *Justus Liebigs Ann. Chem.* **1897**, *297*, 1–98.
- (51) Altomare, A.; Burla, M. C.; Camalli, M.; Casciarano, G. L.; Giacovazzo, C.; Guagliardi, A.; Moliterni, A. G. G.; Polidori, G.; Spagna, R. SIR 97: a new tool for crystal structure

- determination and refinement. *J. Appl. Crystallogr.* **1999**, *32* (1), 115–119. DOI: 10.1107/S0021889898007717.
- (52) Sheldrick, G. M. A short history of SHELX. *Acta Crystallogr. Sect. A* **2008**, *64* (Pt 1), 112–122. DOI: 10.1107/S0108767307043930.
- (53) Burnett, M. N.; Johnson, C. K. *ORTEP-III: Oak Ridge Thermal Ellipsoid Plot Program for crystal structure illustrations*; Office of Scientific and Technical Information (OSTI), 1996. DOI: 10.2172/369685.
- (54) Farrugia, L. J. ORTEP -3 for Windows - a version of ORTEP -III with a Graphical User Interface (GUI). *J. Appl. Cryst.* **1997**, *30* (5), 565. DOI: 10.1107/S0021889897003117.
- (55) Macrae, C. F.; Edgington, P. R.; McCabe, P.; Pidcock, E.; Shields, G. P.; Taylor, R.; Towler, M.; van de Streek, J. Mercury: visualization and analysis of crystal structures. *J. Appl. Crystallogr.* **2006**, *39* (3), 453–457. DOI: 10.1107/S002188980600731X.
- (56) Neese, F. The ORCA program system. *WIREs Comput. Mol. Sci.* **2012**, *2* (1), 73–78. DOI: 10.1002/wcms.81.
- (57) Schäfer, A.; Horn, H.; Ahlrichs, R. Fully optimized contracted Gaussian basis sets for atoms Li to Kr. *J. Chem. Phys.* **1992**, *97* (4), 2571–2577. DOI: 10.1063/1.463096.
- (58) Becke. Density-functional exchange-energy approximation with correct asymptotic behavior. *Phys. Rev. A* **1988**, *38* (6), 3098–3100. DOI: 10.1103/PhysRevA.38.3098.
- (59) Staroverov, V. N.; Scuseria, G. E.; Tao, J.; Perdew, J. P. Comparative assessment of a new nonempirical density functional: Molecules and hydrogen-bonded complexes. *J. Chem. Phys.* **2003**, *119* (23), 12129–12137. DOI: 10.1063/1.1626543.
- (60) Grimme, S.; Antony, J.; Ehrlich, S.; Krieg, H. A consistent and accurate ab initio parametrization of density functional dispersion correction (DFT-D) for the 94 elements H-Pu. *J. Chem. Phys.* **2010**, *132* (15), 154104. DOI: 10.1063/1.3382344.
- (61) Grimme, S.; Ehrlich, S.; Goerigk, L. Effect of the damping function in dispersion corrected density functional theory. *J. Comput. Chem.* **2011**, *32* (7), 1456–1465. DOI: 10.1002/jcc.21759.
- (62) Klamt, A.; Schüürmann, G. COSMO: a new approach to dielectric screening in solvents with explicit expressions for the screening energy and its gradient. *J. Chem. Soc. Perkin Trans. 2* **1993** (5), 799–805. DOI: 10.1039/P29930000799.

5.6. Supporting Information

X-Ray crystal structure determinations

Crystallographic information: CCDC-2086160 (for **[Zn(1)(MeOH)]·MeOH**), CCDC-2086684 (for **[Zn(1)(py)]**), CCDC-2086163 (for **[Zn(1)(H₂O)]**), CCDC-2086161 (for **[Zn(2)(H₂O)]₂·H₂O**), and CCDC-2086162 (for **[Zn(3)(H₂O)(EtOH)]**) contain the supplementary crystallographic data for this paper. The data can be obtained free of charge from The Cambridge Crystallographic Data Center via www.ccdc.cam.ac.uk/structures.

Table S1: Crystallographic data of **[Zn(1)(MeOH)]·MeOH**, **[Zn(1)(py)]**, and **[Zn(1)(H₂O)]**.

compound (unit cell)	[Zn(1)(MeOH)]·MeOH	[Zn(1)(py)]	[Zn(1)(H₂O)]
CCDC	2086160	2086684	2086163
description	orange block	yellow plate	orange rhombohedron

Quenched Lewis Acidity: Studies on the Medium Dependent Fluorescence of Zinc(II)
Complexes

sum formula	C ₁₇ H ₁₈ N ₄ O ₇ Zn · C H ₄ O	C ₂₁ H ₁₉ N ₅ O ₆ Zn	C ₁₆ H ₁₆ N ₄ O ₇ Zn
<i>M</i> / g·mol ⁻¹	487.79	502.80	441.72
crystal system	orthorhombic	triclinic	triclinic
space group	<i>Pbca</i> <i>ba-c</i>	<i>P</i> $\bar{1}$	<i>P</i> $\bar{1}$
<i>a</i> / Å	13.5885(3)	9.2831(3)	8.2597(2)
<i>b</i> / Å	16.1753(4)	10.4320(4)	9.4419(3)
<i>c</i> / Å	19.5542(6)	12.2241(5)	11.7529(3)
α / °	90	83.479(3)	99.982(2)
β / °	90	78.454(3)	90.772(2)
γ / °	90	72.082(3)	96.782(2)
<i>V</i> / Å ³	4297.98(19)	1101.87(7)	895.85(4)
<i>Z</i>	8	2	2
ρ / g·cm ⁻³	1.508	1.515	1.638
μ / mm ⁻¹	1.195	1.163	1.420
crystal size/ mm	0.22 x 0.40 x 0.43	0.09 x 0.12 x 0.17	0.14 x 0.22 x 0.24
<i>T</i> / K	200	170	170
λ (MoK α)/ Å	0.71073	0.71073	0.71073
θ -range/ °	2.2-28.5	2.8-28.6	3.1-28.5
reflns. collected	30326	12925	10564
indep. reflns. (<i>Rint</i>)	5264 (0.050)	5250 (0.026)	4252 (0.015)
parameters	288	298	261
<i>R</i> <i>I</i>	0.0388	0.0370	0.0237
<i>wR</i> <i>2</i>	0.0870	0.1030	0.0604
<i>Goof</i>	1.00	1.05	1.04

Table S2: Crystallographic data of [Zn(2)(H₂O)]₂·H₂O and [Zn(3)(H₂O)(EtOH)].

compound (unit cell)	[Zn(2)(H ₂ O)] ₂ ·H ₂ O	[Zn(3)(H ₂ O)(EtOH)]
CCDC	2086161	2086162
description	orange block	red block
sum formula	2 (C ₁₈ H ₂₀ N ₄ O ₇ Zn) · H ₂ O	C ₁₈ H ₁₆ F ₆ N ₄ O ₆ Zn
<i>M</i> / g·mol ⁻¹	957.56	563.74
crystal system	triclinic	monoclinic
space group	<i>P</i> $\bar{1}$	<i>P</i> ₂ <i>1</i> / <i>c</i>
<i>a</i> / Å	9.8097(7)	9.0574(2)
<i>b</i> / Å	10.8009(7)	14.2024(4)
<i>c</i> / Å	20.7131(13)	17.8475(4)
α / °	87.254(5)	90
β / °	79.764(5)	96.792(2)
γ / °	85.457(5)	90
<i>V</i> / Å ³	2151.6(3)	2279.73(10)
<i>Z</i>	2	4
ρ / g·cm ⁻³	1.478	1.643
μ / mm ⁻¹	1.190	1.168
crystal size/ mm	0.09 x 0.17 x 0.17	0.13 x 0.14 x 0.16
<i>T</i> / K	133	220
λ (MoK α)/ Å	0.71073	0.71073
θ -range/ °	2.1-28.6	1.8-28.4

Quenched Lewis Acidity: Studies on the Medium Dependent Fluorescence of Zinc(II) Complexes

reflns. collected	23445	16805
indep. reflns. (<i>Rint</i>)	10092 (0.083)	5445 (0.095)
parameters	574	328
<i>R</i> 1	0.0534	0.0568
<i>wR</i> 2	0.1243	0.1918
<i>Goof</i>	0.90	1.10

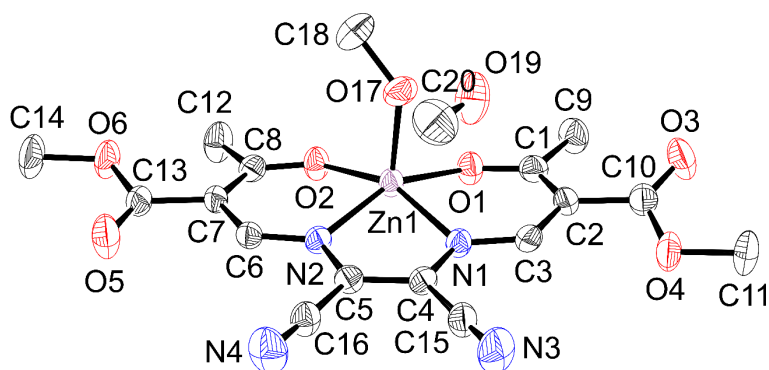


Figure S1: Thermal ellipsoid representation of the molecular structures with the applied numbering scheme of $[\text{Zn}(\mathbf{1})(\text{MeOH})]\cdot\text{MeOH}$. Hydrogen atoms are omitted for clarity. Ellipsoids are drawn at 50% probability.

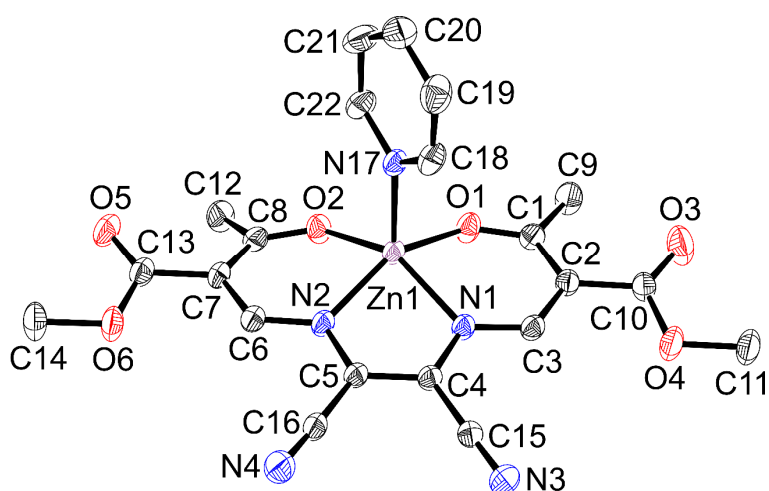


Figure S2: Thermal ellipsoid representation of the molecular structures with the applied numbering scheme of $[\text{Zn}(\mathbf{1})(\text{py})]$. Hydrogen atoms are omitted for clarity. Ellipsoids are drawn at 50% probability.

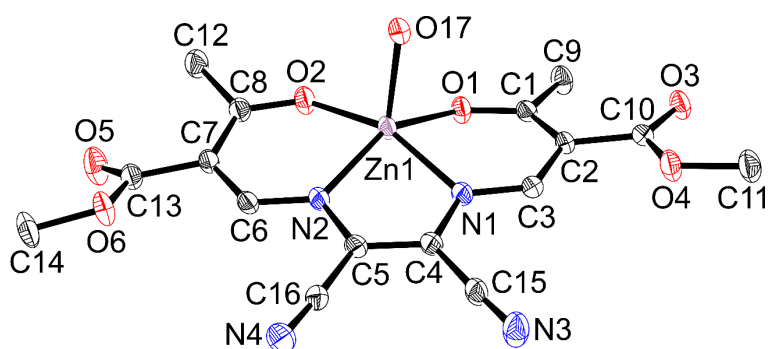


Figure S3: Thermal ellipsoid representation of the molecular structures with the applied numbering scheme of $[\text{Zn}(\mathbf{1})(\text{H}_2\text{O})]$. Hydrogen atoms are omitted for clarity. Ellipsoids are drawn at 50% probability.

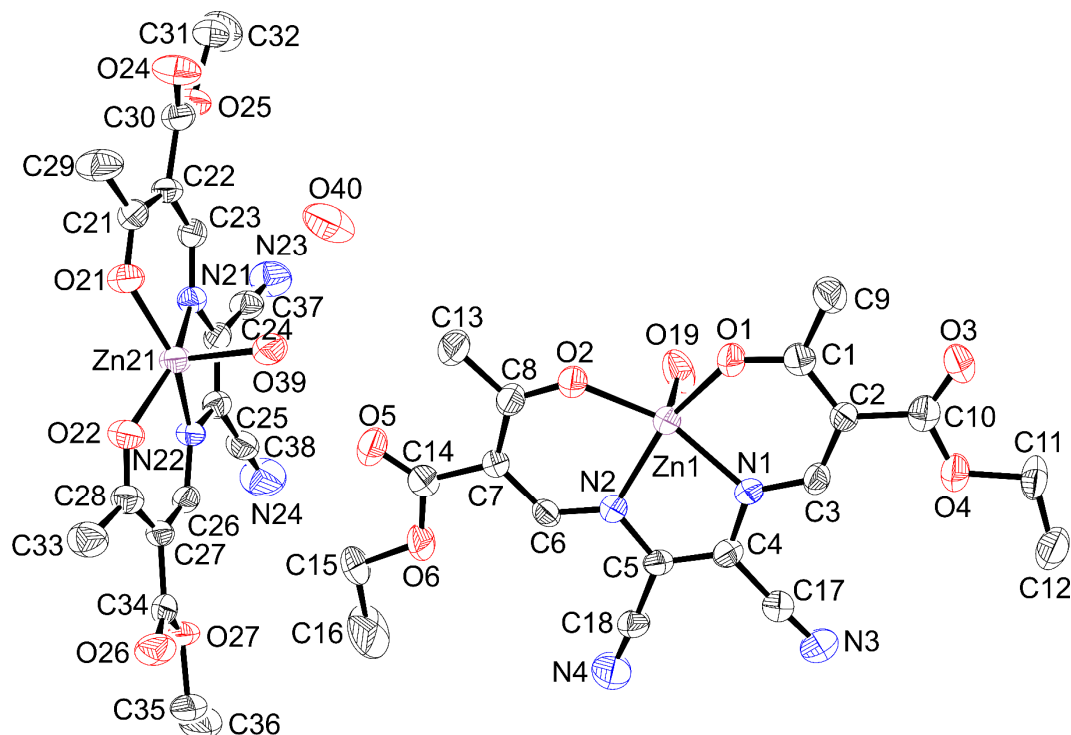


Figure S4: Thermal ellipsoid representation of the molecular structures with the applied numbering scheme of $[\text{Zn}(\mathbf{2})(\text{H}_2\text{O})]_2 \cdot \text{H}_2\text{O}$. Hydrogen atoms are omitted for clarity. Ellipsoids are drawn at 50% probability.

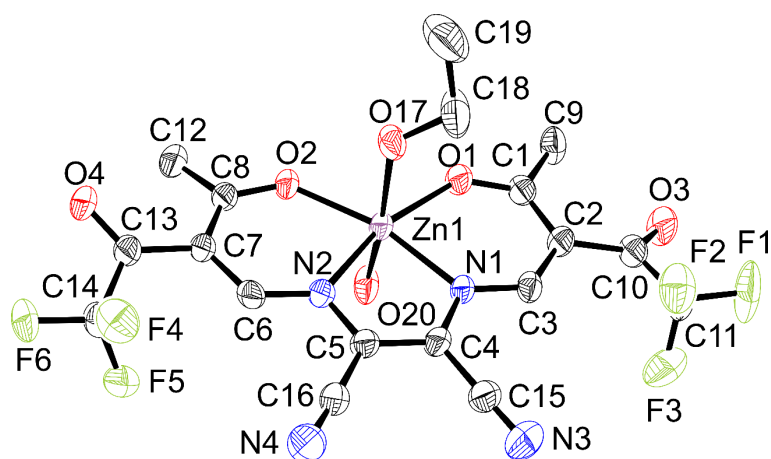


Figure S5: Thermal ellipsoid representation of the molecular structures with the applied numbering scheme of $[\text{Zn}(\mathbf{3})(\text{H}_2\text{O})(\text{EtOH})]$. Hydrogen atoms are omitted for clarity. Ellipsoids are drawn at 50% probability.

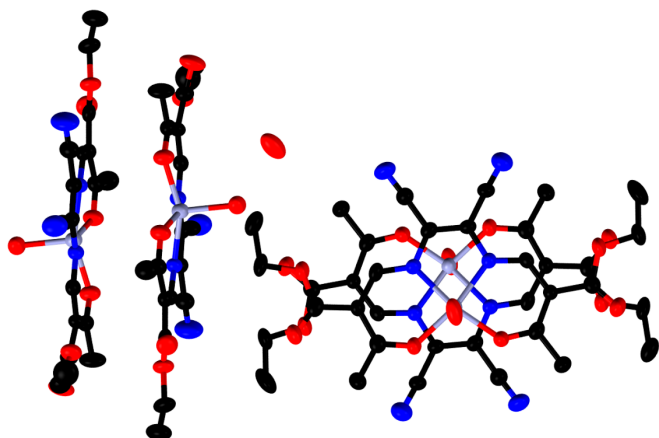


Figure S6: Side view and top view of the stacked dimers of $[\text{Zn}(\mathbf{2})(\text{H}_2\text{O})]_2 \cdot \text{H}_2\text{O}$. Hydrogen bonds are omitted for clarity. Ellipsoids are shown at 50% probability level.

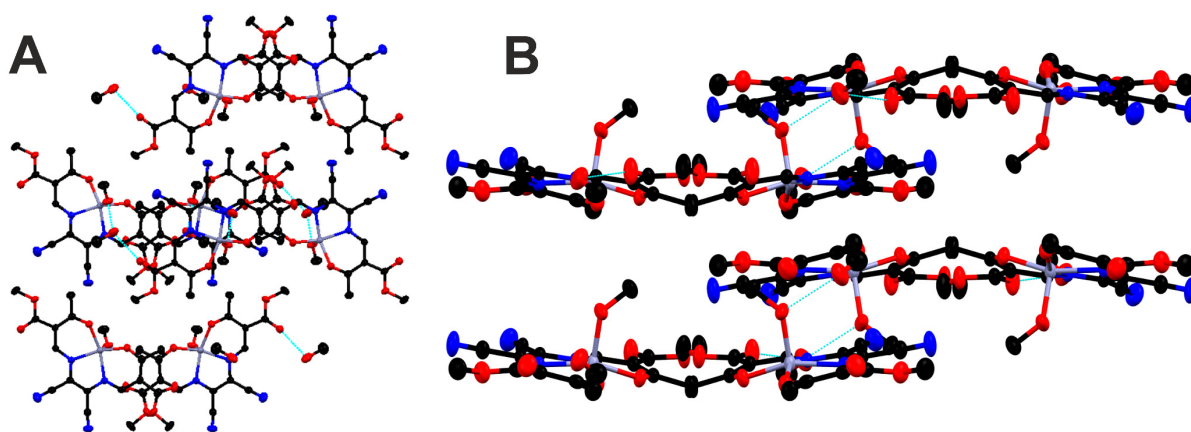


Figure S7: Molecular packing of $[\text{Zn}(\mathbf{1})(\text{MeOH})] \cdot \text{MeOH}$ along $[100]$ (A) and $[010]$ (B). Hydrogen atoms are omitted for clarity.

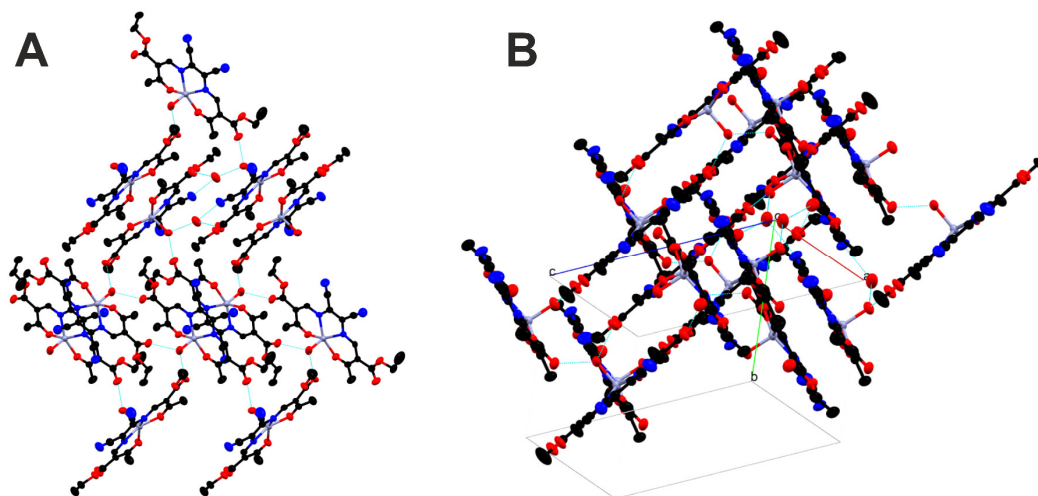


Figure S8: Molecular packing of $[\text{Zn}(\mathbf{2})(\text{H}_2\text{O})]_2 \cdot \text{H}_2\text{O}$ along $[100]$ (A) and $[??]$ (B). Hydrogen atoms are omitted for clarity.

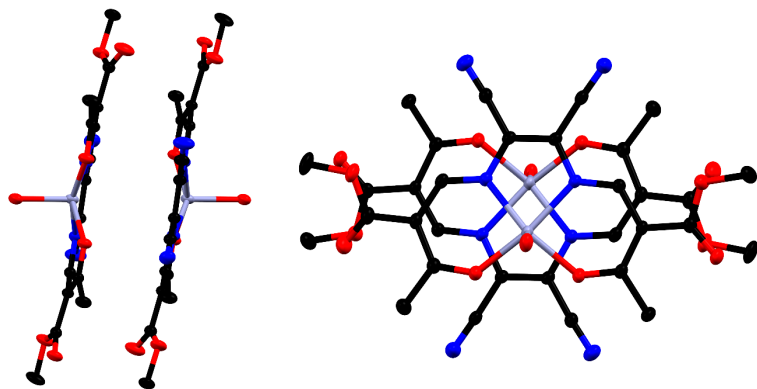


Figure S9: Side view and top view of the stacked dimers in $[\text{Zn}(\mathbf{1})(\text{H}_2\text{O})]$. Hydrogen bonds are omitted for clarity. Ellipsoids are shown at 50% probability level.

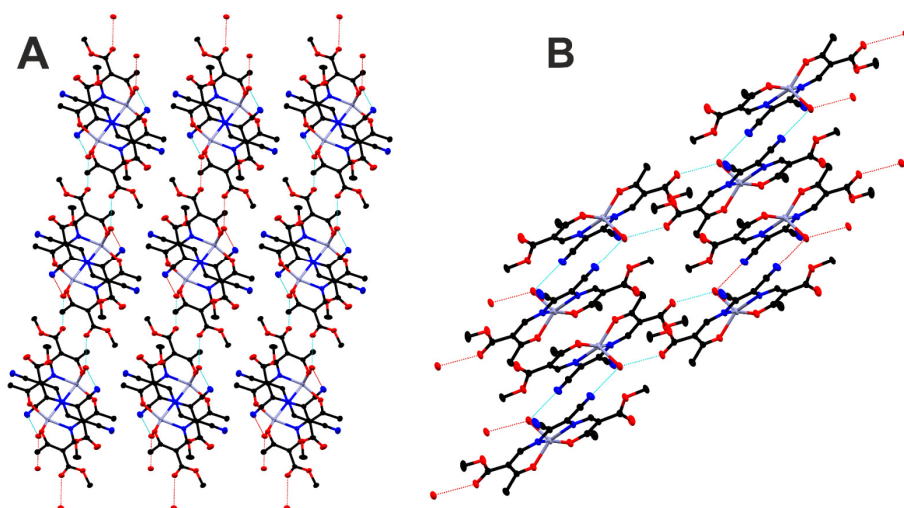


Figure S10: Molecular packing of $[\text{Zn}(\mathbf{1})(\text{H}_2\text{O})]$ along $[100]$ (A) and $[010]$ (B). Hydrogen atoms are omitted for clarity.

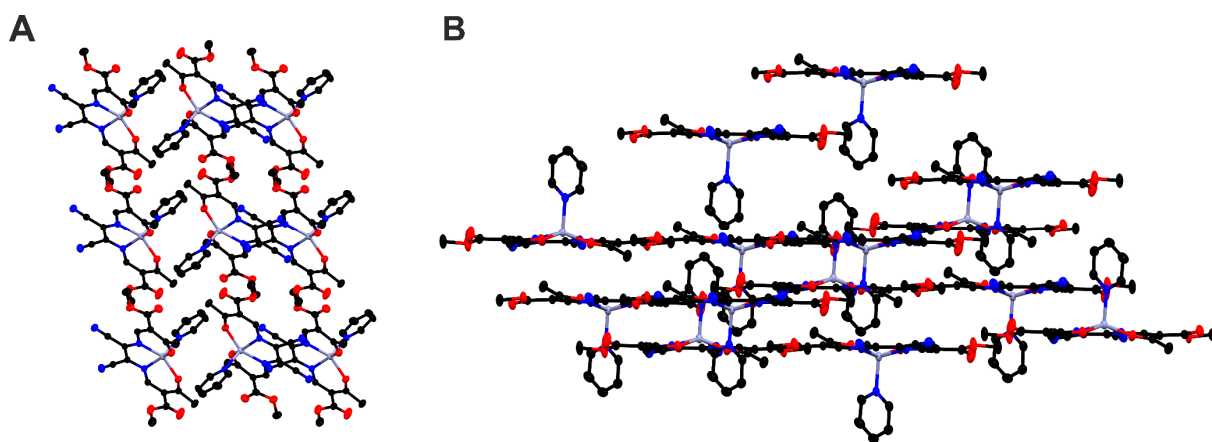


Figure S11: Molecular packing of $[\text{Zn}(\mathbf{1})(\text{py})]$ along $[010]$ (A) and $[??]$ (B). Hydrogen atoms are omitted for clarity.

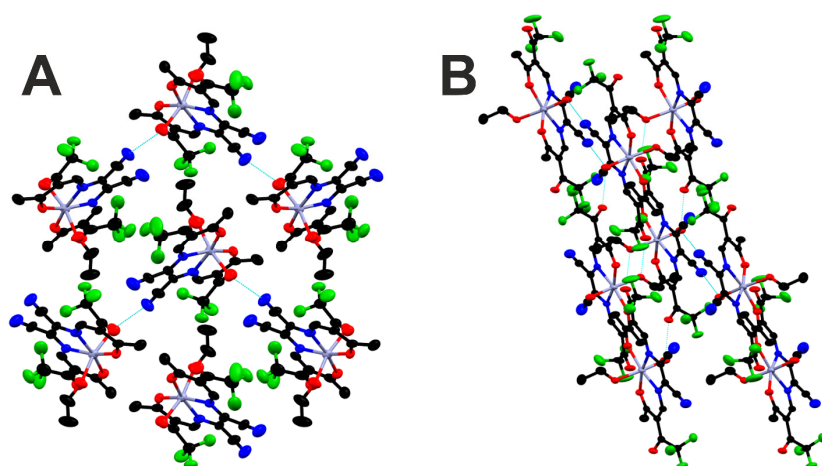


Figure S12: Molecular packing of $[\text{Zn}(\mathbf{3})(\text{H}_2\text{O})(\text{EtOH})]$ along $[100]$ (A) and $[010]$ (B). Hydrogen atoms are omitted for clarity.

Table S3: Selected distances [\AA] and angles [$^\circ$] of the π - π and M- π interactions of $[\text{Zn}(\mathbf{1})(\text{MeOH})]\cdot\text{MeOH}$, $[\text{Zn}(\mathbf{1})(\text{H}_2\text{O})]$, $[\text{Zn}(\mathbf{1})(\text{py})]$, and $[\text{Zn}(\mathbf{2})(\text{H}_2\text{O})]_2\cdot\text{H}_2\text{O}$. Cg(I) is the centroid of the ring number I, α is the dihedral angle between the rings, β is the angle between the vector Cg(I)-Cg(J) and the normal to ring I, γ is the angle between the vector Cg(I)-Cg(J) and the normal to ring J.

Compound	Cg(I)	Cg(J)	Cg-Cg [\AA]	α [$^\circ$]	β [$^\circ$]	γ [$^\circ$]
$[\text{Zn}(\mathbf{1})(\text{MeOH})]\cdot\text{H}_2\text{O}$	Zn1-N1-C4-C5-N2	Zn1-N1-C4-C5-N2 [a]	3.7068(12)	0.00(9)	19.1	19.1
	Zn1-N1-C4-C5-N2	Zn1 [a]	3.636	-	11.02	-
$[\text{Zn}(\mathbf{1})(\text{H}_2\text{O})]$	Zn1-N1-C4-C5-N2	Zn1-O2-C8-C7-C6-N2 [b]	3.7993(7)	8.82(5)	21.7	14.9
	Zn1-N1-C4-C5-N2	Zn1 [b]	3.874	-	10.44	-
$[\text{Zn}(\mathbf{1})(\text{py})]$	O3	N17-C18-C19-C20-C21-C22 [c]	3.367(3)	-	-	6.93
$[\text{Zn}(\mathbf{2})(\text{H}_2\text{O})]_2\cdot\text{H}_2\text{O}$	Zn1-N1-C4-C5-N2	Zn1-N1-C4-C5-N2 [d]	4.025(2)	0.00(17)	22.2	22.2
	Zn1-N1-C4-C5-N2	Zn1 [d]	3.801	-	3.61	-

[a] = 1-X, -Y, 1-Z; [b] = 1-X, 1-Y, 1-Z; [c] = -1+X, Y, Z; [d] = -X, -Y, 1-Z

Table S4: Hydrogen bonds and angles of $[\text{Zn}(\mathbf{1})(\text{MeOH})]\cdot\text{MeOH}$, $[\text{Zn}(\mathbf{2})(\text{H}_2\text{O})]_2\cdot\text{H}_2\text{O}$, and $[\text{Zn}(\mathbf{3})(\text{H}_2\text{O})(\text{EtOH})]$.

Compound	Donor	Acceptor	D-H [\AA]	H \cdots A [\AA]	D \cdots A [\AA]	D-H \cdots A [$^\circ$]
$[\text{Zn}(\mathbf{1})(\text{MeOH})]\cdot\text{H}_2\text{O}$	O17-H17 [a]	O19	0.76(3)	1.84(3)	2.604(3)	175(3)
	O19-H19 [b]	O5	0.82(3)	0.82(3)	2.679(3)	170(3)

Quenched Lewis Acidity: Studies on the Medium Dependent Fluorescence of Zinc(II)
Complexes

	C18–H18A [c]	N3	0.98	2.54	3.296(4)	134
[Zn(1)(H ₂ O)]	O17–H17A [d]	O3	0.79(2)	2.02(2)	2.8012(16)	170.8(19)
	O17–H17B [e]	N4	0.75(3)	2.34(2)	2.9044(19)	133(3)
[Zn(1)(py)]	C11–H11B [f]	O4	0.98	2.54	3.470(3)	159
	C20–H20 [g]	O3	0.95	2.48	3.348(3)	152
[Zn(2)(H ₂ O)] ₂ ·H ₂ O	O19–H19A [h]	O26	0.60(4)	2.12(4)	2.692(5)	162(5)
	O19–H19B [i]	O3	0.84(7)	1.83(6)	2.671(5)	177(10)
	O39–H39A [j]	O40	0.77(6)	1.91(6)	2.672(6)	171(5)
	O39–H39B [k]	O5	0.68(7)	2.06(6)	2.733(5)	178(10)
	O40–H40A [l]	O24	0.94(10)	2.52(10)	2.838(6)	100(7)
	O40–H40A [m]	N23	0.94(10)	2.29(10)	3.015(6)	134(8)'
	O40–H40B [l]	O24	1.04(12)	2.15(10)	2.838(6)	121(7)
[Zn(3)(H ₂ O) (EtOH)]	O17–H17 [n]	O3	0.77(8)	2.00(8)	2.761(5)	172(11)
	O20–H20A [o]	F6	0.83(7)	2.54(7)	3.092(5)	125(6)
	O20–H20A [o]	O4	0.83(7)	1.99(7)	2.792(5)	163(7)'
	O20–H20B [p]	N4	0.67(6)	2.28(6)	2.952(7)	177(8)

[a] [?]; [b] $\frac{1}{2}-x, \frac{1}{2}+y, 1-z$; [c] $\frac{1}{2}-x, y, -1/2+z$; [d] $1-x, 1-y, 2-z$; [e] $2-x, 1-y, 1-z$; [f] $-x, -y, 2-z$; [g] $1-x, -y, 1-z$; [h] $x, 1+y, z$; [i] $-x, 1-y, 1-z$; [j] ?; [k] ?; [l] $-x, -y, -z$; [m] $1-x, -y, -z$; [n] $1+x, y, z$; [o] $-1+x, y, z$; [p] $2-x, 1/2+y, 3/2-z$.

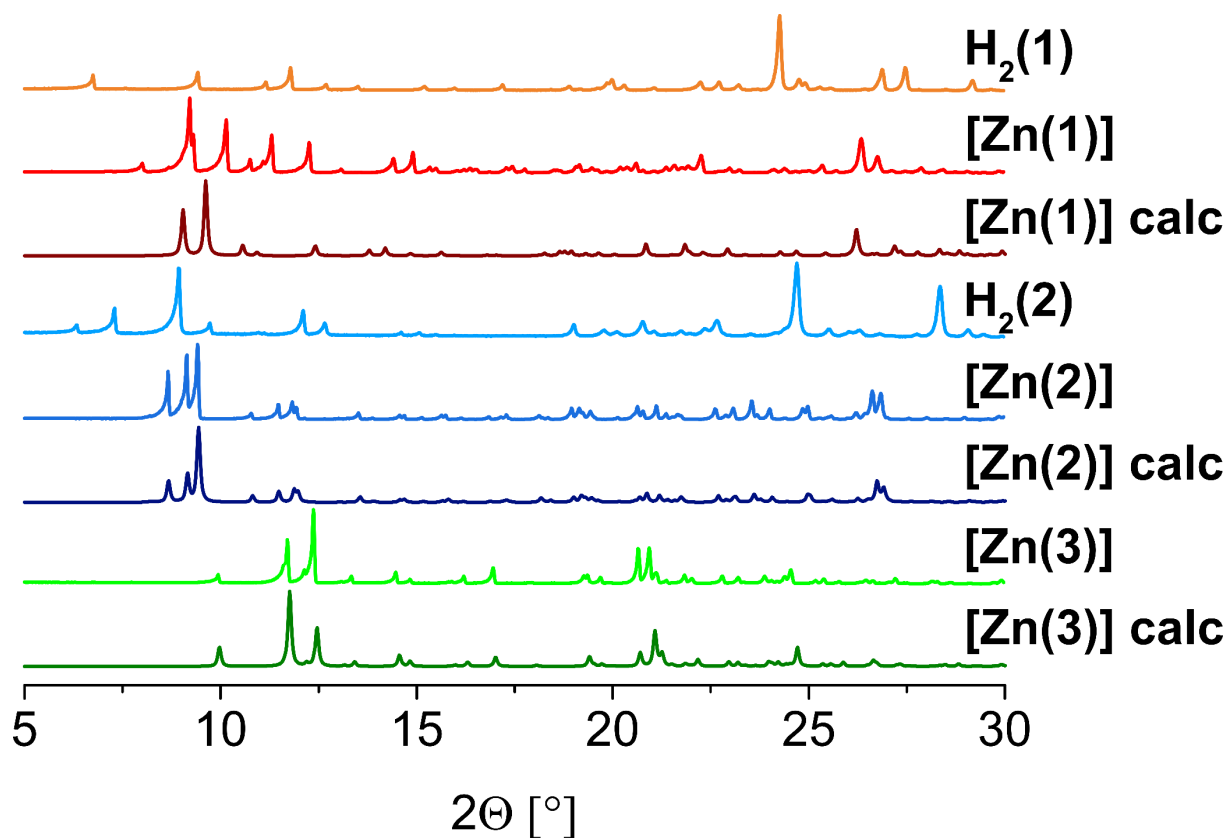


Figure S13: PXRD pattern of **[Zn(1–3)]** in the range of 5–30° 2θ at room temperature and the calculated PXRD pattern of the single crystal of **[Zn(1)(MeOH)]·MeOH**, **[Zn(2)(H₂O)]₂·H₂O**, and **[Zn(3)(H₂O)(EtOH)]** measured at 200/133/220 K.

Quenched Lewis Acidity: Studies on the Medium Dependent Fluorescence of Zinc(II) Complexes

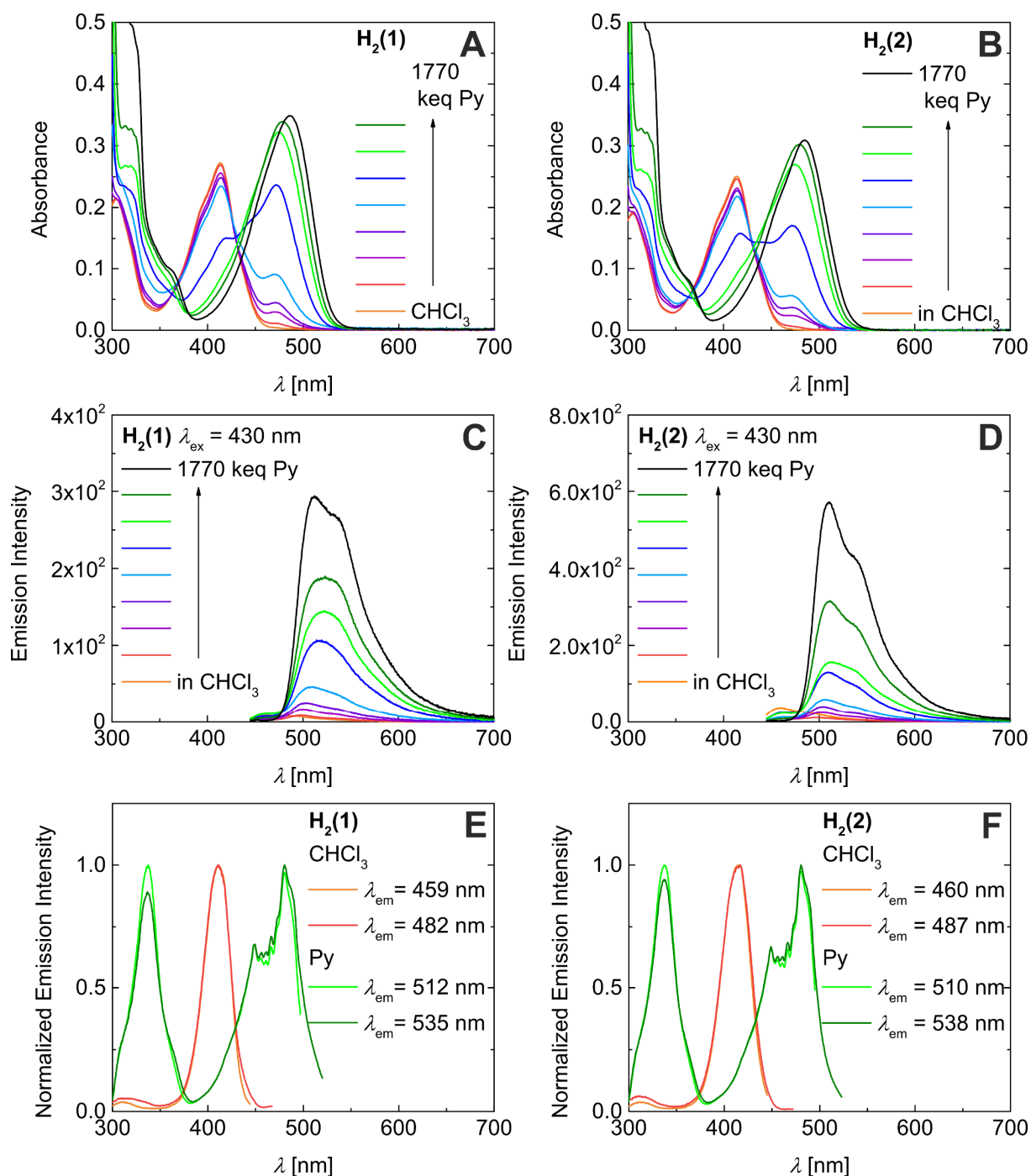


Figure S14: Absorbance (A, B), emission (C, D), and fluorescence excitation (E, F) spectra of $H_2(1)$ and $H_2(2)$ in various chloroform/pyridine mixtures (7×10^{-6} M).

Titration steps: 0 keq; 8.8 keq; 43.2 keq; 84.3 keq; 160.9 keq; 354.0 keq; 590.0 keq; 885.0 keq; 1769.9 keq.

Quenched Lewis Acidity: Studies on the Medium Dependent Fluorescence of Zinc(II) Complexes

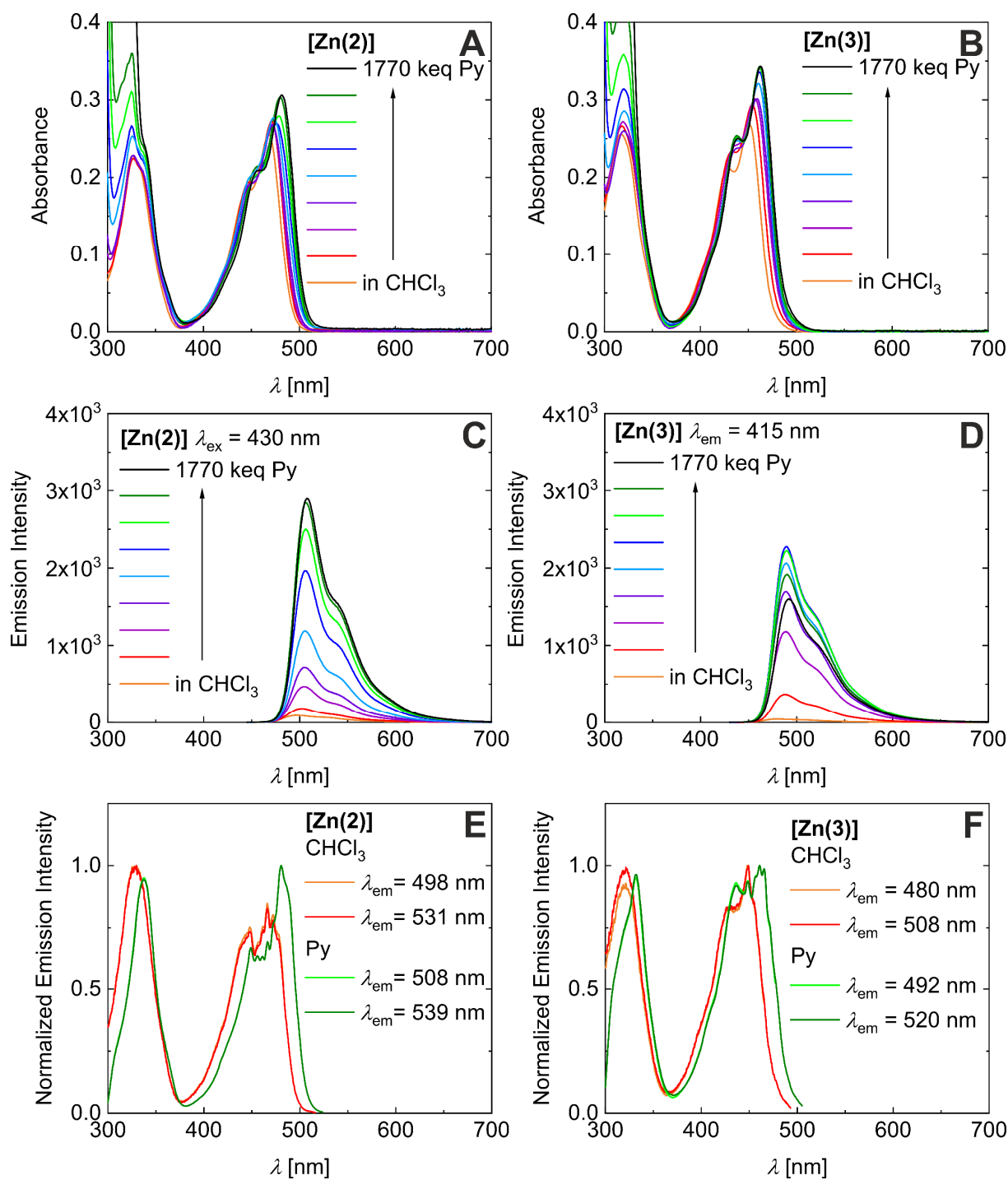


Figure S15: Absorbance (A, B), emission (C, D), and fluorescence excitation (E, F) spectra of [Zn(2)] and [Zn(3)] in various chloroform/pyridine mixtures (7×10^{-6} M).

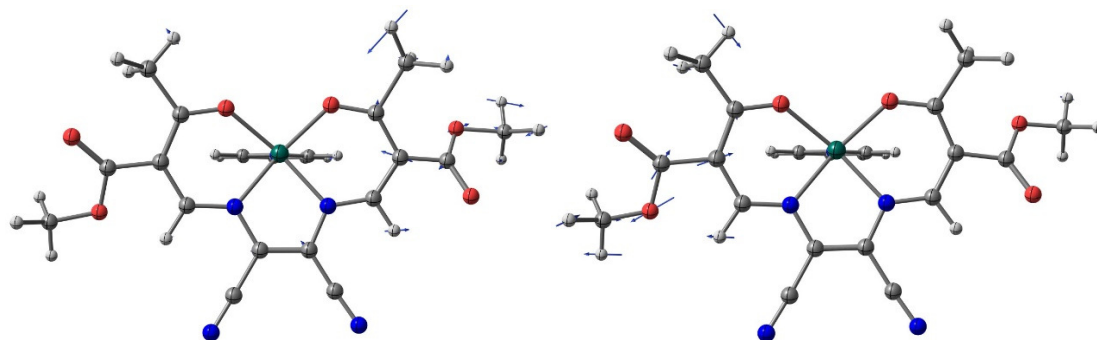


Figure S16: Visualization of harmonic vibrational modes in $[\text{Zn}(\mathbf{1})\text{py}]$; (left) mode at 1067 cm^{-1} ; (right) mode at 1050 cm^{-1} ; vectors denote dominant directions of nuclear motion (an animated gif-file of mode *1050* can be found in the ESI).

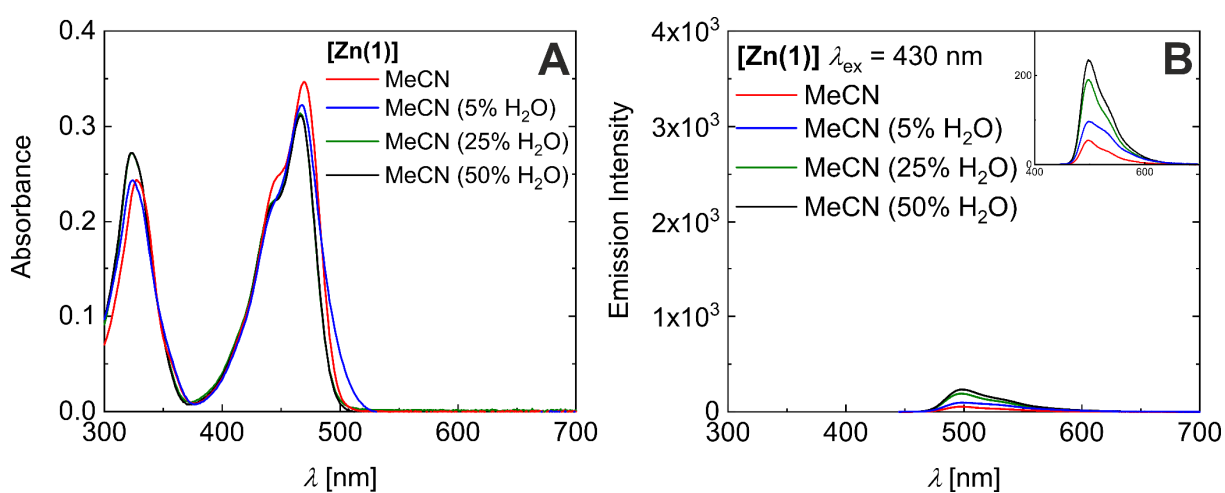


Figure S17: Absorbance (A) and emission (B) spectra of $[\text{Zn}(\mathbf{1})]$ in MeCN with varying amount of water ($7 \times 10^{-6}\text{ M}$).

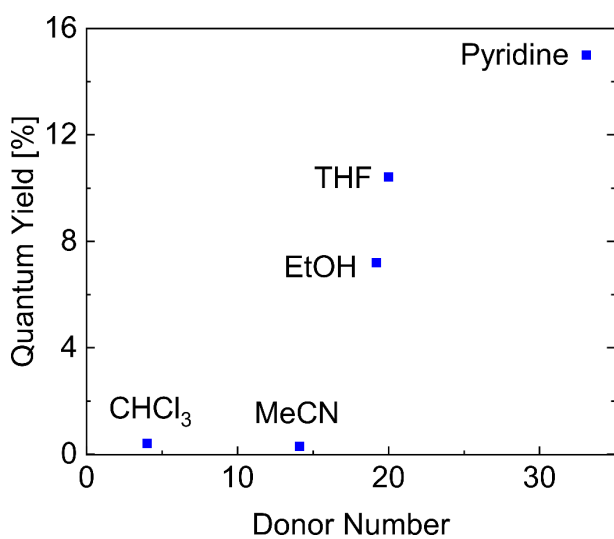


Figure S18: Plot of the quantum yield of $[\text{Zn}(\mathbf{1})]$ solutions vs the donor number of the respective solvent.

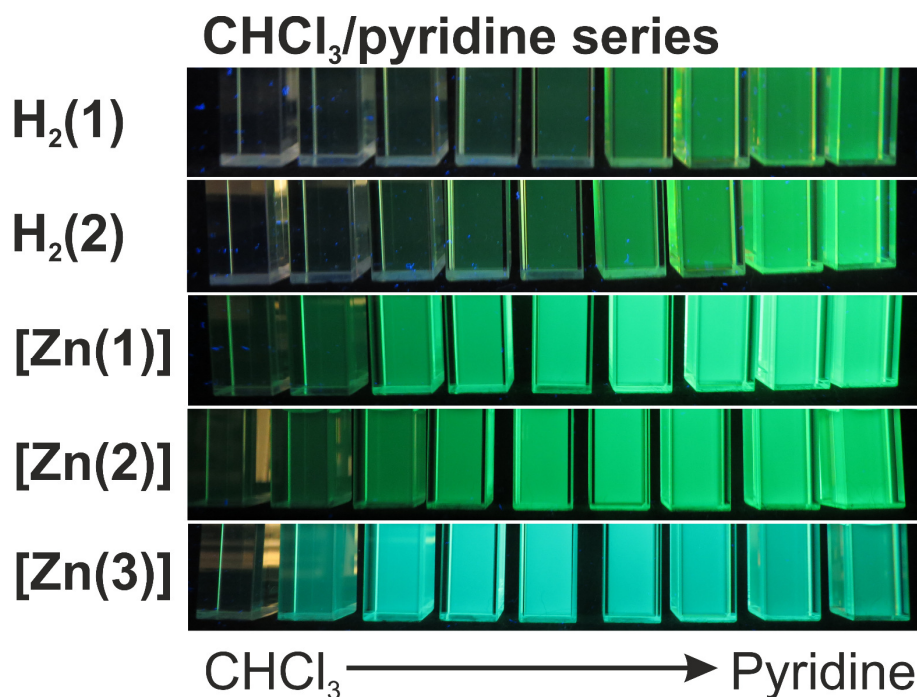


Figure S19: Photographs of the CHCl₃/pyridine series of the ligands and the zinc(II) complexes upon irradiation with $\lambda_{\text{ex}} = 365$ nm.

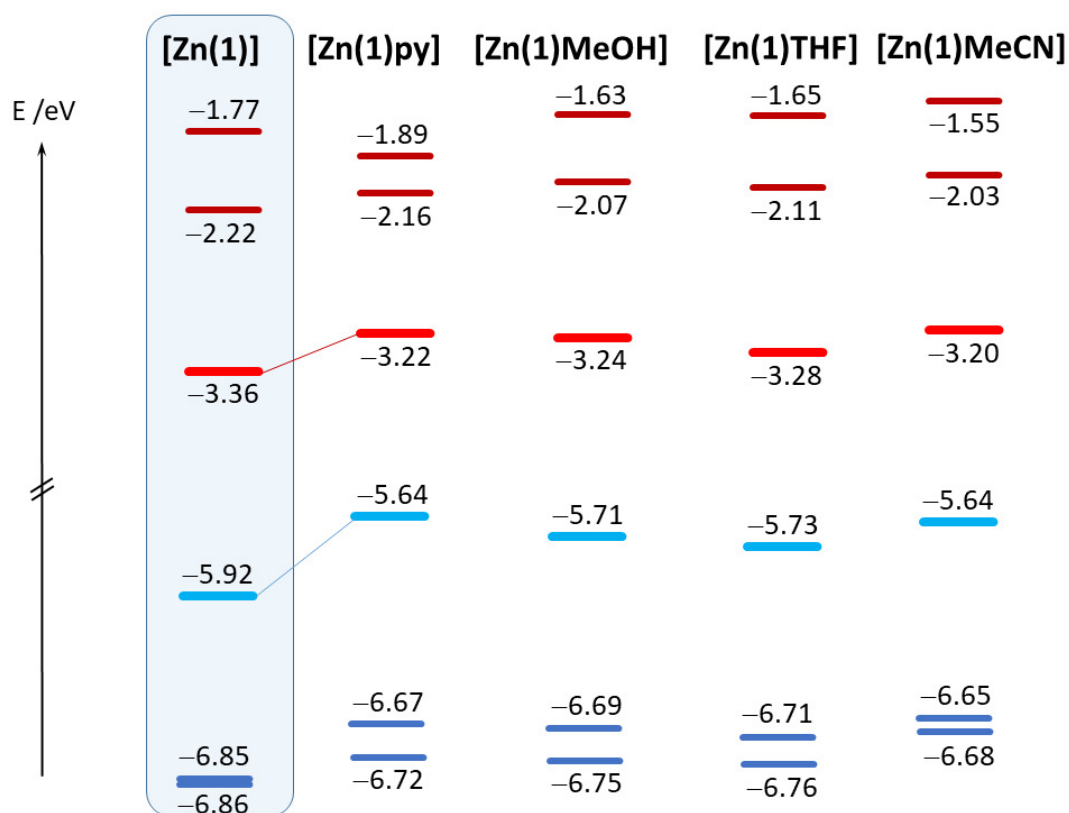


Figure S20: Frontier Kohn-Sham MO diagrams four-coordinate and five-coordinate complexes of [Zn(1)]; blue: occupied; red: virtual.

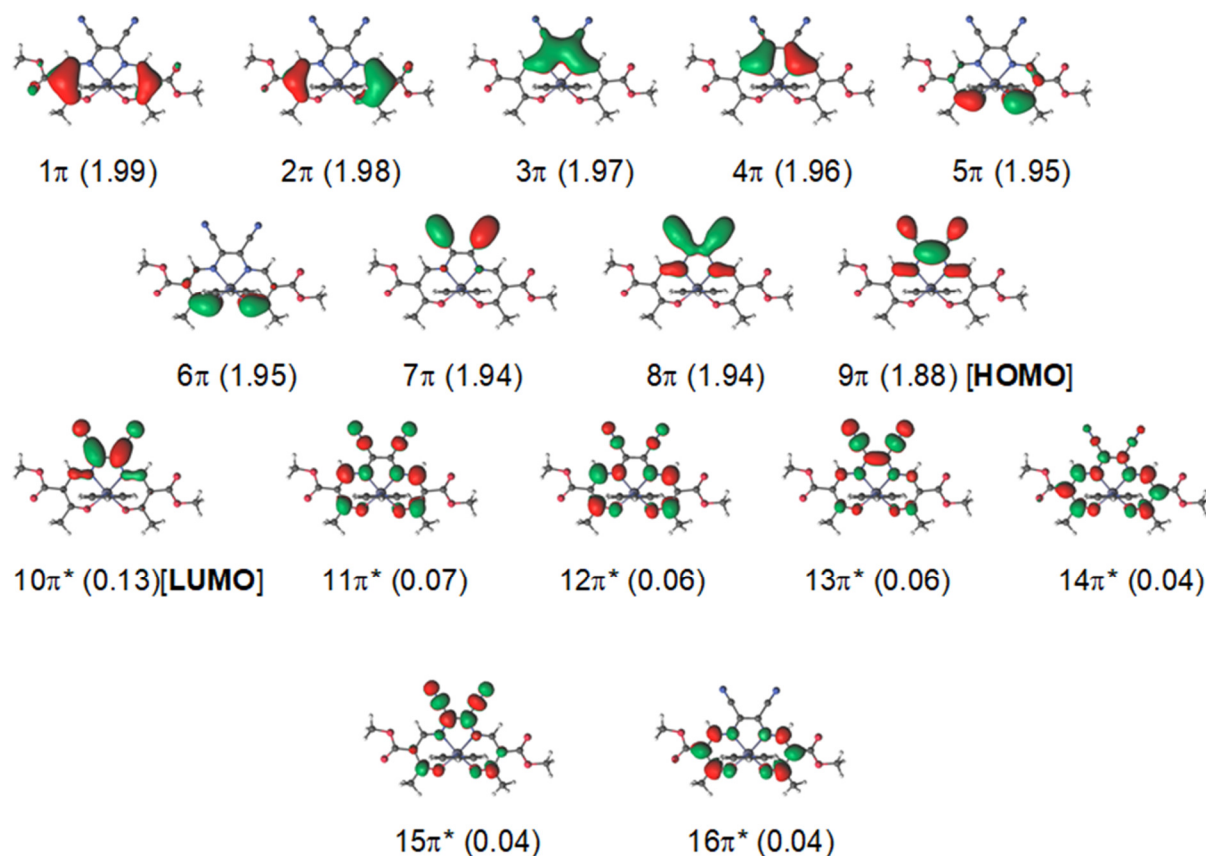


Figure S21: CASSCF(18,16) natural orbitals of the singlet ground state, S_0 . In parenthesis the corresponding occupation numbers. HOMO and LUMO are marked. The HOMO markedly has a π -bonding character between the two backbone C atoms and a π -anti-bonding character with the cyano-groups (nodal plane between the nitrile groups and the C=C backbone). On the contrary, the LUMO exhibits a π -bonding character between the C atoms of the π -backbone and the nitrile groups, and an anti-bonding character between the two C atoms of the backbone. Similar features have been reported from our KS-DFT analysis. Orbitals of the S_1 and T_1 states are qualitatively very similar to the ones reported for the S_0 state. Thus, the S_1 state, as characterized by a HOMO-to-LUMO excitation experience a partial transfer of charge from the π -backbone to the nitrile group.

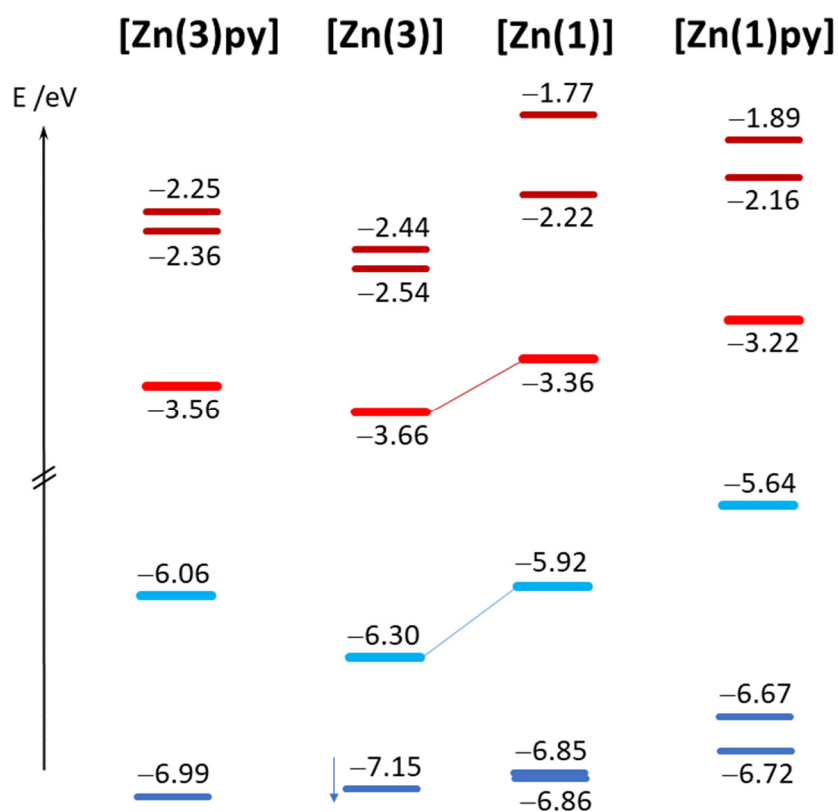


Figure S22: Frontier Kohn-Sham MO diagrams four-coordinate and five-coordinate complexes of **[Zn(3)]** and **[Zn(1)]**; blue: occupied; red: virtual.

Table S5: Selected coordination metrics in optimized structures of **[Zn(1)X]** (BP86/TZVP).

	[Zn(1)]	[Zn(1)(py)]	[Zn(1)(H₂O)]	[Zn(1)(MeCN)]	[Zn(1)(MeOH)]	[Zn(1)(THF)]
Zn-O_{eq}	1.970	2.029	2.010	2.020	2.011	2.011
Zn-O_{eq}	1.971	2.031	2.011	2.021	2.016	2.005
Zn-N_{eq}	2.033	2.081	2.060	2.071	2.065	2.062
Zn-N_{eq}	2.031	2.079	2.065	2.071	2.063	2.066
Zn-X_{ax}	-	2.068	2.118	2.070	2.107	2.106
O_{eq}-Zn-O_{eq}	97.4	95.0	95.9	95.2	96.8	96.2
O_{eq}-Zn-X_{ax}	-	104.0	100.9	103.1	103.8	100.6
O_{eq}-Zn-X_{ax}	-	104.1	105.0	103.6	101.3	103.0
N_{eq}-Zn-X_{ax}	-	101.8	98.3	101.4	95.8	98.8
N_{eq}-Zn-X_{ax}	-	102.1	96.7	100.0	98.8	98.1

Quenched Lewis Acidity: Studies on the Medium Dependent Fluorescence of Zinc(II) Complexes

Table S6: Selected coordination metrics in optimized structures of $[\text{Zn}(\mathbf{3})\text{X}]$ and $[\text{Zn}(\text{sal})\text{X}]$ (BP86/TZVP).

	$[\text{Zn}(\mathbf{3})]$	$[\text{Zn}(\mathbf{3})(\text{py})]$	$[\text{Zn}(\text{sal})]$	$[\text{Zn}(\text{sal})(\text{py})]$
Zn-O_{eq}	1.967	2.030	1.948	2.001
Zn-O_{eq}	1.967	2.034	1.950	1.999
Zn-N_{eq}	2.033	2.083	2.067	2.120
Zn-N_{eq}	2.032	2.079	2.067	2.117
Zn-X_{ax}	-	2.048	-	2.087
O_{eq}-Zn-O_{eq}	98.7	94.9	96.4	95.1
O_{eq}-Zn-X_{ax}	-	105.1	-	100.3
O_{eq}-Zn-X_{ax}	-	103.4	-	99.9
N_{eq}-Zn-X_{ax}	-	103.6	-	103.2
N_{eq}-Zn-X_{ax}	-	104.4	-	102.9

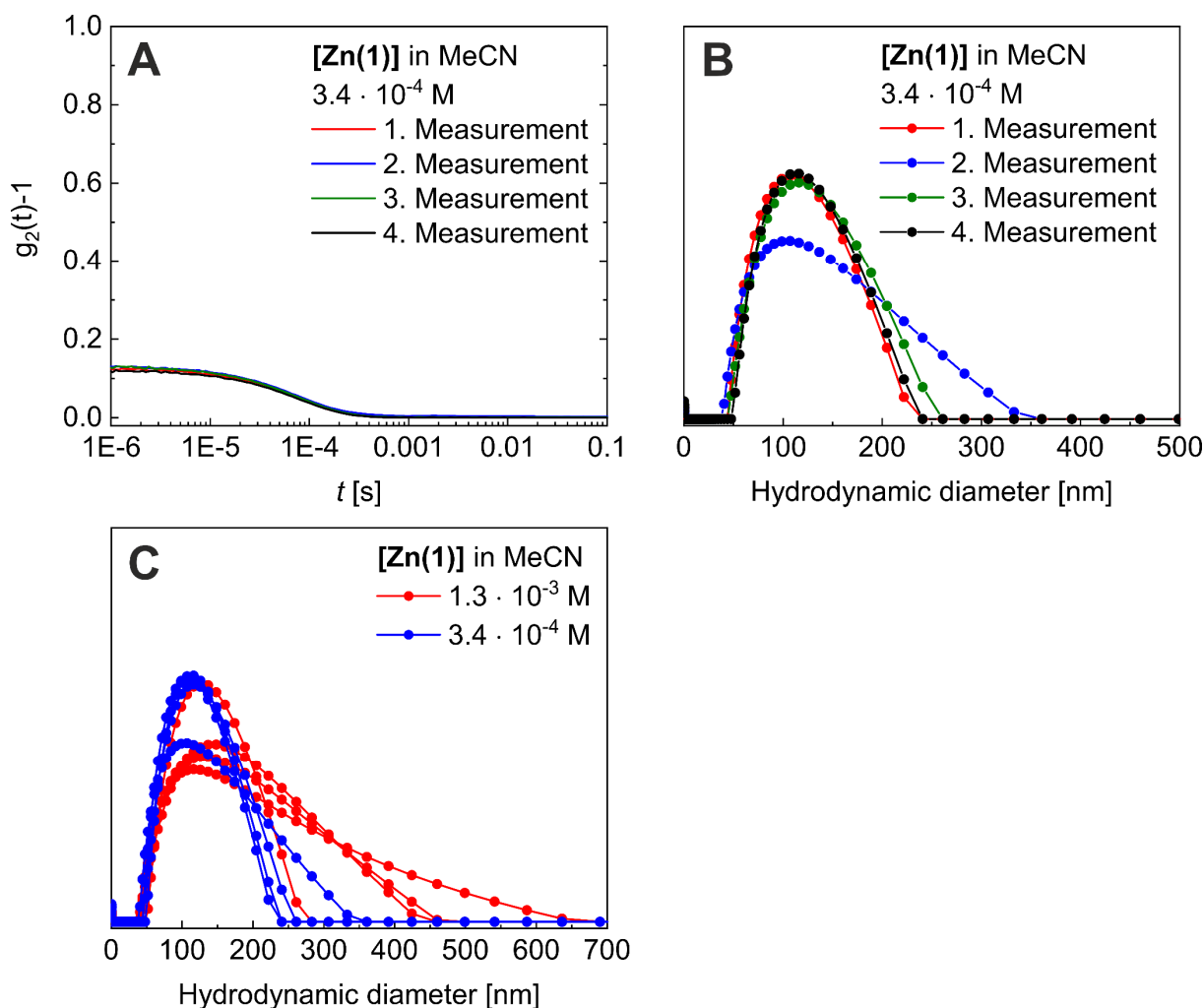


Figure S23: DLS measurements of $[\text{Zn}(\mathbf{1})]$ in MeCN (A/B) (3.4×10^{-4} M): Autocorrelation function $g_2(t)-1$ vs t (A) and corresponding D_{hydro} distribution (B). D_{hydro} distribution of $[\text{Zn}(\mathbf{1})]$ in MeCN at different concentrations (1.3×10^{-3} M: red; 3.4×10^{-4} M: blue) (C). All measurements were repeated 4 times and measured at 25°C . The solutions were filtered through a prefilter with pore size $1.0/0.45 \mu\text{m}$ to remove dust particles.

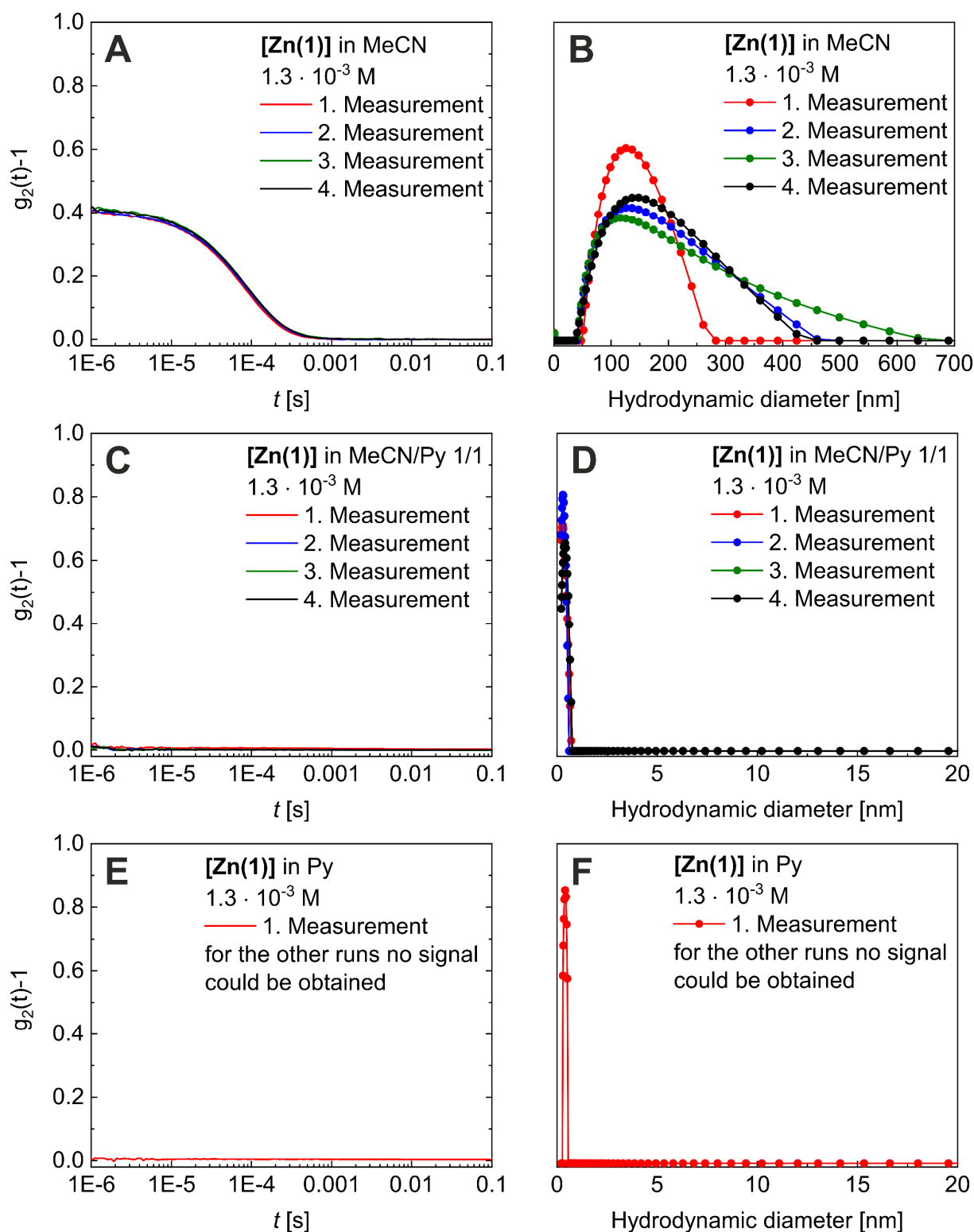


Figure S24: DLS measurements of [Zn(1)] in MeCN (A/B), MeCN/Py 1/1 (C/D), and pyridine (E/F) (1.3×10^{-3} M): Autocorrelation function $g_2(t)-1$ vs t (A/C/E) and corresponding D_{hydro} distribution (B/D/F). All measurements were repeated 4 times and measured at 25°C. The solutions were filtered through a prefilter with pore size 1.0/0.45 μm to remove dust particles.

Table S7: Selected coordination metrics in optimized dimeric structures of $[\text{Zn}(\mathbf{1})]$ and $[\text{Zn}(\text{sal})]$ (BP86/TZVP).

	Zn_2O_2 core		macrocycle $(\text{ZnO})_2$		
	$[\text{Zn}(\text{sal})]_2$	$[\text{Zn}(\mathbf{1})]_2$	$[\text{Zn}(\mathbf{1})]_2$	$[\text{Zn}(\mathbf{1})]_2 \cdot \text{py}$	$[\text{Zn}(\mathbf{1})\text{py}]_2$
Zn1-O_{eq}	2.023	2.035	2.014	2.028	2.023
Zn1-O_{eq}	1.970	1.983	1.994	2.049	2.042
Zn1-N_{eq}	2.093	2.046	2.062	2.104	2.092
Zn1-N_{eq}	2.067	2.028	2.084	2.083	2.084
Zn1-O_{ax}	2.146	2.175	2.115	2.517	2.599
Zn1-N_{ax}	-	-	-	2.132	2.130
Zn2-O_{eq}	2.022	2.036	2.026	2.021	2.036
Zn2-O_{eq}	1.972	1.984	2.004	2.005	2.031
Zn2-N_{eq}	2.089	2.046	2.055	2.057	2.077
Zn2-N_{eq}	2.065	2.027	2.071	2.066	2.090
Zn2-O_{ax}	2.147	2.175	2.099	2.109	2.618
Zn2-N_{ax}	-	-	-	-	2.119
Zn1-Zn2	2.989	3.051	5.829	6.111	6.379

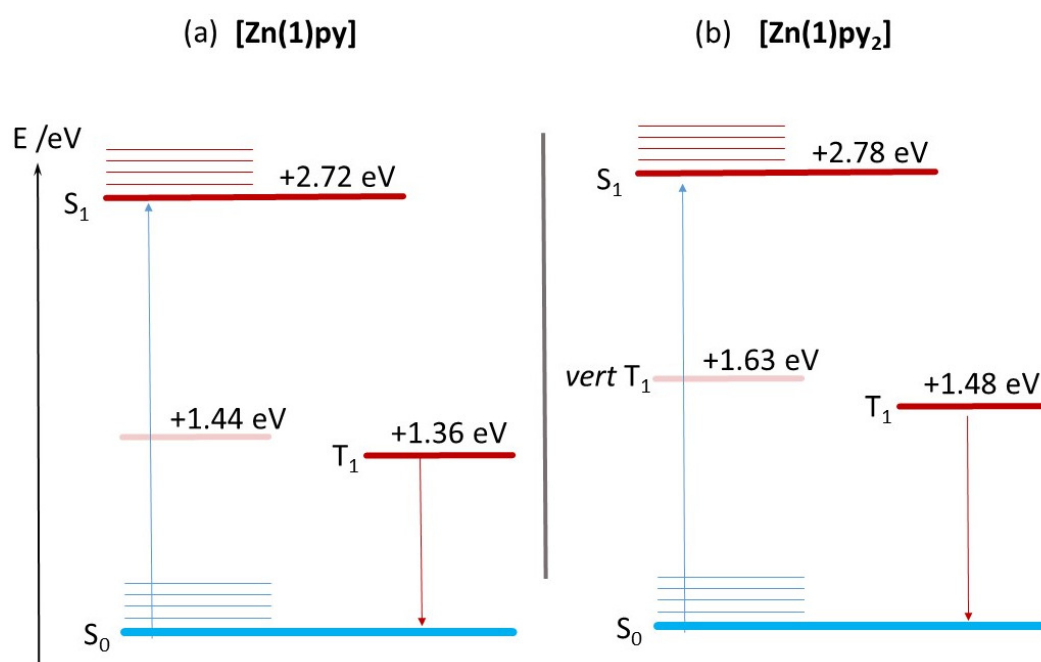


Figure S25: Jablonski diagrams of $[\text{Zn}(\mathbf{1})\text{py}]$ (a) and $[\text{Zn}(\mathbf{1})\text{py}_2]$ (b); data from KS-DFT and TD-DFT ($S_0 \rightarrow S_1$) (TPSSh/TZVP).

7 Self-Assembled Fluorescent Block Copolymer Micelles with Responsive Emission

Hannah Kurz, Christian Hils, Jana Timm, Gerald Hörner, Andreas Greiner, Roland Marschall, Holger Schmalz, Birgit Weber*

H. Kurz, Dr. G. Hörner, Prof. Dr. B. Weber: Department of Chemistry, Inorganic Chemistry IV, University of Bayreuth, Universitätsstrasse 30, 95447 Bayreuth (Germany), E-mail: weber@uni-bayreuth.de

C. Hils, Prof. Dr. A. Greiner, Dr. H. Schmalz: Macromolecular Chemistry and Bavarian Polymer Institute, University of Bayreuth, Universitätsstrasse 30, 95447 Bayreuth (Germany)

Dr. J. Timm, Prof. Dr. R. Marschall: Department of Chemistry, Physical Chemistry III, University of Bayreuth, Universitätsstrasse 30, 95447 Bayreuth (Germany)

Published in: *Angew. Chem. Int. Ed.* **2022**, *61*, e202117570. (DOI: [10.1002/anie.202117570](https://doi.org/10.1002/anie.202117570)).

Reproduced by permission from WILEY-VCH GmbH.

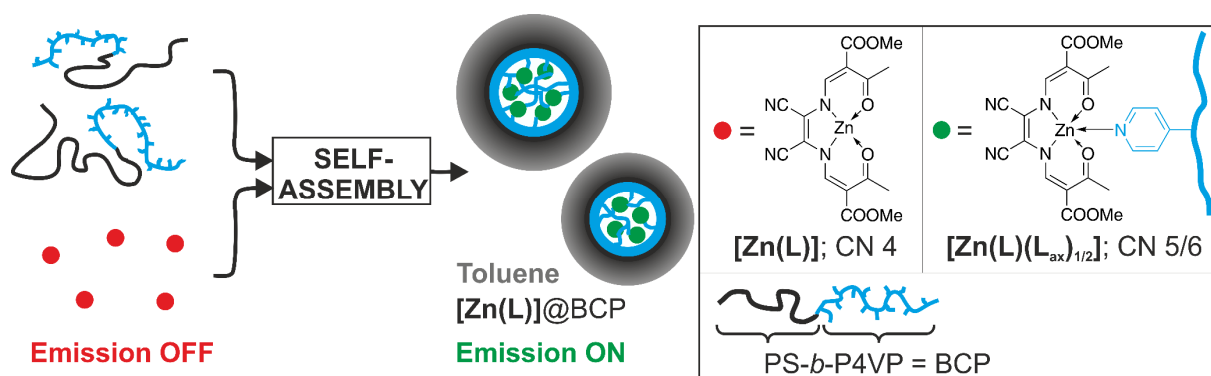
Abstract: Responsive fluorescent materials offer a high potential for sensing and (bio-)imaging applications. To investigate new concepts for such materials and to broaden their applicability, the previously reported non-fluorescent zinc(II) complex **[Zn(L)]** that shows coordination-induced turn-on emission was encapsulated into a family of non-fluorescent polystyrene-*block*-poly(4-vinylpyridine) (PS-*b*-P4VP) diblock copolymer micelles leading to brightly emissive materials. Coordination-induced turn-on emission upon incorporation and ligation of the **[Zn(L)]** in the P4VP core outperform parent **[Zn(L)]** in pyridine solution with respect to lifetimes, quantum yields, and temperature resistance. The quantum yield can be easily tuned by tailoring the selectivity of the employed solvent or solvent mixture and, thus, the tendency of the PS-*b*-P4VP diblock copolymers to self-assemble into micelles. A medium-dependent off-on sensor upon micelle formation could be established by suppression of non-micelle-borne emission background pertinent to chloroform through controlled acidification indicating an additional pH-dependent process.

6.1 Introduction

A very topical area of supramolecular research aims at tailor-made responsive materials through encapsulation of functional units in nanocontainers such as coordination cages or micelles. Self-assembled materials of this kind offer nanoscale confinements that are interesting for applications in the field of drug delivery,¹⁻⁵ as reaction vessels,⁶⁻⁹ or storage rooms for reactive/instable molecules.¹⁰ Medium properties such as polarity will typically differ significantly between the insoluble, nanoscopic core of the micelles (confinement) and the surrounding medium (solvent and soluble micelle corona). If photoluminescent, in particular nanocontainers can perform favorably as optical sensors, due to their high sensitivity towards the nature and properties of the nanoscopic environment, including viscosity or polarity, concentration-dependent effects such as aggregation, and intermolecular interactions.¹¹⁻¹⁴ In most reported cases, the nanocontainers are not directly involved in the diagnostic modulation of emission but offered a pseudo-stationary, passive nanoconfinement for the incorporation of photoluminescent (multicomponent) compounds in a non-luminescent matrix.^{15,16} For instance, Müller *et al.* reported on the determination of the critical micelle concentration (cmc) of block copolymer micelles, by using the fluorophore pyrene as a sensor for polarity changes upon micelle formation.^{13,17-19} Complementary approaches utilized fluorescent surfactants.²⁰⁻²³ Notably, both approaches are based on intrinsically fluorescent building blocks, in which the emissive properties can be modulated by external stimuli.

In this study, we provide access to a new type of micelle sensor materials via a conceptually different approach. Herein, the block copolymer plays two roles, (i) as the micelle building unit and (ii) as the chemical stimulus to activate the emission of a latent fluorophore (see Scheme 1). Previous work from our labs has shown that the polystyrene-*block*-poly(4-vinylpyridine) (PS-*b*-P4VP) diblock copolymer can indeed act as a host for functional complexes through self-assembly in selective solvents such as THF and toluene.²⁴ As Göbel *et al.* have demonstrated, the incorporation of switchable iron(II) spin crossover complexes or zinc(II) coordination polymers is driven by the coordination by the pendant pyridine units of the P4VP block.²⁵⁻²⁷ In this study, these pyridine moieties are used as anchoring units for sub-coordinated zinc complexes. We adapt the effect of coordination-activated emission of Schiff base zinc(II) complexes which had been put forward by Di Bella *et al.* Such zinc(II) complexes feature no emission in the stacked state in non-coordinating solvents, whereas coordination-induced destacking results in a *turn-on* of a strong green emission.²⁸⁻³⁵

Herein, we show that Di Bella's concept can indeed be transferred to micelles so that fluorescent micelles are synthesized via self-assembly from non-fluorescent hosts and non-fluorescent guests. As shown in Scheme 1, we report on the synthesis and characterization of fluorescent micelles through encapsulation of the non-fluorescent zinc(II) module $[\text{Zn}(\text{L})]$ into micelles derived from a family of non-fluorescent PS-*b*-P4VP diblock copolymers. The encapsulated zinc(II) complex showed decent quantum yields of bright green fluorescence which tends to increase with the amount of anchoring sites in the micelle cores. Excited-singlet state lifetimes indicate a massive stabilization of the emissive state against thermal deactivation upon encapsulation of $[\text{Zn}(\text{L})]$ into the micelles. Responsivity of emission was studied by varying solvent quality including the effect of medium-responsive self-assembly behavior and by addition of acids. Their potential as a thermally robust medium-responsive fluorescent *turn-on* sensor is highlighted.



Scheme 1: Representation of the basic principle of the self-assembly of fluorescent micelles in toluene using the non-fluorescent zinc(II) module $[\text{Zn}(\text{L})]$ with the used abbreviations. L: planar-directing N_2O_2 ligand equipped with nitrile substituents.

6.2 Results and Discussion

In selective non-polar solvents such as toluene, micelles are formed through self-assembly of the PS-*b*-P4VP BCPs. The low solubility of P4VP favors aggregation of the P4VP blocks to define the dense core of the micelles, whereas the soluble PS blocks form the corona with a significantly lower segment density.^{24,36,37} Empty micelles have been prepared from three different PS-*b*-P4VP BCPs with varying composition but comparable overall molecular weights ($\text{S}_{58}\text{V}_{42}$ ¹⁵⁷, $\text{S}_{65}\text{V}_{35}$ ¹³¹, and $\text{S}_{85}\text{V}_{15}$ ¹⁵⁴; subscripts: weight fraction of the respective block in wt%; superscript: number average molecular weight in kg mol^{-1}). $[\text{Zn}(\text{L})]@BCP$ micelles were prepared by heating the respective BCP and $[\text{Zn}(\text{L})]$ (100:1 (w/w)) for 2 h under reflux in toluene. Afterwards, the solvent was removed and the compounds were dried *in vacuo*.

The hydrodynamic diameters (D_h) and core diameters (D_{core}) of the BCP micelles were determined by dynamic light scattering (DLS) and transmission electron microscopy (TEM), respectively (Table 1, Figure 1, S1–4). Hydrodynamic diameters D_h vary only slightly ($150 < D_h < 170$ nm), irrespective of composition and/or complex load. By contrast, TEM measurements reveal a significant dependence of D_{core} on the weight fraction of the insoluble P4VP block for all micelles.

Table 1: D_h (DLS) and D_{core} (TEM) of the neat BCP and $[\text{Zn}(\text{L})]@\text{BCP}$ micelles in toluene.

Compound	D_h [nm]	D_{core} [nm]
$\text{S}_{58}\text{V}_{42}^{157}$	170 ± 46	64 ± 7
$[\text{Zn}(\text{L})]@\text{S}_{58}\text{V}_{42}^{157}$	167 ± 42	56 ± 8
$\text{S}_{65}\text{V}_{35}^{131}$	151 ± 39	51 ± 6
$[\text{Zn}(\text{L})]@\text{S}_{65}\text{V}_{35}^{131}$	152 ± 37	47 ± 6
$\text{S}_{85}\text{V}_{15}^{154}$	159 ± 40	30 ± 5
$[\text{Zn}(\text{L})]@\text{S}_{85}\text{V}_{15}^{154}$	160 ± 44	31 ± 4

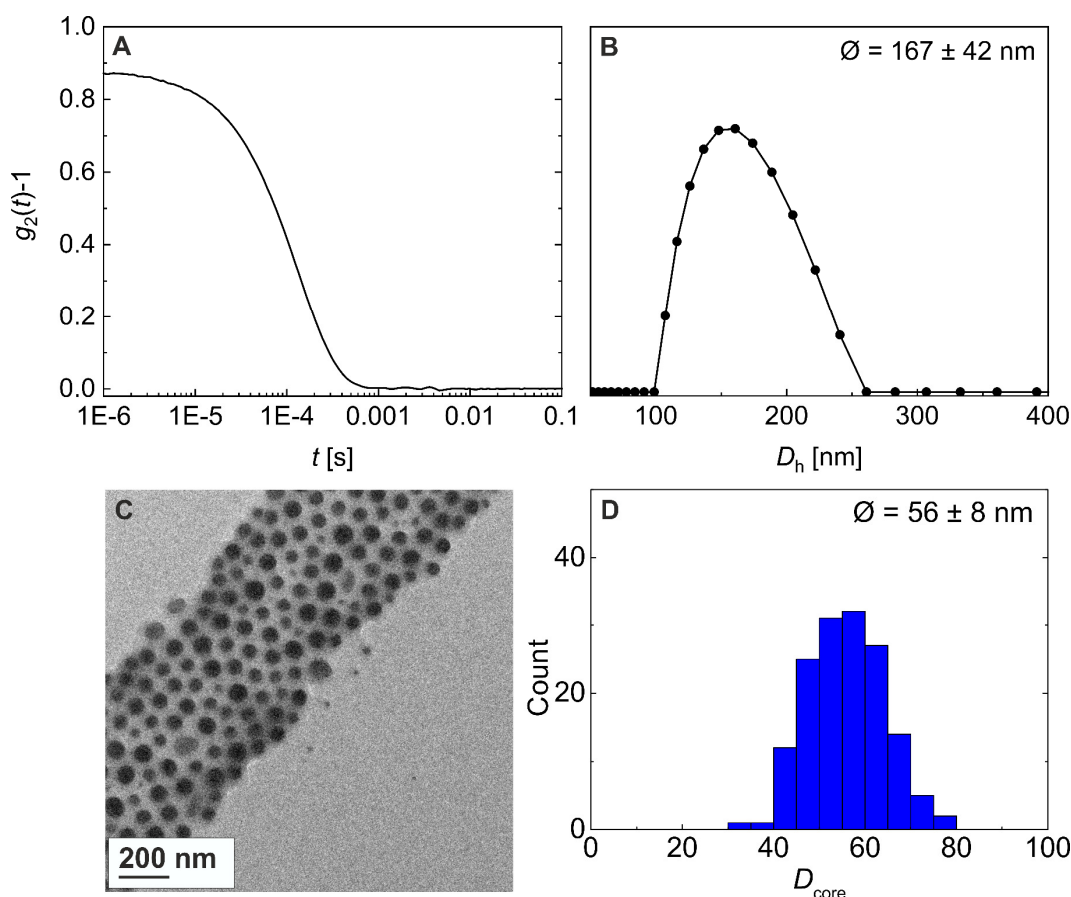


Figure 1: Autocorrelation function $g_2(t)-1$ vs. t (A) and D_h distribution of $[\text{Zn}(\text{L})]@\text{S}_{58}\text{V}_{42}^{157}$ micelles in toluene (B). TEM image of $[\text{Zn}(\text{L})]@\text{S}_{58}\text{V}_{42}^{157}$ micelles in toluene (C) and corresponding core size (D_{core}) distribution derived from TEM image analysis (D). Due to the higher electron density contrast the Zn-complex loaded P4VP cores of the micelles appear dark in TEM (C).

For instance, the compound $[\text{Zn}(\text{L})]@\text{S}_{85}\text{V}_{15}^{154}$ with the lowest P4VP fraction features the smallest D_{core} (31 ± 4 nm), whereas a nearly doubled D_{core} (56 ± 8 nm) was observed for $[\text{Zn}(\text{L})]@\text{S}_{58}\text{V}_{42}^{157}$. Besides this size correlation, TEM measurements confirm that the incorporation of $[\text{Zn}(\text{L})]$ does not alter the morphology of the micelles as in all cases spherical micelles were obtained. DLS measurements show that all micelles were well-dispersed in toluene and that the observed aggregation of the micelles in TEM images is due to drying effects upon sample preparation (Figure S1, S3).

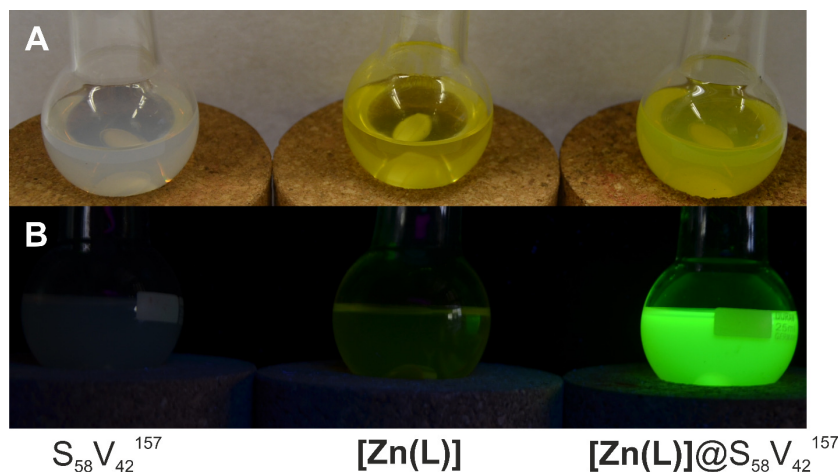


Figure 2: Photograph of the solutions from left to right of $\text{S}_{58}\text{V}_{42}^{157}$ BCP (3.3 g L^{-1}), $[\text{Zn}(\text{L})]$ (0.033 g L^{-1}), and $[\text{Zn}(\text{L})]@\text{S}_{58}\text{V}_{42}^{157}$ (3.3 g L^{-1} BCP and 0.033 g L^{-1} $[\text{Zn}(\text{L})]$) in toluene after heating under reflux for 10 min. Samples under day light (A) and in the dark under irradiation with $\lambda_{\text{ex}} = 365$ nm (B).

Obviously, formation of $[\text{Zn}(\text{L})]@\text{BCP}$ hybrids in toluene results in a drastically enhanced emission. For instance, dispersions of micellar $[\text{Zn}(\text{L})]@\text{S}_{58}\text{V}_{42}^{157}$ feature a strong green emission (see Figure 2 right panel and video in the Supporting Information). By contrast, heating of either $\text{S}_{58}\text{V}_{42}^{157}$ or $[\text{Zn}(\text{L})]$ separately in toluene does not result in an emissive solution (see Figure 2 left and middle panel and S5B). The close-to-perfect match of both absorption and emission spectra of $[\text{Zn}(\text{L})]@\text{BCP}$ in toluene with the data of neat five-coordinate $[\text{Zn}(\text{L})\text{py}]$ in pyridine, strongly hints towards incorporation of the initially non-fluorescent $[\text{Zn}(\text{L})]$ into the micelle core and ligation of the pendant pyridine moieties of P4VP within the micelle core. All $[\text{Zn}(\text{L})]@\text{BCP}$ composites give absorption spectra, which nicely match the absorbance behavior of neat $[\text{Zn}(\text{L})]$ in pyridine (Figure 3A for normalized spectra and Figure S5C, D);³⁵ namely two main absorbance bands at $\lambda = 458$ nm and $\lambda = 482$ nm. Additionally, the corrected (for details please see Supporting Information) emission and fluorescence excitation spectra of the $[\text{Zn}(\text{L})]@\text{BCP}$ composites fully reflect the photoluminescent properties of $[\text{Zn}(\text{L})]$ in pyridine (Figure 3B for normalized spectra and

Figure S5E, F).³⁵ A strong green double-peak emission with the emission maximum at $\lambda_{em,max} = 509$ nm, which can be clearly attributed to five-coordinate $[\text{Zn}(\text{L})\text{x}]$, is observed for all compounds (x : axial ligand). While the emission wavelength is similar for isoconcentrated samples ($c = 0.2$ g L⁻¹) of all three $[\text{Zn}(\text{L})]@\text{BCP}$ micelles, a remarkable difference in the emission intensity is observed (Figure S5E and photographs in Figure S6). Thereby, a higher P4VP content results in a higher emission intensity.

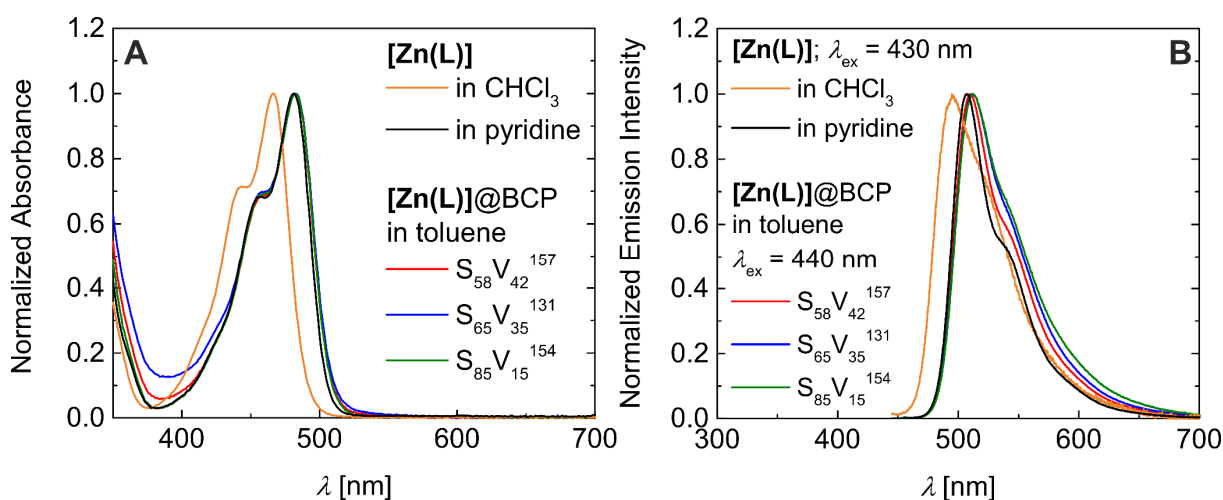


Figure 3: Normalized absorbance spectra of $[\text{Zn}(\text{L})]@\text{BCP}$ vs. BCP in toluene (A). Normalized emission spectra of $[\text{Zn}(\text{L})]@\text{BCP}$ in toluene ($\lambda_{ex} = 440$ nm, B).

Table 2: Quantum yields (Φ_{Em}) and excited state lifetimes (τ) (with relative intensities) of $[\text{Zn}(\text{L})]$ in pyridine and $[\text{Zn}(\text{L})]@\text{BCP}$ in toluene derived from the lifetime measurements.

Compound	Φ_{Em} [%]	τ_1 [ns] at 293 K	τ_2 [ns] at 293 K
$[\text{Zn}(\text{L})]$ in pyridine	15	1.3 (100%)	-
$[\text{Zn}(\text{L})]@\text{S}_{58}\text{V}_{42}^{157}$ in toluene	33	3.0 (62%)	1.7 (38%)
$[\text{Zn}(\text{L})]@\text{S}_{65}\text{V}_{35}^{131}$ in toluene	23	2.9 (51%)	1.5 (49%)
$[\text{Zn}(\text{L})]@\text{S}_{85}\text{V}_{15}^{154}$ in toluene	16	2.8 (34%)	1.2 (66%)

This finding is reflected as well in the quantum yields (Φ_{Em}) and the excited state lifetimes (τ) of $[\text{Zn}(\text{L})]@\text{BCP}$ in toluene (Table 2). Hereby, $[\text{Zn}(\text{L})]@\text{S}_{85}\text{V}_{15}^{154}$ features the smallest quantum yield with 16 %, whereas a quantum yield of 33 % is observed for $[\text{Zn}(\text{L})]@\text{S}_{58}\text{V}_{42}^{157}$. The enhanced quantum yield goes along with longer lifetimes of the biexponential decays. This apparent correlation of the P4VP ratio and emission might be correlated with the amount of potential donors. Indeed, simplified calculations reveal a significant divergence in the number of 4VP units relative to $[\text{Zn}(\text{L})]$ (ratios $[\text{4VP}] : [\text{Zn}] = 190 : 1$ for $\text{S}_{58}\text{V}_{42}^{157}$, $158 : 1$ for $\text{S}_{65}\text{V}_{35}^{131}$, and $68 : 1$ for $\text{S}_{85}\text{V}_{15}^{154}$; Table S1, detailed calculation is given in the Supporting Information). However, the general absence of the four-coordinate species, as deduced from the absorbance

spectra of all samples, contradicts this idea. Rather, the significant divergence in the excited state lifetimes may be referred to fluctuations through micelle dynamics that enables a higher degree of swelling. Clearly, non-radiative deactivation is promoted in micelles with a smaller D_{core} that feature an increased surface to volume ratio. Moreover, the shorter P4VP block length enables a higher toluene content inside the core leading to increased dynamics.

Interestingly, the quantum yields of all $[\text{Zn}(\text{L})]@\text{BCP}$ micelles ($\Phi_{\text{Em}} = 16\text{--}33\%$) are higher than the quantum yield of neat $[\text{Zn}(\text{L})]$ in pyridine ($\Phi_{\text{Em}} = 15\%$). This finding is also reflected in the longer excited state lifetimes of all $[\text{Zn}(\text{L})]@\text{BCP}$ composites in toluene compared to neat $[\text{Zn}(\text{L})]$ in pyridine (Table 2). Neat $[\text{Zn}(\text{L})]$ in pyridine features a monoexponential fluorescence decay with a lifetime of $\tau = 1.3$ ns at room temperature. By contrast, time-correlated single photon counting (TCSPC) measurements of all $[\text{Zn}(\text{L})]@\text{BCP}$ compounds gave biexponential decays with a longer lifetime of $\tau_1 = 2.8\text{--}3.0$ ns and a second shorter lifetime of $\tau_2 = 1.2\text{--}1.7$ ns.

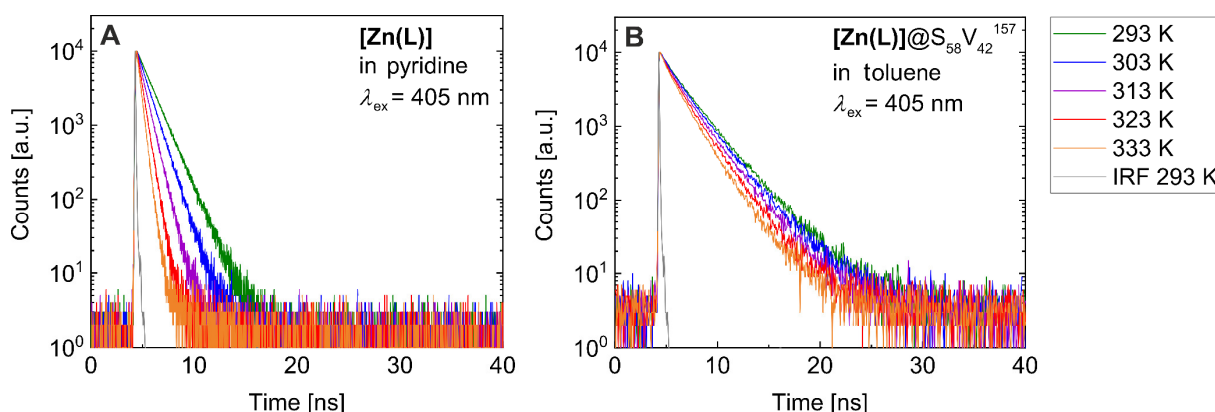
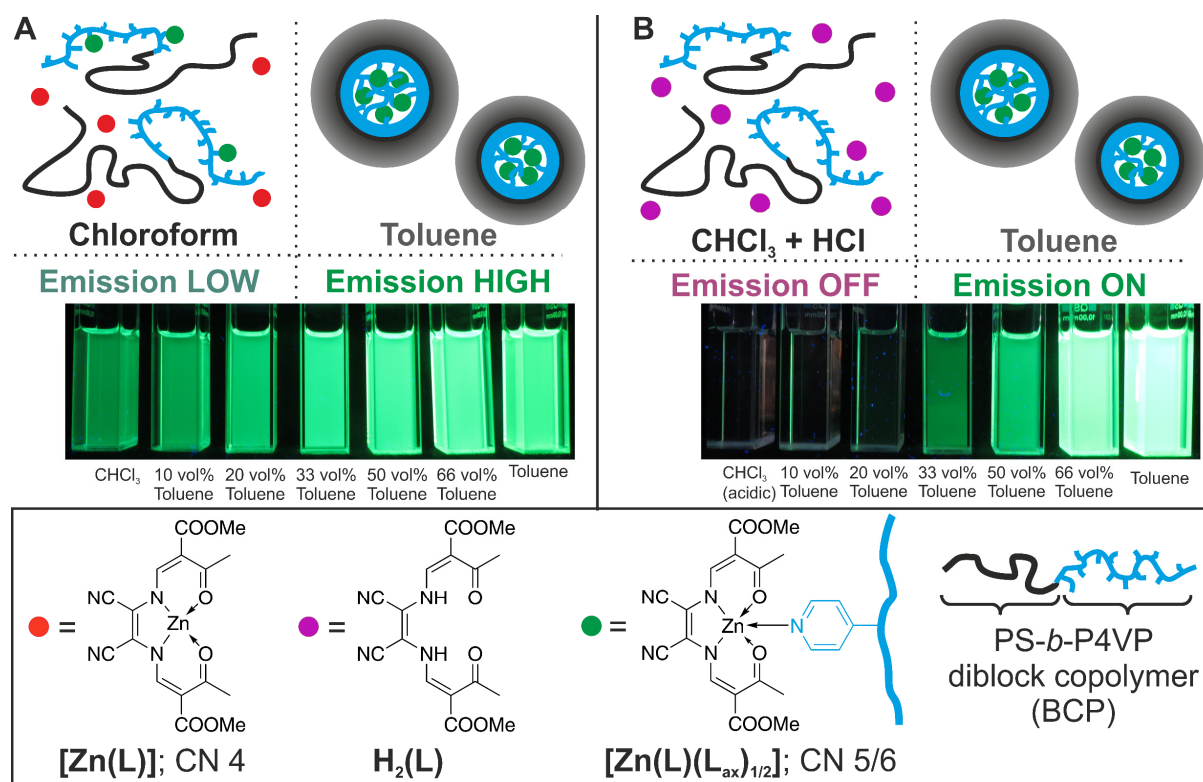


Figure 4: Temperature-dependent fluorescence decays of $[\text{Zn}(\text{L})]$ in pyridine (A) and $[\text{Zn}(\text{L})]@\text{S}_{58}\text{V}_{42}^{157}$ micelles (B) in toluene ($\lambda_{\text{ex}} = 405$ nm; $\lambda_{\text{em}} = 509$ nm) detected by time-correlated single photon counting (TCSPC).

Increased quantum yields of fluorophores due to embedment into micelles have been observed before.^{38–40} Typically, the more favorable photophysics is associated with the decreased mobility of the fluorophore inside the micelles, which disfavours non-radiative deactivation. In the present case, this effect is even more impressive upon heating (Figure 4, Figure S7, S8 and Table S2). In contrast to the drastic lifetime decrease of neat $[\text{Zn}(\text{L})]$ in pyridine upon heating to 333 K (Arrhenius activation energy $E_{\text{A}} = 26.1 \pm 1.1$ kJ mol⁻¹), $[\text{Zn}(\text{L})]@\text{BCP}$ show only a minor temperature dependence ($[\text{Zn}(\text{L})]@\text{S}_{58}\text{V}_{42}^{157}$: $E_{\text{A}}(\tau_1) = 5.3 \pm 0.6$ kJ mol⁻¹, $E_{\text{A}}(\tau_2) = 5.1 \pm 1.4$ kJ mol⁻¹, Figure S9). Strong changes of the viscosity can be ruled out within the measured

temperature range, because even the highest temperature of 333 K is well below the glass transition of P4VP ($T_g \approx 420$ K).⁴¹



Scheme 2: Representation of the basic principle of the medium-dependent self-assembly of an emission enhancement material based on BCP micelle formation in a CHCl₃-toluene series (A) and a CHCl₃(acidic)-toluene series (B).

The pyridine concentration dependency of the emission intensity of free [Zn(L)] was previously studied directly in chloroform/pyridine mixtures, where a *turn-on* emission was observed upon addition of the coordinating solvent pyridine.³⁵ As the [Zn(L)]@BCP composites show a remarkable thermally stable fluorescence in the micelle form, the question arose whether the micelle form is essential for the high emission and whether it is possible to form medium-responsive sensor materials based on externally triggered self-assembly induced emission. The impact of the micelle formation was studied in non-coordinating solvent mixtures composed of a selective solvent for the PS block (toluene) inducing micelle formation and a non-selective solvent, in which the BCP is molecularly dissolved in form of unimers (chloroform). Chloroform (CHCl₃) is known as a non-selective solvent for the PS-*b*-P4VP diblock copolymers, allowing high solubility of both blocks.²⁴ This results in molecularly dissolved PS-*b*-P4VP diblock copolymers (unimers) in toluene-poor mixtures up to a threshold concentration of 20 vol% (Figure S10, S11). The same observation holds for the composite [Zn(L)]@S₅₈V₄₂¹⁵⁷, ruling out significant influence of the host on the micelle formation

(Table 3, Figure S12, S13). Remarkably, the $[\text{Zn}(\text{L})]@\text{BCP}$ composites show a medium-responsive emission behavior, making them highly interesting for sensor applications (Scheme 2).

Table 3: Hydrodynamic diameters: D_h (DLS) of the empty BCP $\text{S}_{58}\text{V}_{42}^{157}$ and $[\text{Zn}(\text{L})]@\text{S}_{58}\text{V}_{42}^{157}$.

	CHCl ₃ -toluene series		CHCl ₃ (acidic)-toluene series
	D_h [nm] of $\text{S}_{58}\text{V}_{42}^{157}$	D_h [nm] of $[\text{Zn}(\text{L})]@\text{S}_{58}\text{V}_{42}^{157}$	D_h [nm] of $[\text{Zn}(\text{L})]@\text{S}_{58}\text{V}_{42}^{157}$
CHCl ₃	- [a]	- [a]	- [a]
10 vol% toluene	- [a]	- [a]	- [a]
20 vol% toluene	- [a]	- [a]	- [a]
33 vol% toluene	90 ± 25	93 ± 27	104 ± 29
50 vol% toluene	114 ± 34	120 ± 37	131 ± 32
66 vol% toluene	150 ± 45	148 ± 42	163 ± 47
100 vol% toluene	156 ± 34	161 ± 38	160 ± 37

[a] no micelle formation observed (Figure S10, S12, and S14).

Across an isoconcentrated series of $[\text{Zn}(\text{L})]@\text{S}_{58}\text{V}_{42}^{157}$ in CHCl₃-toluene mixtures, the emission clearly increases with increasing toluene content (Scheme 2A). Consequently, while the overall pyridine amount provided by the P4VP units of the BCP is not altered in the micelle formation process, the local effective concentration needs to be massively affected, when going from the molecularly dissolved form in CHCl₃ to the micelle form in toluene. Indeed, the effective pyridine concentration is drastically lower in the molecularly dissolved form ($5 \cdot 10^{-4}$ M) compared to the micelle form (11 M) (calculations are given in the Supporting Information). Based on the optical properties of $[\text{Zn}(\text{L})]@\text{S}_{58}\text{V}_{42}^{157}$ in the CHCl₃-toluene series, we conclude that the emission changes are due the medium-dependent self-assembly of the micelles as shown in Scheme 2A.

Despite the low effective pyridine concentration in the molecularly dissolved form, still a non-negligible amount of potentially coordinative pyridine units is present, which interferes with the aimed *off-on* behavior of the sensor. We reported previously on the close-to-zero emission of the ligand $\text{H}_2(\text{L})$ in both solvents, CHCl₃ and pyridine.³⁵ To obtain a sharp *off-on* emission, we used acidified chloroform to consciously disrupt the parent zinc(II) complex to form the free ligand $\text{H}_2(\text{L})$ and a soluble but not further defined zinc(II) species, according to: $[\text{Zn}(\text{L})] + 2 \text{H}^+ \rightarrow \text{H}_2(\text{L}) + * \text{Zn}^{2+}$.³⁵ For this reason, CHCl₃ was acidified by extraction with hydrochloric acid (see Experimental Section for details) and denoted as CHCl₃(acidic) in the following. Upon micelle formation across the CHCl₃(acidic)-toluene series of $[\text{Zn}(\text{L})]@\text{S}_{58}\text{V}_{42}^{157}$, coordinated $[\text{Zn}(\text{L})]$ in the micelle core is increasingly protected from the acid by the basic pyridine substituents. This effect is further increased by the decreasing content

of acid across the series and the lower accessibility of the core in toluene-rich mixtures. This principle indeed allows *turn-on* emission upon micelle formation as shown in Scheme 2B.

DLS measurements of the CHCl₃-toluene and CHCl₃(acidic)-toluene series show that the shape and size of the micelles are not significantly affected, neither by the presence of acid nor [Zn(L)]. DLS measurements of both series confirm that micelles are formed from a volume fraction of 33 vol% toluene onwards (D_h values in Table 3 and corresponding autocorrelation functions and D_h distributions in Figure S10–S15). A further rise of the toluene percentage results in an increase of D_h up to approximately 160 nm. While the presence of [Zn(L)] does not alter D_h at all, the values are slightly increased for the acidified CHCl₃(acidic)-toluene mixtures. This finding indicates that the presence of acid results in enhanced swelling of the micelles.

Through extended absorbance, emission, and fluorescence excitation studies across both solvent series we could establish a direct correlation between the onset of micelle formation and on-set of the emission rise. As the dynamics of block copolymer micelles are rather slow, we allowed all solutions to equilibrate for at least 30 min prior to measurements.⁴² As expected, the absorbance behavior of [Zn(L)]@S₅₈V₄₂¹⁵⁷ in the non-acidified CHCl₃-toluene series is only marginally dependent on the CHCl₃-toluene mixing ratio. Only a minor red-shift from $\lambda = 471$ nm (CHCl₃) to $\lambda = 483$ nm (toluene) can be deduced (Figure S16A). This shift is in line with the observations made with free [Zn(L)] in CHCl₃/pyridine mixtures at increased pyridine loads. It likewise indicates an enhanced coordination of [Zn(L)] at a higher toluene content.³⁵ The slight absorbance changes observed even below 33 vol% toluene indicate some sort of pre-aggregation prior to micelle formation, that is also reflected in the scattering of the neat BCP in the absorbance measurements even below micelle formation (Figure S17A). In the emission spectra, a successive emission intensity increase can be observed with increasing toluene content. Nevertheless, no *off-on* sensor behavior could be obtained due to a non-negligible emission intensity observed for [Zn(L)]@S₅₈V₄₂¹⁵⁷ in non-acidified CHCl₃ (see photograph in Scheme 2A and Figure S16B, D). Fluorescence excitation spectra confirm that this emission is based on axially coordinated [Zn(L)] (Figure S16C). Obviously, no medium-dependent *turn-on* sensor material was obtained due to a non-negligible concentration of potentially coordinative P4VP units in CHCl₃. However, the strongly increased effective pyridine concentration upon micelle formation and the stabilization of radiative pathways upon encapsulation result in a drastic emission enhancement.

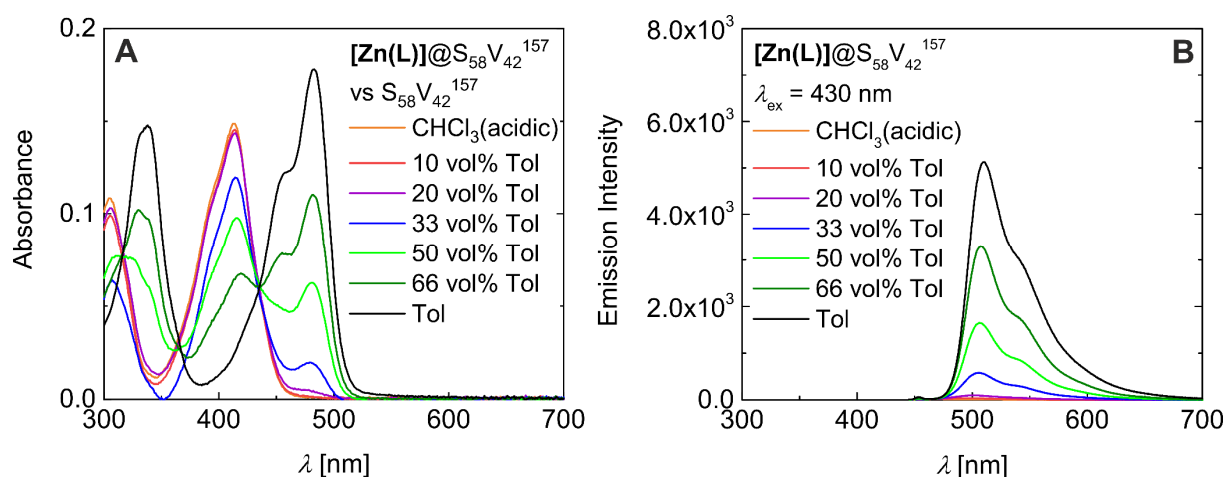


Figure 5: Absorbance (A) and emission (B) spectra of $[\text{Zn}(\text{L})]@S_{58}V_{42}^{157}$ in a $\text{CHCl}_3(\text{acidic})$ -toluene series ($\lambda_{\text{ex}} = 430 \text{ nm}$). Please note that the weak emission band at approximately $\lambda = 450 \text{ nm}$ is a measurement artefact.

Based on absorption spectra recorded of neat $[\text{Zn}(\text{L})]$ and encapsulated $[\text{Zn}(\text{L})]@S_{58}V_{42}^{157}$ across a CHCl_3 - $\text{CHCl}_3(\text{acidic})$ mixture series (Figure S18A, S19A and associated DLS profiles for $[\text{Zn}(\text{L})]@S_{58}V_{42}^{157}$ in Figure S20), we can attribute the acid-dependent effects on the integrity of the zinc complex itself. The maximum absorbance band at $\lambda = 414 \text{ nm}$ in acidified CHCl_3 can be clearly attributed to the ligand $\text{H}_2(\text{L})$, which indicates (reversible) dissociation of the complex $[\text{Zn}(\text{L})]$. Notably, acidification of CHCl_3 results in a drastic emission reduction in both cases, $[\text{Zn}(\text{L})]$ and $[\text{Zn}(\text{L})]@S_{58}V_{42}^{157}$ (Figure S18B, S19B). The impact of acid was further verified by addition of acetic acid to a toluene solution of $[\text{Zn}(\text{L})]@S_{58}V_{42}^{157}$. Even addition of tiny amounts of organic acid results in the formation of the ligand and a drastic emission quenching, while conserving the micelle form (Figure S21, S22).

Remarkably, the absorption spectra of $[\text{Zn}(\text{L})]@S_{58}V_{42}^{157}$ remain indicative of the free ligand $\text{H}_2(\text{L})$ up to a volume fraction of 20 vol% toluene in the series $\text{CHCl}_3(\text{acidic})$ -toluene (Figure 5A). Likewise, these solutions show no significant fluorescence, in accordance with the almost negligible emission of the ligand ($\Phi_{\text{Em}} \approx 10^{-4}$).³⁵ The normalized fluorescence excitation spectra confirm that the very weak emission is solely based on the ligand (normalized spectra in Figure S23). Only upon a further increase of the toluene content the specific absorbance band of $[\text{Zn}(\text{L})]$ at $\lambda = 479 \text{ nm}$ re-appears (Figure 5A). Comparison with the absorbance behavior of neat $[\text{Zn}(\text{L})]$ in pyridine indicates that the absorbance behavior in toluene-rich mixtures is dominated by P4VP-coordinated $[\text{Zn}(\text{L})]$ within the micelle core.³⁵ The change in absorption is accompanied by a *switch-on* emission (Figure 5B). The striking emission increase starting at 33 vol% toluene is shown in a photograph in Scheme 2B. Interestingly, the emission increases above 33 vol% toluene in a nearly linear manner (Figure 6). Hereby, two correction possibilities

are plotted to show that this trend is retained for both possibilities: The correction of the emission versus the absorbance value at $\lambda_{\text{ex}} = 430$ nm using the pure solvent as background (red) and using the neat BCP micelles as background (black). Notably, both linear fits (pink and cyan lines) cross the x-axis at approximately 25 vol% toluene. These values not only strongly support our finding that the micelle formation occurs in between 20 to 33 vol% as observed by DLS, but also that the micelle formation is the decisive requirement for efficient fluorescence. Thereby the micelles act as a host of a very special kind as they also provide the chemical stimulus for the *turn-on* emission (Scheme 3).

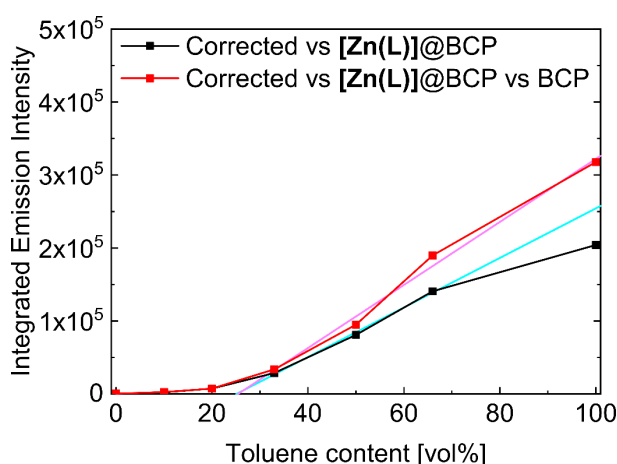
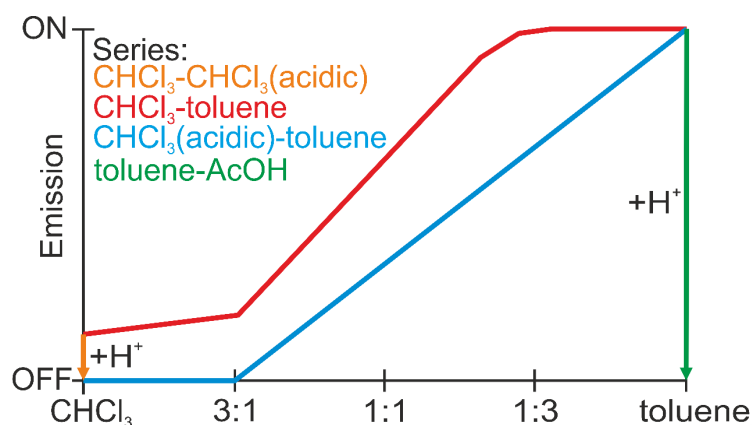


Figure 6: Plot of the integrated emission intensity vs. toluene content of $[\text{Zn}(\text{L})]@ \text{S}_{58}\text{V}_{42}^{157}$. Two background correction possibilities are plotted to show that this trend is retained for both possibilities: Correction of the emission vs. the absorbance value at $\lambda_{\text{ex}} = 430$ nm i) of the pure solvent (red) and ii) of the empty BCP micelles (black). Please note that the emission intensity increase is slightly smaller when the scattering effects of the BCP micelles in the UV/Vis measurements are not taken into account (black curve). Hereby, the rather high scattering especially in pure toluene results in an artificially decreased emission. For this reason, this point was neglected in the linear fit (pink and cyan line).



Scheme 3: Summary of the medium-dependent emission behavior of $[\text{Zn}(\text{L})]@ \text{S}_{58}\text{V}_{42}^{157}$.

6.3 Conclusion

In this work PS-*b*-P4VP diblock copolymer (BCP) micelles with varying fractions of pyridine anchor residues are shown to be excellent, multifunctional platforms for the intra-micellar fixation and activation of proto-fluorophores. The family of [Zn(L)]@BCP materials, which anchor and activate non-fluorescent [Zn(L)] within the micelles, exhibits a strong green emission with significantly enhanced quantum yields as compared to parent [Zn(L)] in pyridine. Embedding of the fluorophore within the insoluble P4VP core effectively prevents dynamic quenching, yielding longer fluorescent lifetimes, higher fluorescence quantum yields and very efficient protection against temperature variation. In combination with facile processability, these favorable emission properties offer a wide applicability as strongly emissive pH-responsive films. Embedding and activation of [Zn(L)] parallels the medium-responsive self-assembly of the diblock copolymer, yielding very weakly emissive aggregates in chloroform where the molecularly dissolved form is observed, whereas in toluene efficient micelle formation supports bright emission. According to DLS measurements, the micelle formation occurs in between 20 to 33 vol% toluene, which coincides with the onset of emission. An even sharper contrast between the emission of the molecularly dissolved form and the micelle form could be obtained through depression of the weak background in chloroform. Acidification to yield the close-to-zero emissive ligand H₂(L) provides remarkable *turn-on* emission that is coupled to the micelle formation in the acidified CHCl₃(acidic)/toluene series of [Zn(L)]@S₅₈V₄₂¹⁵⁷. Alternatively, the emission in toluene can be switched off upon addition of organic acids, while maintaining the micelle form. The basic principle to couple coordination-induced emission with self-assembled BCP micelles offers a new strategy to design fluorescent sensor materials for a broad application range.

6.4 Notes and References

Acknowledgement

Financial supports from the Fonds der Chemischen Industrie (Kekulé-Stipendium), MINT-Lehramt Plus, German Research foundation (SFB840; projects A2, A10, and project 463161096 (B.W.)), the BayNAT program, and the University of Bayreuth are gratefully acknowledged. We thank Dr. Markus Drechsler (Keylab Electron and Optical Microscopy, Bavarian Polymer Institute, University of Bayreuth) for TEM measurements, Prof. Dr. Hans-Werner Schmidt for access to the fluorospectrometer for the steady-state measurements, Lisa Leitner for the introduction to the DLS instrument, and Prof. Dr. Mirijam Zobel for access to

the DLS litesizer. We acknowledge the Keylab “Synthesis and Molecular Characterization” of the Bavarian Polymer Institute (University of Bayreuth) for providing access to the anionic polymerization facilities. Open Access funding enabled and organized by Project DEAL.

Conflict of Interest

The authors declare no conflict of interest.

Keywords: Block Copolymers • Fluorescence • Micelles • Schiff Bases • Sensors

References

- (1) Cabral, H.; Miyata, K.; Osada, K.; Kataoka, K. Block Copolymer Micelles in Nanomedicine Applications. *Chem. Rev.* **2018**, *118* (14), 6844–6892. DOI: 10.1021/acs.chemrev.8b00199.
- (2) Iyisan, B.; Kluge, J.; Formanek, P.; Voit, B.; Appelhans, D. Multifunctional and Dual-Responsive Polymersomes as Robust Nanocontainers: Design, Formation by Sequential Post-Conjugations, and pH-Controlled Drug Release. *Chem. Mater.* **2016**, *28* (5), 1513–1525. DOI: 10.1021/acs.chemmater.5b05016.
- (3) Cheng, C.-C.; Sun, Y.-T.; Lee, A.-W.; Huang, S.-Y.; Fan, W.-L.; Chiao, Y.-H.; Chiu, C.-W.; Lai, J.-Y. Hydrogen-bonded supramolecular micelle-mediated drug delivery enhances the efficacy and safety of cancer chemotherapy. *Polym. Chem.* **2020**, *11* (16), 2791–2798. DOI: 10.1039/d0py00082e.
- (4) Tawfik, S. M.; Azizov, S.; Elmasry, M. R.; Sharipov, M.; Lee, Y.-I. Recent Advances in Nanomicelles Delivery Systems. *Nanomaterials* **2020**, *11* (1), 70. DOI: 10.3390/nano11010070.
- (5) Niu, D.; Li, Y.; Shi, J. Silica/organosilica cross-linked block copolymer micelles: a versatile theranostic platform. *Chem. Soc. Rev.* **2017**, *46* (3), 569–585. DOI: 10.1039/c6cs00495d.
- (6) Fang, Y.; Powell, J. A.; Li, E.; Wang, Q.; Perry, Z.; Kirchon, A.; Yang, X.; Xiao, Z.; Zhu, C.; Zhang, L.; Huang, F.; Zhou, H.-C. Catalytic reactions within the cavity of coordination cages. *Chem. Soc. Rev.* **2019**, *48* (17), 4707–4730. DOI: 10.1039/c9cs00091g.
- (7) Gaitzsch, J.; Huang, X.; Voit, B. Engineering Functional Polymer Capsules toward Smart Nanoreactors. *Chem. Rev.* **2016**, *116* (3), 1053–1093. DOI: 10.1021/acs.chemrev.5b00241.
- (8) Boucher-Jacobs, C.; Rabnawaz, M.; Katz, J. S.; Even, R.; Guironnet, D. Encapsulation of catalyst in block copolymer micelles for the polymerization of ethylene in aqueous medium. *Nat. Commun.* **2018**, *9* (1), 841. DOI: 10.1038/s41467-018-03253-5.
- (9) Gao, J.; Le, S.; Thayumanavan, S. Enzyme Catalysis in Non-Native Environment with Unnatural Selectivity Using Polymeric Nanoreactors. *Angew. Chem. Int. Ed.* **2021**, *60*, 27189–27194. DOI: 10.1002/anie.202109477.
- (10) Grommet, A. B.; Feller, M.; Klajn, R. Chemical reactivity under nanoconfinement. *Nat. Nanotechnol.* **2020**, *15* (4), 256–271. DOI: 10.1038/s41565-020-0652-2.
- (11) Zhou, Y.; Gao, H.; Zhu, F.; Ge, M.; Liang, G. Sensitive and rapid detection of aliphatic amines in water using self-stabilized micelles of fluorescent block copolymers. *J. Hazard. Mat.* **2019**, *368*, 630–637. DOI: 10.1016/j.jhazmat.2019.01.097.
- (12) Wang, S.; Jin, B.; Chen, G.; Luo, Y.; Li, X. Aggregation-induced emission from the crowded coronal chains of block copolymer micelles. *Polym. Chem.* **2020**, *11* (29), 4706–4713. DOI: 10.1039/d0py00432d.
- (13) Pergushov, D. V.; Remizova, E. V.; Feldthusen, J.; Zezin, A. B.; Müller, A. H. E.; Kabanov, V. A. Novel Water-Soluble Micellar Interpolyelectrolyte Complexes. *J. Phys. Chem. B* **2003**, *107* (32), 8093–8096. DOI: 10.1021/jp027526l.

- (14) Valeur, B.; Berberan-Santos, M. N. *Molecular Fluorescence*; Wiley-VCH Verlag GmbH & Co. KGaA, 2012. DOI: 10.1002/9783527650002.
- (15) Pallavicini, P.; Diaz-Fernandez, Y. A.; Pasotti, L. Micelles as nanosized containers for the self-assembly of multicomponent fluorescent sensors. *Coord. Chem. Rev.* **2009**, *253* (17-18), 2226–2240. DOI: 10.1016/j.ccr.2008.11.010.
- (16) Qiao, M.; Ding, L.; Lv, F. Surfactant assemblies encapsulating fluorescent probes as selective and discriminative sensors for metal ions. *Coord. Chem. Rev.* **2021**, *432*, 213696. DOI: 10.1016/j.ccr.2020.213696.
- (17) Burkhardt, M.; Martinez-Castro, N.; Tea, S.; Drechsler, M.; Babin, I.; Grishagin, I.; Schweins, R.; Pergushov, D. V.; Gradzielski, M.; Zezin, A. B.; Müller, A. H. E. Polyisobutylene-block-poly(methacrylic acid) diblock copolymers: self-assembly in aqueous media. *Langmuir* **2007**, *23* (26), 12864–12874. DOI: 10.1021/la701807b.
- (18) Colombani, O.; Ruppel, M.; Schubert, F.; Zettl, H.; Pergushov, D. V.; Müller, A. H. E. Synthesis of Poly(n-butyl acrylate)-block-poly(acrylic acid) Diblock Copolymers by ATRP and Their Micellization in Water. *Macromolecules* **2007**, *40* (12), 4338–4350. DOI: 10.1021/ma0609578.
- (19) Li, H.; Hu, D.; Liang, F.; Huang, X.; Zhu, Q. Influence factors on the critical micelle concentration determination using pyrene as a probe and a simple method of preparing samples. *R. Soc. Open Sci.* **2020**, *7* (3), 192092. DOI: 10.1098/rsos.192092.
- (20) Wang, H.; Zhao, W.; Liu, X.; Wang, S.; Wang, Y. BODIPY-Based Fluorescent Surfactant for Cell Membrane Imaging and Photodynamic Therapy. *ACS Appl. Bio Mater.* **2020**, *3* (1), 593–601. DOI: 10.1021/acsabm.9b00977.
- (21) Smith McWilliams, A. D.; Ergülen, S.; Ogle, M. M.; los Reyes, C. A. de; Pasquali, M.; Martí, A. A. Fluorescent surfactants from common dyes – Rhodamine B and Eosin Y. *Pure Appl. Chem.* **2020**, *92* (2), 265–274. DOI: 10.1515/pac-2019-0219.
- (22) Yin, P.; Wu, P.; Xiao, Z.; Li, D.; Bitterlich, E.; Zhang, J.; Cheng, P.; Vezenov, D. V.; Liu, T.; Wei, Y. A double-tailed fluorescent surfactant with a hexavanadate cluster as the head group. *Angew. Chem. Int. Ed.* **2011**, *50* (11), 2521–2525. DOI: 10.1002/anie.201006144.
- (23) Xu, Z.; Li, P.; Qiao, W.; Li, Z.; Cheng, L. Surface and fluorescence properties of a novel fluorescent surfactant. *Colloids Surf. A* **2006**, *290* (1-3), 172–177. DOI: 10.1016/j.colsurfa.2006.05.024.
- (24) O'Driscoll, S.; Demirel, G.; Farrell, R. A.; Fitzgerald, T. G.; O'Mahony, C.; Holmes, J. D.; Morris, M. A. The morphology and structure of PS-b-P4VP block copolymer films by solvent annealing: effect of the solvent parameter. *Polym. Adv. Technol.* **2011**, *22* (6), 915–923. DOI: 10.1002/pat.1596.
- (25) Göbel, C.; Hils, C.; Drechsler, M.; Baabe, D.; Greiner, A.; Schmalz, H.; Weber, B. Confined Crystallization of Spin-Crossover Nanoparticles in Block-Copolymer Micelles. *Angew. Chem. Int. Ed.* **2020**, *59* (14), 5765–5770. DOI: 10.1002/anie.201914343.
- (26) Weber, B. Synthesis of Coordination Polymer Nanoparticles using Self-Assembled Block Copolymers as Template. *Chem. Eur. J.* **2017**, *23* (72), 18093–18100. DOI: 10.1002/chem.201703280.
- (27) Göbel, C.; Hörner, G.; Greiner, A.; Schmalz, H.; Weber, B. Synthesis of Zn-based 1D and 2D coordination polymer nanoparticles in block copolymer micelles. *Nanoscale Adv.* **2020**, *2* (10), 4557–4565. DOI: 10.1039/D0NA00334D.
- (28) Paul, M. K.; Dilipkumar Singh, Y.; Bedamani Singh, N.; Sarkar, U. Emissive bis-salicylaldiminato Schiff base ligands and their zinc(II) complexes: Synthesis, photophysical properties, mesomorphism and DFT studies. *J. Mol. Struct.* **2015**, *1081*, 316–328. DOI: 10.1016/j.molstruc.2014.10.031.
- (29) Consiglio, G.; Failla, S.; Oliveri, I. P.; Purrello, R.; Di Bella, S. Controlling the molecular aggregation. An amphiphilic Schiff-base zinc(II) complex as supramolecular fluorescent probe. *Dalton Trans.* **2009**, (47), 10426–10428. DOI: 10.1039/b914930a.

- (30) Xie, D.; Jing, J.; Cai, Y.-B.; Tang, J.; Chen, J.-J.; Zhang, J.-L. Construction of an orthogonal ZnSalen/Salophen library as a colour palette for one- and two-photon live cell imaging. *Chem. Sci.* **2014**, *5* (6), 2318. DOI: 10.1039/c3sc53299b.
- (31) Forte, G.; Oliveri, I. P.; Consiglio, G.; Failla, S.; Di Bella, S. On the Lewis acidic character of bis(salicylaldehydato)zinc(II) Schiff-base complexes: a computational and experimental investigation on a series of compounds varying the bridging diimine. *Dalton Trans.* **2017**, *46* (14), 4571–4581. DOI: 10.1039/c7dt00574a.
- (32) Consiglio, G.; Oliveri, I. P.; Cacciola, S.; Maccarrone, G.; Failla, S.; Di Bella, S. Dinuclear zinc(II) salen-type Schiff-base complexes as molecular tweezers. *Dalton Trans.* **2020**, *49* (16), 5121–5133. DOI: 10.1039/d0dt00494d.
- (33) Oliveri, I. P.; Malandrino, G.; Di Bella, S. Phase transition and vapochromism in molecular assemblies of a polymorphic zinc(II) Schiff-base complex. *Inorg. Chem.* **2014**, *53* (18), 9771–9777. DOI: 10.1021/ic5013632.
- (34) Strianese, M.; Guarnieri, D.; Lamberti, M.; Landi, A.; Peluso, A.; Pellecchia, C. Fluorescent salen-type Zn(II) Complexes As Probes for Detecting Hydrogen Sulfide and Its Anion: Bioimaging Applications. *Inorg. Chem.* **2020**, *59* (21), 15977–15986. DOI: 10.1021/acs.inorgchem.0c02499.
- (35) Kurz, H.; Hörner, G.; Weser, O.; Manni, G. L.; Weber, B. Quenched Lewis Acidity: Studies on the Medium Dependent Fluorescence of Zinc(II) Complexes. *Chem. Eur. J.* **2021**, *27* (27), 15159–15171. DOI: 10.1002/chem.202102086.
- (36) Kumar, L.; Horechyy, A.; Bittrich, E.; Nandan, B.; Uhlmann, P.; Fery, A. Amphiphilic Block Copolymer Micelles in Selective Solvents: The Effect of Solvent Selectivity on Micelle Formation. *Polymers* **2019**, *11* (11), 1882. DOI: 10.3390/polym11111882.
- (37) Ali, N.; Park, S.-Y. Micellar structures of poly(styrene-*b*-4-vinylpyridine)s in THF/toluene mixtures and their functionalization with gold. *Langmuir* **2008**, *24* (17), 9279–9285. DOI: 10.1021/la800860q.
- (38) Fan, J.; Ding, L.; Fang, Y. Surfactant Aggregates Encapsulating and Modulating: An Effective Way to Generate Selective and Discriminative Fluorescent Sensors. *Langmuir* **2019**, *35* (2), 326–341. DOI: 10.1021/acs.langmuir.8b02111.
- (39) Kai, T.; Kishimoto, M.; Akita, M.; Yoshizawa, M. Encapsulation-induced emission enhancement (EIEE) of Eu(III)-complexes by aromatic micelles in water. *Chem. Comm.* **2018**, *54* (8), 956–959. DOI: 10.1039/c7cc09450g.
- (40) Geng, J.; Goh, C. C.; Tomczak, N.; Liu, J.; Liu, R.; Ma, L.; Ng, L. G.; Gurzadyan, G. G.; Liu, B. Micelle/Silica Co-protected Conjugated Polymer Nanoparticles for Two-Photon Excited Brain Vascular Imaging. *Chem. Mater.* **2014**, *26* (5), 1874–1880. DOI: 10.1021/cm4040374.
- (41) Parashar, P.; Ramakrishna, K.; Ramaprasad, A. T. A study on compatibility of polymer blends of polystyrene/poly(4-vinylpyridine). *J. Appl. Polym. Sci.* **2011**, *120* (3), 1729–1735. DOI: 10.1002/app.33314.
- (42) Denkova, A. G.; Mendes, E.; Coppens, M.-O. Non-equilibrium dynamics of block copolymer micelles in solution: recent insights and open questions. *Soft Matter* **2010**, *6*, 2351–2357. DOI: 10.1039/C001175B.

6.5 Supporting Information

Experimental section

$\text{H}_2(\text{L})$ and $[\text{Zn}(\text{L})]$ were synthesized as described in literature.¹ Please note that the complex is only sparingly soluble in neat toluene even at a lower concentration of 0.025 g/L. The polystyrene-*block*-poly(4-vinylpyridine) (PS-*b*-P4VP) diblock copolymers (BCPs) were synthesized by sequential anionic polymerization of styrene and 4-vinylpyridine according to literature.²⁻⁴ The nanocontainers are based on three different PS-*b*-P4VP-BCPs with varying composition but comparable overall molecular weights ($\text{S}_{58}\text{V}_{42}^{157}$, $\text{S}_{65}\text{V}_{35}^{131}$, and $\text{S}_{85}\text{V}_{15}^{154}$: subscripts give the fraction of the respective block in wt%; superscript denotes the number average molecular weight in kg mol^{-1}).⁵ Toluene was of analytical grade and used without further purification. Chloroform was extracted with aqueous saturated NaHCO_3 solution and dried over CaCl_2 . CHCl_3 (acidic) was prepared by extracting 50 mL dried CHCl_3 three times with 15 mL 4 M hydrochloric acid.

$[\text{Zn}(\text{L})]@\text{BCP}$. Diblock copolymer S_xV_y^z (0.150 g) and $[\text{Zn}(\text{L})]$ (0.0015 g) were heated in 60 mL toluene for 2 h under reflux. After cooling, the solvent was removed *in vacuo* and the yellow solid was dried *in vacuo*.

Characterization

Transmission electron microscopy (TEM) measurements were performed on a CEM902 microscope from Carl Zeiss Microscopy (Oberkochen, Germany). Samples were dispersed in toluene ($c = 0.67 \text{ g L}^{-1}$) and the unfiltered solutions were dropped directly on a carbon coated TEM grid. The measurements were performed at an electron acceleration voltage of 80 kV. Micrographs were taken with an Orius 830 SC200W/DigitalMicrograph version 2.3 system from Gatan (Munich, Germany). Measurements were also performed on a Zeiss/LEO EM922Omega (Carl Zeiss Microscopy, Oberkochen, Germany) at an acceleration voltage of 160kV. Micrographs were taken with a CCD UltraScan camera system (Gatan, Munich, Germany) and acquiring software Digital Micrograph version 1.9 (Gatan, Munich, Germany). The software “ImageJ” developed by Wayne Rasband was used for the particles size determinations.⁶ The diameter of 150 particles was determined and averaged.

Dynamic light scattering (DLS) measurements were conducted on an AntonPaar Litesizer 500 in fluorescence quartz glass cuvettes with a 1 cm light pathway from Hellma. The measurements were performed in backscattering mode and consisted of six consecutive runs. The samples were dispersed in toluene ($c = 0.2 \text{ g L}^{-1}$) and were not filtered. The experimental

data were fitted with a cumulative fit. Measurements were also performed on an ALV DLS/SLS-SP 5022F compact goniometer system with an ALV 5000/E cross-correlator at a scattering angle of $q = 90^\circ$ and at $T = 23^\circ\text{C}$, using a HeNe laser (max. 35 mW, $\lambda = 632.8\text{ nm}$) as the light source. The time-dependent scattering intensity was monitored with an APD (avalanche photodiode)-based pseudo cross correlation system. All samples were filled into NMR tubes (VWR, 5 mm outer diameter) for measurement. For each sample at least 3 measurements were performed. The data were evaluated using ALV Correlator software (version V.3.0.0.17 10/2002) and the implemented ALV regularized fit option ($g_2(t)$, CONTIN-analysis).

Absorption spectra were performed on a Cary 60 UV-Vis spectrometer from Agilent Technologies. The samples were dispersed in toluene ($c = 0.2\text{ g L}^{-1}$) and were not filtered. For **steady-state photoluminescence** (PL) a FP-8600 fluorescence spectrometer from JASCO was employed that is equipped with a 150 W Xe lamp as excitation source. **Time-correlated single photon counting** (TCSPC) measurements to determine emission lifetimes were performed on a FluoTime 300 spectrofluorometer from PicoQuant, using a 405 nm diode laser for excitation (Coherent COMPASS 405-50 CW), which was controlled by the PDL 820 PicoQuant laser driver. **Quantum yields** were determined at room temperature using a 78mm integrating sphere and a 300 W Xe lamp as excitation source. All measurements were conducted in quartz cells with a 1 cm lightpath from Hellma.

Correction of the optical data

Neat BCP in the respective solvent mixture was used as background for the $[\text{Zn(L)}]@\text{BCP}$ samples in the absorbance measurements to subtract the contributions of the neat BCP micelles on the absorption behavior (see Figure S5A/C/D and S15A in the SI). Please note, that the emission data was corrected against the absorbance at the excitation energy.

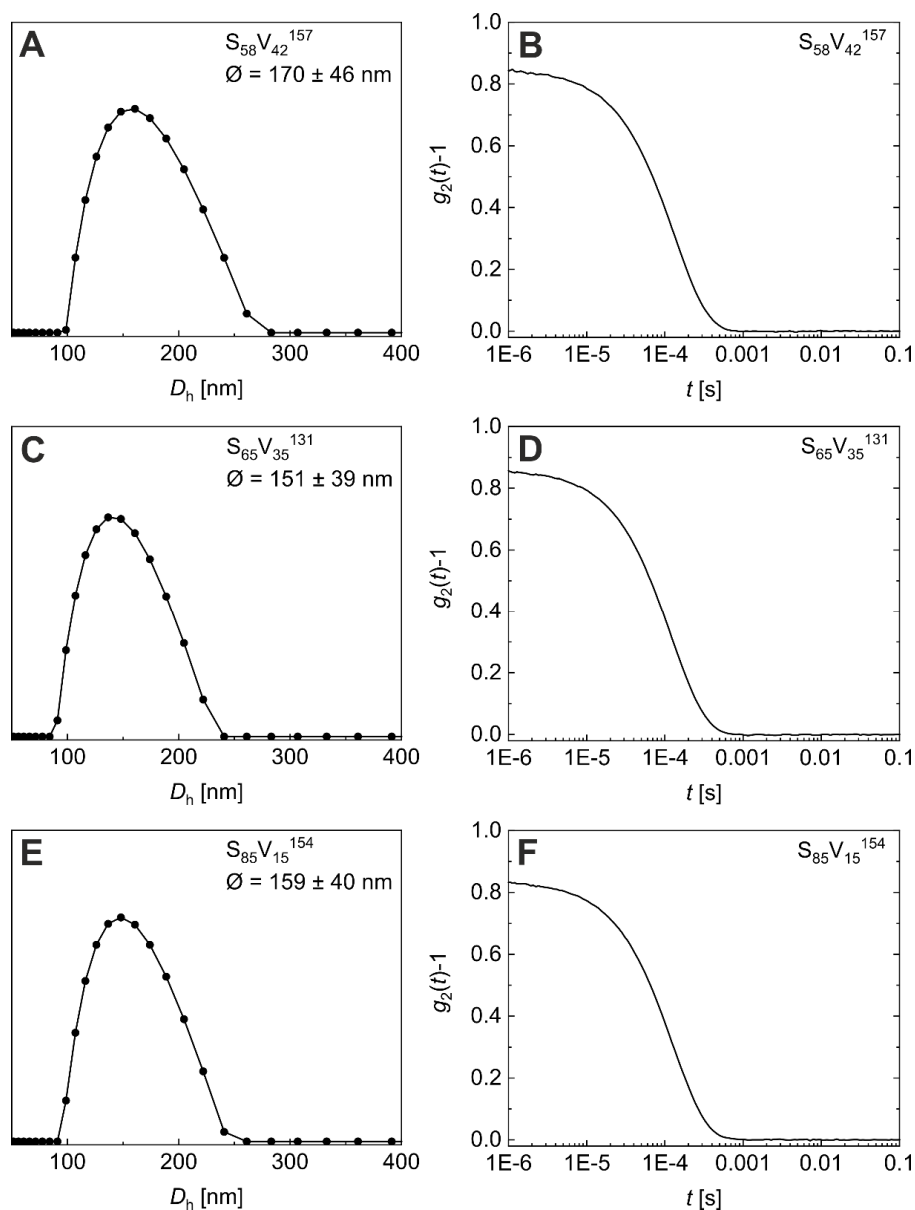


Figure S1: DLS measurements of neat BCP micelles in toluene: Hydrodynamic diameter (D_h) distributions and corresponding autocorrelation functions $g_2(t)-1$ vs t of $S_{58}V_{42}^{157}$ (A, B), $S_{65}V_{35}^{131}$ (C, D), and $S_{85}V_{15}^{154}$ (E, F).

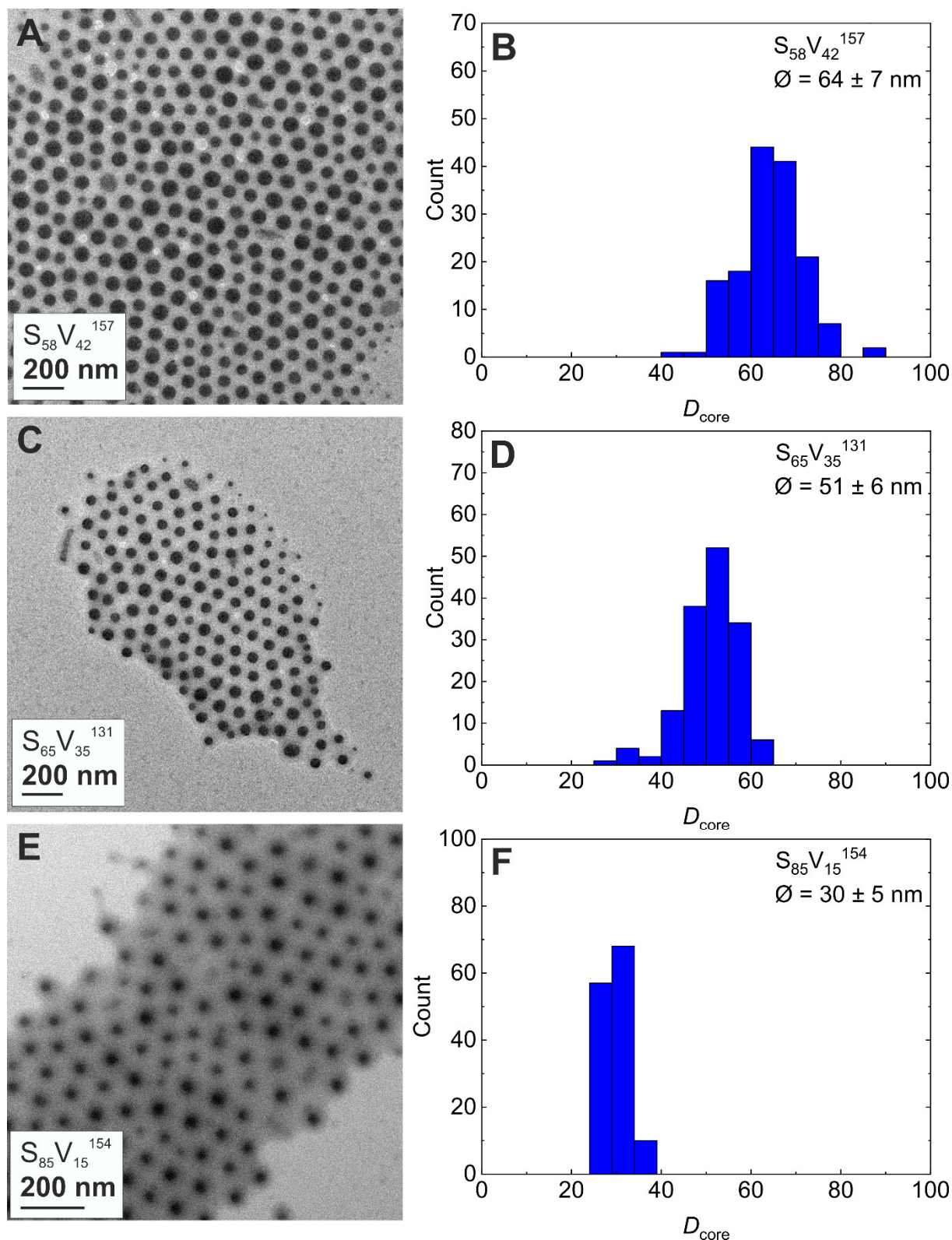


Figure S2: TEM images of neat $S_{58}V_{42}^{157}$ (A), $S_{65}V_{35}^{131}$ (C), and $S_{85}V_{15}^{154}$ (E) micelles in toluene and corresponding core size (D_{core}) distributions derived from TEM image analysis (B, D, F). Please note the different scale in E. The micelle core can be observed in TEM measurements due to the higher electron density contrast of the dense P4VP block compared to the PS corona.

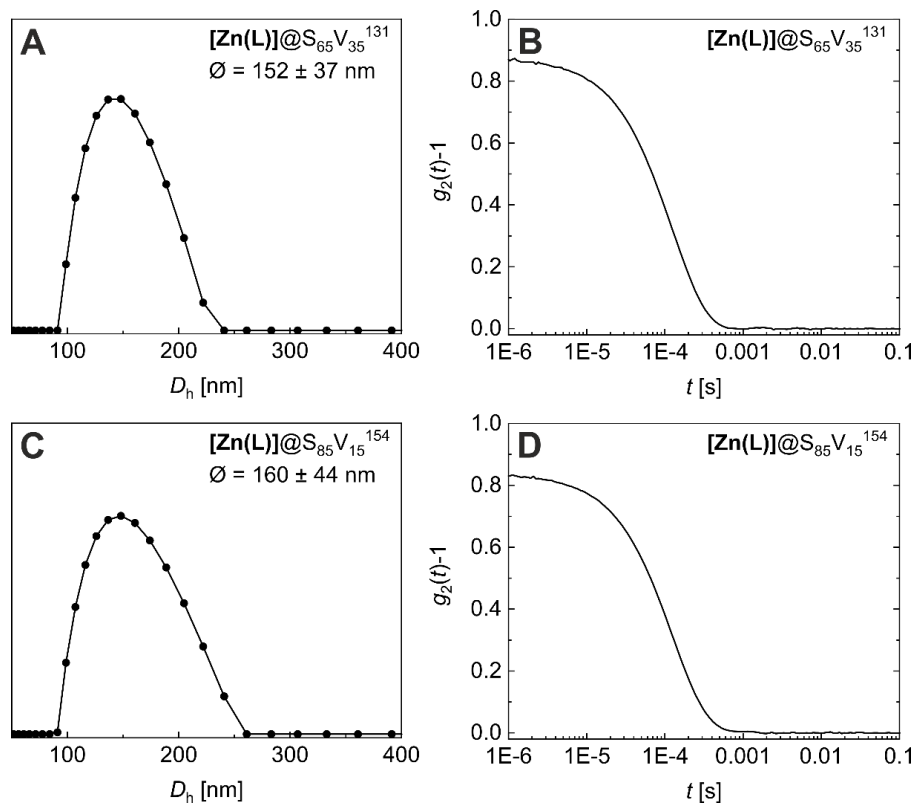


Figure S3: DLS measurements of $[\text{Zn}(\text{L})]@\text{BCP}$ in toluene: Hydrodynamic diameter (D_h) distributions and corresponding autocorrelation functions $g_2(t)-1$ vs t of $[\text{Zn}(\text{L})]@\text{S}_{65}\text{V}_{35}^{131}$ (A, B) and $[\text{Zn}(\text{L})]@\text{S}_{85}\text{V}_{15}^{154}$ (C, D).

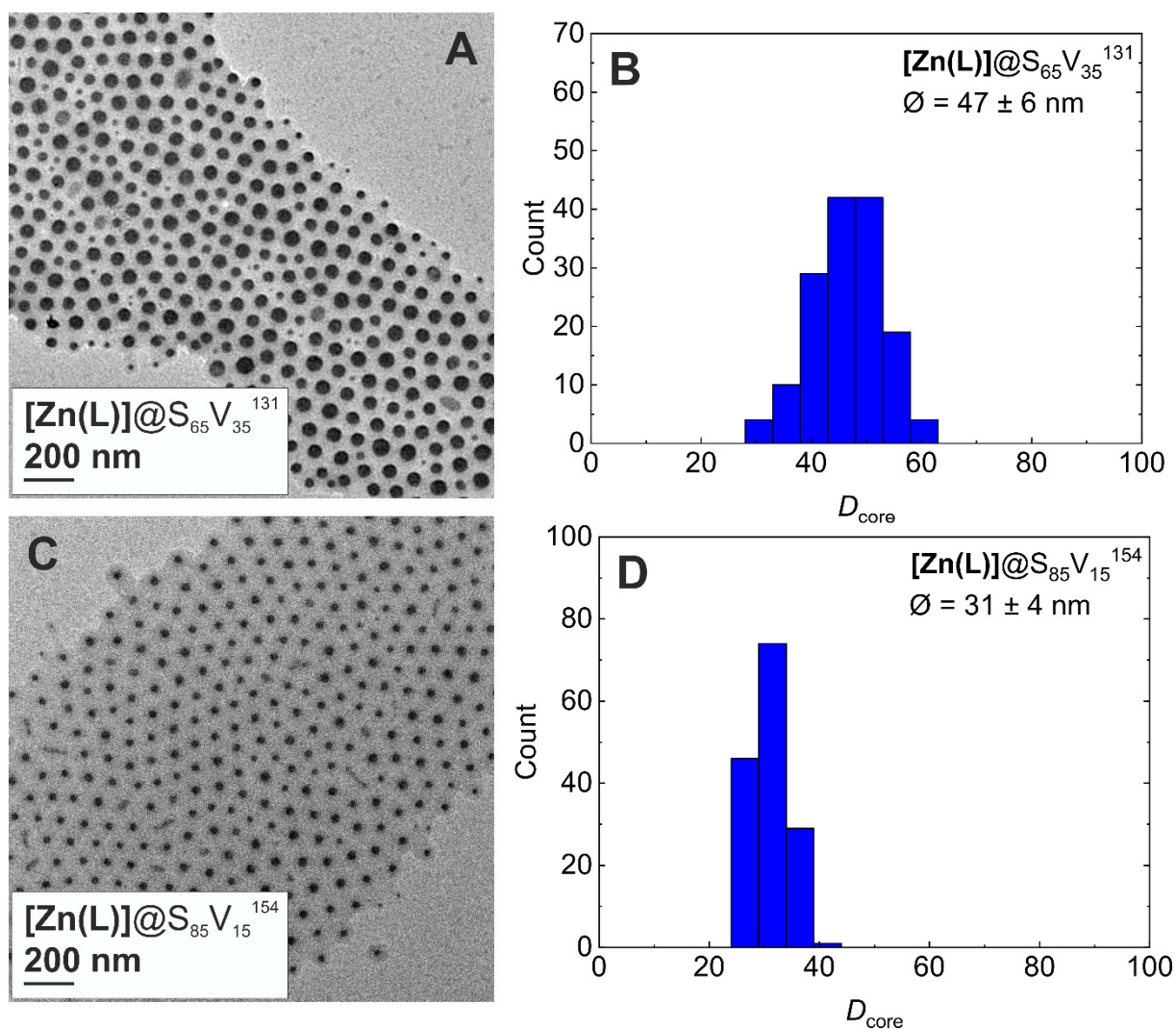


Figure S4: TEM images of $[\text{Zn(L)}]@S_{65}V_{35}^{131}$ (A) and $[\text{Zn(L)}]@S_{85}V_{15}^{154}$ (C) micelles in toluene and corresponding core size (D_{core}) distributions derived from TEM image analysis (B, D). Due to the higher electron density contrast the Zn-complex loaded P4VP cores of the micelles appear dark in TEM.

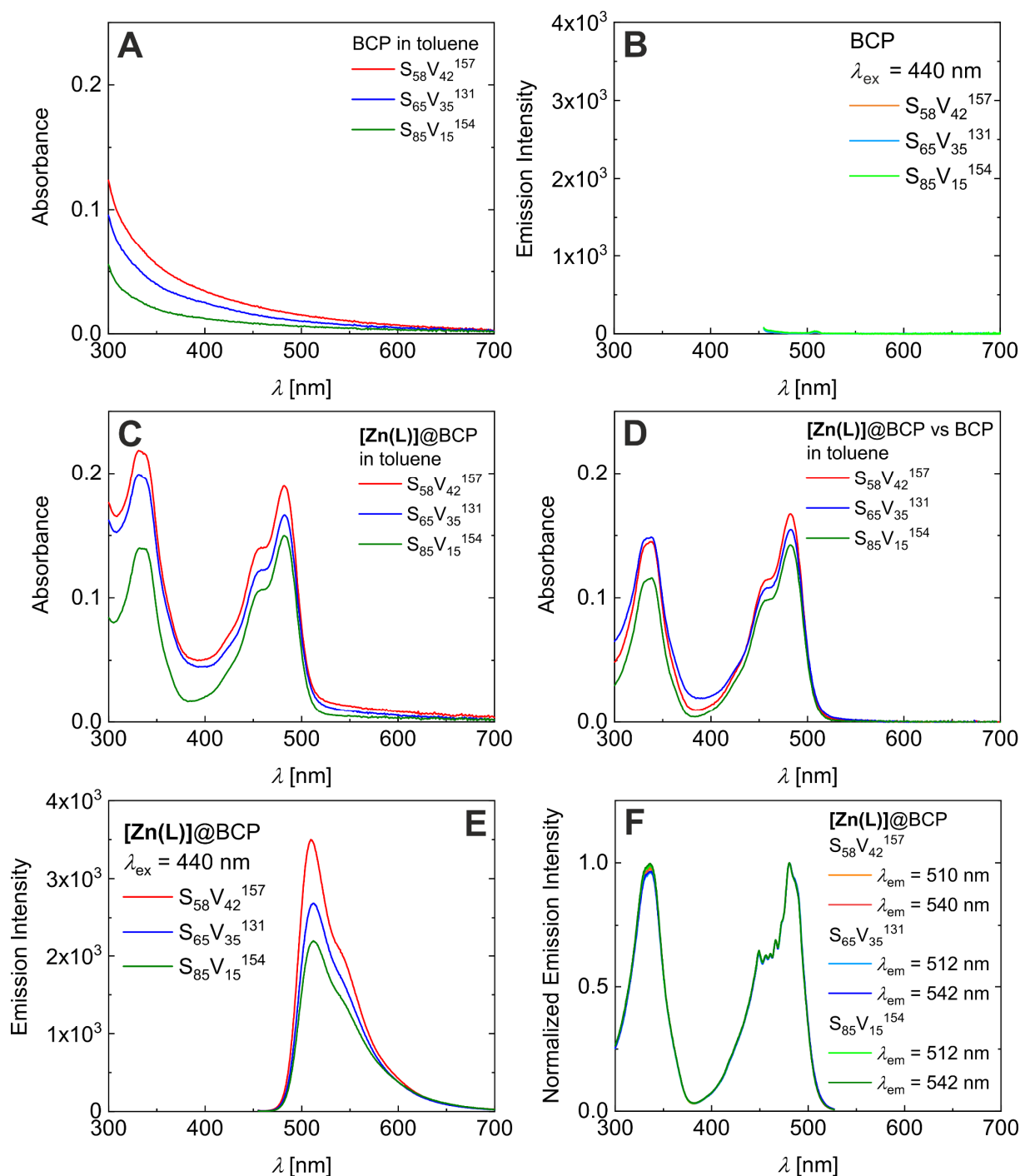
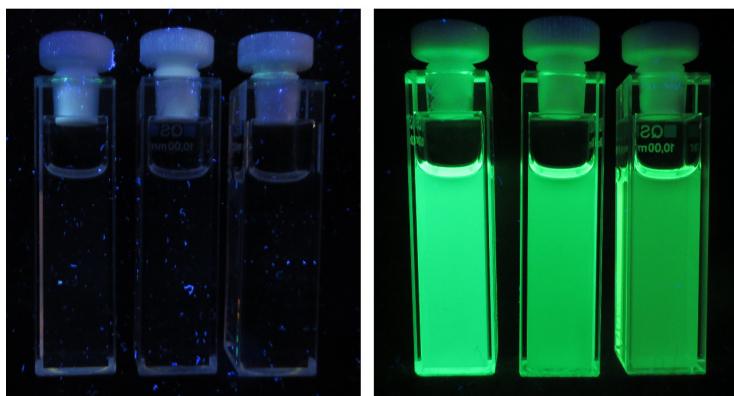


Figure S5: Absorbance (A) and emission ($\lambda_{ex} = 440$ nm, B) spectra of neat BCP micelles in toluene. Absorbance spectra of [Zn(L)]@BCP micelles in toluene corrected vs neat toluene (C) and vs the neat BCP micelles (D), respectively. Emission spectra (E) and fluorescence excitation spectra (F) of [Zn(L)]@BCP micelles in toluene.

BCP in toluene

[Zn(L)]@BCP in toluene



$S_{58}V_{42}^{157}$ $S_{65}V_{35}^{131}$ $S_{85}V_{15}^{154}$
 $S_{58}V_{42}^{157}$ $S_{65}V_{35}^{131}$ $S_{85}V_{15}^{154}$

Figure S6: Photograph of the neat BCP micelles (A) and [Zn(L)]@BCP micelles (B) in toluene ($c = 0.2$ g/L) under irradiation with $\lambda_{\text{ex}} = 365$ nm.

Calculation of equivalents of vinylpyridine compared to [Zn(L)(H₂O)(MeOH)]

The calculation is exemplary given for the $S_{58}V_{42}^{157}$ BCP.

$$m(P4VP) = 0.42 \cdot 0.004 \text{ g} = 1.68 \cdot 10^{-3} \text{ g}$$

$$n(4VP) = \frac{m(P4VP)}{M(4VP)} = \frac{1.68 \cdot 10^{-3} \text{ g}}{105.14 \text{ g mol}^{-1}} = 1.60 \cdot 10^{-5} \text{ mol}$$

$$\begin{aligned}
 n([\text{Zn}(\text{L})(\text{H}_2\text{O})(\text{MeOH})]) &= \frac{m([\text{Zn}(\text{L})(\text{H}_2\text{O})(\text{MeOH})])}{M([\text{Zn}(\text{L})(\text{H}_2\text{O})(\text{MeOH})])} = \frac{4 \cdot 10^{-5} \text{ g}}{473.75 \text{ g/mol}} \\
 &= 8.44 \cdot 10^{-8} \text{ mol}
 \end{aligned}$$

The equivalents of vinylpyridine relative to [Zn(L)(H₂O)(MeOH)] can be calculated:

$$Eq = \frac{n(4VP)}{n([\text{Zn}(\text{L})(\text{H}_2\text{O})(\text{MeOH})])} = \frac{1.60 \cdot 10^{-5} \text{ mol}}{8.44 \cdot 10^{-8} \text{ mol}} = 190$$

Table S1: Calculated $n(4VP)$ and equivalents of vinylpyridine relative to [Zn(L)(H₂O)(MeOH)].

	$n(4VP)$ [mol]	Equivalents
$S_{58}V_{42}^{157}$	$1.60 \cdot 10^{-5}$	190
$S_{65}V_{35}^{131}$	$1.33 \cdot 10^{-5}$	158
$S_{85}V_{15}^{154}$	$5.71 \cdot 10^{-6}$	68

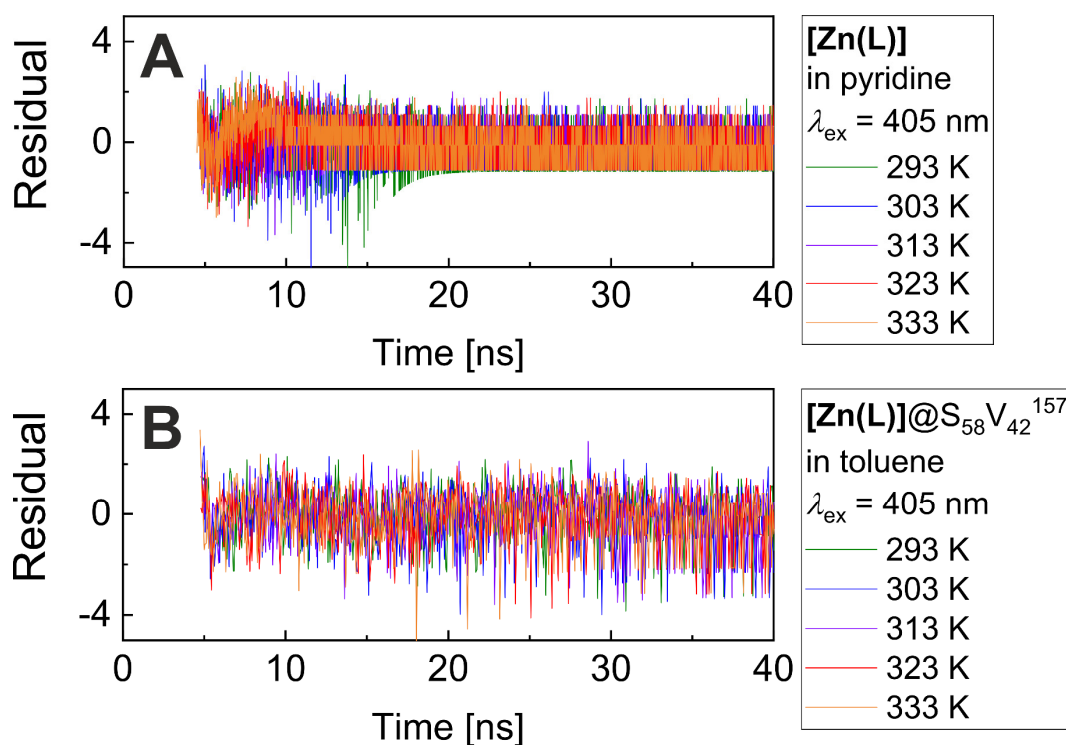


Figure S7: Residuals of the TCSPC detected fluorescence decays of [Zn(L)] in pyridine (A) and of [Zn(L)]@S₅₈V₄₂¹⁵⁷ micelles in toluene (B) ($\lambda_{\text{ex}} = 405 \text{ nm}$; $\lambda_{\text{em}} = 509 \text{ nm}$).

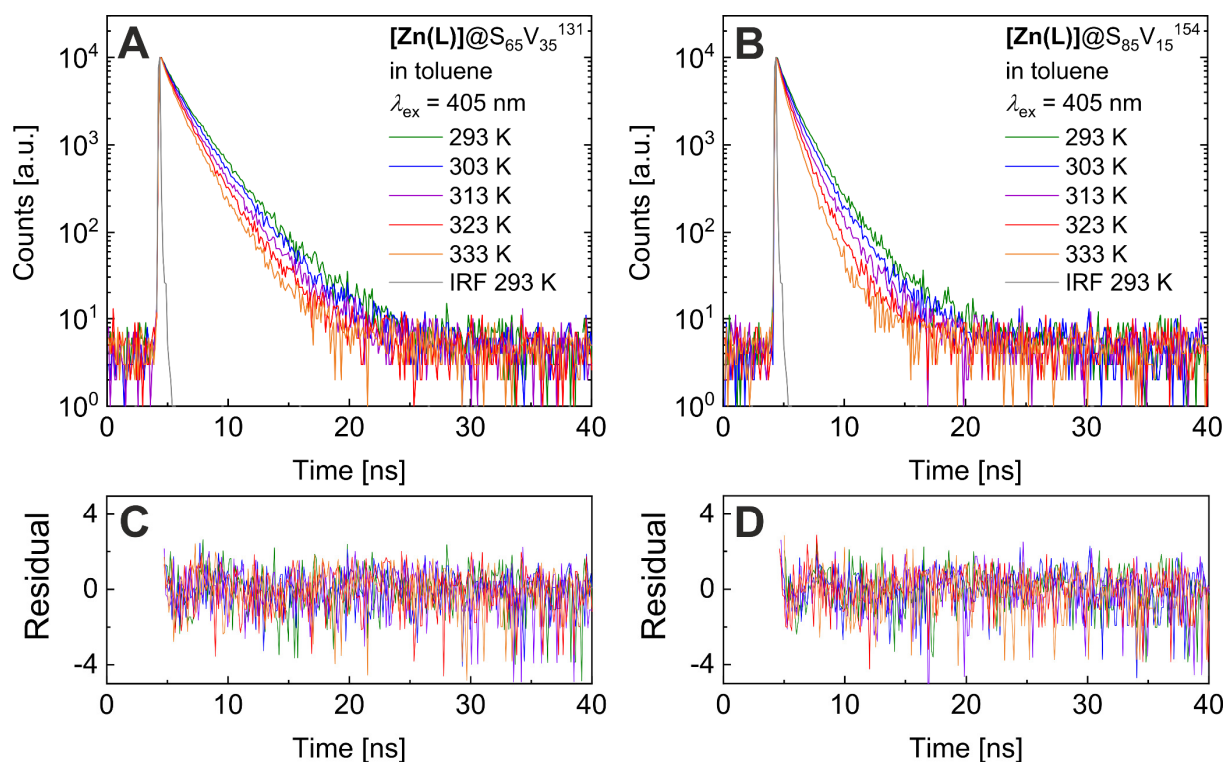
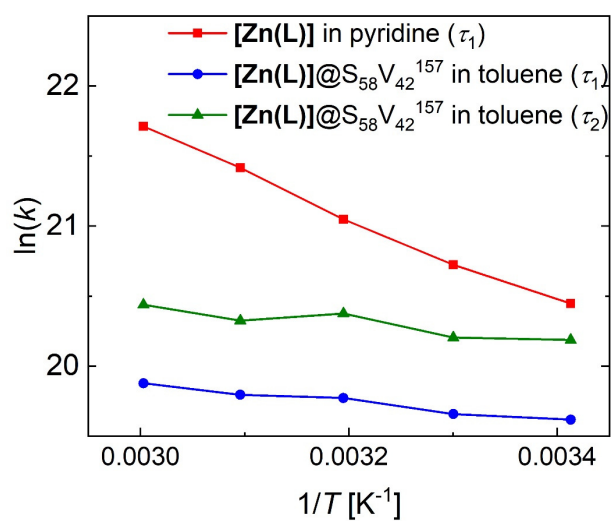


Figure S8: TCSPC detected fluorescence decays of [Zn(L)]@S₆₅V₃₅¹³¹ (A) with residuals (C) and [Zn(L)]@S₈₅V₁₅¹⁵⁴ (B) with residuals (D) in toluene ($\lambda_{\text{ex}} = 405 \text{ nm}$; $\lambda_{\text{em}} = 509 \text{ nm}$; IRF = instrumental resolution file).

Table S2: Lifetimes τ of $[\text{Zn}(\text{L})]$ in pyridine and $[\text{Zn}(\text{L})]@\text{BCP}$ in toluene derived from the lifetime measurements at different temperatures.

		293 K	303 K	313 K	323 K	333 K
$[\text{Zn}(\text{L})]$ in pyridine	τ_1 [ns]	1.319	1.000	0.723	0.500	0.372
$[\text{Zn}(\text{L})]@\text{S}_{58}\text{V}_{42}^{157}$ in toluene	τ_1 [ns]	3.020	2.901	2.587	2.530	2.330
	τ_2 [ns]	1.710	1.680	1.415	1.490	1.330
$[\text{Zn}(\text{L})]@\text{S}_{65}\text{V}_{35}^{131}$ in toluene	τ_1 [ns]	2.940	2.700	2.433	2.331	2.052
	τ_2 [ns]	1.490	1.357	1.169	1.159	1.009
$[\text{Zn}(\text{L})]@\text{S}_{85}\text{V}_{15}^{154}$ in toluene	τ_1 [ns]	2.780	2.380	2.104	1.830	1.970
	τ_2 [ns]	1.236	1.071	0.920	0.837	0.822

Figure S9: Arrhenius-plot of $[\text{Zn}(\text{L})]$ in pyridine and $[\text{Zn}(\text{L})]@\text{S}_{58}\text{V}_{42}^{157}$ in toluene derived from τ_1 and τ_2 .

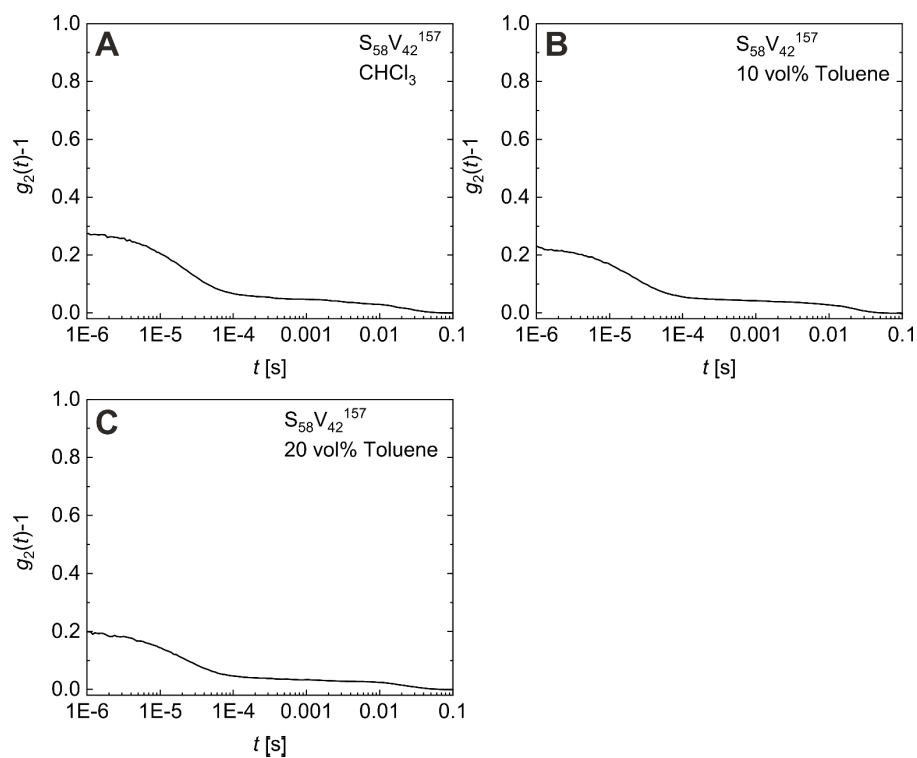


Figure S10: DLS measurements of neat $S_{58}V_{42}^{157}$ in a $CHCl_3$ -toluene series: Autocorrelation function $g_2(t)-1$ vs t of $S_{58}V_{42}^{157}$: 0% toluene (A), 10% toluene (B), and 20% toluene (C). The D_h distributions were not determined due to the very weak scattering intensity.

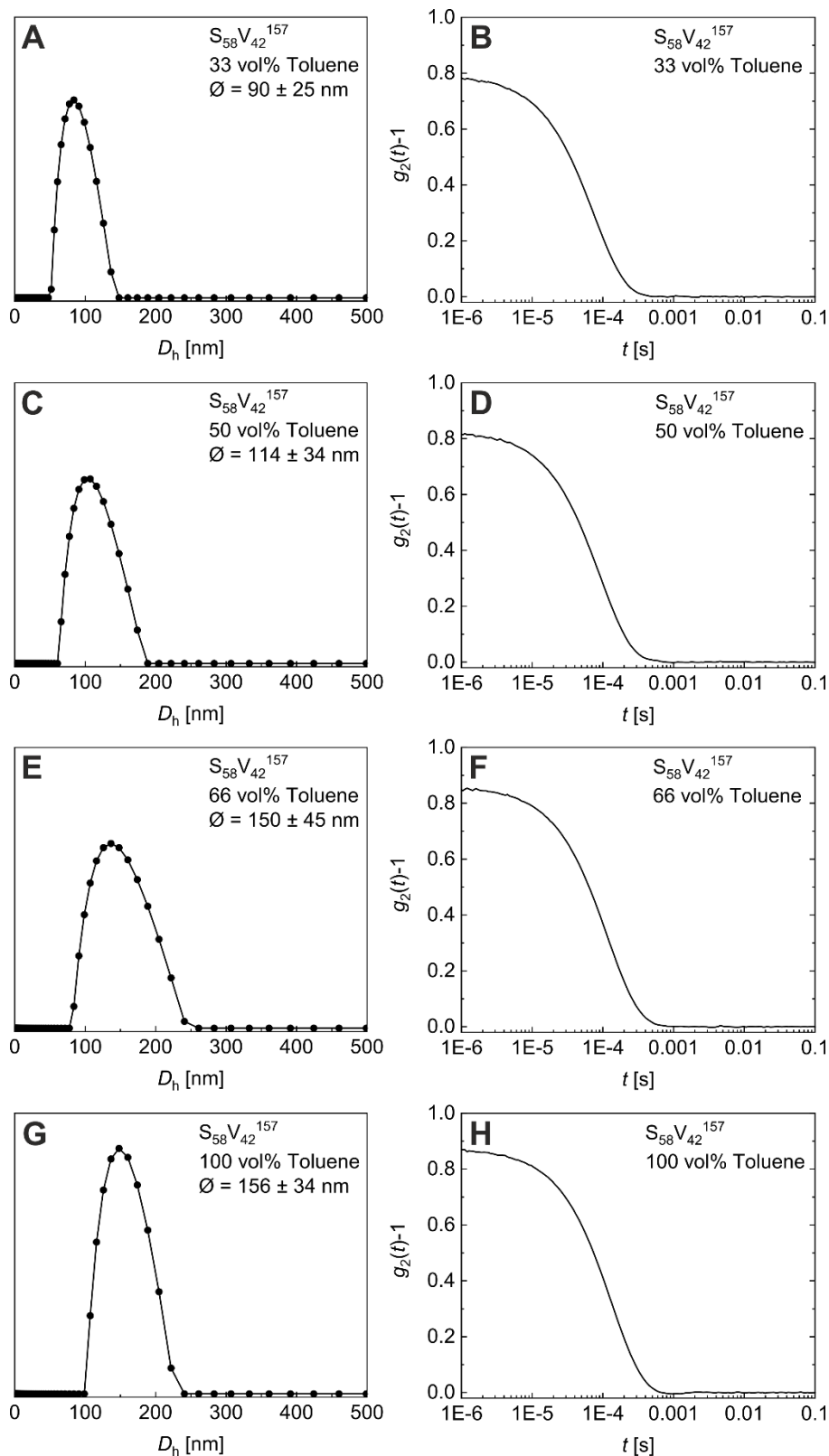


Figure S11: DLS measurements of neat $S_{58}V_{42}^{157}$ micelles in a CHCl_3 -toluene series: D_h distributions and corresponding autocorrelation functions $g_2(t)-1$ vs t of $S_{58}V_{42}^{157}$: 33% toluene (A/B), 50% toluene (C/D), 66% toluene (E/F), and 100% toluene (G/H).

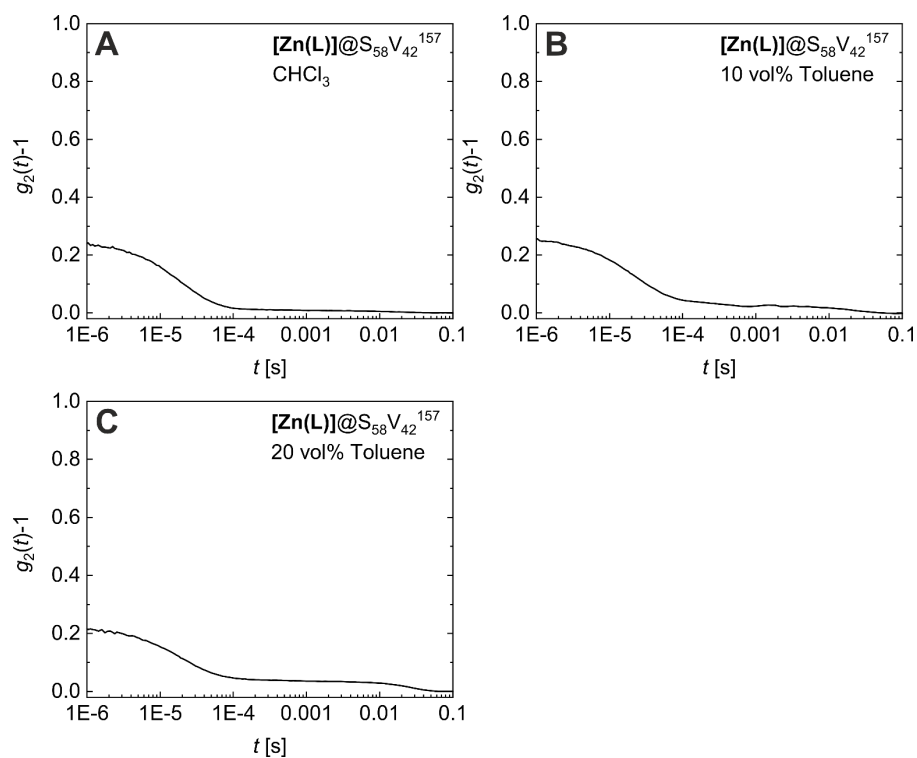


Figure S12: DLS measurements of $[\text{Zn(L)}]@S_{58}V_{42}^{157}$ in a CHCl_3 -toluene series: Autocorrelation function $g_2(t)-1$ vs t of $[\text{Zn(L)}]@S_{58}V_{42}^{157}$: 0% toluene (A), 10% toluene (B), and 20% toluene (C). The D_h distributions were not determined due to the very weak scattering intensity.

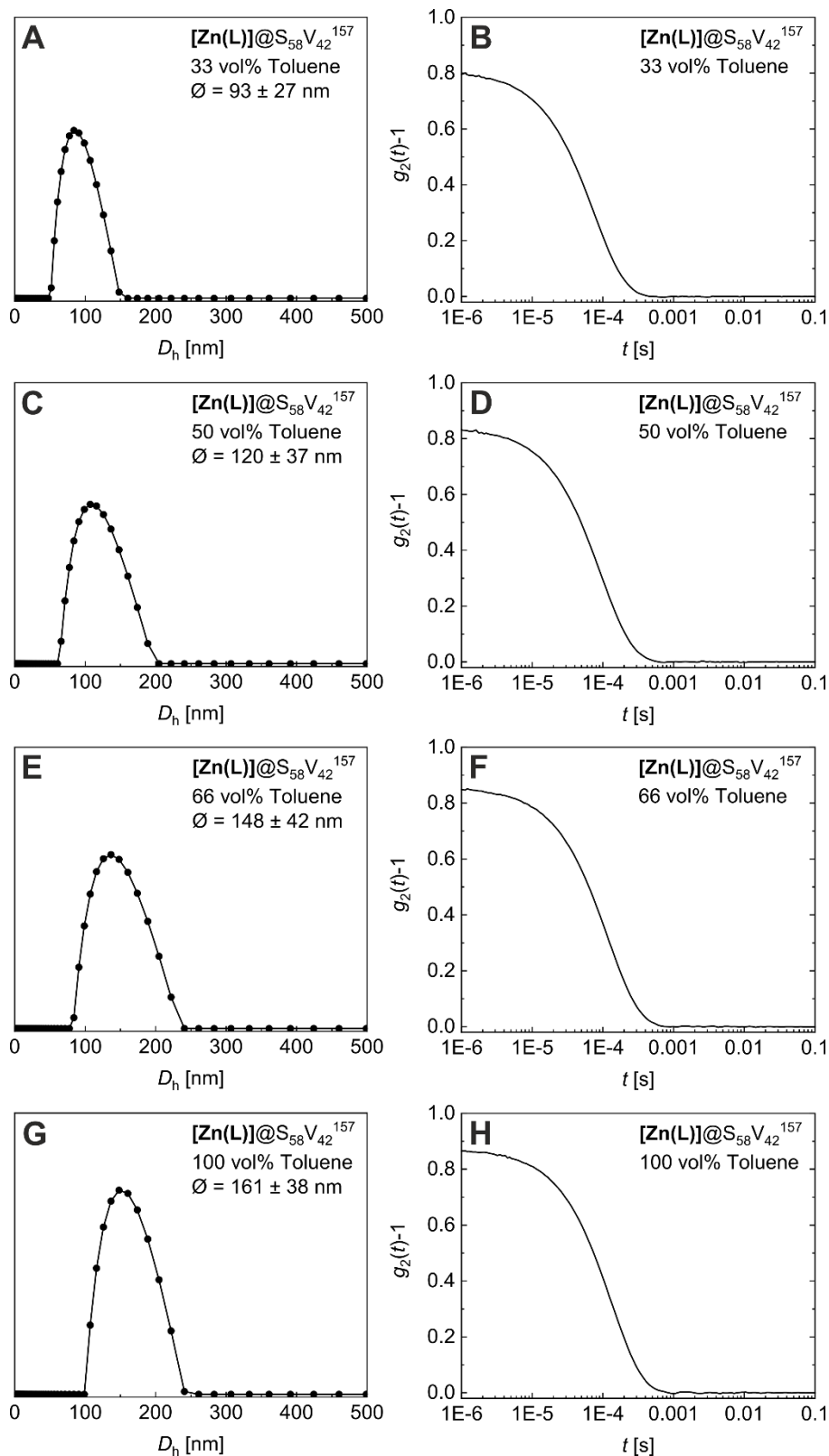


Figure S13: DLS measurements of $[\text{Zn(L)}]@S_{58}V_{42}^{157}$ micelles in a CHCl_3 -toluene series: D_h distributions and corresponding autocorrelation functions $g_2(t)-1$ vs t of $S_{58}V_{42}^{157}$: 33% toluene (A/B), 50% toluene (C/D), 66% toluene (E/F), and 100% toluene (G/H).

Calculation of $[4VP_{eff}]$ in the molecularly dissolved ($CHCl_3$) and in the micelle form (toluene)

Exemplarily for $[Zn(L)]@S_{58}V_{42}$ ¹⁵⁷:

$$m(4VP) = 0.42 \cdot 0.004 \text{ g} = 1.68 \cdot 10^{-3} \text{ g}$$

$$n(4VP) = \frac{m(4VP)}{M(4VP)} = \frac{1.68 \cdot 10^{-3} \text{ g}}{105.14 \text{ g mol}^{-1}} = 1.60 \cdot 10^{-5} \text{ mol}$$

In the molecularly dissolved form of the BCP, the BCP is solved in 30 mL chloroform.

$$[4VP_{eff, \text{molecularly dissolved}}] = \frac{n(4VP)}{V} = \frac{1.60 \cdot 10^{-5} \text{ mol}}{0.03 \text{ L}} = 5.33 \cdot 10^{-4} \frac{\text{mol}}{\text{L}}$$

In the micelle form of the BCP, the poly(4-vinylpyridine) block forms the core of the micelles (diameter 43 nm).

$$V(\text{core}) = \frac{4}{3}\pi r^3 = \frac{4}{3}\pi \cdot (21.5 \cdot 10^{-9})^3 = 4.16 \cdot 10^{-20} \text{ L}$$

$$m(\text{core}) = \delta(4VP) \cdot V(\text{core}) = 1150 \frac{\text{g}}{\text{L}} \cdot 4.16 \cdot 10^{-20} \text{ L} = 4.78 \cdot 10^{-17} \text{ g}$$

$$n(\text{core}) = \frac{m(\text{core})}{M(4VP)} = \frac{4.78 \cdot 10^{-17} \text{ g}}{105.14 \text{ g mol}^{-1}} = 4.55 \cdot 10^{-19} \text{ mol}$$

$$[4VP_{eff, \text{micelle}}] = \frac{n(\text{core})}{V(\text{core})} = \frac{4.55 \cdot 10^{-19} \text{ mol}}{4.16 \cdot 10^{-20} \text{ L}} = 10.94 \frac{\text{mol}}{\text{L}}$$

Please note, that the calculated values are based on the following assumptions:

- All polymer chains form micelles
- All pyridine substituents are available for ligation

For this reason, the exact values are not determinable. However, the order of magnitude shows that the local pyridine concentration inside the micelles is strongly increased compared to the molecularly dissolved form.

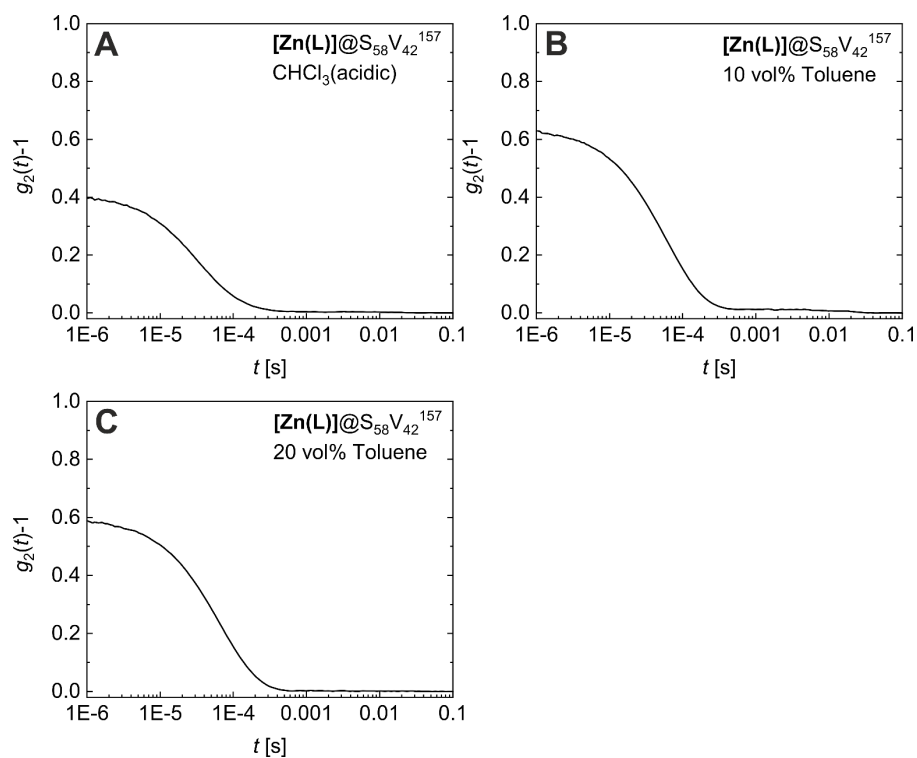


Figure S14: DLS measurements of $[\text{Zn}(\text{L})]@S_{58}V_{42}^{157}$ in a $\text{CHCl}_3(\text{acidic})$ -toluene series: Autocorrelation function $g_2(t)-1$ vs t of $[\text{Zn}(\text{L})]@S_{58}V_{42}^{157}$: 0% toluene (A), 10% toluene (B), and 20% toluene (C). The D_h distributions were not determined due to the very weak scattering intensity.

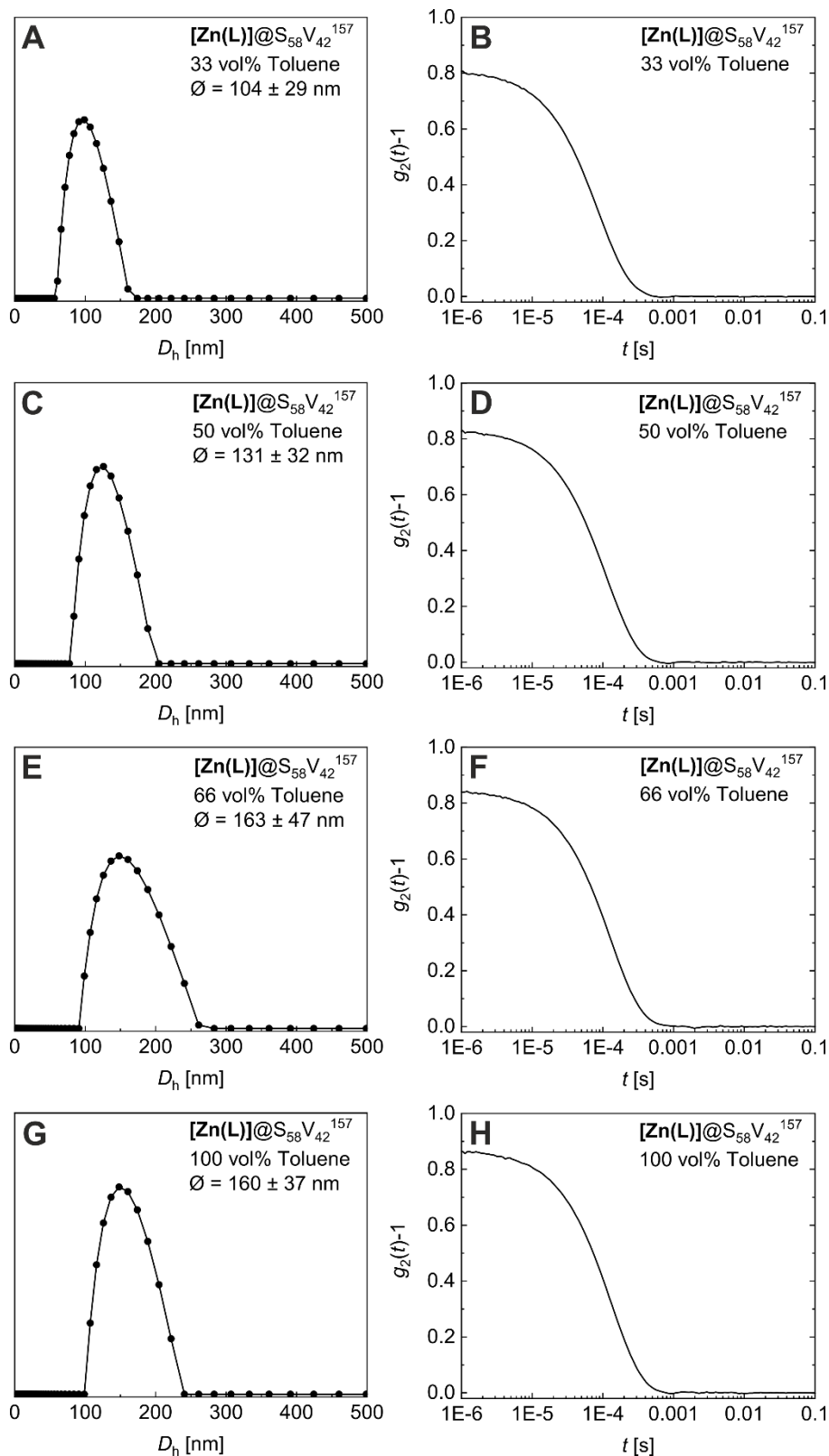


Figure S15: DLS measurements of $[\text{Zn(L)}]@S_{58}V_{42}^{157}$ micelles in a $\text{CHCl}_3(\text{acidic})$ -toluene series: D_h distributions and corresponding autocorrelation functions $g_2(t)-1$ vs t of $S_{58}V_{42}^{157}$: 33% toluene (A/B), 50% toluene (C/D), 66% toluene (E/F), and 100% toluene (G/H).

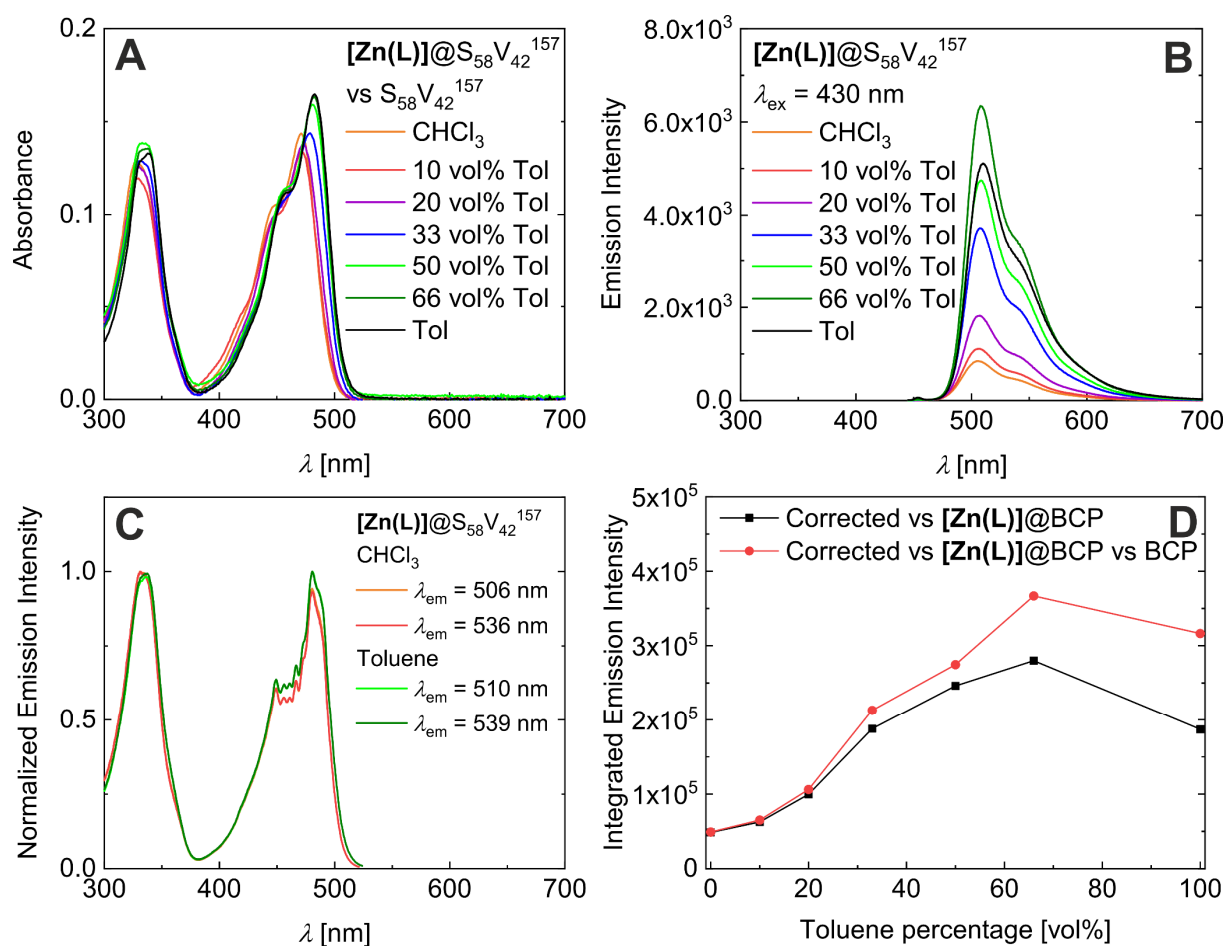


Figure S16: Absorbance and emission spectra of $[\text{Zn(L)}]@S_{58}V_{42}^{157}$ in a CHCl_3 /toluene series (A/B; $\lambda_{\text{ex}} = 430 \text{ nm}$). Fluorescence excitation spectra of $[\text{Zn(L)}]@S_{58}V_{42}^{157}$ in CHCl_3 and toluene (C). Plot of the integrated emission intensity vs. toluene content of $[\text{Zn(L)}]@S_{58}V_{42}^{157}$ (D). Both correction possibilities are plotted to show that this trend is retained for both possibilities: The correction of the emission vs. the absorbance value at $\lambda_{\text{ex}} = 430 \text{ nm}$ using the pure solvent as background (red) and using the neat BCP micelles as background (black). The weak emission at approximately $\lambda = 450 \text{ nm}$ is due to a measurement artefact.

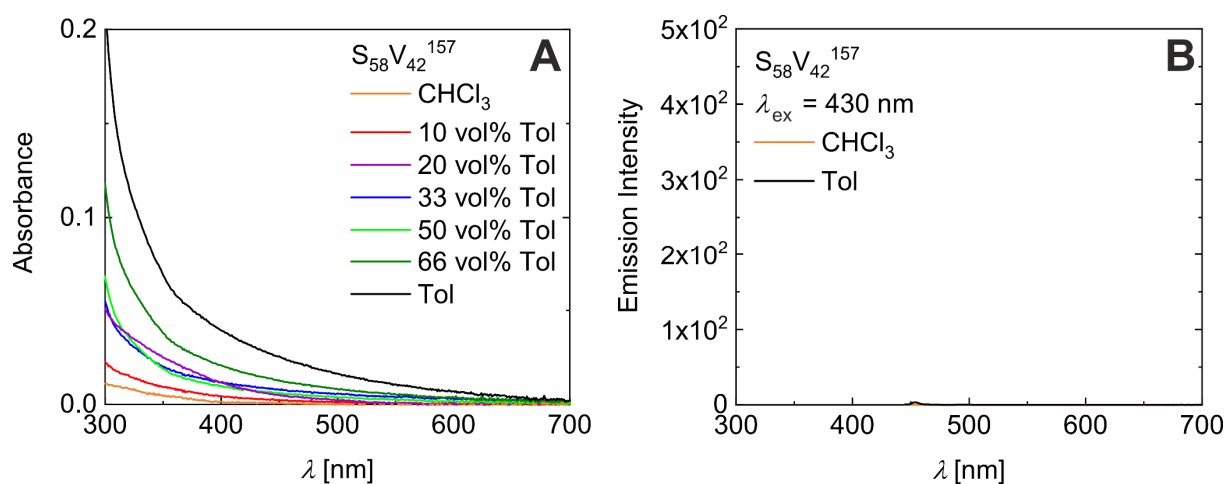


Figure S17: Absorbance spectra of $S_{58}V_{42}^{157}$ in a $CHCl_3$ -toluene series (A). Emission spectra of $S_{58}V_{42}^{157}$ in $CHCl_3$ and toluene ($\lambda_{ex} = 430$ nm, B). The weak emission at approximately $\lambda = 450$ nm is due to a measurement artefact.

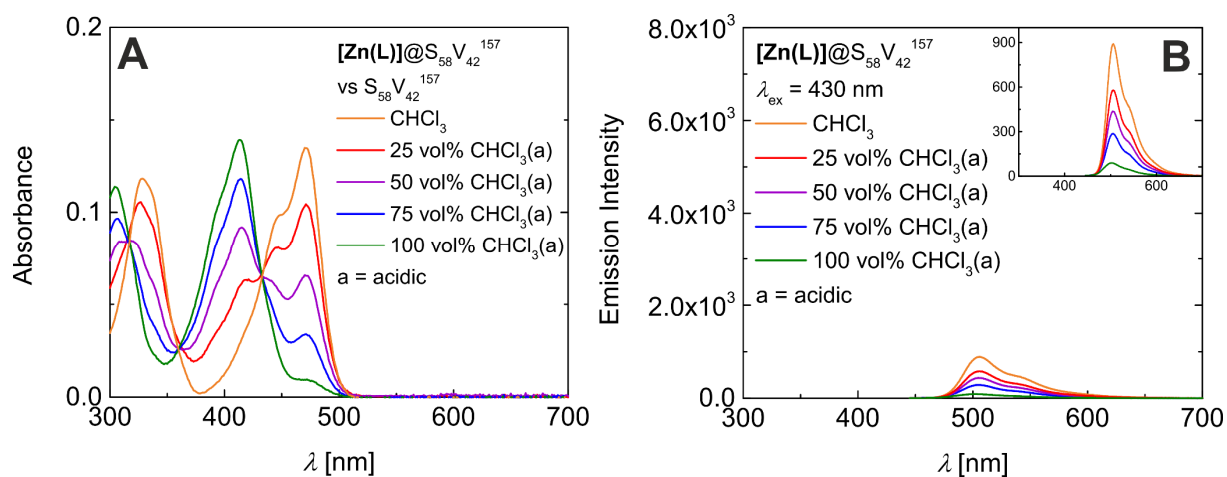


Figure S18: Absorbance and emission spectra of $[Zn(L)]@S_{58}V_{42}^{157}$ in a $CHCl_3$ - $CHCl_3$ (acidic) series (A/B; $\lambda_{ex} = 430$ nm). The weak emission at approximately $\lambda = 450$ nm is due to a measurement artefact.

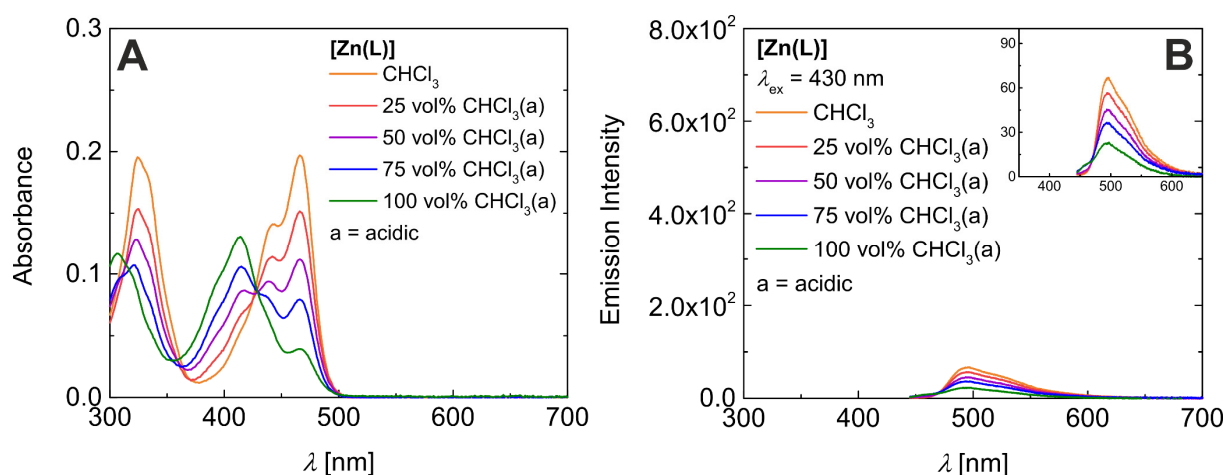


Figure S19: Absorbance and emission spectra of $[\text{Zn}(\text{L})]$ in a $\text{CHCl}_3\text{-CHCl}_3(\text{acidic})$ series (A/B; $\lambda_{\text{ex}} = 430 \text{ nm}$). The weak emission at approximately $\lambda = 450 \text{ nm}$ is due to a measurement artefact.

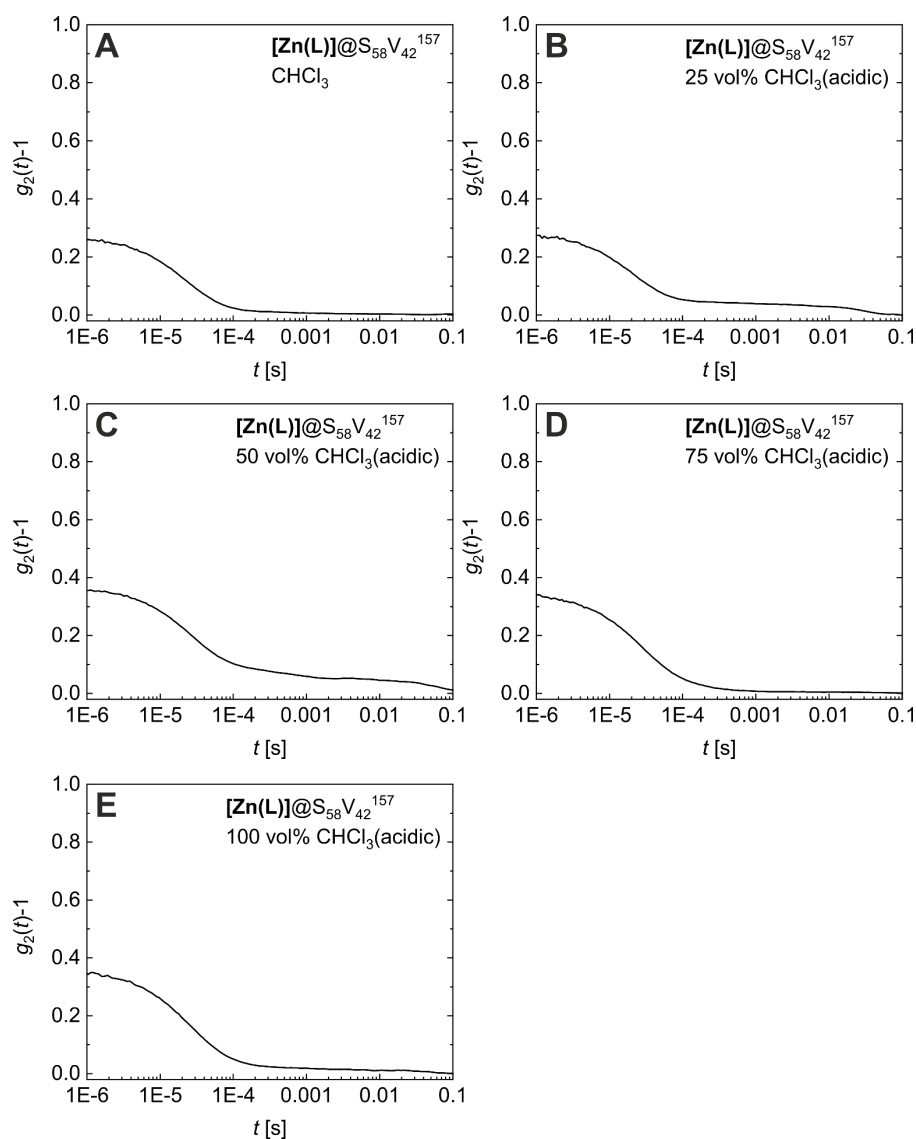


Figure S20: DLS measurements of $[\text{Zn}(\text{L})]@S_{58}V_{42}^{157}$ in a $\text{CHCl}_3\text{-CHCl}_3(\text{acidic})$ series: Autocorrelation function $g_2(t)-1$ vs. t of $[\text{Zn}(\text{L})]@S_{58}V_{42}^{157}$ in CHCl_3 (A), 25 vol% $\text{CHCl}_3(\text{acidic})$ (B), 50 vol%

CHCl₃(acidic) (C), 75 vol% CHCl₃(acidic) (D), and 100 vol% CHCl₃(acidic) (E). The D_h distributions were not determined due to the very weak scattering intensities.

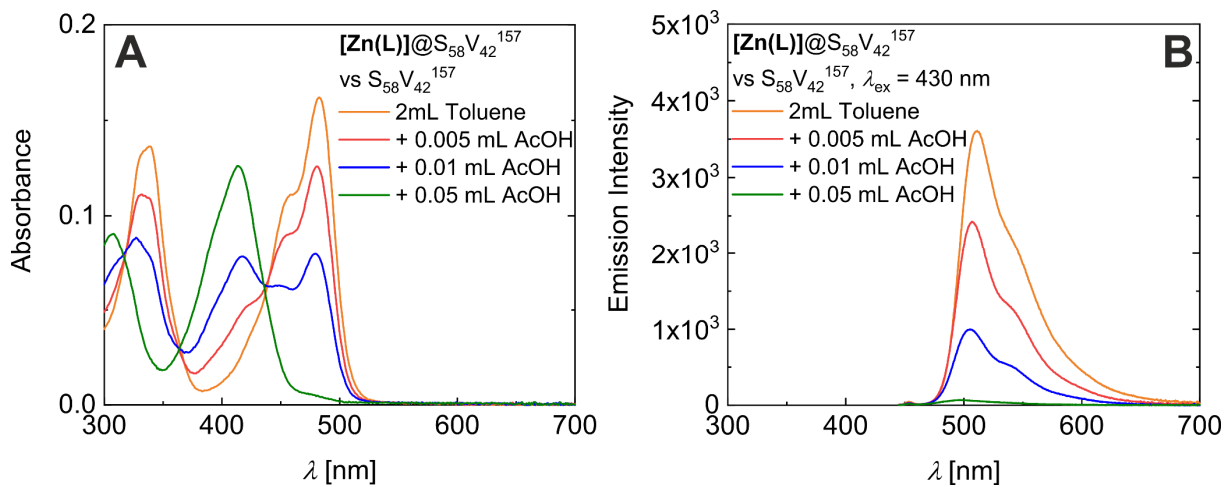


Figure S21: Absorbance (A) and emission (B, $\lambda_{\text{ex}} = 430$ nm) spectra of [Zn(L)]@ S₅₈V₄₂¹⁵⁷ in toluene in dependence of the amount of added acetic acid. The weak emission at approximately $\lambda = 450$ nm is due to a measurement artefact.

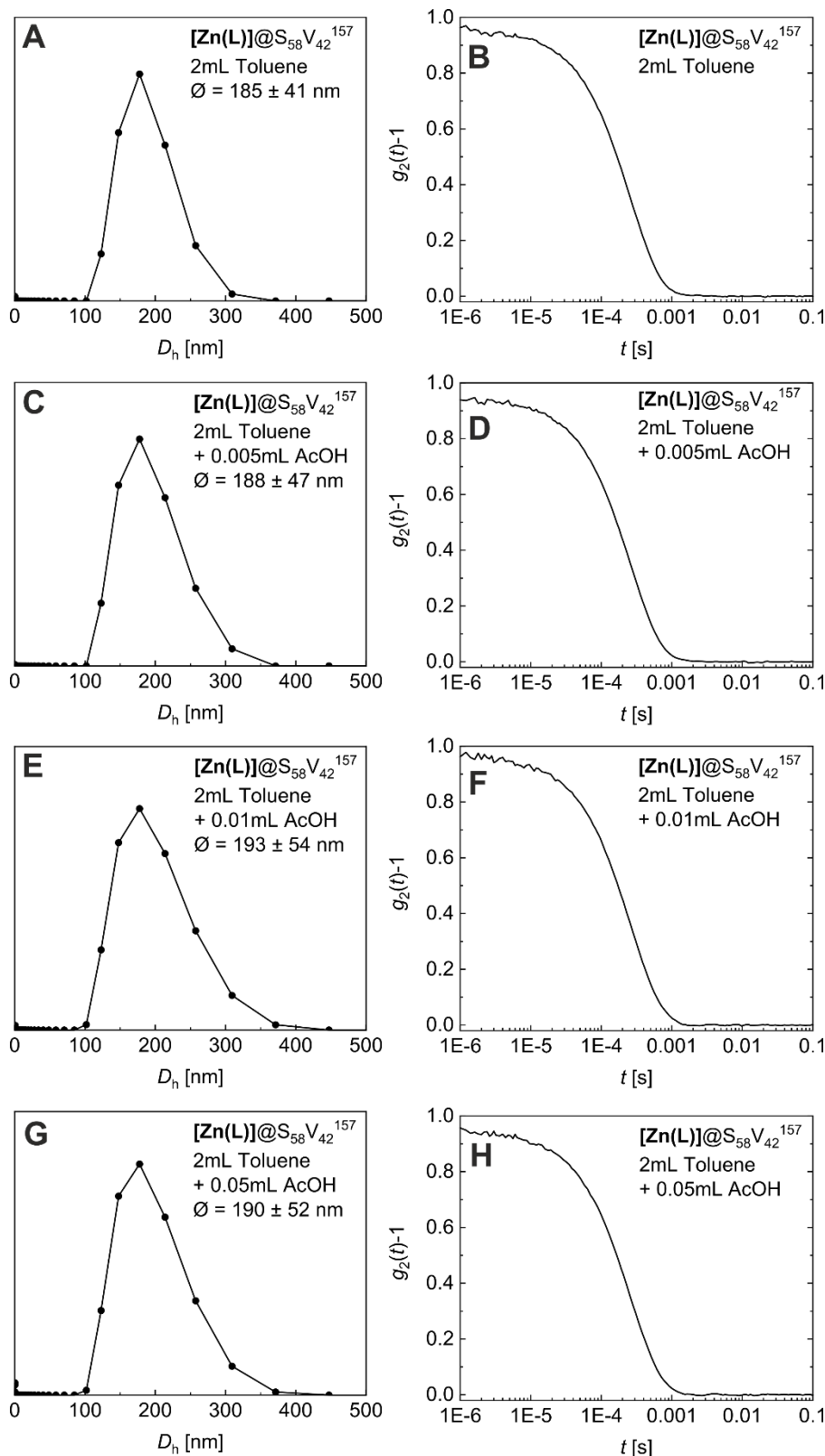


Figure S22: DLS measurements of $[\text{Zn}(\text{L})]@S_{58}V_{42}^{157}$ micelles in toluene in dependence of the amount of added acetic acid: D_h distributions and corresponding autocorrelation functions $g_2(t)-1$ vs. t of $[\text{Zn}(\text{L})]@S_{58}V_{42}^{157}$: toluene (A/B), 2 mL toluene + 0.005 mL AcOH (C/D), 2 mL toluene + 0.01 mL AcOH (E/F), and 2 mL toluene + 0.05 mL AcOH (G/H). The measurements were performed on a different instrument.

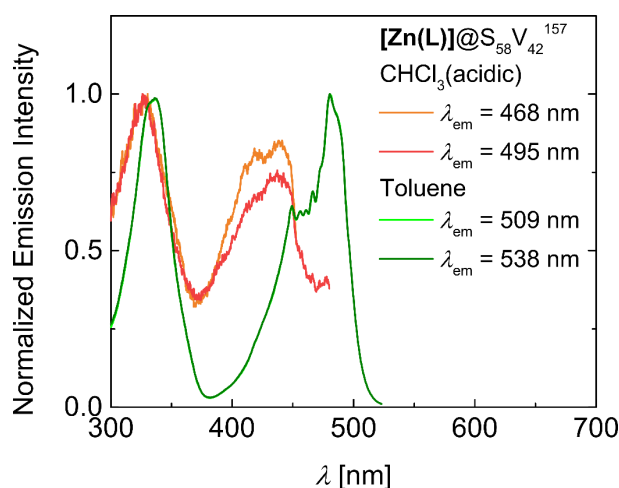


Figure S23: Normalized fluorescence excitation spectra of $[\text{Zn}(\text{L})]@S_{58}V_{42}^{157}$ in toluene and $\text{CHCl}_3(\text{acidic})$.

References

- (1) Kurz, H.; Hörner, G.; Weser, O.; Manni, G. L.; Weber, B. Quenched Lewis Acidity: Studies on the Medium Dependent Fluorescence of Zinc(II) Complexes. *Chem. Eur. J.* **2021**, *27* (27), 15159–15171. DOI: 10.1002/chem.202102086.
- (2) Göbel, C.; Hils, C.; Drechsler, M.; Baabe, D.; Greiner, A.; Schmalz, H.; Weber, B. Confined Crystallization of Spin-Crossover Nanoparticles in Block-Copolymer Micelles. *Angew. Chem. Int. Ed.* **2020**, *59* (14), 5765–5770. DOI: 10.1002/anie.201914343.
- (3) Göbel, C.; Hörner, G.; Greiner, A.; Schmalz, H.; Weber, B. Synthesis of Zn-based 1D and 2D coordination polymer nanoparticles in block copolymer micelles. *Nanoscale Adv.* **2020**, *2* (10), 4557–4565. DOI: 10.1039/D0NA00334D.
- (4) Göbel, C.; Marquardt, K.; Baabe, D.; Drechsler, M.; Loch, P.; Breu, J.; Greiner, A.; Schmalz, H.; Weber, B. DOI: 10.26434/chemrxiv-2021-jbj2n.
- (5) W. S. Rasband. *ImageJ Bethesda, National Institute of Health, Maryland, USA, 1997.*

8 List of Publications

The following publications were published during the work on this thesis and are a part of this thesis:

1. Hannah Kurz, Konstantin Schötz, Ilias Papadopoulos, Frank W. Heinemann, Harald Maid, Dirk M. Guldi, Anna Köhler, Gerald Hörner, and Birgit Weber*, *J. Am. Chem. Soc.* **2021**, *143*, 3466–3480. “A Fluorescence-Detected Coordination-Induced Spin State Switch” doi: 10.1021/jacs.0c12568
2. Hannah Kurz, Gerald Hörner, Oskar Weser, Giovanni Li Manni, Birgit Weber*, *Chem. Eur. J.* **2021**, *27*, 15159-15171. “Quenched Lewis Acidity: Studies on the Medium Dependent Fluorescence of Zinc(II) Complexes” doi: 10.1002/chem.202102086
3. Hannah Kurz, Christian Hils, Jana Timm, Gerald Hörner, Andreas Greiner, Roland Marschall, Holger Schmalz, Birgit Weber*, *Angew. Chem. Int. Ed.* **2022**, *61*, e202117570. “Self-Assembled Fluorescent Block Copolymer Micelles with Responsive Emission” doi: 10.1002/anie.202117570

The following publications were published during the work on this thesis and are not a part of this thesis:

1. Charles Lochenie, Konstantin Schötz, Fabian Panzer, Hannah Kurz, Bernadette Maier, Florian Puchtler, Seema Agarwal, Anna Köhler*, Birgit Weber*, *J. Am. Chem. Soc.* **2018**, *140*, 2, 700–709. "Spin-Crossover Iron(II) Coordination Polymer with Fluorescent Properties: Correlation between Emission Properties and Spin State" doi: 10.1021/jacs.7b10571 (Please note, that I was involved in the revision process, but not in the first submission process).
2. André Bloesser, Jana Timm, Hannah Kurz, Wolfgang Milius, Shusaku Hayama, Josef Breu, Birgit Weber, Roland Marschall*, *Sol. RRL* **2020**, *4*, 1900570. “A Novel Synthesis Yielding Macroporous CaFe₂O₄ Sponges for Solar Energy Conversion” doi: 10.1002/solr.201900570

3. Hannah Kurz, Joan Sander, Birgit Weber*, *Z. Anorg. Allg. Chem.* **2020**, *646*, 800–807. “Influence of CF₃ Substituents on the Spin Crossover Behavior of Iron(II) Coordination Polymers with Schiff Base-like Ligands” doi: 10.1002/zaac.201900354
4. André Bloesser, Hannah Kurz, Jana Timm, Florian Wittkamp, Christopher Simon, Shusaku Hayama, Birgit Weber*, Ulf-Peter Apfel, and Roland Marschall*, *ACS Appl. Nano Mater.* **2020**, *3*, 11587–11599. “Tailoring the Size, Inversion Parameter, and Absorption of Phase-Pure Magnetic MgFe₂O₄ Nanoparticles for Photocatalytic Degradations” doi: 10.1021/acsanm.0c02705
5. Hannah Kurz, Gerald Hörner, Birgit Weber*, *Z. Anorg. Allg. Chem.* **2021**, *647*, 896–904. “An Iron(II) Spin Crossover Complex with a Maleonitrile Schiff base-like Ligand and Scan Rate-dependent Hysteresis above Room Temperature” doi: 10.1002/zaac.202000407
6. Thilini K. Ekanayaka, Hannah Kurz, Ashley S. Dale, Guanhua Hao, Aaron Mosey, Esha Mishra, Alpha T. N’Diaye, Ruihua Cheng, Birgit Weber and Peter A. Dowben*, *Mater. Adv.* **2021**, *2*, 760–768. “Probing the unpaired Fe spins across the spin crossover of a coordination polymer” doi: 10.1039/d0ma00612b
7. Antoine Viard, Hannah Kurz, Abhijeet Lale, Lutz Heymann, Birgit Weber, Samuel Bernard, Michael Knauer, and Günter Motz*, *ACS Appl. Mater. Interfaces* **2021**, *13*, 8745–8753. “Superparamagnetic Silicon Carbonitride Ceramic Fibers Through In Situ Generation of Iron Silicide Nanoparticles During Pyrolysis of an Iron-Modified Polysilazane” doi: 10.1021/acsami.0c20885
8. Christopher Simon, Mohamed Barakat Zakaria, Hannah Kurz, David Tetzlaff, André Blösser, Morten Weiss, Jana Timm, Birgit Weber, Ulf-Peter Apfel, Roland Marschall*, *Chem. Eur. J.* **2021**, *27*, 16990–17001. “Magnetic NiFe₂O₄ Nanoparticles Prepared via Non-Aqueous Microwave-Assisted Synthesis for Application in Electrocatalytic Water Oxidation” doi: 10.1002/chem.202101716
9. Christopher Simon, André Blösser, Mirco Eckardt, Hannah Kurz, Birgit Weber, Mirijam Zobel, Roland Marschall*, *Z. Anorg. Allg. Chem.* **2021**, *647*, 2061–2072. “Magnetic properties and structural analysis on spinel MnFe₂O₄ nanoparticles prepared via non-aqueous microwave synthesis” doi: 10.1002/zaac.202100190

Contributions to national and international conferences

1. Hannah Kurz, Charles Lochenie, Kristina Wagner, Matthias Karg, Birgit Weber* **POSTER** “Synthesis and Optical Properties of Phenanthroline-derived Schiff Base-like Dinuclear Ru(II)-Ni(II) Complexes”, 7. ECOSTbio, 2017, Dublin, Ireland, 14.-15.12.2017.
2. Hannah Kurz, Charles Lochenie, Birgit Weber* **POSTER** “Phenanthroline-derived schiff base-like dinuclear Ru(II)-Ni(II) complexes and their optical properties”, 14. Koordinationschemie-Treffen, 2018, Heidelberg, Deutschland, 11.-13.03.2018.
3. Hannah Kurz, Konstantin Schötz, Fabian Panzer, Birgit Weber* **POSTER** “Synthesis and optical properties of phenazine-derived Schiff base-like complexes”, 8. ECOSTbio, 2018, Berlin, Deutschland, 09.-11.04.2018.
4. Hannah Kurz, Charles Lochenie, Birgit Weber* **POSTER** “Synthesis and Optical Properties of Phenanthroline-derived Schiff Base-like Dinuclear Ru(II)-Ni(II) Complexes”, 43. International Conference on Coordination Chemistry, 2018, Sendai, Japan, 30.07-04.08.2018. **POSTER PRIZE**
5. Hannah Kurz, Birgit Weber* **POSTER** “Phenazine-derived Schiff base-like Ni(II) complexes and their optical properties”, 16. Koordinationschemie-Treffen, 2020, Freiburg, Deutschland, 01.-03.03.2020.
6. Hannah Kurz, Joan Sander, Birgit Weber* **POSTER with Flashtalk** “Influence of CF₃ substituents on the spin crossover behavior of iron(II) coordination polymers with Schiff base-like ligands”, 5. Bordeaux Olivier Kahn Discussions, 2020, virtual version (Bordeaux, France), 08.-10.06.2020.
7. Hannah Kurz, Konstantin Schötz, Gerald Hörner, Birgit Weber* **POSTER** “Fluorescent phenazine-derived N₂O₂ chelated Ni(II) complexes”, 27. Lecture Conference on Photochemistry, 2020, virtual version (Kiel, Germany), 14.-15.09.2020.
8. Hannah Kurz, Gerald Hörner, Birgit Weber* **ORAL PRESENTATION** “A Fluorescence-Detected Coordination-Induced Spin State Switch”, International Conference of Photochemistry, 2021, virtual version (Geneva, Switzerland), 18.-23.07.2021.
9. Hannah Kurz, Gerald Hörner, Birgit Weber* **INVITED ORAL PRESENTATION** “A Fluorescence-Detected Coordination-Induced Spin State Switch”, 2BSwitch Symposium, 2021, virtual version, 30.08-02.09.2021

9 Acknowledgement

First of all, I would like to thank my supervisor Prof. Dr. Birgit Weber for giving me the opportunity to do my PhD in her workgroup and providing me with such an interesting topic. I am very grateful for your ongoing support, your helpful mentoring, the freedom in research, and the great trust in my abilities. Your optimism and your persistence has been very inspiring for me and I learned a lot from you over the past years.

I would also like to thank my former and current lab colleagues Johannes Weihermüller, Katja Dankhoff, Christoph Göbel, Sophie Schönfeld, Andreas Dürrmann, Constantin Schreck, and Michael Fink for the good working atmosphere and the great support. Moreover, I would like to thank Dr. Charles Lochenie, from whom I learned a lot and who started this fascinating project. Special thanks to my lab colleague Florian Daumann for the great atmosphere in the lab and his never-ending good mood.

I would like to thank Dr. Gerald Hörner, who always encouraged me to work hard on my goals and who helped me a lot in improving my scientific writing skills. Thank you very much for your patience!

I would also like to thank all my under-graduate, graduate and HiWi students, who taught me how to supervise and motivate people, namely: Christian Böhm, Markus Kötzsche, Florian Daumann, Joan Sander, Marie Bergmann, Tilman Durst, Tobias Seifert, Lion Schumacher.

I thank my cooperation partners Prof. Dr. Anna Köhler, Konstantin Schötz, Ilias Papadopoulos, Dr. Frank W. Heinemann, Dr. Harald Maid, Prof. Dr. Dirk Guldi, Dr. Giovanni Li Manni, Oskar Weser, Christian Hils, Prof. Dr. Andreas Greiner, Prof. Dr. Roland Marschall, and Dr. Holger Schmalz. Additionally, I would like to thank the Inorganic Chemistry II for the good collaboration and especially our former secretary Marlies Schilling, our secretary Dana Dopheide, and the technicians Heidi Maisel, Anna Dietel, Christine Fell, and Sandra Keller. I would also like to thank Dr. Ulrike Lacher for the MS spectrometry, Florian Puchtler for PXRD measurements, Dr. Jana Timm for the support with the fluorescence spectrometer, the MCII for access to the fluorescence spectrometer, and the ACI (Zobel) for access to the litesizer. Further thanks go to the mechanic staff, the glassblowers, the purchasing department, and finally to the team of the Mensa and the salad bar for providing such excellent food during the whole time in Bayreuth.

Acknowledgement

A huge thank you goes to all my fellow students and friends who accompanied me through my studies and doctoral thesis and without whom my time in Bayreuth would not have been half as enjoyable.

Last but not least, I would like to thank my family and Max, who have been there for me in both good and bad times and always supported and believed in me.

10 (Eidesstattliche) Versicherungen und Erklärungen

(§ 9 Satz 2 Nr. 3 PromO BayNAT)

Hiermit versichere ich eidesstattlich, dass ich die Arbeit selbstständig verfasst und keine anderen als die von mir angegebenen Quellen und Hilfsmittel benutzt habe (vgl. Art. 64 Abs. 1 Satz 6 BayHSchG).

(§ 9 Satz 2 Nr. 3 PromO BayNAT)

Hiermit erkläre ich, dass ich die Dissertation nicht bereits zur Erlangung eines akademischen Grades eingereicht habe und dass ich nicht bereits diese oder eine gleichartige Doktorprüfung endgültig nicht bestanden habe.

(§ 9 Satz 2 Nr. 4 PromO BayNAT)

Hiermit erkläre ich, dass ich Hilfe von gewerblichen Promotionsberatern bzw. -vermittlern oder ähnlichen Dienstleistern weder bisher in Anspruch genommen habe noch künftig in Anspruch nehmen werde.

(§ 9 Satz 2 Nr. 7 PromO BayNAT)

Hiermit erkläre ich mein Einverständnis, dass die elektronische Fassung der Dissertation unter Wahrung meiner Urheberrechte und des Datenschutzes einer gesonderten Überprüfung unterzogen werden kann.

(§ 9 Satz 2 Nr. 8 PromO BayNAT)

Hiermit erkläre ich mein Einverständnis, dass bei Verdacht wissenschaftlichen Fehlverhaltens Ermittlungen durch universitätsinterne Organe der wissenschaftlichen Selbstkontrolle stattfinden können.

Bayreuth, den 25.04.2022

Ort, Datum

Unterschrift